JET–R(00)02

Many Authors

Descriptive Analysis of 1999 Task Force P Data

JET–R(00)02

Descriptive Analysis of 1999 Task Force P Data

Many Authors.

EURATOM/UKAEA Fusion Association, Culham Science Centre,
Abingdon, Oxfordshire, OX14 3EA, UK.

July 2000

PREFACE

As part of the winding-up of the JET Joint Undertaking, an agreement was established with UKAEA to validate the 1999 Gas Box data and make a descriptive analysis of the data. This report constitutes one of the deliverables specified under the agreement and describes the descriptive data analysis work undertaken examining results from the Task Force A and P campaigns in 1999. A wide range of issues are covered in this report, including:- inboard launched pellet fuelling studies; helium exhaust and transport; the effect of edge-q on neo-classical tearing mode stability and the possibility of stabilising these modes with ICRH; an overview of results from the 1999 international collaborative JET experiments on the RI mode; analysis carbon films on MkIIGB tiles and studies of hydrogen released from tiles using laser desorption; and SOL characterisation studies using tile thermocouples and probe measurements.

CONTENTS

1. PELLET PENETRATION AND MASS RE-DISTRIBUTION

T T C Jones[1], S J Cox[1], L.D. Horton[2], G Saibene[3].

JET Joint Undertaking, Abingdon, Oxfordshire, OX14 3EA, UK.

[1] EURATOM/UKAEA Fusion Association, Culham Science Centre, Abingdon, Oxfordshire, OX14 3DB, UK.

[2] Max-Planck-Institut für Plasmaphysik, IPP-EURATOM Association, Boltzmannstrasse 2, D-85748 Garching, Germany.

[3] EFDA Close SupportUnit Garching, Max-Planck-Institut für Plasmaphysik, Boltzmannstrasse 2, D-85748 Garching, Germany.

1.1 Overview

The physical dependences of pellet fuelling characteristics upon target plasma parameters are expected to be those controlling (i) ablation and (ii) acceleration of the cold ablatant plasmoid cloud. The most comprehensively benchmarked ablation model is employed in the Neutral Gas Shielding (NGS) code [1.1], which takes into account relevant atomic physics processes (excitation and radiation) governing inelastic collisions between plasma particles and the neutral gas cloud surrounding the ablating pellet. The basic process governing the fast radial drift of the cold plasmoid formed by the ablating pellet is a dynamic MHD effect, see e.g. reference [1.2], resulting from electric polarisation of the plasmoid in the non-uniform tokamak magnetic field. The polarisation occurs because the plasmoid is localised within the background plasma; the time taken for the plasmoid to expand in the parallel magnetic field direction to fill a flux tube is governed by the ion thermal velocity, whilst the parallel electron heat-flux into the plasmoid occurs on a much faster (≈1μs) timescale. This situation causes high-pressure local perturbation and vertical charge separation within the plasmoid (due to the oppositely directed ∇B drift of the ions and electrons). This charge separation causes an E×B radially outward acceleration of the plasmoid (i.e. in the -∇B direction) whose duration is determined by the time τ taken for the background plasma to "short out" the vertical electric field; this time corresponds to the shear Alfvén transit time over a connection length i.e. $\tau = \pi qR/v_A$ (≈ a few μs) which is still shorter than the time required for the high kinetic pressure of the plasmoid to equilibrate along the magnetic field. Therefore a finite distance Δ is traversed by the plasmoid in the direction of increasing R before the acceleration stops due to the eventual destruction of the electric polarisation field.

The net deposition of the pellet material in the target plasma is a combination of (i) the penetration distance $\lambda_{penetration}$ of the ablating pellet and (ii) the plasmoid displacement distance Δ. The physics of the processes involved in ablation and plasmoid drift, outlined in the previous paragraph, lead to the following dependences of these two quantities on plasma parameters:

(i) $\lambda_{penetration} \propto v_{pell}^{1/3} \cdot f(T_e)$ (1.1)

where v_{pell} is the pellet injection speed and $f(T_e)$ is a strongly decreasing function of the target plasma electron temperature. This relationship holds for spatially uniform target plasma; the

effect of profile shape is to change the exponent of v_{pell} and the particular form of $f(T_e)$. A large experimental database from various tokamaks using outboard-launch pellets has been found to agree with expressions of the form of equation (1.1) (see reference [1.1]).

(ii) $\Delta \propto a.\tau^2 \propto \Delta\beta_{av}\, q^2\, R$ (1.2)

where a is the E×B acceleration of the plasmoid ($a \propto kT_{plasmoid} / R$), τ is the duration of plasmoid acceleration (see above) and $\Delta\beta_{av}$ is the average enhancement of β resulting from fast plasmoid re-heating by parallel electron conduction, averaged spatially along a connection length [1.2]. Local β enhancement of order unity could occur although the spatially averaged enhancement $\Delta\beta_{av}$ must be lower, since the plasmoid can only expand to a fraction of the connection length during the acceleration phase.

Note that the direction of the radial displacement Δ is the same for both inboard- and outboard- launch pellets, and this is the underlying reason for the expected difference in fuelling effectiveness of the two launch configurations, as the displacement is towards the magnetic axis for inboard-launch pellets, and away from the axis for conventional outboard-launch pellets. The processes of ablation and E×B drift for the two cases are illustrated schematically in Fig.1.1. For inboard launch, there is the possibility of interaction between the two processes, since the E×B drift is much faster than the pellet injection speed, therefore the drifting plasmoid can "overtake" the pellet and pre-cool a zone of background plasma before the pellet reaches it, hence enhancing the penetration distance $\lambda_{penetration}$.

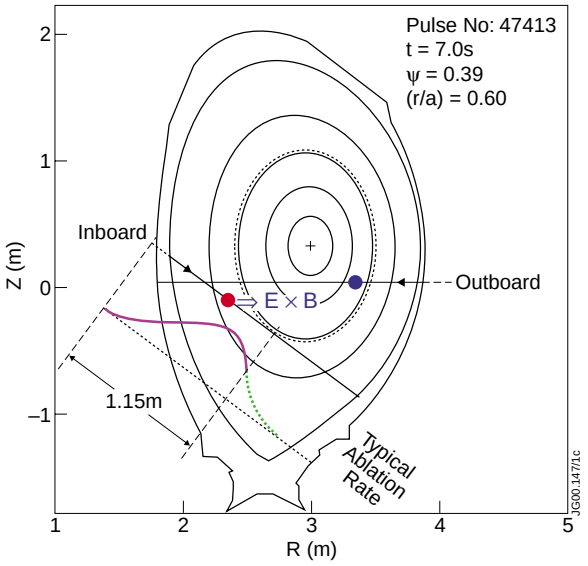

Fig.1.1: Geometry of outboard- and inboard-pellet launch trajectories in a typical JET plasma equilibrium. Typical ablation profile and schematic indication of E×B drift beyond ablation zone are shown for inboard-launch.

The physical dependences implied by equations (1.1) and (1.2) above led to the choice of basic parameter scans in the experiments carried out in JET and discussed in the present work. Any differences in fuelling characteristics and density profile response between otherwise similar discharges with inboard- and outboard- pellet launch should be attributable mostly to the E×B drift effects. The dominant driving term is the pressure of the ablatant plasmoid, and so heating power and stored energy and β of the target plasma are expected to have the most influence. Since it is electron thermal energy which is responsible for the fast re-heat of the plasmoid, and since it is T_e which dictates mainly the pellet penetration distance, RF heating was mostly used and varied between about 2MW and 7.5MW. Equation 2.2 also implies a possible dependence on q (and magnetic field through β) so limited scans of I_p and B_T were also carried out. The

present pellet fuelling/mass re-distribution experiments were exclusively carried out in L-mode plasmas. L-mode target plasmas have better reproducibility, particularly for RF heating, and the vertical D_{alpha} measurements can be used to give an indication of ablation rate (from the light intensity) since the background D_{alpha} intensity is low in L-mode and there are no ELMs.

The objective is to identify the effects of fast radial ablatant drift and any possible differences in pellet penetration between inboard and outboard pellet launch, and to look for evidence of systematic dependence on the target plasma parameters. The key diagnostic requirement is for accurate relative timing of the pellet before the LIDAR time slice in order to observe the prompt density profile response. If the delay time between the pellet entering the plasma and the LIDAR measurement exceeds about 50ms then the density profile relaxes significantly and information about the initial mass distribution is lost. In practice it proved very difficult to obtain the required precise timing relationship between launch of the first pellet and the LIDAR time-slice within the required accuracy. The reason for this is that the pellet centrifuge fundamental time-sequence derives from the phase of the rotor arm which is asynchronous with the JET Central Timing System clock. A large number of discharges have been checked for suitable timing, pellet quality etc. Matching pairs of discharges with inboard (High Field Side, or HFS) and outboard (Low Field Side, or LFS) launch into similar target plasmas have nevertheless been selected, which fulfil the necessary criteria, in the following conditions:

- 5 discharge pairs constituting a scan of heating power (2.5MA/3.2T, 2.7MW to 7.8MW, RF + 1 CX PINI) + 1 discharge pair (2.5MA/3.2T, 3MW NB only)
- 2 discharge pairs at two values of B_T and constant I_p=2.5MA (2.5MW NB+RF), and 2 corresponding pairs with 3MW NBI only
- 3 discharge pairs varying I_p at constant q (I_p=2.1-2.5MA, 2.5MW NB+RF)
  These pulses are included in the list in section 1.4.

In the course of this work the following analysis tools have been successfully re-instated at JET using the codes made available by L Baylor:

- NGS ablation calculation using JET PPF profiles as input
- Mapping of temporal D_{alpha} signal onto flux surface geometry via pellet trajectory and speed

These tools have been applied to some of the discharges identified above.
Parallel work by G L Schmidt at PPPL using the KK3 ECE data has shown that in these L-mode target discharges the ECE suffers a cut-off after pellet injection, so evidence of pellet mass re-distribution from the prompt T_e profile response is not generally available.

1.2 Results

Global fuelling efficiency

Figure 1.2 shows the total plasma electron content evolution during repetitive pellet injection in separate L-mode plasmas, inboard and outboard launch. The data are derived from the vertical

KG1 interferometer channel measurements, fringe jump corrected where necessary and integrated toroidally to give the volume integral. The following features should be noted:

- There is a significant total particle loss (exhausted to the divertor cryopump) within a short time interval (10s of milliseconds) for outboard launch
- For inboard launch, there are signs of a short delay until net particle exhaust occurs, and the initial rate of particle exhaust is slower
- The initial increase in particle content from the pellets is similar for both inboard and outboard launch.

The differences between inboard and outboard launch are attributable to differences in the net deposition profile of the pellet fuelled particles in the plasma, being more peripheral for outboard launch as discussed later in this section. The fact that the initial increase in particle content is similar for the two launch directions demonstrates (i) that the survivability of the pellets along the curved in-vessel inboard track and the more direct outboard flight tube are similar at the speed of 160ms^{-1} used in these experiments and (ii) the amount of pellet mass which becomes ionised in the plasma must be approximately similar in the two cases. The subsequent time evolution of the particle content is governed by particle transport and pumping of the plasma exhaust.

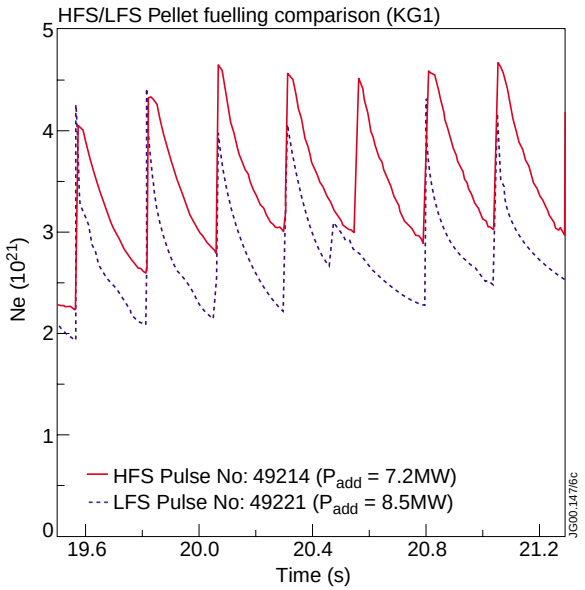

Fig.1.2: Comparison of global fuelling by inboard-(HFS) and outboard-launch (LFS) pellets in L-mode target plasmas

Figure 1.3 shows the remainder of the increment in plasma particle content 50ms after pellet entry, expressed as fraction of nominal pellet mass assuming 30% transmission loss. This assumption means that about 70% of the (4mm)^3 deuterium ice pellet is considered to enter the plasma in one piece, the remaining mass entering as small fragments or gas with very low fuelling efficiency. The data in this figure show that at low power, there is minimal particle exhaust after 50ms, but at higher power the net exhaust is already significant, and there

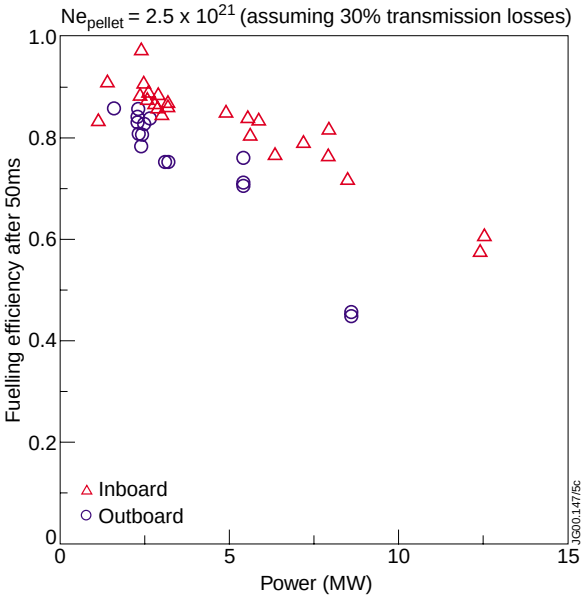

Fig.1.3: Plasma particle content from interferometer measurements taken 50ms after the pellet in L-mode target plasmas

is a clear indication of higher particle exhaust for outboard-launch relative to inboard. This trend with heating power can be due both to transport and initial mass distribution effects. However, it will be shown later in this section that there is **no** evidence of more peripheral distribution of the pellet mass for inboard-launch as the heating power is increased in these experiments, therefore the dominant effect determining the trend in Fig.1.3 is ascribed to particle transport and its dependence on heating power. Due to the difference in frequency between pellet delivery (5 or 10Hz) and LIDAR repetition rate (4Hz) it was possible to perform time-dependent particle transport analysis under the assumption that the plasma conditions and response were identical upon injection of successive pellets; such analysis is reported in reference [1.3].

Comparison of prompt density profile response with ablation profile

A key observation indicating whether the E×B drift effect might be operating to a significant extent in the case of inboard launch, is whether particles are deposited beyond the zone of ablation (i.e. closer to the magnetic axis). The comparison with outboard launch under similar conditions provides additional insight, since the E×B drift operates in the opposite way, driving ablatant away from the axis. Comparison of inboard- and outboard-launch also helps to compensate for any competing effects from particle transport occurring in the interval between initial particle deposition and the time of LIDAR density profile measurement although at lower power (<5MW), these effects appear to be minimal within 50ms of the pellet (fig.1.3.).

Figures 1.4a and 1.4b show the change $\Delta n_e(\rho)$ in density profile (from LIDAR measurements) after outboard and inboard pellet injection respectively, for the target plasma parameters indicated. Also shown are the computed particles deposited per unit volume according to the NGS code calculation [on the same scale as $\Delta n_e(\rho)$]. The radial co-ordinate ρ is the square-root of the poloidal flux function, the choice of this co-ordinate is dictated by the way in which the profile mapping is carried out in the ORNL NGS code. Figure 1.4b also shows the vertical D_{alpha} signal, measured as a function of time and mapped onto the co-ordinate ρ using the known pellet injection velocity and trajectory.

In the data of Fig.1.4a (outboard-launch) there is no significant increase of density beyond the zone of ablation, as computed by the NGS code and indicated by the D_{alpha} data (which are in good agreement). Of course, none would be expected from the initial deposition of pellet mass since the E×B drift effect would carry ablatant away from the core. There is, however, the possibility that particle transport might cause diffusive flow of the resultant plasma particles towards the core but this effect is evidently not significant on the timescale involved here. In Fig.1.4b (inboard-launch), however, there is significant accumulation of particles within the core region. Whilst the NGS code prediction obviously has its limitations, a feature of the particular JET inboard-launch geometry is that the trajectory becomes tangential to the flux-surface at about $\rho = 0.7$. Therefore a “cut-off” in ablation at this radius is a necessary geometric consequence and is not dependent on the details of the NGS modelling. Figure 1.4b also shows the mapped D_{alpha} signal (in arbitrary units of intensity), as discussed in the previous paragraph. The D_{alpha}

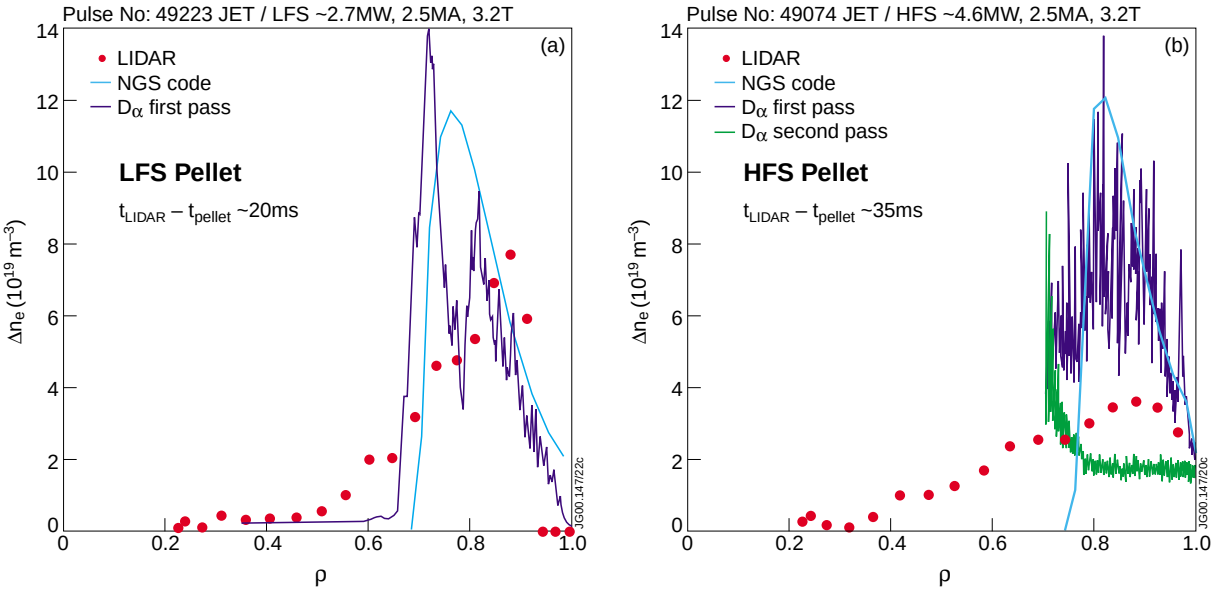

Fig.1.4: Comparison of density profile change with ablation profile, computed from NGS code. (a) Outboard (or Low Field Side) launch (b) Inboard (or High Field Side) launch, also showing D_{alpha} ablation light mapped to radial co-ordinate

trace is plotted in two colours; the blue trace corresponds to ablation on the "first-pass" of the pellet up to the tangency point, and changes to green thereafter corresponding to the pellet's "second-pass". From the D_{alpha} trace, there is an indication that some ablation indeed occurs beyond the tangency radius at the power level used (4.6MW), as the D_{alpha} intensity clearly does not reach its background level until the second-pass. From the features in Figs 1.4a and 1.4b the following conclusions may be drawn:

- Inboard-launch pellet unambiguously fuels the core region beyond the zone of ablation, in contrast with outboard-launch, consistent with the effect of E×B drift.
- On the timescales shown here (~30ms), particle transport appears to be insignificant.
- For outboard-launch pellet fuelling, the change in electron density profile aligns spatially rather closely with the NGS predicted ablation profile and the profile indicated by the D_{alpha} data.
- There is good agreement between the D_{alpha} data and the NGS predicted abalation profile.

Figures 1.5a and 1.5b show similar plots for inboard-launch pellets at two power levels, 2.6MW and 7.2MW respectively. The inboard-launch pellet "overshoots" the tangency radius, and at high power the ablation stops short of this point. Consequently, in both cases, the pellet ablation and initial deposition are peripheral, yet the LIDAR density profile response clearly indicates core fuelling in a region where direct ablation does not occur. Again, the observation can be explained by E×B drift effects having a dominant role in determining the net particle deposition of the inboard-launch pellet.

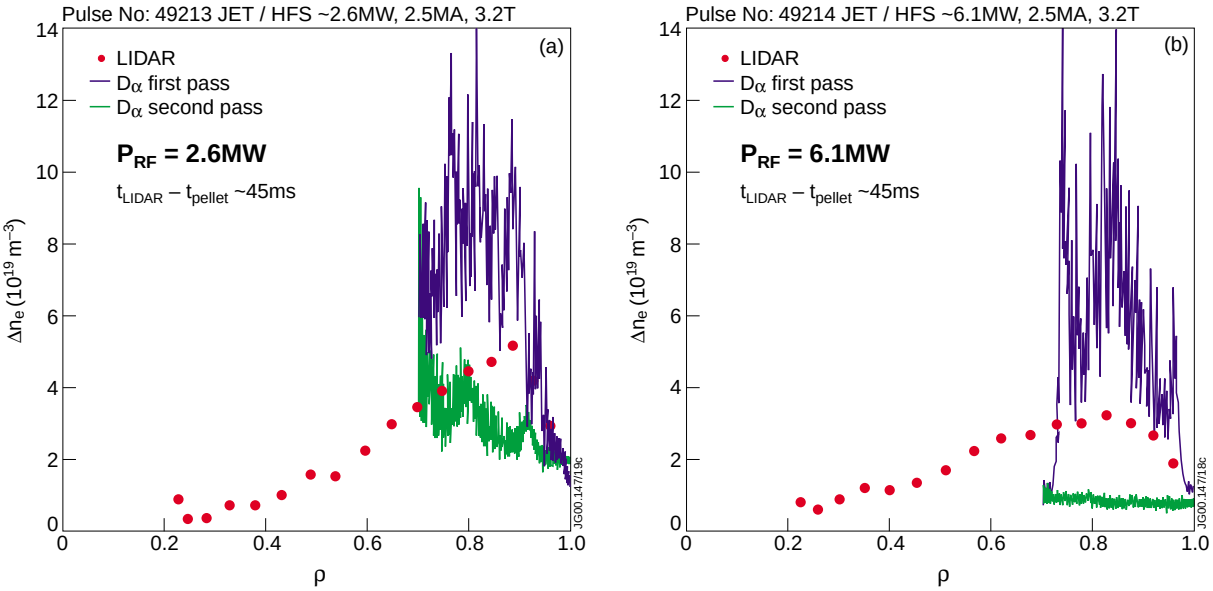

Fig.1.5: Comparison of density profile change with D_{alpha} ablation light mapped to radial co-ordinate for Inboard (or High Field Side) launch. (a) Low power L-mode (b) High power L-mode

Dependence of core fuelling characteristics on target plasma parameters

From the discussion in the previous paragraphs it will be apparent that several competing effects dictate the net fuelling to the plasma core, namely ablation/penetration, E×B drift and particle transport following initial deposition. The inboard-launch results suggest a dominant role from E×B drift effects, and it is of particular interest to investigate how this might vary with target plasma parameters and whether any of the expected physical dependences might be exhibited. An indication of possible E×B drift is assumed to be the increase in particle content in the core region of the plasma beyond the ablation zone, taken to be $\rho < 0.7$ for both inboard- and outboard-launch pellets. As discussed earlier, this zone is not directly accessible to inboard-launch pellets due to the launch geometry. One of the difficulties in performing these experiments concerns the variation in the time interval between pellet entry and the LIDAR density profile measurement, since if this is greater than several 10s of milliseconds the diffusive flow set up by the density gradient causes the profile to relax and also results in significant global particle exhaust. In addition, variation in the pellet size from pulse to pulse could also mask any underlying trend in core fuelling. In analysing the data from the L-mode scans these effects have been partly compensated for by expressing the change in particle content in the region $\rho < 0.7$ as a fraction of the total particle content change accounted for in the entire plasma volume. In this way, variation in pellet and in global particle exhaust due to different time delays and indeed to changes in particle transport coefficients at different additional heating power, plasma current and toroidal field are somewhat taken into account.

In the light of the discussion in the previous paragraph, Figs 1.6, 1.7, 1.8, 1.9 and 1.10 give the % change of particle content in the region $\rho < 0.7$ as a fraction of the total particle content change accounted for in the entire plasma volume, i.e. the % ratio:

$$\int_{\rho=0}^{\rho=0.7} \Delta n_e(\rho) J_V(\rho) d\rho \Big/ \int_{\rho=0}^{\rho=1} \Delta n_e(\rho) J_V(\rho) d\rho \qquad (1.3)$$

where $J_V(\rho)$ is the volume Jacobian.

The adoption of the global particle content change in the denominator in equation (1.3) introduces an additional source of error which is incorporated in the error estimates indicated in Figs 1.6-1.10. The total errors principally originate from the LIDAR measurement errors, which are mainly random in nature; however, there are enough data points to indicate a clear trend of different behaviour comparing inboard- and outboard-launch.

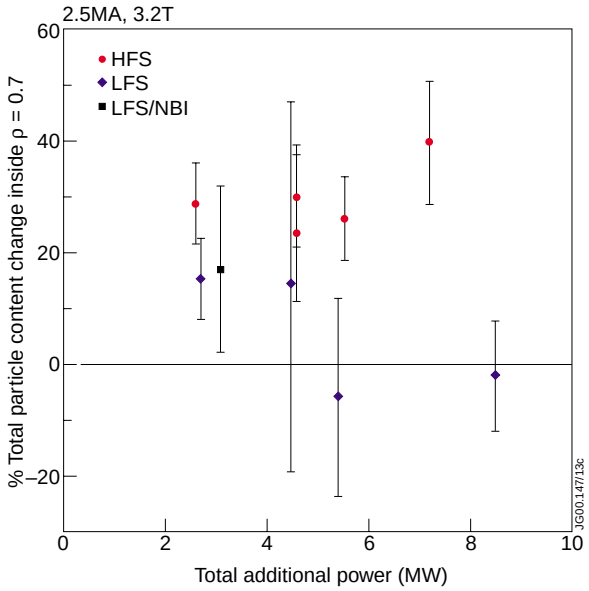

Fig.1.6: Comparison of core fuelling efficiency of inboard (or HFS) and outboard (LFS) pellet launch, expressed as the percentage change in total plasma particle content accounted for within $\rho < 0.7$, as a function of plasma input power

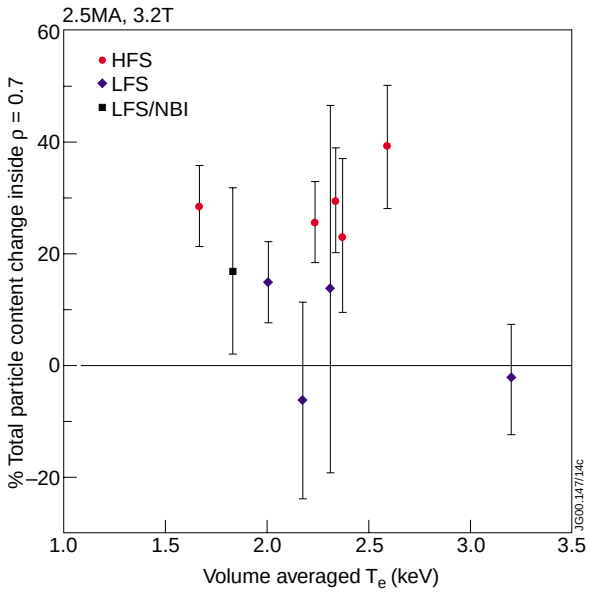

Fig.1.7: Core fuelling efficiency dependence on volume averaged electron temperature of target plasma for inboard- and outboard-launch pellets

The following conclusions from the data in Figs 1.6-1.10 may be drawn:

- Inboard-launch pellet fuelling results in systematically greater core fuelling than outboard-launch under all conditions
- At higher power/target plasma stored energy, outboard-launch pellets produce virtually no core fuelling, whilst inboard-launch core fuelling is maintained (Fig.1.6)
- There is essentially no dependence of inboard-launch core fuelling on target electron temperature (Fig.1.7), despite the associated reduction of penetration distance. Outboard-launch pellets show the expected trend of decreasing core fuelling with increasing electron temperature. These results imply there is a competing effect for inboard-launch which offsets the reduction in penetration, attributed to E×B drift

- There is an indication of increasing inboard-launch core fuelling effectiveness with increasing average electron pressure (Fig.1.8); this observation is consistent with the fact that the available electron thermal energy represents the heat available to produce the ablatant β excursion ($\Delta\beta_{av}$) which is the main driving term in equation 1.2 above
- No significant trend can be established, from the available data, on the influence of magnetic field and q (Figs 1.9 & 1.10)

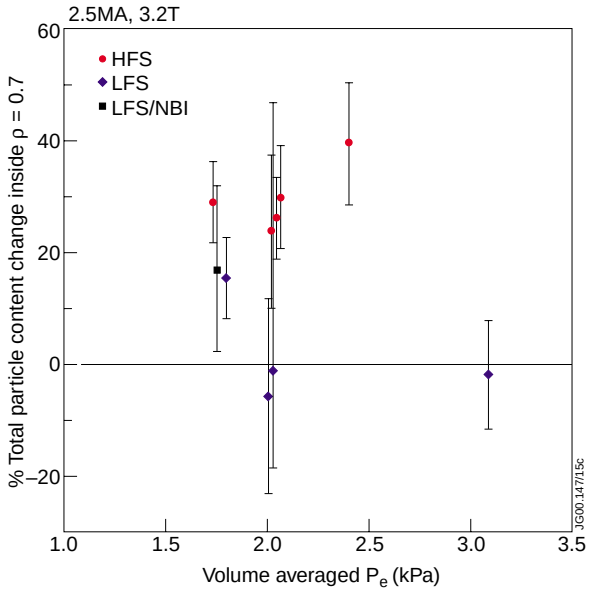

Fig.1.8: Core fuelling efficiency and dependence on volume averaged electron pressure of target plasma for inboard- and outboard-launch pellets

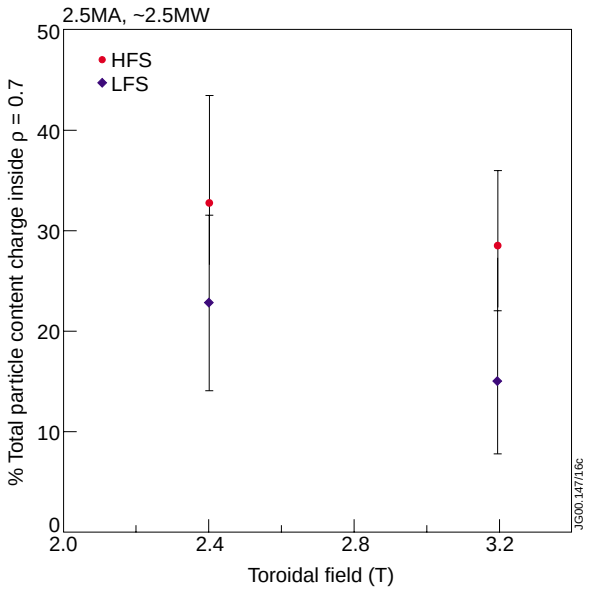

Fig.1.9: Core fuelling efficiency dependence on toroidal magnetic field, varied at constant plasma current and heating power, for inboard- and outboard-launch pellets

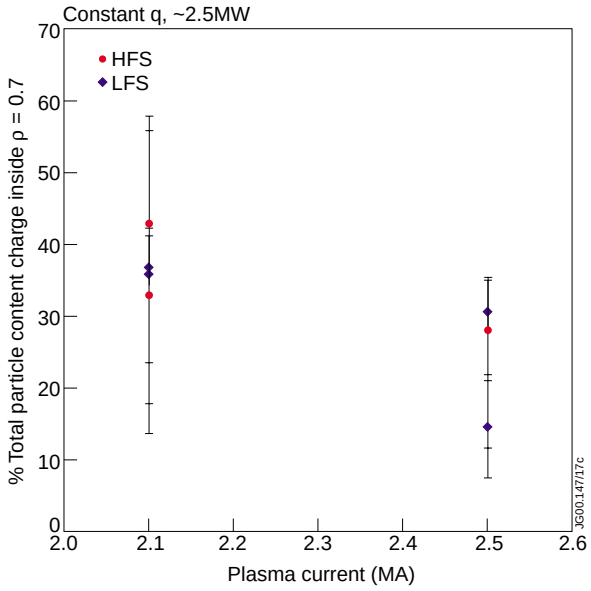

Fig.1.10: Core fuelling efficiency dependence on plasma current, varied at constant q, for inboard- and outboard-launch pellets

Discussion

The principal result derived from the present experiments is that inboard-launch pellets exhibit superior core fuelling characteristics over a range of L-mode plasma parameters. The fact that these characteristics are maintained at the higher target plasma temperatures and stored energies is a very favourable result from the point of view of exploitation for H-mode fuelling. To some extent this is a not unexpected result, based on the present physical understanding of the underlying processes in which the plasmoid β enhancement is the main driving term for the E×B drift. Experiments with a variety of pellet launch geometries in ASDEX-UG and DIIID [1.4, 1.5] had already demonstrated the benefits of injecting inboard of the magnetic axis (and in fact gave the impetus to installing an inboard track in JET). Nevertheless, the net fuelling effectiveness is a competition between ablation, drift effects and particle transport and it was important to demonstrate in JET-sized plasmas that the favourable characteristics can still be maintained.

H-mode pellet fuelling is discussed in chapter 2 of this report, but Fig.1.11 is included here to indicate the direct comparison of inboard- and outboard-launch pellet fuelling in ELMy H-mode plasmas. Note that during the Autumn 1999 campaign, only 2 or 3 outboard/inboard comparison pulse in H-mode were performed, because outboard-launch pellet fuelling is ineffective in H-mode. In contrast, as the data in Fig.1.11 show, inboard-launch pellets are remarkably effective, in line with the established L-mode trend.

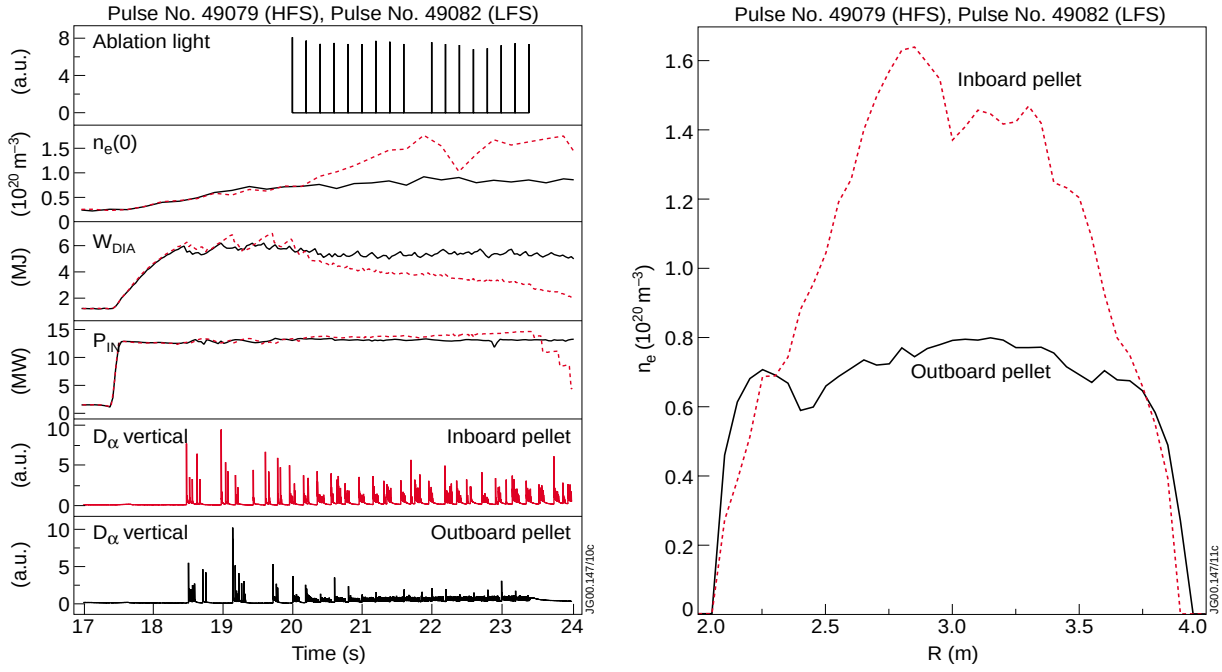

Fig.1.11: Comparison of outboard- and inboard-launch pellet fuelling of ELMy H-mode plasmas. (a) time traces indicating differences in central density and global energy confinement. (b) density profiles at time of maximum central density

1.3 Summary and future directions

Core fuelling characteristics of inboard- versus outboard-launch pellets have been analysed in L-mode plasmas over a range of target plasma conditions. Favourable fuelling characteristics of inboard-launch pellets have been confirmed, and they are maintained over the range of plasma conditions investigated. In particular, the ability of inboard-launch pellets to fuel to the plasma core (beyond the ablation zone) is maintained or even enhanced at higher stored energies of the target plasma, consistent with the effect of E×B drift which appears to compensate for the reduction in penetration. This result is very beneficial for the prospect of H-mode re-fuelling by inboard-launch pellets, and experimental results in H-mode appear to confirm this statement.

These observations are consistent with present knowledge of ablation and MHD theory of the E×B drift. However, the results are not sufficient to permit any quantitative tests of the emerging models. Since the E×B drift is essentially dependent on a local perturbation, information from fast 2-D diagnostics such as soft X-rays could be valuable. However, the soft X-ray emission is an indirect measure of density and its interpretation was considered to be too complex to be included in the present analysis. In principle, the fast ECE data could be used alone or in conjunction with soft X-ray data. As already noted, however, the density perturbations caused by the pellets in general rendered the ECE data unusable due to cut-off. In order to progress this work further it would probably be better to perform a limited series of further experiments to provide a co-ordinated set of diagnostic measurements including LIDAR, fast ECE and soft X-rays. There might be some advantage in reducing the pellet size (and hence the magnitude of the density perturbation) to avoid the ECE cut-off problem. Also, technical changes to the centrifuge sequencer control should be implemented in order to allow the time of the first pellet to be set with more confidence, since many JET pulses had to be repeated during the Autumn 1999 campaign to get satisfactory synchronisation of the pellet with the LIDAR time.

1.4 Shot List

Table 1.4.1: Week 42 Inboard & Outboard pellet comparison pulses, L-mode target plasmas

Shot	B	I	P_{nbi}	P_{icrh}	T_e	n_e	IN/OUT	t pellet #1	t LIDAR	Δt	f_{pell}	v_{pell}	comment
#	T	MA	MW	MW	keV	$x10^{19}/m^{-3}$		s	s	s	Hz	m/s	
Week 42													
49029	3.2	2.5	0.93	6.1	2.5	2.2	IN	58.036	58.13	0.094	5	152	
49030	3.2	2.5	0.93	4.6	2.2	2	IN	58.103	58.13	0.027	5	152	
49040	3.2	2.5	0.92	2	2.2	1.8	IN	58.314	58.38	0.066	5	155	
49044													2nd pellet
49045	3.2	2.5	0.92	4.5	2.2	2	OUT	58.123	58.13	0.007	5	160	no PPF
49073	3.2	2.5	0	4.6	2.4	1.9	IN	58.087	58.13	0.043	10	155	
49074	3.2	2.5	0	4.6	2.3	2.1	IN	58.094	58.13	0.036	10	155	
49075	3.2	2.5	0	4.5	2.1	2.1	OUT	58.073	58.13	0.057	10	160	no PPF
49076	3.2	2.5	0	4.5	2.3	2	OUT	58.1	58.13	0.030	10	160	no PPF

Table 1.4.2: Week 44 Inboard & Outboard pellet comparison pulses, L-mode target plasmas

Shot	**B**	**I**	**P_{nbi}**	**P_{icrh}**	**T_e**	**n_e**	**IN/OUT**	**t pellet #1**	**t LIDAR**	**Δt**	**f_{pell}**	**v_{pell}**	**comment**
#	T	MA	MW	MW	keV	$x10^{19}/m^{-3}$		s	s	s	Hz	m/s	
Week 44													
49213	3.2	2.5	1.1	1.5	1.7	2	IN	58.086	58.13	0.044	4	150	
49214	3.2	2.5	1.1	6.1	2.6	2.5	IN	58.084	58.13	0.046	4	148	
49223	3.2	2.5	1.1	1.6	2	1.7	OUT	58.113	58.13	0.017	4	149	
49221	3.2	2.5	1.1	7.4	3.2	3	OUT	58.334	58.38	0.046	4	148	
49224	3.2	2.5	3.1	0	1.8	1.8	OUT	58.126	58.13	0.004	4	160	no PPF
49225	3.2	2.5	3.2	0	1.7	1.8	OUT	58.042	58.13	0.088	4	146	
49227	3.2	2.5	3.2	0	2.2	1.9	IN	**58.357**	58.38	0.023	4	148	**2nd pellet**
49212	3.2	2.5	1.1	0	1.2	1.7	IN	57.806	57.88	0.074	4	150	

Table 1.4.3: Week 44 (contd.) and Week 46 Inboard & Outboard pellet comparison pulses, L-mode target plasmas

Shot	**B**	**I**	**P_{nbi}**	**P_{icrh}**	**T_e**	**n_e**	**IN/OUT**	**t pellet #1**	**t LIDAR**	**Δt**	**f_{pell}**	**v_{pell}**	**comment**
#	T	MA	MW	MW	keV	$x10^{19}/m^{-3}$		s	s	s	Hz	m/s	
Week 44													
49230	2.7	2.1	1.1	1.4	1.4	1.7	IN	58.313	58.38	0.067	4	151	
49238	2.4	2.5	3.8	0	1.2	2.7	IN	57.304	57.38	0.076	5	154	2nd pellet
49243	2.4	2.5	3.7	0	1.5	2	OUT	57.036	57.13	0.094	5	152	
Week 46													
49462	2.7	2.1	0.8	1.5	1.5	1.5	OUT	58.595	58.63	0.035	4	160	no PPF
49487	2.4	2.5	1	1.4	1.9	1.8	IN	58.089	58.13	0.041	4	148	
49491	2.4	2.5	1	1.4	1.6	2	OUT	58.093	58.13	0.037	4	145	
49494	2.7	2.1	1	1.5	1.5	1.6	OUT	58.58	58.63	0.050	4	147	
49496	2.7	2.1	1	1.4	1.4	1.9	IN	58.096	58.13	0.034	4	148	

Acknowledgements

The authors acknowledge with thanks the contribution of Dr L R Baylor (Oak Ridge National Laboratory, TN, USA) in the provision of the NGS code and D_{alpha} mapping program, and also for valuable input during the experimental campaign and during the analysis. Thanks are also due to P T Lang (IPP, Garching, Germany) for input during the experiments and in the analysis. The authors also thank G L Schmidt (Princeton Plasma Physics Laboratory, Princeton, NJ, USA) for investigating the possibility of interpreting ECE data to yield information on pellet mass distribution. The work discussed here could not have been carried out without the dedicated engineering and technical support of A D Walden, S Wijetunge, B L Willis and P Twynam.

References

[1.1] L R Baylor, A Géraud et al., Nucl Fusion **37** (1997) 445

[1.2] H W Müller *et al.*, Phys Rev Lett **83** 11 (1999) 2199

[1.3] L Garzotti *et al.*, Contributed paper, 27th EPS Conference on Controlled Fusion and Plasma Physics, Budapest (2000)

[1.4] P T Lang et al., Phys Rev Lett **79** 8 (1997) 1487

[1.5] L R Baylor, T C Jernigan, S K Combs and W A Houlberg, Combined Workshops of ITER Expert Groups, Garching, Germany (12th-16th April, 1999)

2. H-MODE DENSITY LIMITS AND CONFINEMENT WITH PELLET AND GAS FUELLING

G Saibene[1], T T C Jones[2].

JET Joint Undertaking, Abingdon, Oxfordshire, OX14 3EA, UK.

[1] EFDA Close Support Unit Garching, Max-Plank-Institut fur Plasmaphysik, Boltzmannstrasse 2, D-85748 Garching, Germany. – gabriella.saibene@ipp.mpg.de

[2] EURATOM/UKAEA Fusion Association, Culham Science Centre, Abingdon, Oxfordshire, OX14 3DB, UK.

2.1 Overview

This section describes the main results of the H-mode pellet experiments carried out in JET during the autumn 1999 Campaign. The analysis concentrates on the **H**igh **F**ield **S**ide (HFS) pellet injection experiments although HFS pellet fuelling is compared to **L**ow **F**ield **S**ide (LFS) injection and the improved efficiency is documented. The influence of pellet size and injection frequency is also presented.

HFS pellet injection allows access to plasma densities well above the Greenwald density limit, although, at the highest densities (~1.6 n_{GR}), this is at the price of a substantial reduction of the global energy confinement time. The main difference between gas and pellet fuelled plasmas in JET lies in the strong density peaking obtained with HFS pellets. As it is shown in the following section, optimisation of the plasma parameters, pellet size and injection frequency result in an increase of the density achievable with high confinement, compared to existing JET gas fuelled discharges.

Lastly, we show some preliminary results of mitigation of the fast energy loss at an ELM crash induced by a pellet, compared to a standard spontaneous ELM.

2.2 Results

The JET pellet centrifuge system was modified in 1999 to incorporate an additional in-vessel tube to allow pellet launch from the inboard, high field side of the magnetic axis. The inboard launch point is approximately on the midplane and the trajectory is tangential to the flux surface at normalised minor radius of about 0.5. The standard size of a pellet is ~4mm^3 and the speed at birth is up to 500ms^{-1} with a maximum design repetition rate of 10Hz. In the experiments described in this report, the pellet speed was reduced to about 160 ms^{-1} (speeds in excess of 160 ms^{-1} resulted in mechanical break-up of the ice pellet during the flight in the guide tube). The size of the pellet was also varied, from the nominal 4mm^3 down to approximately half size (corresponding to a variation in the nominal atom content per pellet from 3 to 1.5 10^{21}).

Comparison of HFS and LFS pellet fuelling in H-mode

The main aim of the pellet fuelling experiments in ELMy H-modes was to demonstrate the ability of HFS pellet injection to increase the density of ELMy H-modes to values near or above the GDL (**G**reenwald **D**ensity **L**imit), and to the improve the trade-off between energy confinement

and density, compared to gas fuelled plasmas. Enhanced fuelling efficiency with HFS injection had been demonstrated already in other Tokamaks (see for instance [2.1] from AUG), although the absolute plasma parameters (in particular the plasma temperature profiles) are sufficiently different in JET to warrant a specific test experiment. This was carried out in two separate plasma discharges at 2.5MA/2.4T, with 12 MW of NB additional heating power. In each case, a standard, unfuelled ELMy H-mode was established for approx. 2.5s before starting the pellet string. The nominal deuterium pellet content was ~3 10^{21}/pellet ("large" pellets) and the injection frequency 10Hz. As expected, HFS pellet injection is much more effective in fuelling the plasma core than LFS injection. This is clearly illustrated in fig.2.1 which compares the two discharges 49079 (HFS) and 49082 (LFS). The NB power waveform, not shown in the figure, is constant at 12 MW. With HFS injection, the line average density of #49079 increases very rapidly (<2s) to above the GDL, whilst with LFS injection the density saturates at ~ 80% of the GDL. At the same time, the plasma energy content of #49079 deteriorates as the density approaches a quasi steady state. The decrease of the density corresponds to strong plasma cooling (note that the central Te is of the order of 1 keV after 22s, compared to ~3 keV for 49082). The reduce confinement of #49079 is not correlated to increased main chamber neutral pressure which is higher for the LFS injection pulse (fig.2.1).

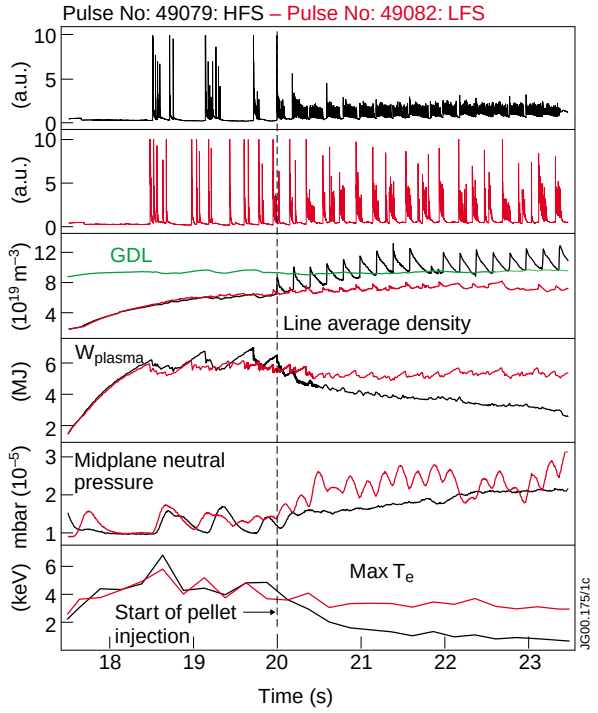

Fig.2.1: Comparison of #49079 (HFS pellets) and 49082 (LFS pellets). The two discharges have same I_p, B_t, shape and input power. The pellet string starts at 20s in both cases. The figure shows the divertor H_α, line average density (and the GDL, $10^{19}m^{-3}$), total plasma stored energy (MJ), neutral pressure at the midplane (mbar), and the maximum electron temperature (keV). The NB power is 12 MW and constant in the time window.

The different plasma density response to HFS and LFS pellet injection is illustrated in more detail in fig.2.2. With LFS injection, the pedestal density is increased ~50% above that obtained with HFS injection. On the contrary, the response of the central density is higher when the pellet is injected from the HFS than LFS, and the time averaged central density is increased by ~25% for the HFS injection case. The lack of fast time resolved density profiles for these discharges does not allow quantitative determination of fuelling efficiencies. Nevertheless, this comparison indicates that the reduction in the energy confinement of # 49079 (HFS) is not related to the value of the edge density, which is higher for the LFS injection discharge. Figure 2.2(b) and 2.2(c) show the response of the central and pedestal density to a single pellet.

HFS injection results in longer effective particle confinement times than LFS injection. This density behavior is consistent with models of high-β plasmoid drifts in an axisymmetric toroidal geometry, which predict plasmoid acceleration towards larger major radius [2.2].

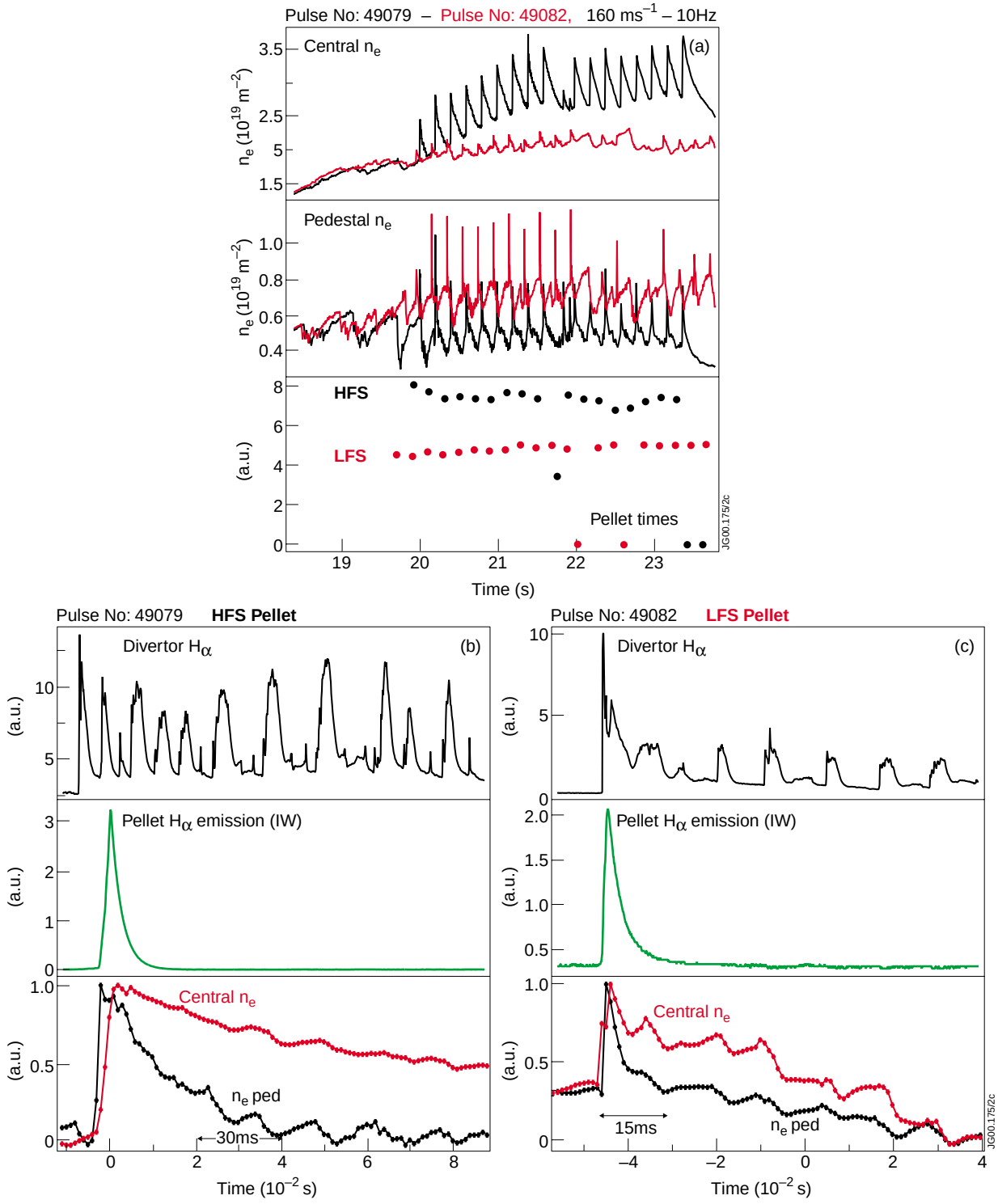

Fig.2.2: (a): line integrated density (central chord and pedestal chord, from FIR data) for the same plasma discharges as fig.2.1. The timing of each pellet is shown for the two discharges. (b) and (c): divertor H_α, inner wall H_α (pellet "signature") and density traces for one HFS and LFS pellet, respectively. The first spike in the H_α trace of pulse 49079 (fig.b) is a spontaneous ELM occurring just before the pellet.

Finally, the injection of a pellet is associated with transient MHD activity in the plasma core, probably fishbones (note the oscillations in the H_α signal after the pellet spike in fig.2.2, for both HFS and LFS). Although the characterisation of the MHD response to pellet injection is not complete, the difference in the slow density response (scale ~ 100ms) between HFS and LFS pellet injection seems to be independent of transient MHD.

Effect of pellet size and input power on density and confinement.

Figures 2.3, 2.4 and 2.5 show the time evolution of some chosen plasma parameters for 3 discharges that have the same I_p/B_t (2.5MA/2.4T), shape (δ=0.34), heating type (NB) and are all fuelled by HFS pellets. The difference between the 3 plasmas is in the size of the pellets and in the level of additional heating. More specifically:

- #49249 has approx. *17MW* of NB and is fuelled with *large* pellets from 20.2s (fig.2.3)
- #49251 has the same NB input power than #49249, but the fuelling after 20s is with *small* pellets (fig.2.4)
- #49250 which has *12MW* of NB power and small pellets from 20s (fig.2.5)

The first clear result that emerges from fig.2.3 is that the repetitive injection of large pellets is very effective in increasing the core density of H-mode plasmas. For pulse #49249 the average density is in excess of the Greenwald density limit for several confinement times (~10 τ_E), showing quite clearly that the Greenwald limit does not represent any fundamental physics limit

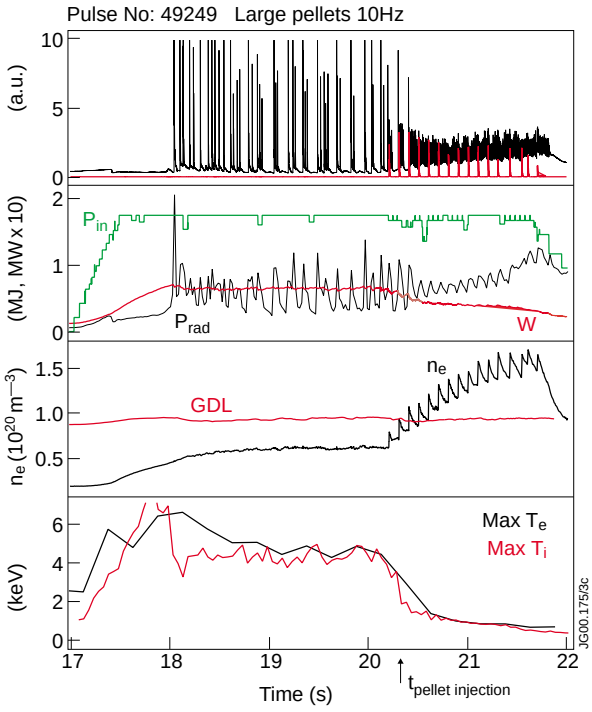

Fig.2.3: Divertor H_α, inner wall H_α (pellet "signature"), input power (MW), total radiated power (MW) and total stored energy (MJ), line averaged density and Greenwald density, Max Te and Ti for pulse #49249 (high power, large pellets)

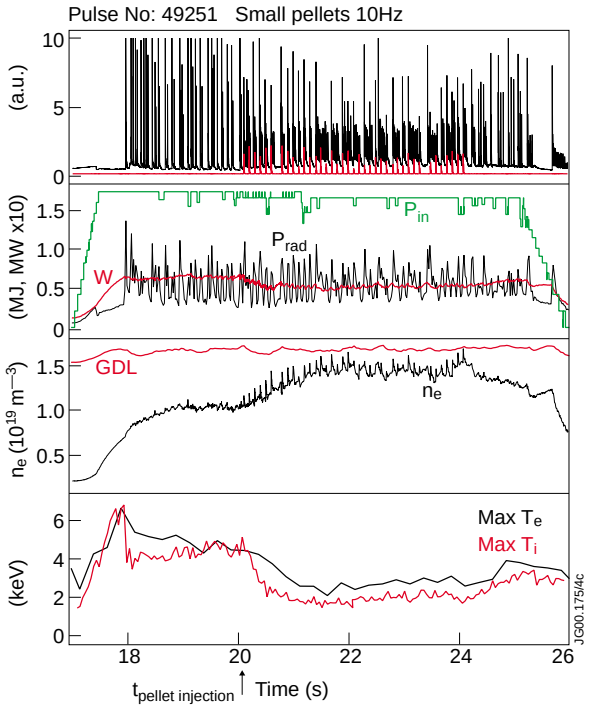

Fig.2.4: Same traces as figure 2.3, for pulse #49251 (high power, small pellets).

for the core density of the plasma. This result is consistent with similar findings in DIII-D and AUG pellet fuelled discharges [2.3, 2.4]. On the other hand, we can clearly see that the increase in the density is associated to a progressive reduction of the plasma stored energy, in a similar fashion to the case of gas-fuelled discharges, but at higher absolute values of the density. The decrease in stored energy is due to the cooling of the plasma, down to central T_e and T_i of the order of 1keV. The reduction in the temperature is not compensated by the increase in the density, and this of course results in a loss of plasma pressure (fig.2.6).

This reduction in temperature is likely to be due both to the variation of the power deposition profile of the NB, that at this high density is highly peripheral (fig.2.7), but also

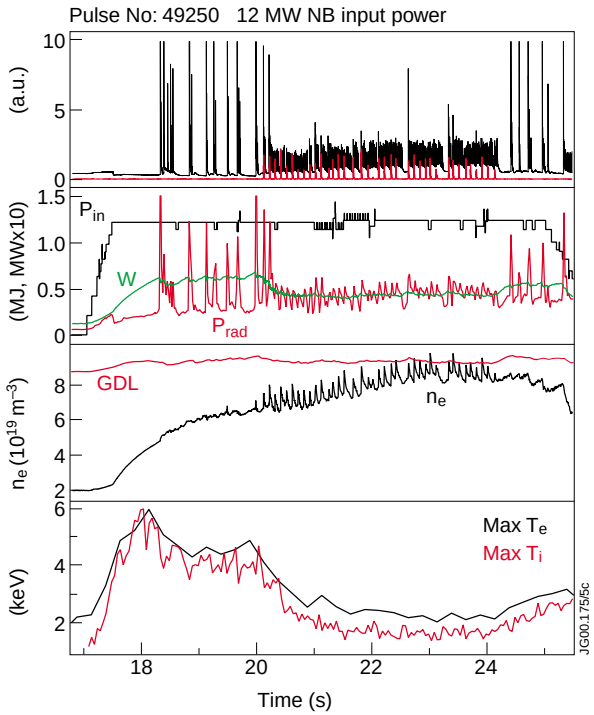

Fig.2.5: Same traces as figure 2.3, for pulse #49250 (low power, small pellets).

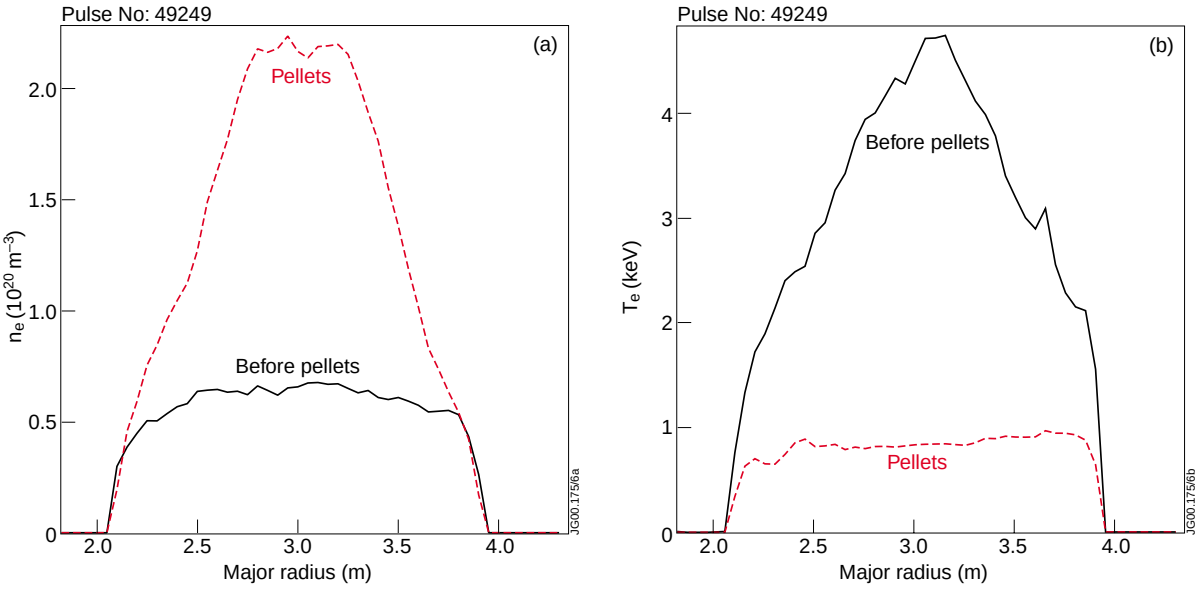

Fig.2.6: Electron density (a) and electron temperature (b) profiles from #49249. The "before pellets" profiles are an average of the data between 18.8 and 19.8s; the "pellets" profiles are averaged between 20.8 and 21.4s

to a change in transport. In fact, the temperature profiles, as the density evolves, are not stiff, and at the highest density, T_e and T_i become flat. The central temperatures corresponding to this heavy fuelling, are lower than one would obtain if the temperature decreased maintaining a constant temperature scale length. As shown in fig.2.6, the core loss mechanisms associated to ∇T are "switched off" at high density, and losses driven by ∇n (and radiation) are now likely to

play a role. The interpretation of these results requires detailed transport analysis, still in progress for these discharges.

The results of the reduction in the pellet size, with all the other parameters of the discharge unchanged (fig.2.4), is quite dramatic. The plasma density increase is reduced, although the central fuelling provided by HFS pellet injection is still sufficient to bring the plasma density up to ~90% of the Greenwald density. The combination of high power and reduced pellet size results in a moderate reduction of the maximum temperature, which is compensated by the density increase (and peaking). This is seen in fig.2.8, which shows the time-average density and temperature profiles for pulse #49251, compared to a gas fuelled discharge (discussed later). The plasma maintains good global energy confinement (only ~10% stored energy loss compared to the NB only phase preceding the pellet injection) at ~90% of the GDL. This improved performance at high density is dependent on the high power NB used in #49251 (in apparent contrast to the results from AUG [2.4]). This can be seen by comparing with the global plasma performance of #49250, illustrated in fig.2.5. The plasma reaction to the pellet injection is similar to #49249, leading to a strong reduction in the core

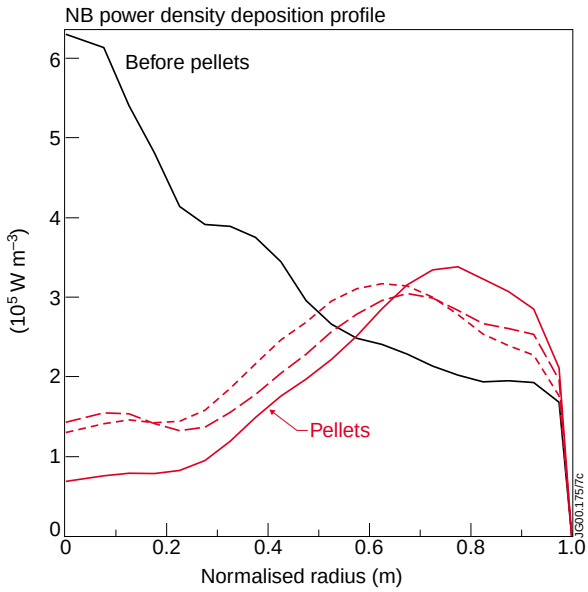

Fig.2.7: Variation of the spatial profile of the power density deposited by the NB, calculated by the PENCIL code. The profiles are taken in the same time window as described in the caption to fig.2.6. The changes in the NB deposition profile in the "pellets" case is due to the relative timing of the calculation compared to the pellet injection time.

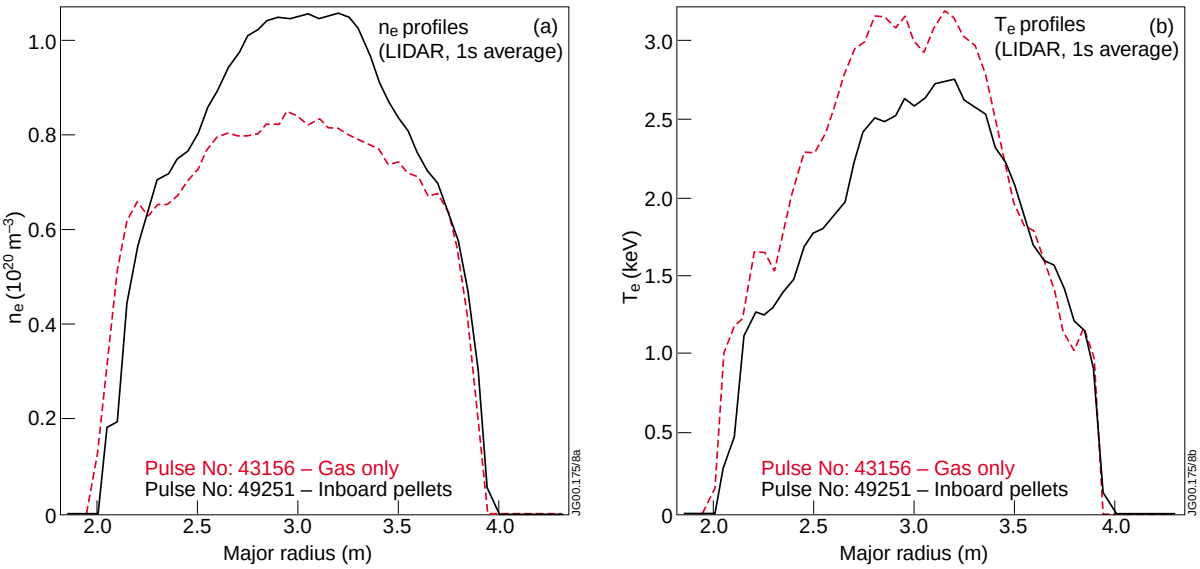

Fig.2.8: Comparison of electron density (a) and electron temperature profiles (b) of #43156 (gas) and #49251 (pellets). The profiles are averaged over 1s in the steady state phase of each discharge.

temperature and flattening of the temperature profiles. The reduction in the plasma stored energy is not as severe as in #49249, but still in excess of 20% of its initial value before the pellet string. More detailed analysis is required to fully understand the role of additional heating, in particular including the study of ICRF H-minority heated discharges, which are characterised by a heating deposition profile almost independent of density.

Performance optimisation: injection frequency

The results described so far highlight the fact that the plasma performance is particularly sensitive to the scenario used for heating and fuelling the plasma. A further demonstration of this fact, as well as an interesting indication on possible ways to further improve performance of high density, pellet fuelled H-modes, comes from the so called "pellet notches" experiments. These experiments consisted of the repeated interruption of the pellet string, with the aim of profiting from the comparatively fast energy recovery time compared to the characteristic particle loss time, to obtain high "time-average" plasma performance. The experiments were carried out in plasmas with the same plasma current, toroidal field and shape as the experiments described earlier in this section (2.5MA/2.4T, δ=0.34), and NB input power ~15-16MW. Small pellets were injected from the HFS, at a nominal 10Hz frequency. The best demonstration results were obtained in pulse 49504. In this pulse, the NB beam power was applied for ~2.5s, then the pellet string started at 21s and continued at 10Hz for 3s. At ~23.9, the pellet string was stopped twice, in a sequence of 6 pellets "off" – 4 pellets "on" ("notches"). This is illustrated in fig.2.9 for a restricted time window, where the numbers 1 to 4 identify the pellet phases.

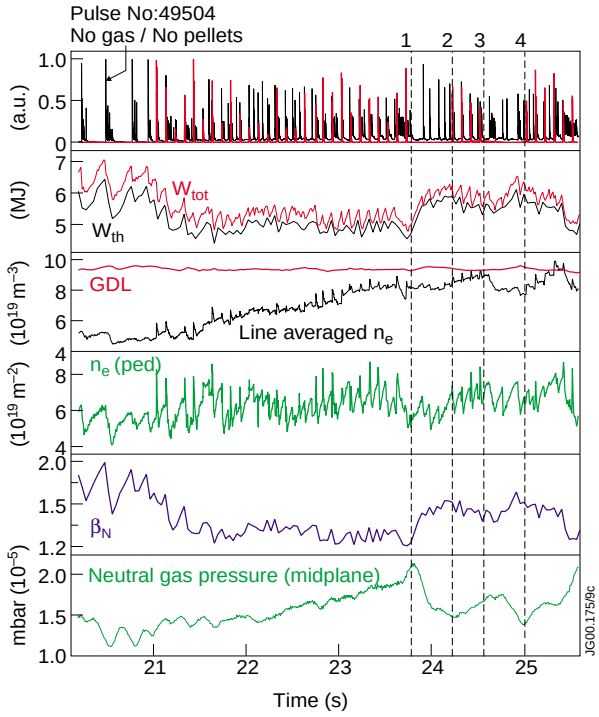

Fig.2.9: Pulse 49504: Divertor H_a, inner wall H_a (pellet "signature"), total (W_{tot}) and thermal (W_{th}) plasma stored energy (MJ), line average density and Greenwald density, line integral density at the edge pedestal location, b_N (total) and neutral pressure at the midplane. The NB power (not shown) is ~15MW and constant.

The effect of the notches can be evaluated by comparing the average thermal stored energy in phases 2+3+4 to that of phase 1 and of the no gas/no pellet period of the pulse. During phase 1, the density increases to ~85% of GDL while the stored energy is reduced by ~15-20% compared to the unfuelled phase. During the notches, we observe a recovery of the stored energy in a time scale of the order of τ_E and the value of the average thermal stored energy reaches the value before the pellet injection. At the same time the density slowly oscillates, but in average it

remains ~85% of the GDL. The longer effective loss time for the particles is probably also due the increased recycling at the edge (compared to the recycling before the pellet string starts) which persists also during the pellet-off period. The improved plasma performance with this "optimised" pellet injection frequency is also seen in the increase of the plasma β, compared to the early high density phase of the discharge. The global effect of the notches in the pellet string

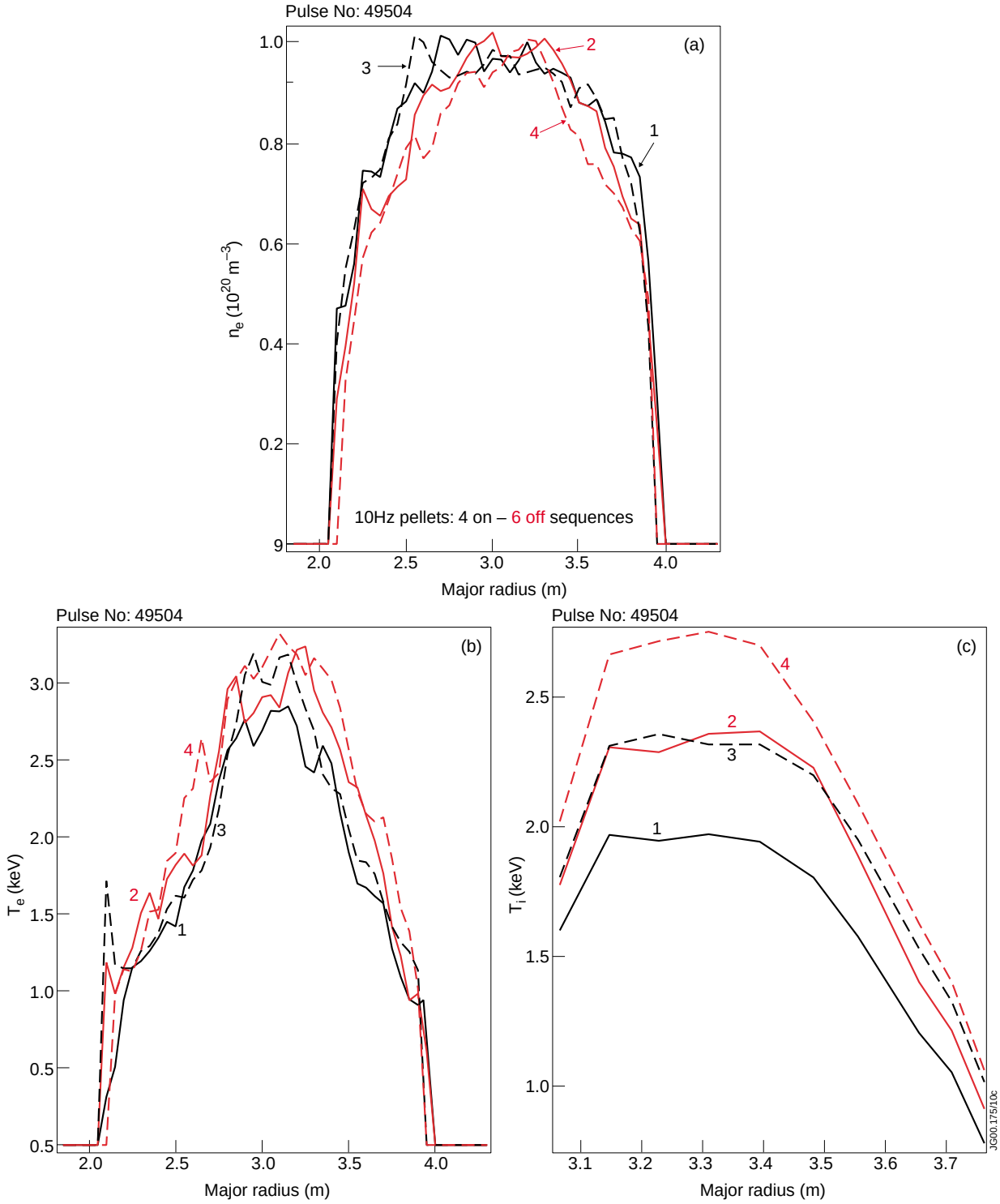

Fig.2.10: Pulse 49504: (a) electron density profiles, (b) electron temperature profiles and (c) ion temperature profiles representative of the 4 phases of the discharge with pellet notches.

can be better understood by looking at the changes in the plasma density and temperature profiles. These are shown in fig.2.10, and the numbers for each profile identify time slices in the pulse as indicated in fig.2.9.

Figure 2.10(a) shows that, during the pellet off periods, the density loss is limited to the outer 50% of the plasma radius, whilst the central density is essentially unchanged. In the same periods, there is an increase of both ion and electron temperature, (fig.2.10(b) and (c), more pronounced for the ions) and therefore an increase of the plasma stored energy. It is interesting to note that the power density deposition profile of the NB does not change substantially during the notches, so that the changes in the confinement are probably due to improved transport.

The combination of pellet size, frequency and of the corresponding input power for achieving the best performance at high density is still to be optimised, in particular for the control of the average value of the density and to achieve demonstration of steady state performance.

Comparison with gas fuelled H-modes

The performance of ELMy H-modes with HFS pellet injection can be compared to that of gas fuelled plasmas. For this comparison, we have selected data from gas scans performed in the MkII JET campaign, since these were carried out with plasma current, field and shape very similar to the plasma parameters of the pellet experiments described in this section. The results are summarised in fig.2.11, where the confinement enhancement factor H97 (calculated according to the scaling ITER97-P(y)) is plotted against the corresponding fraction of the Greenwald density. Although densities up to ~1.6 n_{GR} have been achieved in pellet fuelled H-modes, with H97 ~0.4-0.5 (see fig.2.3, for instance), fig.2.11 includes only discharges with densities between ~50 and 100% of n_{GR}. This expanded x-axis is more convenient to compare at a glance gas and pellet fuelled plasmas.

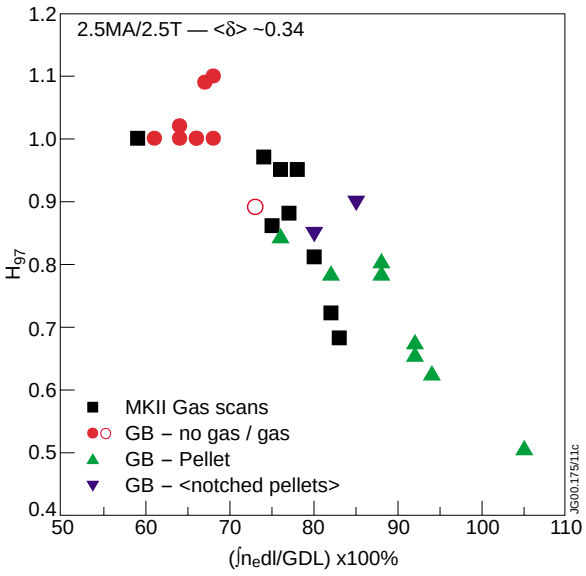

Fig.2.11: Confinement enhancement factor H97 as function of the fraction of the Greenwald density limit (fgdl). The plot compares results from gas scans carried out with the MkII divertor with discharges from the GB divertor campaign (unfuelled, with gas and with HFS pellets). All the discharges have I_p = 2.5MA, B_t=2.4 to 2.7T, and average triangularity δ~ 0.34. All discharges are with Neutral Beam heating, ranging from ~11 to 17 MW.

As mentioned earlier, the pellet fuelled discharges still suffer from a progressive degradation of the energy confinement for increasing densities [2.5]. The main difference with the dataset of gas fuelled discharges is in the improved trade-off between density and plasma energy content and in the higher absolute value of the densities obtained with HFS pellet injection compared to

gas fuelling. These results are probably described better by introducing a re-normalisation of H97 that eliminates the $n^{0.4}$ density dependence of the H factor (fig.2.12). The use of this re-normalised H factor is justified for the present sets of data, since all the discharges have the same plasma current, very similar B_t and shape parameters.

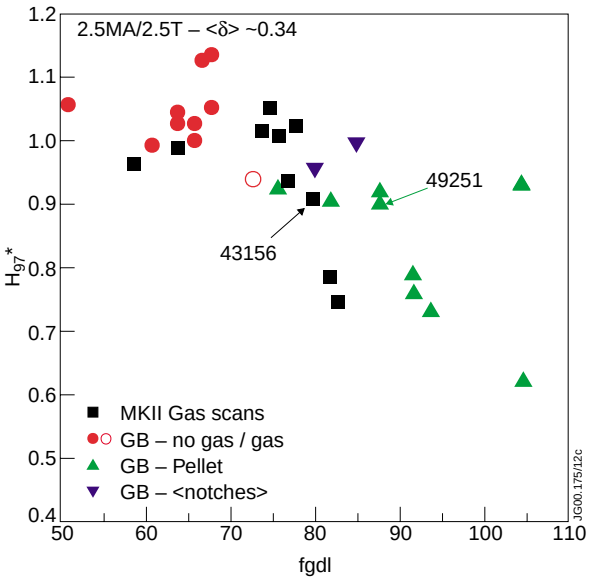

Fig.2.12: Re-normalised H97 (H97), as function of the fraction of the Greenwald density limit (fgdl). Same set of data as fig.2.11.*

Figure 2.12 shows that the best pellet fuelled discharges can maintain good energy confinement up to 85-90% of the Greenwald density limit. The improvement due to pellet notches (inverted triangles in the plots) can also be seen, as discussed in the previous subsection. Another interesting set of discharges is the gas fuelled pulse 43156 (12MW NB) and the pellet fuelled pulse 49251 (17MW NB), labelled in fig.2.12. These are amongst the best performing pulses of their kind in the data set, and we can see the pellet pulse achieves around 90% of the GDL with a very small reduction in confinement. The comparison of the T_e and n_e profiles for the two discharges is shown in fig.2.8. The combination of peaking of the density with a relatively small reduction in the temperature and a reduction of Z_{eff} from 1.8 to 1.2, results in increased extrapolated performance for the pellet discharge as compared to the gas fuelled pulse.

ELM mitigation by HFS pellet injection

Early results from JET LFS pellet fuelled H-modes [2.6] indicated that pellet-induced ELMs are generally characterised by a reduction of the prompt energy loss at the ELM, compared to a "spontaneous" ELM. This result is of great interest for a next step machine, ITER in particular, due to the concerns about Carbon erosion by ELMs, and divertor target lifetime in general. These early indications seem to be confirmed by data from the HFS pellet injection experiments. The comparison of the energy loss has been done between two successive ELMs in a discharge: the last "spontaneous" ELM compared to the ELM caused by the first pellet. This choice has been made to ensure that the background plasma characteristics are as similar as possible for the two ELMs. The results presented are preliminary due to the small number of such events studied so far.

The fast energy loss at the ELM is reduced by ~ a factor of 2 for the pellet induced ELM compared to the spontaneous ELM, although the total energy loss is similar in the two cases. This is shown in fig.2.13. The estimate of the fast energy drop at the ELM is done following ref [2.7], excluding from the calculation the apparent drop of the energy due to eddy currents induced by the ELM itself. Another interesting characteristic of the pellet induced ELM is the long time

constant for the loss of the rest of the stored energy, after the fast drop. This may be related to the increase in the edge (and core) density associated with the pellet ELM (fig.2.14), increasing the energy loss by particles, typically much slower than pure conductive losses (spontaneous ELM, fig.2.15). This corresponds to a smaller T_e drop at the pedestal for the case of the pellet ELM than for the spontaneous one.

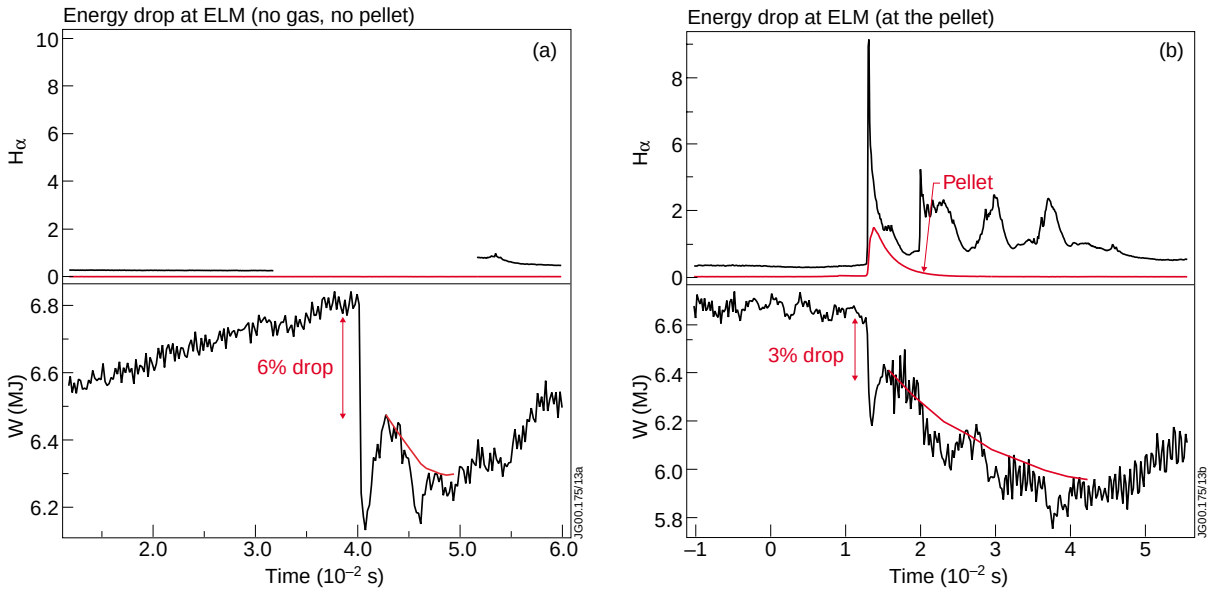

Fig.2.13: Divertor H_a and pellet signal, fast stored energy drop at the ELM for (a) spontaneous ELM and (b) a pellet induced ELM, from pulse 49079. The "slow" energy loss is drawn to guide the eye.

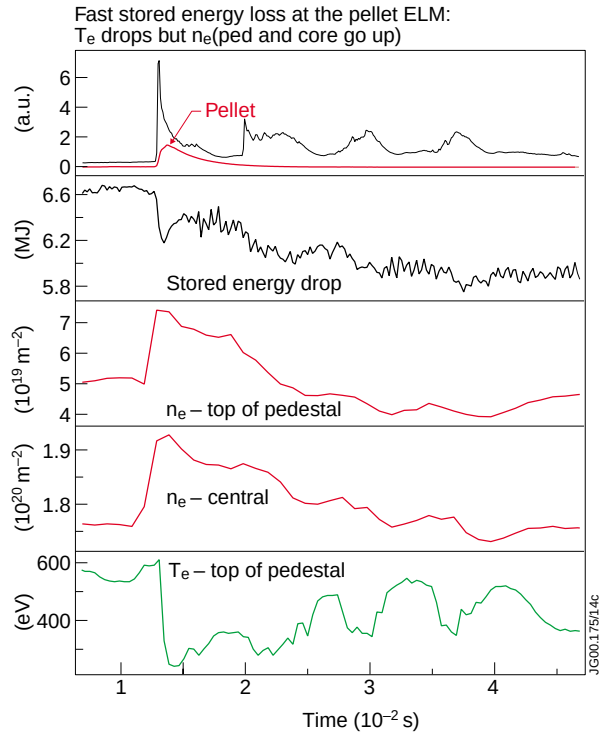

Fig.2.14: Divertor H_a, pellet signature, fast stored energy drop at the ELM, pedestal density, core density and pedestal electron temperature for a pellet induced ELM.

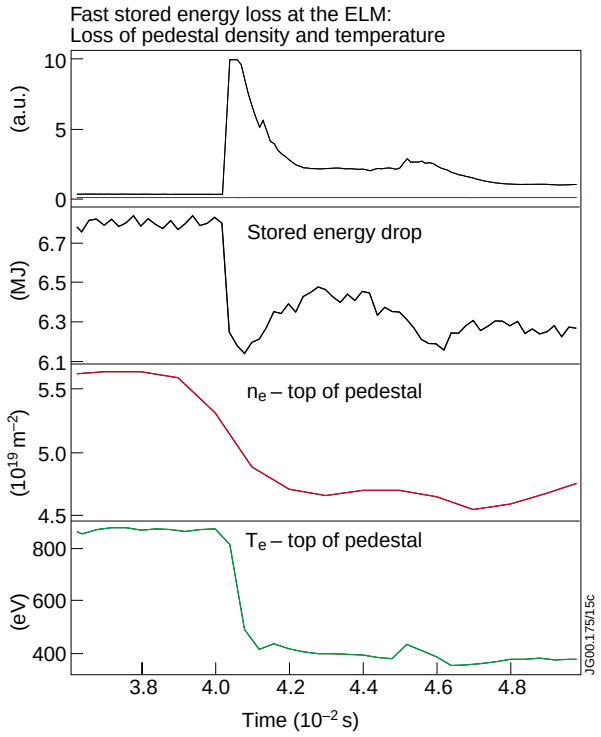

Fig.2.15: Divertor H_a, fast stored energy drop at the ELM, pedestal density, and pedestal electron temperature for a spontaneous ELM.

2.3 Summary and future directions

HFS pellet fuelling in ELMy H-modes has produced plasmas at high density with negligible confinement degradation. Densities ~85-90% of the Greenwald density limit were obtained with a reduction on the stored energy content of <10%, compared to the unfuelled value. These results were obtained with careful optimisation of the plasma parameters, in particular of the pellet size and injection frequency. Furthermore, high additional heating power seems to be required to maintain performance at high density/high fuelling rates.

Further analysis of the results awaits transport analysis of the discharges presented in this section, in particular of comparable gas and pellet fuelled discharges, as well as of power scans, pellet size comparisons, etc. More work is also required to investigate the question of T profile stiffness (or lack of) at very high density. The same consideration applies to the characterisation of MHD modes induced by pellets.

The analysis carried out so far indicates that the extrapolated performance of the best pellet fuelled pulses should be in the range required for ITER-FEAT. More detailed calculations are in progress to quantify this statement, including the effect of density profile peaking and reduced Z_{eff}.

The data presented in this section originate from a sub-set of the experiments carried out in 1999. Low triangularity and combined heating discharges have not been included in the report. The choice is partially dictated by time constraint, but also by the fact that the 2.5MA/2.4 T, high triangularity discharges form the best and more consistent set of H-mode experiments with pellets.

The analysis carried out so far indicates that new experiments should focus on HFS pellet injection in high power H-modes (including combined heating), possibly increasing the range of I_p/B_t, and on creating a database at high power to compare gas and pellet fuelling.

Finally, measurements with good time resolution of the electron temperature at the pedestal of pellet fuelled discharges are very scarce, due to the cut-off at high density of the ECE and, in most cases, the data in the PPF should not be used. The lack of fast core ECE data is another limitation for the analysis of these discharges and should be considered when planning future experiments.

Acknowledgements

My acknowledgements go to the JET team of the JET Joint Undertaking, to their dedication and professionalism that has permitted to carry out the experimental programme until the end of 1999. The quantity and quality of the scientific results produced under very difficult circumstances is the best testimony to the capabilities of that team. I also thank all the people involved in the data analysis presented in this section, in particular M Charlet for the painstaking re-processing of the density from FIR, K-D Zastrow for C-X ion temperature data and L D Horton and G F Matthews for their patience and efficiency in the coordination of the data analysis for the 1999 data.

References

[2.1] P J Lang et al, ECA Vol 23J (1999) 1389-1392

[2.2] H W Mueller et al, ECA Vol 23J (1999) 109-112

[2.3] R Maingi et al., Fusion Energy 1998, Proc of the 17th IAEA Conf. EXP2/10, 793

[2.4] O Gruber et al, Fusion Energy 1998, Proc of the 17th IAEA Conf. OV4/3, 213

[2.5] G Saibene et al, Nuclear Fusion 39 (1999), 1133

[2.6] P Kupshus et al., ECA 21A (1997), 45-48

[2.7] R Mohanti et al., ECA 21A (1997), 101-104

3. HELIUM EXHAUST

D Stork[1], S J Cox[1], M Groth[2], H Guo[3], P J Harbour[1], L D Horton[4], K D Lawson[1], A C Maas[5], C F Maggi[4], G Saibene[6], M von Hellermann[7].

JET Joint Undertaking, Abingdon, Oxfordshire, OX14 3EA, UK.

[1] EURATOM/UKAEA Fusion Association, Culham Science Centre, Abingdon, Oxfordshire, OX14 3DB, UK.

[2] UMIST, Manchester M60 1QD, UK

[3] Redmond Plasma Physics Laboratory, University of Washington, Seattle, USA.

[4] Max-Planck-Institut für Plasmaphysik, IPP-EURATOM Association, Boltzmannstrasse 2, D-85748 Garching, Germany.

[5] CEA Cadarache, DRFC/SIPP/CFM, F-13108 Saint Paul Lez Durance Cedex, France.

[6] EFDA Close Support Unit Garching, Max-Planck-Institut für Plasmaphysik, Boltzmannstrasse 2, D-85748 Garching, Germany.

[7] FOM Instituut voor Plasmafysica Rijnhuizen, EURATOM Association, Postbus 1207, NL-3430 BE Nieuwegein, The Netherlands.

3.1 Overview

Control of helium (He) ash produced in deuterium-tritium (DT) fusion reactions is one of the key issues affecting the performance of a fusion reactor. The removal of He ash would be determined by a combination of: the intrinsic transport of helium in the plasma τ_p(He), where τ_p is the particle confinement time; enrichment and compression of helium in the divertor, η(He); and the pumping efficiency for helium S_p(He).

Thus the problem is one of *system integration* and is only partially determined by basic plasma physics. Several studies have identified target *figures of merit* for these quantities. The Wolf-Reiter-Kever condition [3.1] requires that $\tau_p^*(\mathrm{He})/\tau_E \leq 15$, where $\tau_p^* = \tau_p/(1-R_{eff})$, with R_{eff} as the He recycling coefficient, and τ_E the energy confinement time. If this quantity is kept below the critical value then the build-up of He ash, and consequent reactor fuel dilution, can be avoided. The ITER design [3.2] requires $\eta \geq 0.2$ where

$$\eta = \left(P_{He}/2P_{D_2}\right)_{Divertor} \Big/ \left(n_{He}/n_D\right)_{core}$$

In the JET experiments, a realistic simulation of the ITER plasma shape was combined with a helium pumping capability of the JET Pumped Divertor (PD) cryopump using Argon frosting. The experiments were performed in the *'MkIIGB'* divertor configuration [3.3].

3.2 Results

Calibration of the Argon frosting

The pumping speed of the PD cryopump for helium was first measured as a function of various Argon frost coatings using sequential He and D_2 gas pulses. The results are shown in Fig 3.1. The experiments established the systematic behaviour of the pumping as a function of the ratio of the deuterium + helium gas condensed on the Supercritical Helium (ScHe) cooled PD panels

to the amount of argon frost condensed ($N(D_2+He):N(Ar)$). The experiments showed that (see Fig.3.1):

- $S_p(He)$ is a universal function of $r(D_2,He:Ar) = N(D_2+He):N(Ar)$ where N(Ar) is the amount of Argon layed down in *the most recent frosting;*
- $S_p(He)$ does not depend on the thickness of the Argon layer (for given r);
- a refresh layer restores the pumping to its original value;
- a maximum value of $S_p(He) \sim 90 m^3 \cdot s^{-1}$ could be achieved. This is about 75% of the PD pumping speed for deuterium ($S_p(D_2) \sim 120 m^3 \cdot s^{-1}$).

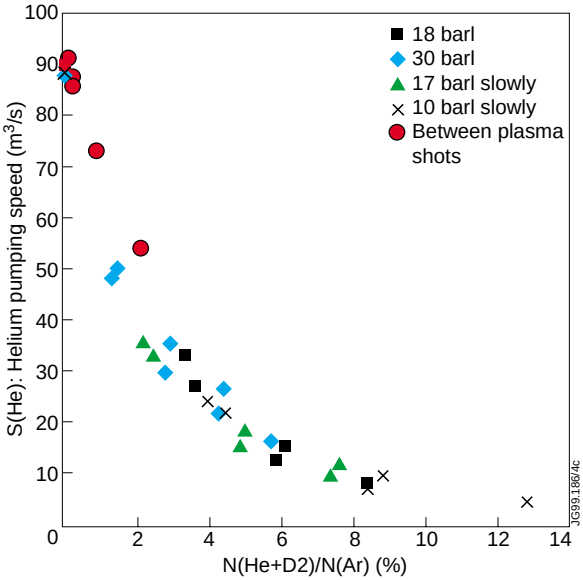

Fig.3.1: Pumping speed for the Argon frosted cryo-pump as a function of $He+D_2$ loading

Experiments with plasma

The experiments were performed in diverted plasma configurations as shown in Fig.3.2. Helium gas was puffed into plasmas heated by neutral beam injection (NBI) at various power levels. The plasma helium concentration was measured using Charge Exchange Recombination Spectroscopy (CXRS) of the helium ions on the D^o NBI. The divertor helium content was measured using a Penning gauge fitted with a spectrometer to view the He light in the discharge [3.4]. Edge impurity spectrometers were tuned to the HeII line. Spectroscopy was also used to examine any Argon contamination of the plasma.

Results were taken on the decay of He in L mode plasma (Ip=2·35MA, B_T=2.5T with 2·5MW NBI) with strike zones on the divertor Vertical Targets (V) – see Fig 3.2. More extensive data on He removal were taken in ELMy H-mode plasmas with Ip=1·9MA, B_T=2·0T (similar q values to the ITER reference design [3.2]). Parameter scans in the ELMy H-mode compared He removal for:

- corner (C) strike zone position vs vertical target (V) strike zone position (see Fig.3.2
- low triangularity ($\delta \sim 0{\cdot}22$) vs high triangularity ($\delta \sim 0{\cdot}35$);

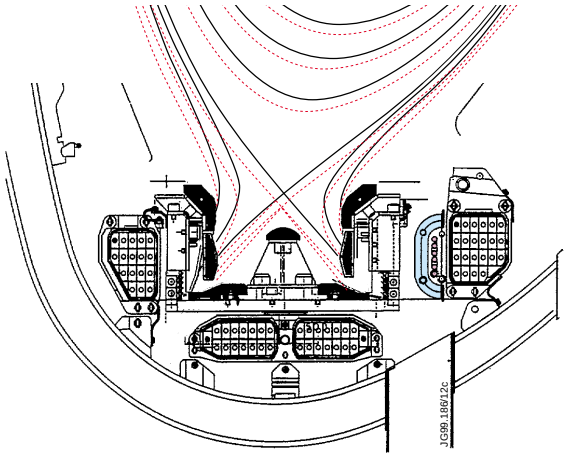

Fig.3.2: Divertor configurations for ELMy H-modes: Solid lines – vertical target. Dashed lines – corner configuration. The vertical target configuration was also used for L-mode

- medium NBI power (10MW) vs high NBI power (14·5MW);
- no added D_2 gas puffing vs strong D_2 gas puffing ($\phi_D \sim 10^{22}$ s^{-1}).

Between plasma shots, the He pumping speed of the PD Argon frost layer was calibrated with puffs of He gas into the Torus. It was found that a similar dependence on r(D_2, He;Ar) held as in the gas-only calibration runs (see Fig 3.1) showing that the effect of D_2 loading of the Argon layer was independent of the origin of the D_2. It was also found that the Argon layer provided adequate pumping for two or three plasma shots.

Results: (I) L-mode

A value of $\tau_p^*(\mathrm{He})/\tau_E \sim 10$ was obtained for L mode discharges. No L-mode parameter scans were performed, as experiments concentrated on the more reactor-relevant ELMy H-mode.

Results: (II) ELMy H-mode

A comparison of a low triangularity/Corner strike zone (C/SFE/LT) discharge with a low triangularity/vertical target strike zone discharge (V/SFE/LT) is shown in Fig.3.3. In general, the ELMy H-modes had good quality with high confinement (H97 factors of 1·25-1·4) and low Z_{eff} with little sign of Argon contamination.

Figure 3.3 shows that $\tau_p^*(\mathrm{He})$ is much lower in the LT/C configuration, due to the enhanced pumping of He arising from the higher pressure at the pump throat (Fig.3.3(d)) in this configuration. At these elevated pump speeds, a value of $\tau_p^*(\mathrm{He})/\tau_E \sim 7.6$ was achieved, well within the range required by a reactor and similar to values achieved in DIIID [3.5], JT-60U [3.6] and ASDEX-U [3.7]. The decay time of the He concentration was similar at all radii within the plasma being about 25% higher towards the plasma edge. The He profile thus relaxed in a similar manner with $\nabla n(\mathrm{He})/n(\mathrm{He})$ remaining approximately constant.

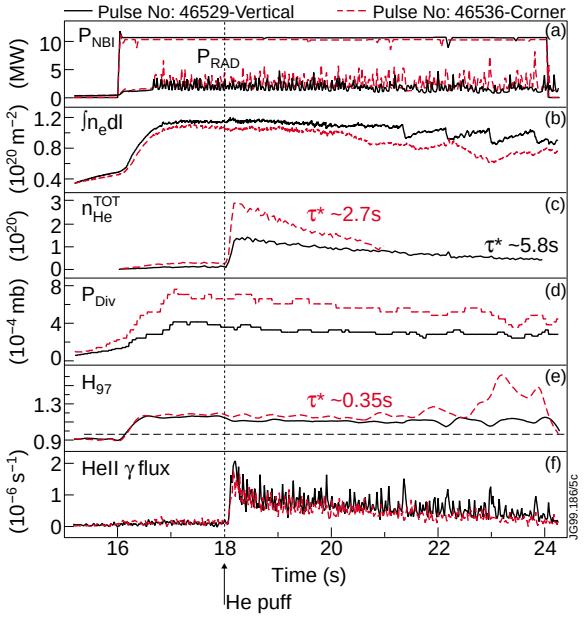

Fig.3.3: Comparison of helium concentration decay (c) and (f) for two ELMy H-modes (1.9MA/2T) at constant input power

Other results which were achieved in the ELMy H-mode are:

- $\tau_p^*(\mathrm{He})$ is essentially independent of triangularity;
- $\tau_p^*(\mathrm{He})/\tau_E$ is essentially independent NBI power input;
- $\eta(\mathrm{He})$ enrichment values of were in the range ~ 0·5-1·0.

The He enrichment in the divertor is thus sufficient for a reactor such as ITER. There is a tendency for η to decline as the efficiency of the pumping is raised (Fig.3.4) but the ITER criterion is always satisfied.

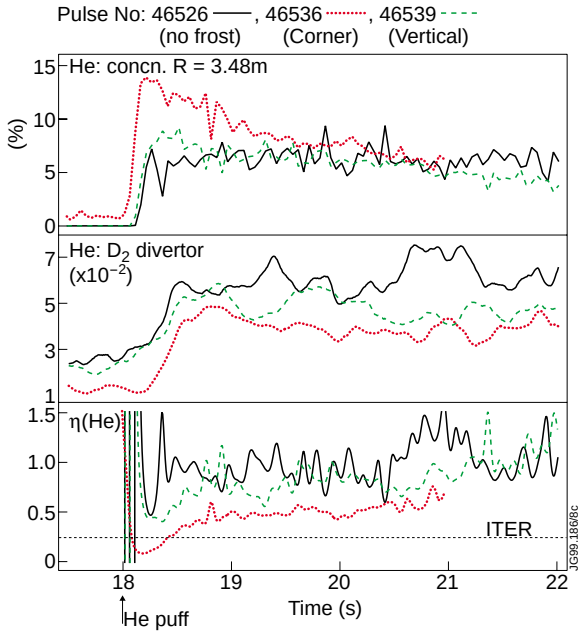

Fig.3.4: Comparison of bulk plasma HE concentration and divertor helium ratios for three identically heated 1.9MA/2T ELMy H-modes at constant q.

The *mean* He removal rate in the LT/C configuration in Fig.3.4 is $S_p(He)\cdot p_{div}(He) \sim (50m^3\cdot s^{-1})\cdot(3\cdot5\,10^{-5}mb) \sim 1\cdot8\,10^{-3}mb\cdot m^3\cdot s^{-1}$. The ratio of removal rate to the plasma volume ($V_p \sim 80m^3$) is similar to the design basis ratio for ITER [3.2]: $S_p(He)\cdot p_{div}(He)/Vp \sim 2\cdot3\cdot10^{-5}$ $mb\cdot s^{-1}$ for JET compared to $\sim 1\cdot8\ 10^{-5}mb\cdot s^{-1}$ for ITER.

Strong gas puffing tends to cause $\tau_p^*(He)/\tau_E$ to increase by ~ 40%, but this is mainly because τ_E declines as the electron density in the gas puff discharges, where the electron density reaches ~ 70% of the Greenwald Limit.

Since successive plasma shots are performed on the same Argon frost layer, because of the shot to shot variation in $r(D_2, He:Ar)$, identical shots with different $S_p(He)$ can be compared. Using this method the value of He particle confinement time ($\tau_p(He)$) can be established. By definition:

$$\tau_p^*(He) = \tau_p(He)/(1-R_{eff}) \qquad (1)$$

where $R_{eff} = (1-\varepsilon_{scr})R_{ret}$; R_{ret} being the *'return coefficient'* and ε_{scr} the 'screening efficiency' of the plasma for a particular species. R_{eff} can also be expressed in terms of R_{ret} using the fuelling efficiency (γ) for a returning species:

$$R_{eff} = \gamma R_{ret}/(1-(1-\gamma)R_{ret}) \qquad (2)$$

The return coefficient relates to pump efficiency (ε_p) and wall pumping efficiency (ε_w) as:

$$R_{ret} = (1-\varepsilon_p)(1-\varepsilon_w) \qquad (3)$$

Thus, using the absence of wall pumping of helium ($\varepsilon_w = 0$) and expressing ε_p as $S_p\cdot p_{div}/\Phi_{out}$, where Φ_{out} is the He outflux one can rewrite (1), using (2) and (3) as:

$$\tau_p^*(He) = \tau_p(He)\left[1+\gamma\left(\frac{\Phi_{out}}{S_p\cdot p_{div}} - 1\right)\right] \qquad (4)$$

Hence if $\tau_p^*(He)$ is plotted against $^1/S_p\cdot p_{div}$ for constant plasma configuration and conditions (Φ_{out} and γ constant), *extrapolation to infinite pumping speed* gives (since $\gamma<<1$) a value for $\tau_p(He)$. This is shown for two (C/SFE/LT) configuration plasmas in Fig.3.5, where the rudimentary method gives a value of $\tau_p(He) \sim 1\cdot3s$ for a 1·9MA/2·0T ELMy H-mode with 10MW NBI ie: $\tau_p(He)/\tau_E \equiv 4$.

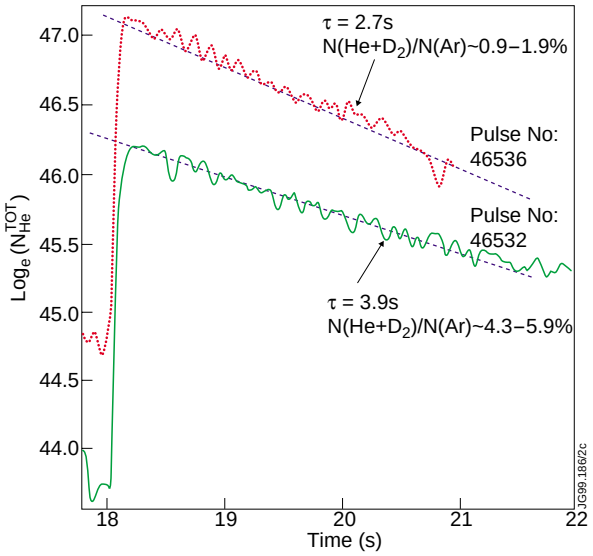

Fig.3.5:(a) Central helium decay rates for identical 1.9MA/2T ELMy H-modes as a function of cryo-pump loading

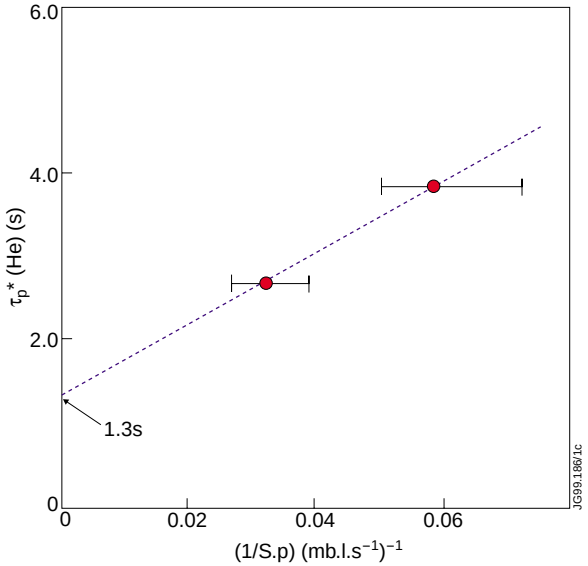

Fig.3.5:(b) Extrapolation of data on τ_p(He) at infinite pumping

3.3 Summary and future directions

The experiments show that He pumping conditions which are relevant to the ITER pumping regime ($S_p(He)\cdot p_{div}(He)/V_p$) can be achieved in JET using the Argon frosted PD cryopump. Also, using the variable, but calibrated, pumping speed for the Argon layer one can infer the helium particle confinement time (τ_p(He)). For a JET ELMy H-mode at 1·9MA/2·0T which has similar properties to the ITER reference design (q_{95} ~3·1; $\beta_N^{thermal}$ ~1·8) a value of τ_p(He) ~ 1·3s has been established.

In JET ELMy H-modes and with optimum pumping without strong gas puffing, the ratio $\tau_p^*(He)/\tau_E$ ~ 7.6 is measured. In configurations with poorer pumping this worsens to ~15. The ratio is independent of plasma triangularity and, over the limited range tested, of NBI power. The ratio also worsens with strong gas puffing principally because τ_E declines as the Greenwald Limit is approached. For a typical Lmode dischar ge a value of $\tau_p^*(He)/\tau_E$ ~ 10 has been measured.

The 'enrichment' parameter for helium in the divertor is in the range $0{\cdot}5 \le \eta(He) \le 1{\cdot}0$ in ELMy H modes. This value exceeds the requirements for an ITER type reactor ($\eta \ge 0{\cdot}2$) by a considerable margin. The values of $\tau_p^*(He)/\tau_E$ show that *helium transport per se will not be a limiting factor in reactor performance* and that accumulation of He ash should not be a problem in a reactor.

3.4 Shot List

Week 50 1998: Monday-Tuesday

Helium pumping/ transport experiments

Pulse List

Session Leaders: D Stork/ G Saibene/ C Maggi

Physicists-in-Charge: P J Harbour/ K D Lawson

Aims achieved:

- Successfully used Argon frost on the PD Cryopump and subsequently ran plasma pulses largely without disruption.
- Measured PD cryopump's pumping speed for Helium in gas only pulses.
- Measured helium transport and plasma residence time in L-mode plasmas at 2.35 MA/ 2.5 T .
- Measured helium transport and plasma residence time in H-mode plasmas at 1.9 MA/ 2.0 T in following cases:
  - V/SFE/LT configuration with and without added gas, at two NBI powers;
  - Corner/SFE/LT configuration at 10 MW;
  - V/SFE/HT configuration at 10 MW.

Dry Run pulses for pumping speed measurements

Note: All measurements done by puffing Helium (~ 12 - 15 mb.l.s^{-1}) for 2 secs (42 -44 secs). τ is conventional exponential decay time.

The ratio R is taken assuming that all the gas introduced since the last Argon frosting has gone to the PD cryopump.

L-mode pulses

- All pulses done at 2.35 MA/ 2.5 T in Vertical target/ SFE/ LT configuration
- Helium concentration was about 3-5%
- Each shot has two He puffs, one at each of the 'steady' densities.
- These pulses show the increased pumping effect of the increasing Argon frost layer. For 46521 the Helium decay is probably no longer significantly affected by any pumping limits. The time constants recorded in the table are *initial* values from analysis using CXDM/ NTOT and CXFM/NTOT
- H97 for these pulses is generally ~ 0.75—0.85

H-mode pulses

- These were all performed at 1.9 MA/ 2.0 T
- The following comparisons can be obtained from this data
  - no He pumping (no frost) vs He pumping at fixed config and NBI power
    46526 vs 46529
  - power scan with He pumping at fixed config
    46529 (10MW) vs 46539 (14.5 MW)
  - corner configuration He pumping vs Vertical target at fixed FE/δ and NBI
    46532, 46536 vs 46529

- He pumping for high δ vs low δ (vert tgt , FE and NBI fixed)
  46538 vs 46529
- He pumping for gas fuelling vs no gas fuelling (config, NBI fixed)
  46541 vs 46539

- The background Helium behaviour in a no puff case was investigated with pulse 46537.
- ***The values of τ^*(He) are taken from CXDM/NTOT.*** There will, of course be some correction due to the falling density, but this will not be significant in most cases

References

[3.1] Reiter D, Wolf G H, Kever H, Nucl Fusion **30**(10) (1990), 2141

[3.2] Janeschitz G, et al., Fusion Energy 1996 (Proc 16th Conf on Fusion Energy, Montreal, 1996, IAEA, Vienna 1997), Vol 2, 755

[3.3] The JET Team (presented by Watkins M L), 17th IAEA Fusion Energy Conf, (Yokohama 1998), IAEA-F1-CN-69OV1/2

[3.4] Hillis D L, et al., Rev Sci Instruments **70**(1999), 359

[3.5] Wade M R, et al., J Nucl Mater **220-222**(1995), 178

[3.6] Sakasai A, et al., J Nucl Mater **220-222**(1995), 405

[3.7] Bosch H-S, et al., J Nucl Mater **241-243**(1997), 82

4. HELIUM EXHAUST AND TRANSPORT STUDIES AT JET

M von Hellermann[1], S.Cox[2], M.Groth[3], P.J.Harbour, L.D.Horton[4], K.D.Lawson[2], A.Maas[5], C.F.Maggi[4], M.G.O'Mullane[2], D.Stork[2], M.Tunklev[6], K-D.Zastrow[2].

JET Joint Undertaking, Abingdon, Oxfordshire, OX14 3EA, UK.

[1] FOM Instituut voor Plasmafysica Rijnhuizen, EURATOM Association, Postbus 1207, NL-3430 BE Nieuwegein, The Netherlands.

[2] EURATOM/UKAEA Fusion Association, Culham Science Centre, Abingdon, Oxfordshire, OX14 3DB, UK.

[3] UMIST, Manchester M60 1QD, UK.

[4] Max-Planck-Institut für Plasmaphysik, IPP-EURATOM Association, Boltzmannstrasse 2, D-85748 Garching, Germany.

[5] CEA Cadarache, DRFC/SIPP/CFM, F-13108 Saint Paul Lez Durance Cedex, France.

[6] ABB Corporate Research, Dept. of Applied Mechanics, S-721 78 Vasteras, Sweden.

4.1 Overview

The following results on helium transport and exhaust were presented partially as an invited lecture at the Fourth International IAEA Workshop on Helium Transport and Exhaust in Fusion Devices, Jekyll Island, Florida, 18 – 21 October 1999 [4.1]. The part concerning the helium exhaust and pumping has already been presented at the 26th EPS conference on Controlled Fusion and Plasma Physics at Maastricht in June 1999 [4.2] those results will be only briefly summarised here.

Transport coefficients are usually derived from transients in gradients and particle flows based on time resolved CX measurements of helium density profiles following gas puffs injected at the plasma edge. This method assumes a source free region in space and time. Systematic errors in transport coefficients are notoriously induced by the necessity of smoothing procedures for the deduction of gradients in time and space from inadequate experimental data.

An alternative concept for the derivation of transport coefficients is presented, which is based on a *forward calculation* using the SANCO impurity transport code. A comparison with experimental profiles enables then an iterative deduction of simplified radial profiles of diffusion coefficient D and convection velocity v taking into account actual particle sources.

Helium transport data are derived for the case of maximum and minimum pump rates controlled by active argon frost pumping. Both '*Gradient*' and '*Forward*' techniques lead essentially to similar values for D and v and show core particle transport to be independent of the helium pump rate or τ_p^*.

A third approach, which leads to a further evidence of consistent transport coefficients is based on a profile relaxation time analysis of He^{2+} profiles following short blips of plasma edge helium gas puffs. Typical relaxation times as predicted from diffusion coefficients and convection velocities follow essentially the energy confinement time ($\tau_p^{relax} \approx \tau_E$).

4.2 Results

Helium exhaust studies in MKIIGB

In the recent MkIIGB pumped divertor configuration active helium pumping using argon frost on the Cryo pumps has been demonstrated successfully for the first time at JET. Time dependent measurements of He^{2+} ion density profiles using CXRS have provided decay times of the confined He^{2+} content which correspond to effective particle confinement times less than 6 times the energy confinement time ($\tau^*_{He}/\tau_E < 7.6$).

Helium transport experiments

Helium transport experiments are usually linked to simultaneous helium exhaust studies, where the first investigates primarily the transport of particles in the confined plasma region between magnetic axis and separatrix, whereas the second goal addresses the efficiency of particle removal from the non-confined region, and is essentially determined by the recycling characteristics of the wall and pump efficiency. However, efficient helium removal ensures the same background plasma conditions, i.e. collisionality etc. Since the latter may be a decisive factor in the extrapolation from present day plasmas to future burning fusion plasmas, it makes sense to combine the experimental aim of efficient helium removal with core transport studies. The two experimental aims are separated by quite distinctive time scales (ranging from tens of msec (transport) and several seconds (exhaust)). Fig.4.1 illustrates the two time windows. During the transport time interval the impurity density profiles changes its characteristic shape and the radial particle flow experiences the maximum excursions (Fig. 4.2).

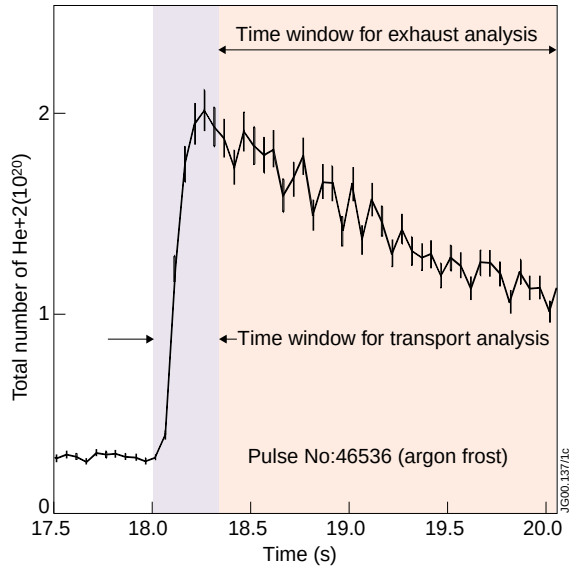

Fig.4.1 Time windows in a helium transport and exhaust experiment. A relatively short time interval (<500ms) is accessible for transport analysis. In the following decay phase the profile characteristics are unchanged and are determined by the ratio v/D.

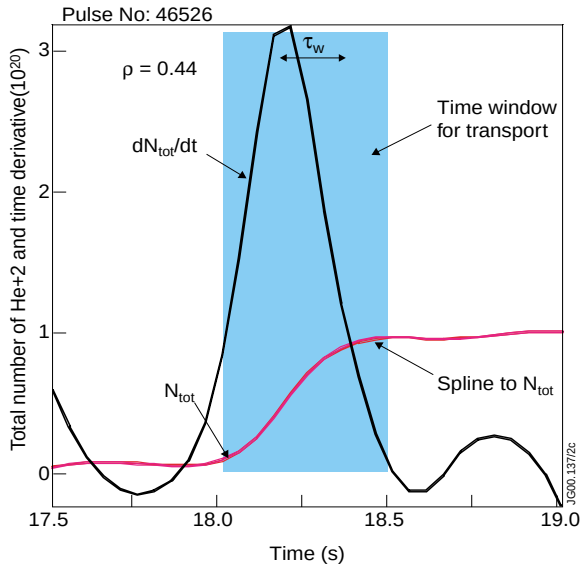

Fig.4.2 Changes of radial particle flow during 'transport time window'. The particle content N_{tot} is derived from smoothed time traces and smoothed radial profiles

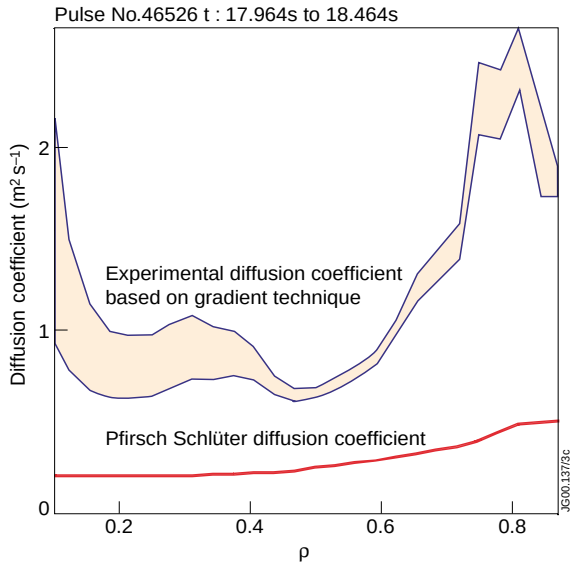

Fig.4.3 Diffusion coefficients derived from gradients and particle flows during transport window. Experimental values are found consistently above neo-classical predictions.

During the actual decay phase (exhaust time window) the v/D ratio is frozen and the characteristic radial shape remains unchanged. In the case of helium gas-puff experiments, both pre- and post-puff steady-state density profiles are similar in shape to that of electrons. That is, a characteristic feature for helium is its flat steady-state concentration profile (n_{He}/n_e=constant). By contrast, typical steady-state C^{6+} and Ne^{10+} concentration profiles are found to be hollow.

The following examples illustrate the chain of steps used in the 'gradient technique' leading eventually to diffusion coefficients and convection velocities. The actual time window with a high correlation between particle flow changes and changes in density gradients is typically of the order 0.5s, that is a time scale characteristic for the profile relaxation [4.3]. The sampling rate of the JET-CX system (50ms) is just about adequate for the gradient analysis with a sufficient number of data points.

Two extreme cases are selected, one with minimum pump rate (#46526, no argon frost) and one with maximum pump rate (#46536, optimised argon frost deposition). The actual core transport is unaffected by the efficiency of helium removal and pump speed. Within experimental error bars the values for particle diffusion and convection are the same in the 'pumped' and 'non-pumped' case. The differences, in particular for the convection velocity, towards the boundary

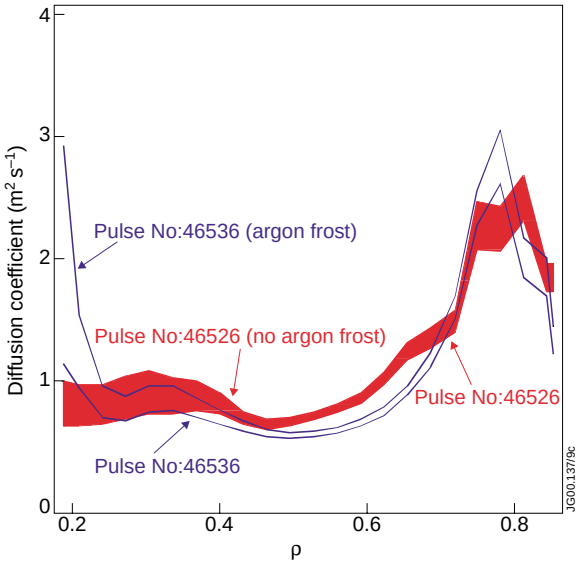

Fig.4.4 Diffusion coefficients in the case of active helium pumping (argon frost) #46536 and no argon frost , #46526. Within errors bars core transport is unchanged

.

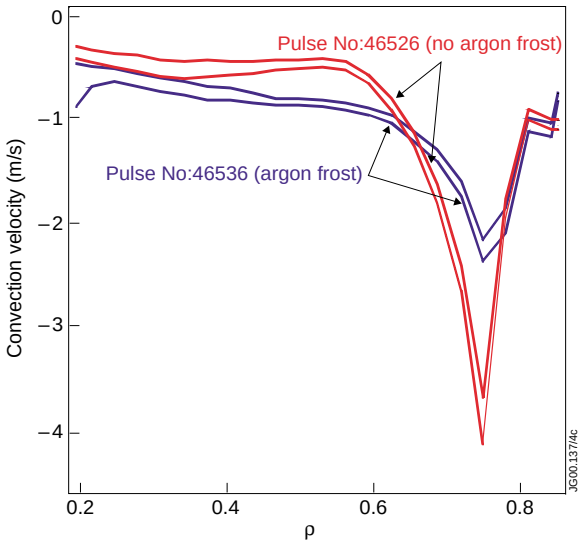

Fig.4.5 Convection velocities in pumped and non-pumped case.

of the confined region may be attributed to either profile errors or an inappropriate neglecting of source terms in either case. Table I gives an overview of transport coefficients deduced from the pulses with active helium exhaust.

Trace impurity behaviour

It is of fundamental interest to ascertain differences between 'trace impurity' transport and bulk plasma ion transport behaviour. In contrast to intrinsic impurities such as carbon or beryllium, seeded impurities (helium, nitrogen, neon or argon) can reach appreciable levels. Since the impurity ion collision frequency scales with Z^2 and is usually derived for the case of impurity ions colliding with bulk background ions, it has been tacitly assumed that the condition : $Z^2 \frac{n_z}{n_e} << 1$ is satisfied. For the case of helium gas puff experiments this quantity is of the order 0.5.

However, experimentally there is no obvious trend for the transport coefficients as a function of collisionality ($\nu^*_{ion-ion}$) or peak helium concentration (Fig.4.5).

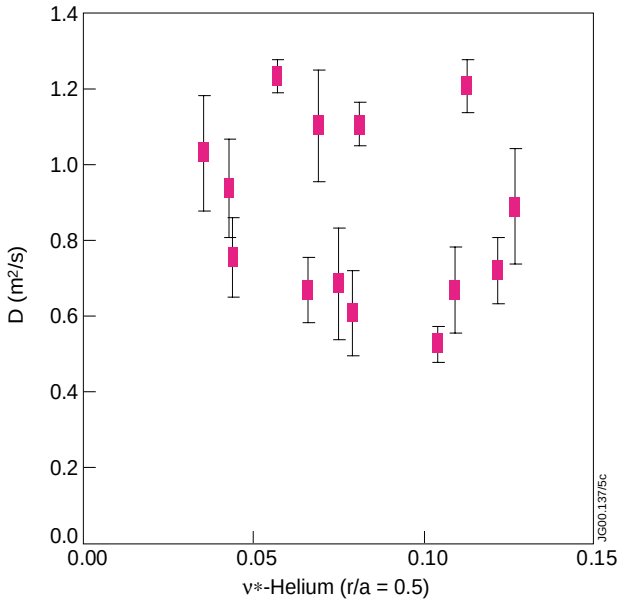

Fig.4.5 No obvious trend for diffusion coefficients and collisionality is recognisable. The data represent both argon-frost and no argon-frost cases (see table I). Peak He concentrations vary between 2.5 and 12 % of the electron density (n_{He}/n_e)

Validity of experimental transport data

An alternative approach to the usual 'gradient' technique is a 'forward' method which makes use of SANCO–CHEAP. This method has been used successfully in recent trace-tritium transport experiments [4.4] and has been applied in this case to helium transport analysis. Its main features may be summarised as follows:

SANCO (**S**tand **A**lone **N**o **CO**rona) solves radial profiles for impurity ion densities and their temporal evolution based on local ionisation and recombination rates as well as transport model for convection and diffusion and also a model for particle influx. The SANCO radial and temporal grid is usually on a finer mesh than the experimental raw data for impurity ion densities. The SANCO-CHEAP procedure is described in the following flow chart:

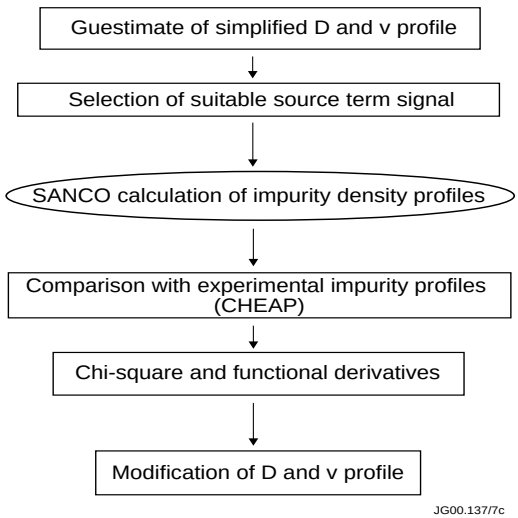

Fig.4.6 Flow-Chart for SANCO-CHEAP.

A comparison of transport data as derived by the 'gradient technique' or by the SANCO-CHEAP method shows that the two methods lead essentially to similar results. The strength of the SANCO-CHEAP method is that it is more physics oriented – it encompasses a particle source term - and, secondly it is probably less prone to systematic errors caused by the smoothing of data as required in the 'gradient' case. However, the SANCO method can at best provide a crude radial transport profile only and it is to some extent dependent on the quality of the source term, which may require some extra modelling.

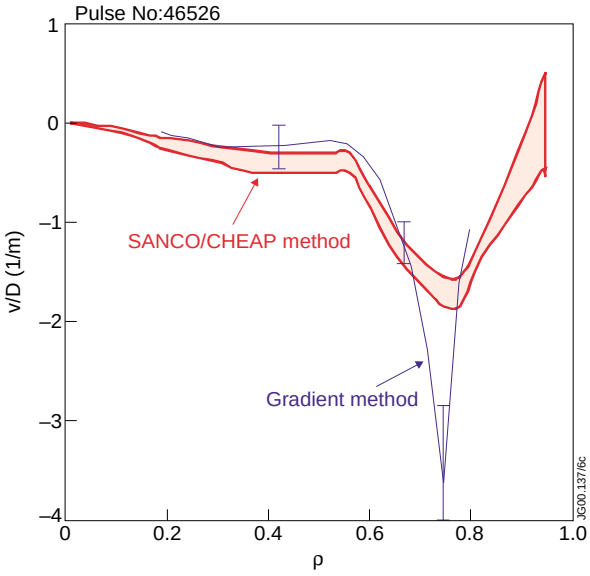

Fig.4.7 Comparison of v/D derived either by the 'gradient' or 'SANCO-CHEAP' method

Time Scales

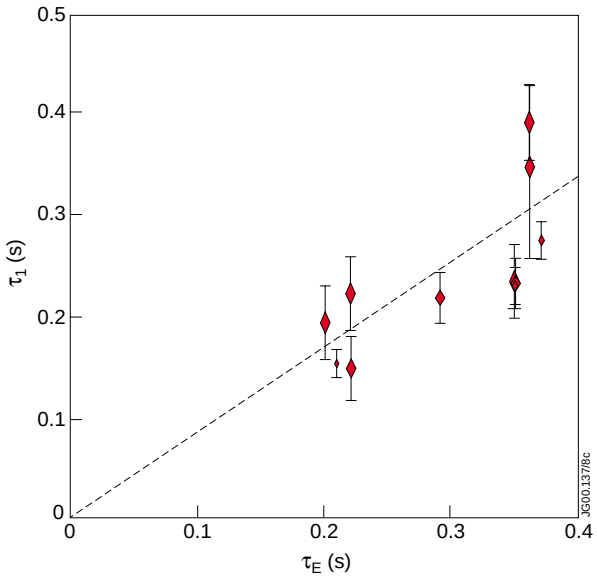

Fig.4.8 Profile relaxation time derived from transport coefficients and energy confinement time.

Two different time scales are characteristic for helium puff and exhaust experiments. One is the exhaust time τ_p^* and the second the profile relaxation time τ_1 . For the case of infinite pumping speed τ_p^* can be extrapolated to its ultimate minimum τ_p , the actual particle confinement time. Particle confinement time τ_p, energy confinement time τ_E and profile relaxation time τ_1 are of the same order of magnitude. Fussmann [4.3] has shown that the profile relaxation time may be approximately represented by the transport coefficients diffusion D and pinch velocity v and plasma minor radius a.

$$\tau_1 = 0.173 \frac{a^2}{D} e^{-0.173 \frac{v \cdot a}{D}}$$

Table I. Survey of transport data and time scales for helium exhaust pulses #46517 to #46541

Pulse	Argon frost	Mode	τ_p*(s)	τ_1(s)	τ_w(s)	τ_E(s)	D(m^2/s)ρ=0.5	v(m/s)
46517	2 bar l/s	L	23.2±2.2	0.149	0.175	0.22	1.22±0.27	-0.33±0.07
46521	10 bar l/s	L	4.6±0.1	0.221	0.225	0.22	0.89±0.15	-0.68±0.09
46522	25 bar l/s	ELMy-H	6.3±0.2	0.3271	0.300	0.36	0.55±0.13	-0.16±0.07
46523		ELMy-H	7.3±0.2	0.230	0.275	0.35	0.853±0.11	-0.65±0.05
46526	no frost	ELMy-H	17.8±0.2	0.280	0.175	0.37	0.68±0.05	-0.32±0.03
46529	30 bar l/s	ELMY-H	4.3±0.1	0.222	0.300	0.35	0.89±0.11	-0.70±0.08
46532		ELMY-H	3.47±0.05	0.243	0.350	0.35	0.80±0.11	-0.53±0.07
46536	30 bar l/s	ELMY-H	2.48±0.08	0.390	0.325	0.36	0.57±0.07	-0.82±0.03
46538	25 bar l/s	ELMY-H	3.3±0.7	0.1561	0.225	0.21	1.17±0.11	-0.30±0.07
46539		ELMY-H	4.47±0.07	0.217	0.300	0.29	0.87±0.11	-0.45±0.07
46541		ELMY-H	4.69±0.08	0.193	0.250	0.20	1.08±0.25	-1.13±0.07

Figure.4.8 shows that the relaxation time τ_1 is of the same order as the energy confinement time and moreover, that the observed relaxation times are consistent with the deduced transport coefficients. A further heuristic time scale is the interval between maximum particle flow and steady state τ_w (cf. Fig.4.2). Table I gives an overview for the different time scales.

4.3 Summary and future directions

The experimental deduction of transport coefficients must always considered with caution. Either due to experimental errors, inadequate resolution in time and space or non-trivial modelling of particle sources considerable systematic error bars must be assumed. However the main characteristics of helium transport have been assessed in the course of recent experiments. The results of the present helium exhaust and transport experiments have given clear evidence that core transport is unaffected by the pumping efficiency. Steady-state conditions with flat concentration profiles are reached on a time scale of less than 0.5s, which is comparable to the energy confinement time. Derived profile relaxation times based on radial transport coefficients are consistent with the same time scale.

A new ‘forward’ approach to transport evaluation, which encompasses source terms and a fully time dependent calculation of all ionisation states, has been successfully tested leading to an iterative procedure for the deduction of diffusion and convection terms.

References

[4.1] M.von Hellermann , M.Groth, P.J.Harbour, L.D.Horton, K.D.Lawson, A.Maas, C.F.Maggi, M.G.O’Mullane, D.Stork, M.Tunklev, K-D.Zastrow ‘Helium exhaust and transport studies at JET’ Fourth International IAEA Workshop on Helium Transport and Exhaust in Fusion Devices, Jekyll Island, Florida, 18 – 21 October 1999

[4.2] D.Stork, S.J.Cox , M.Groth, H.Y.Guo, P.J.Harbour, L.D.Horton, K.D.Lawson, A.C.Maas, C.F.Maggi, P.D.Morgan, G.Saibene and M. von Hellermann 'Helium Transport and Pumping Measurement in Reactor Relevant Plasma Configurations in JET' 26th EPS conference, Maastricht 1999, ECA Vol 233, 205-208

[4.3] G.Fussmann 'Analytical Modelling of Impurity Transport in Toroidal Devices' Nuclear Fusion 26, 983(1986)

[4.4] K-D.Zastrow, P.Andrew, N.P.Basse, P.Breger, R.Budny, W.G.F.Core, J.Ehrenberg, M.von Hellermann, O.N.Jarvis, R.W.T. König, L.Lauro-Taroni, M.J.Loughlin, F.B.Marcus, G.F.Matthews, M.G.O'Mullane, G.J.Sadler, J.D.Strachan, N.Watkins 'Particle Transport in steady-state ELMy H-modes studied by Trace Tritium Injection during JET DTE1' 25th EPS Conference on Plasma Physics and Controlled Fusion (Prague, Czech Republic), 9th - 13th June 1998)

5. HELIUM ENRICHMENT

P D Morgan[1].

JET Joint Undertaking, Abingdon, Oxfordshire, OX14 3EA, UK.

[1] EURATOM/UKAEA Fusion Association, Culham Science Centre, Abingdon, Oxfordshire, OX14 3DB, UK.

5.1 Overview

Helium enrichment studies have been undertaken in JET to ascertain the efficacy of various divertors in removing helium from the core plasma. The He was introduced into the plasma by puffing or bleeding the gas into the main chamber at the midplane position. Janeschitz et al. [5.1] have shown that, for any future power-producing reactor, a minimum value of He enrichment of 0.1 is required, to ensure that the D-T fuel is not excessively diluted by the alpha particles, thereby preventing self-sustained fusion reactions.

For both the fuel and impurity species, the particle compression factor is defined as the ratio of the neutral density in the divertor to the ion density in the main plasma core, ie

$$C = n_0 \text{ (div)} / n_i \text{ (core)}.$$

Replacing neutral density by pressure, the enrichment is then given by the ratio of the helium compression to that of the deuterium, for a single-species fuel, yielding :

$$\eta = \frac{p_{He}}{2p_{D_2}}\Big|_{SubDiv} \Big/ \frac{n_{He^{++}}}{n_{D^+}}\Big|_{Core} \geq 0.1 \qquad 5.1$$

In the results reported, measurements of the core helium concentration were obtained by charge-exchange recombination spectroscopy [5.2]. The helium concentration in the divertor was inferred from partial pressure measurements in the sub-divertor volume by the technique of visible spectroscopy using a Penning gauge as excitation source [5.3].

The main conclusions are that in most operating scenarios there is a de-enrichment of helium, ie η is less than unity, but in all cases the value is sufficiently large to satisfy criterion 5.1. Furthermore, η decreases with increasing core plasma density. The enrichment is mainly insensitive to divertor geometry and divertor plasma configuration.

5.2 Results

The work reported in this section concentrates on results obtained using the MKII GB (gas box) divertor. In the near future, it is intended to submit the work for publication in greater detail [5.4].

Variation of Compression and Enrichment with Core Plasma Density

The variation of helium compression with core plasma density is shown in Fig.5.1 (upper), for two divertor configurations and two modes of confinement. In L-mode confinement the compression increases with increasing density, whereas in H-mode confinement the dependence

is weak. Moreover, the compression in H-mode is lower than that in L-mode at the higher densities. The helium enrichment, also shown in Fig.5.1 (lower), decreases steadily with increasing core plasma density, in both L- and H-mode.

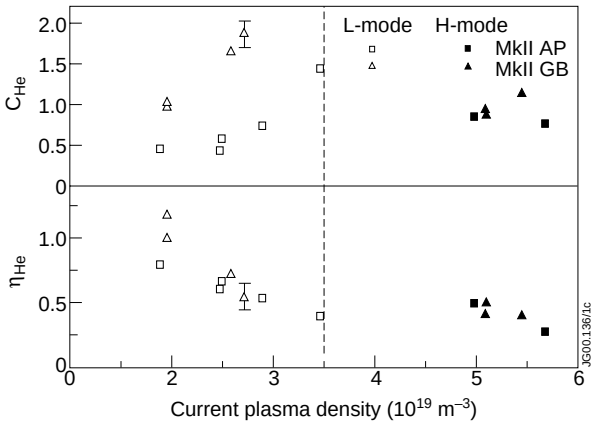

Fig.5.1: Helium compression and enrichment as a function of core plasma density (vertical target plates)

Influence of Divertor Geometry

Measurements of helium compression and enrichment have been undertaken in two divertor geometries, the MKII AP and the MKII GB. Figure 5.1 (upper) shows the compression obtained in both divertors during L- and H-mode operation. It can be seen that the compression obtained using the MKII GB is consistently higher than that obtained in the MKII AP which, being of a more open structure, does not attain such high neutral densities. This leads, consequently, to reduced pumping capabilities. However, in terms of helium enrichment, Fig.5.1 (lower), there is no great difference in performance between the two divertor configurations; the MKII GB attains a modest increase in enrichment over the MKII AP.

Variation with Divertor Plasma Configuration

In Fig.5.2 the variation of helium compression with core plasma density is shown for three different divertor plasma configurations. The plasma strike zones are attached to either the horizontal or vertical target plates or the zones are attached to the corner slots between the two sets of target plates. As can be seen, the compression increases with core plasma density for L-mode confinement and for a given plasma configuration, with the corner configuration showing the highest values. In vertical target configuration, the MKII GB divertor (results denoted by inverted triangles) exhibits higher compression than the MKII AP divertor (triangles). Figure 5.3 shows the corresponding He enrichment.

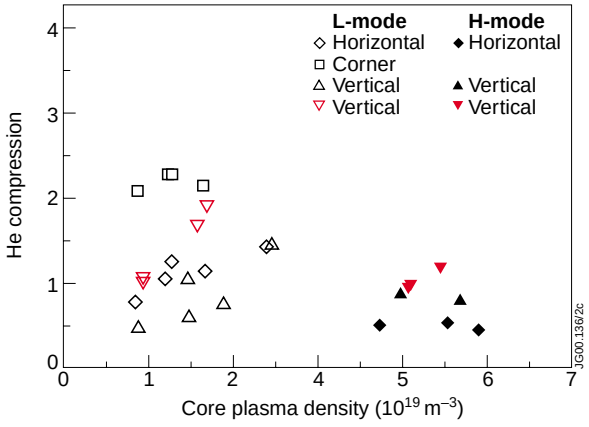

Fig.5.2: Variation of He compression with plasma density in MKII AP and MKII GB (inverted triangles) divertors

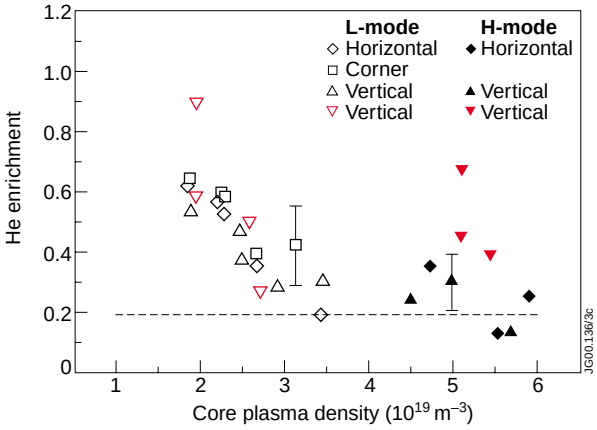

Fig.5.3: Variation of He enrichment with plasma density in MKII AP and MKII GB (inverted triangles) divertors

The Influence of ELMs

In Fig.5.4, traces are shown from two discharges which had the same density and the same level of additional heating power (12 MW NBI). One of the pulses (# 45796) was additionally fuelled with D_2 gas, introduced at the top of the main chamber, to increase the ELM frequency. This increased frequency can be detected by observing the fluctuations in the $D\alpha$ signal at the plasma edge, as shown in the figure. The plasma energy confinement, as indicated by the H_{89} scaling, is degraded by about 10%. The additional gas puff causes the neutral pressure in the divertor to rise, which increases the deuterium compression and leads to reduced helium enrichment. The raised pressure in the divertor probably masks the effects caused by the additional energy deposited on the target through increased ELM frequency. This point is considered in more detail later.

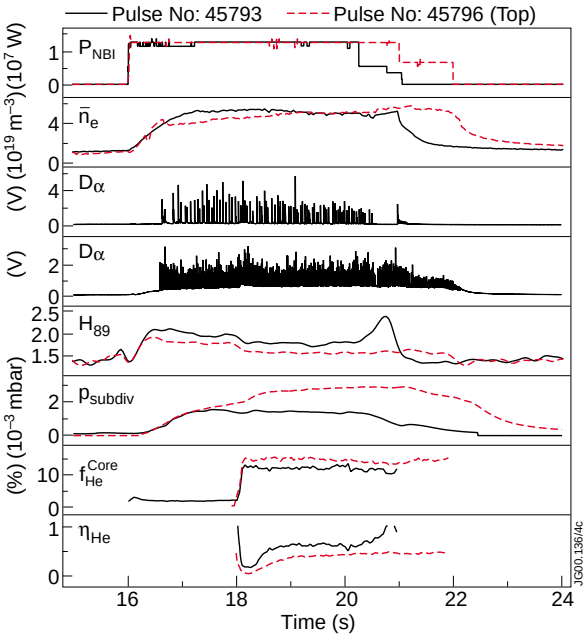

Fig.5.4: Time evolution of various parameters for two H-mode discharges with different ELM frequency

Effect of Induced Scrape-off Layer Flow

A technique that has proved successful in other machines for improving impurity retention in the divertor chamber is the Puff and Pump Method [5.5], by which a strong SOL flow is induced leading to enhanced impurity compression and enrichment. In Fig.5.5, the time evolution of two similar discharges is shown – the location of the strong deuterium puffing being the divertor and the top of the main vessel chamber, respectively. There is no significant difference in the helium compression and enrichment in the two discharges. The explanation for this is that there are large intrinsic SOL flows in JET, as determined using a Mach reciprocating probe near the top of the chamber, and that the puffing of additional D_2 does little to change these.

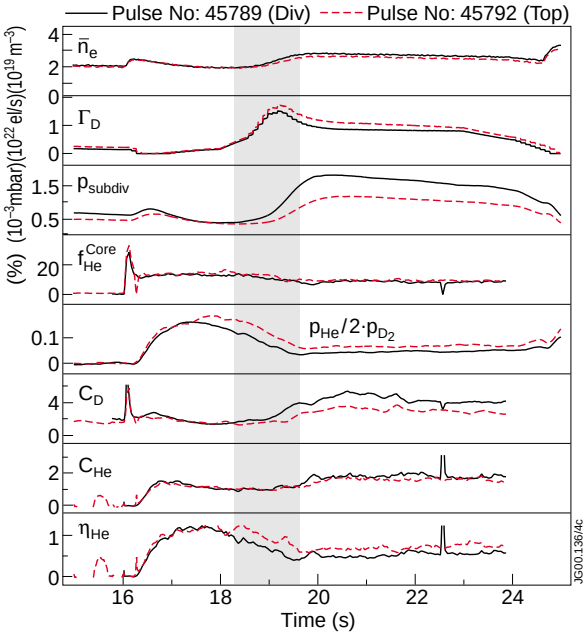

Fig.5.5: Time evolution of various parameters for two L-mode discharges with different fuelling locations

Effect of Active Helium Pumping

In Fig.5.6, the variation of helium enrichment versus core plasma density is shown for the cases of active helium pumping and of no active pumping. The active pumping is achieved by coating the divertor cryo-panels with argon frost. The same upstream conditions were maintained in both cases. The pump-off data were obtained during two separate campaigns. It can be seen that active pumping reduces the helium enrichment by a factor of 2, or more. However, the criterion established as a necessary requirement in the ITER-FDR design, $\eta_{He} \geq 0.1$, is always maintained. Fichtmüller et al [5.6] using modelling predicted that the pumping would reduce enrichment.

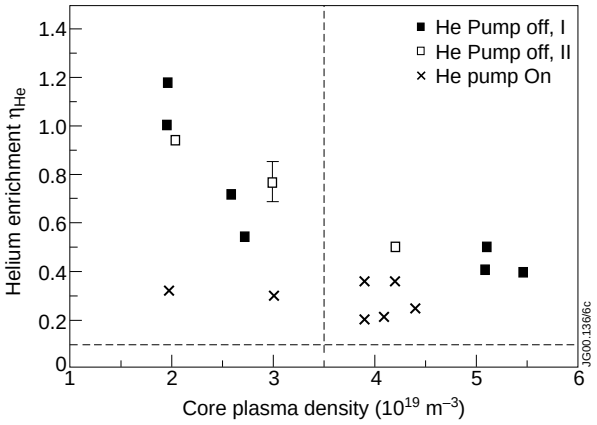

Fig.5.6: Variation of helium enrichment with plasma density, with and without active helium pumping

Comparison with Models and Codes

The experimental measurements have been compared with the results obtained by modelling, using the code DIVIMP/NIMBUS [5.7]. Figure 5.7 shows a comparison between results determined experimentally and those calculated using the numerical code. The results are for the MKII AP and MKII GB divertors, with strike points on the horizontal (H) and Vertical (V) target plates. Whilst the absolute values are not in agreement, with differences up to a factor of 4 being observed, the trends established by measurements are reproduced by the code. This has lent credence to the physical models used to describe neutral and ion leakage from the divertor.

The key parameters are the plasma temperature and density near the target, which determine the location of the ionisation zones of the neutral He and deuterium. As the core electron density increases, the density near the target increases whilst the electron temperature there decreases. This shortens the ionisation mean free path for D, with respect to that for He, reducing the fraction of D atoms that can escape to the main chamber thereby reducing the He enrichment. The modelling predicts an improvement in enrichment with increasing temperature near the target, eg through increased power loading brought about by increased ELM frequency, due to reduced ionisation rates. Further work is required in this area.

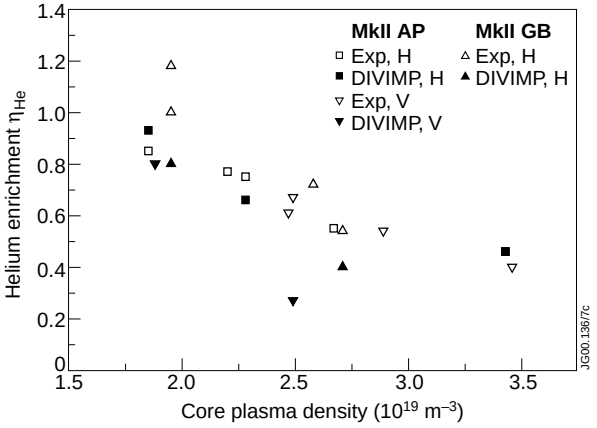

Fig.5.7: Comparison of results from measurements with those calculated using the code DIVIMP

5.3 Summary and Future Directions

The main results of the work are now summarised.

1) The helium enrichment, η, decreases with increasing core plasma density.
2) There is little difference in performance, in terms of the value of η, between the MKII AP and MKII GB divertor geometries. Compression in the MKII GB divertor is higher.
3) An increase in ELM frequency leads to a reduction in the measured enrichment, although the raised divertor pressure could be the root cause.
4) Attempts at improving enrichment by increasing the SOL flow by Puff and Pump methods have not demonstrated improved performance.
5) Active helium pumping reduces the helium enrichment by about a factor of two.
6) Modelling using the DIVIMP code has reproduced the measurement trends.

It is not anticipated that any further analysis of the MKII GB data will be made, as they have already been thoroughly analysed. Suggestions for further studies include improving the modelling codes and a deeper study of the effects of ELMs, where there appear to be differences between experimental observations and predictions from modelling.

5.4 Shot List

Shot #	Bt (T)	Ip (MA)	PNBI (MW)	Pulse Description
45789	2.5	2.4	1.9	L-Mode
45790	2.5	2.4	1.9	L-Mode
45791	2.5	2.4	1.9	L-Mode
45792	2.5	2.4	1.9	L-Mode
45793	2.0	1.9	12.5	H-Mode
45794	2.0	1.9	12.5	H-Mode
45795	2.0	1.9	12.5	H-Mode
45796	2.0	1.9	12.5	H-Mode
46517	2.5	2.35	2.8	L-Mode
46519	2.5	2.35	2.8	L-Mode
46521	2.5	2.35	1.9	L-Mode
46526	1.95	1.86	10.6	H-Mode
46529	1.95	1.87	10.6	H-Mode
46532	1.95	1.87	10.7	H-Mode
46536	2.0	1.9	11.0	H-Mode
46537	2.0	1.9	11.0	H-Mode
46539	2.0	1.9	14.5	H-Mode
46541	2.0	1.9	14.7	H-Mode

Acknowledgements

This work is the result of contributions by many people. Those especially deserving mention are M Groth, H Y Guo, D L Hillis, L D Horton, G F Matthews, D Stork and M G von Hellermann.

References

[5.1] G Janeschitz et al., Plasma Physics and Controlled Fusion **37**, A19, (1995).

[5.2] M von Hellermann, 'Quantative Spectroscopy for Fusion Plasmas', Contributions to High Temperature Plasma Physics, Eds. Spatscheck, & Uhlenbusch, Akademie Verlag Berlin, (1994).

[5.3] M Groth et al., Controlled Fusion and Plasma Physics **22C**, 39, 1998.

[5.4] M Groth et al., to be published (2000).

[5.5] M Wade et al., Nuclear Fusion **38**, 1839, (1998).

[5.6] M Fichtmüller et al., Journal of Nuclear Materials **266-269**, 330, (1999).

[5.7] P Stangeby and J Elder, Journal of Nuclear Materials **196-198**, 285, (1992).

6. TYPE I ELM THRESHOLD AND LOSS OF CONFINEMENT

R. Sartori[1] and the divertor Task Force

JET Joint Undertaking, Abingdon, Oxfordshire, OX14 3EA, UK.

[1] EFDA Close Support Unit Garching, Max-Planck-Institut für Plasmaphysik, Boltzmannstrasse 2, D-85748 Garching, Germany.

6.1 Overview

A spontaneous transition of the plasma from the Type I ELMy H-mode regime to a lower confinement mode, the "loss of confinement", is observed in JET with both the Mark II and the Gas Box (GB) divertors [6.1,6.2,6.3]. JET results with both divertors have shown that a minimum input power is required to maintain in steady state an ELMy H-mode plasma with Type I ELMs [6.1,6.2,6.3,6.4,6.5]. The Type I ELM regime has the high confinement usually associated with an H-mode (H=1), while H-modes with Type III ELMs have reduced confinement. In the Autumn 1999 JET experimental campaign, a new experiment has been carried out to assess the effect of plasma triangularity on the power threshold for Type I ELMs.

6.2 Results

6.2.1 The power threshold for Type I ELMs

The power threshold for Type I ELMs, $P_{thTypeI}$ is defined as the lowest input power P_{IN} necessary to maintain in steady state the Type I ELM regime (defined as the regime where the ELM frequency, f_{ELM}, increases with power). Fig.6.1 illustrates the typical features of a power scan at 2.5MA/2.5T aimed at the determination of $P_{thTypeI}$. When P_{IN} is increased in steps, starting from P_{IN} just above $P_{thL-H,}$ the H-mode changes from Type III ELMs to Type I ELM behaviour.

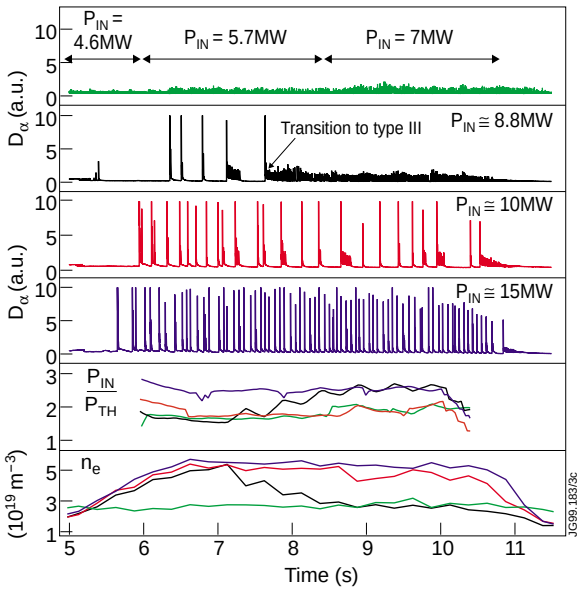

Fig.6.1: Power scan at 2.5MA/2.5T, showing the evolution of D_α, P_{IN}/P_{thL-H} and n_e as the power is increased

It was found that $P_{thTypeI}$ can be expressed as a multiple of the L-H threshold power P_{thL-H} ($P_{thL-H}=0.45\ n_e^{0.75}\ B_t\ R^2$) [6.1,6.2,6.3,6.4,6.5], or, in other words, it is found that the $P_{thTypeI}$ dependence on n_e and B_t is similar to that of the L-H threshold power. Quantitatively, $P_{thTypeI}$ is about twice P_{thL-H}.

In an ELMy H-mode with Neutral Beam Heating, there is a minimum density below which it is impossible to operate. This "natural" density increases with plasma current I_p, although

more slowly than linearly. $P_{thTypeI}$ is found to depend on either I_p or density, which varied together in our experiment. A separate experiment, which showed that P_{thL-H} does not depend on I_p, suggests that the observed dependence may be on density [6.5].

If a plasma has a marginal ratio $P_{IN}/P_{thTypeI}$, it might access the Type I ELM regime and sometimes maintain it for several energy confinement times, but cyclic or permanent (Fig.6.1, discharge with 8.8 MW) transitions to lower confinement are then observed. Such transitions are accompanied by a large decrease in density and stored energy.

In Fig.6.2, steady state Type I ELMy H-modes in deuterium with δ=0.2-0.25 are compared with the Type I ELMy phase of plasmas which experience a transition to Type III ELMs, for a dedicated experiment where P_{IN} was varied in I_p and B_t scans.

The result shows that input powers ($P_{IN}=P_{loss}$ for these steady state discharges) greater than 1.8 times the P_{thL-H} are required to maintain a steady state H-mode with Type I ELMs.

This multiplication factor exhibits some day to day variation (≈ +/- 20% in GB), suggesting an effect of vessel conditioning.

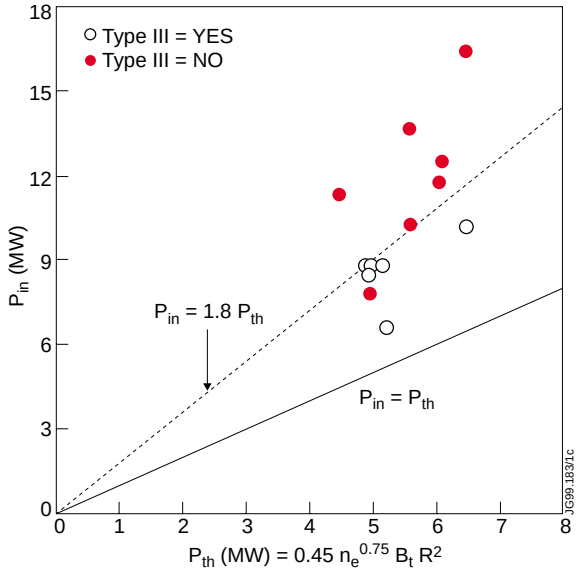

Fig.6.2: P_{IN}/P_{thL-H} necessary for steady state Type I ELM regime for scans in I_p and B_t.

6.2.2 The loss of confinement in the Mark II and GB divertors

Although the loss of confinement has similar behaviour in the Mark II and GB divertors, some significant differences are also observed.

With both divertors, the loss of confinement is associated with operation with input powers P_{IN} too close to the H-mode threshold power P_{thL-H}, but higher power is required to maintain a Type I ELMy H-mode in steady state in GB than in Mark II.

The response to gas fuelling and the behaviour of the pedestal parameters is also similar with the two divertors.

The most significant difference between the Mark II and the GB results is that in Mark II the plasma made a transition to the L-mode regime, while with the GB divertor the plasma remains in H-mode and the transition is to the Type III ELMy regime. This result seems to be in contrast with the observation that the measured H-mode power threshold for GB discharges with the strike points on the vertical target is higher than the H-mode power threshold for Mark II plasmas with the strike points on the horizontal target [6.5] and that, consistently, $P_{thTypeI}$ is higher with the GB divertor. Most probably, what prevented the Mark II plasmas from maintaining

a pressure pedestal was the presence, during the L-mode phase, of a n=1 MHD instability localised in the pedestal region. The nature of this instability as well as the reason why it is not present with the GB divertor is not known. The mode is clearly stable at the power levels required for a steady state H-mode with Type I ELMs.

6.2.3 The new experiment on the effect of plasma triangularity on the power threshold for Type I ELMs

ELMy H-modes with different triangularity δ have different steady state parameters. In particular, the steady state density obtained at high δ is higher than at low δ and the ELM frequency is lower. At δ=0.2-0.25, in Deuterium, the steady state density operating point is on average about 0.5 of the Greenwald limit n_G, although higher current plasmas tend to operate at a lower fraction n_e/n_G than lower current plasmas [6.1,6.2]. At a triangularity of 0.35-0.4, the natural density is $n_e \cong 0.7 n_G$ [6.6]. Higher steady state density implies, at fixed input power, a lower margin above the L-H threshold power. In contrast, previous Mark II results suggested that $P_{thL\text{-}H}$ could be lower at higer δ.

We investigated, with the GB divertor, the variation of $P_{thType1}$ with δ. The experiment was carried out at 2MA/2T with NBI heating and without external fuelling. Triangularities of 0.25 and 0.33 were compared.

P_{IN} was increased in each discharge, in a similar fashion as in Fig.6.1, but with a longer NBI pulse length of 9s.

Figure 6.3 shows the $D\alpha$ trace for the high and low triangularity discharges. In both cases, as P_{IN} is increased the period of reduced confinement becomes shorter (the same behaviour was observed with the Mark II divertor). In fact, for example, the discharge at δ=0.25 with 7.6MW NBI is in the Type I ELMy regime for 65% of the pulse duration (i.e. 13 over 20 energy confinement times τ_e($\tau_e \cong 0.45$s), as opposed to the discharge with 5.9 MW which has Type I ELMs only for 8%

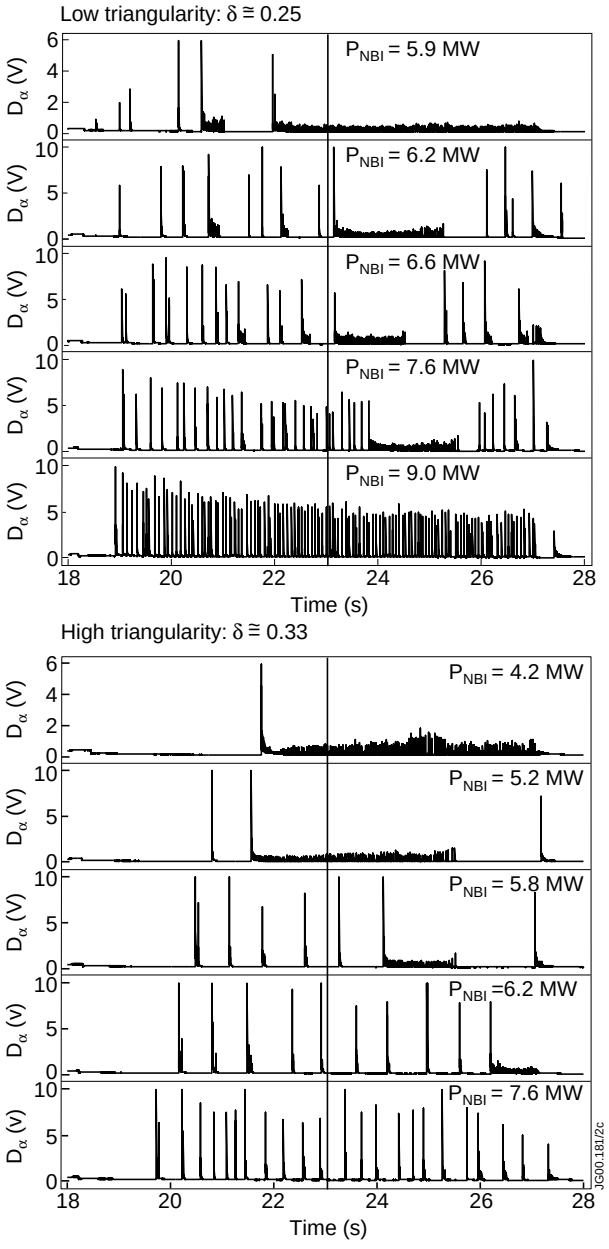

Fig.6.3: D_α traces for the power scan at two different triangularities

of the pulse duration. Long heating pulse duration is important for this kind of experiment. As can be seen from Fig.6.3, for shorter the NBI pulse duration the error in the determination of $P_{thType1}$ becomes larger.

Figure 6.4 shows the ELM frequency as a function of the NBI input power for both the high and low triangularity power scans. The dotted lines indicate discharges that have periods both of Type I and of Type III ELMs. The experiment indicates that the power threshold for Type I ELMs decreases with increasing δ. $P_{thTypeI} \cong 2.2\ P_{thL\text{-}H}$ at δ=0.25 and $P_{thTypeI} \cong 1.8\ P_{thL\text{-}H}$ at δ=0.33.

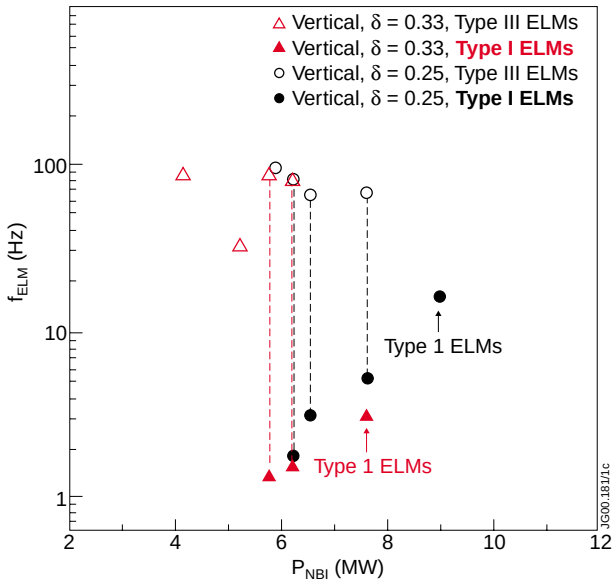

Fig.6.4:ELM frequency versus NBI input power for the power scans at high and low δ.

The high triangularity discharge with steady state Type I ELMs has lower loss power (P_{loss}= P_{IN}-dWdt, where dW/dt is the power required to reheat the plasma between the ELMs) than the low δ plasma with Type I ELMs, indicating that the lower $P_{thTypeI}$ at high δ is not related to the different ELM frequency. P_{loss}/ $P_{thL\text{-}H}$ is also lower at high δ than at low δ. Therefore, the lower power threshold for Type I ELMs at high triangularity might be due either to lower L-H threshold (not included in present scaling laws) or to better stability to Type III ELMs for high δ plasmas.

6.2.4 Pedestal density and temperature

The pedestal plasma temperature, T_e, in the Type III ELM regime increases at low density, as does the critical temperature for the L-H transition. Low power Type III ELMs without external fuelling have low edge density and relatively high edge temperature, as opposed to the Type III ELM regime achieved by strong gas fuelling. Figure 6.5 shows the pedestal T_e vs n_e for plasmas at 2.4 and 3.4T. The data are compared with the Pogutze-Igitkhanov model [6.7]. According to the model, Type III ELMs are caused by resistive interchange instability accompanied by magnetic flutter (RIF). The stability condition for this mode gives the upper boundary for Type III ELMs in the $_{ne}$-$_{Te}$ diagram.

Figure 6.6 shows the comparison of the experimental data with another model, by Chankin and Saibene[6.8], which predicts the critical density for the transition from Type I to Type III ELMs at high density. According to this model, Type III ELMs are caused by resistive ballooning instability.

There is good agreement between the experimental data and the predictions of both models, indicating that more experimental data are required in order to verify the theoretical models.

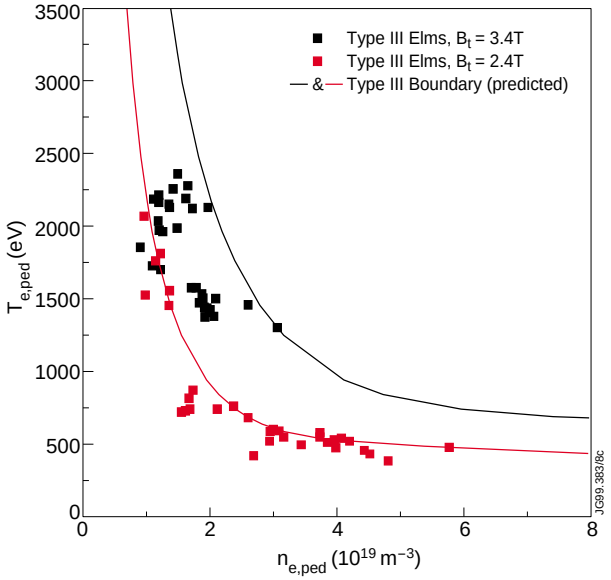

Fig.6.5:Pedestal Te-ne diagram showing the experimental data comparison with the model [6.7].

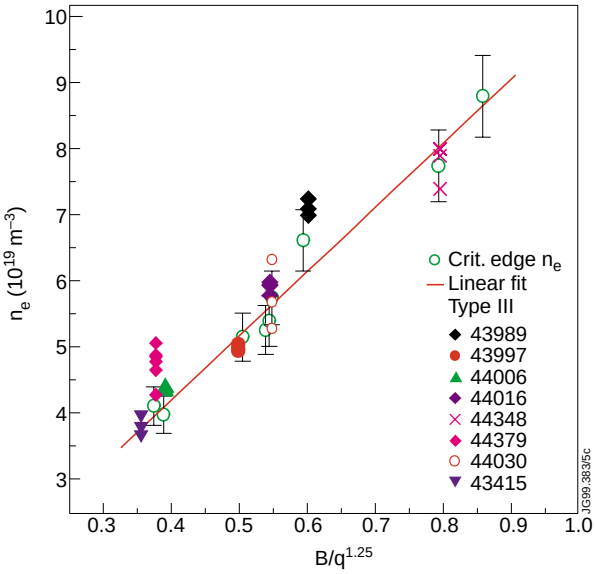

Fig.6.6:The critical density for the transition from Type I to Type III ELMs predicted by the model[6.8] is compared with the experimental data.

6.3 Summary and future directions

The Type I ELMy regime and the good confinement associated with it can be maintained in steady state with input power in excess of twice the L-H threshold power. The new experiment has shown that the power threshold for Type I ELMs decreases with triangularity. Further experiments are needed to establish whether this is due to better stability to Type III ELMs or lower L-H threshold at higher δ. It is necessary to extend the range of plasma parameters (in particular B_t) and to study the pedestal behaviour. There is good general agreement between the data and the models described in [6.7] and [6.8] but further experiments aimed at assessing the B_t and q_{95} dependencies of the Type III to Type I ELMs boundaryat low density are needed.

References

[6.1] Sartori R et al., Plasma Phys. Control. Fusion 40 (1998), 757

[6.2] Horton L D, Sartori R et al., Nuclear Fusion, Vol. 39, No. 8, 1999 (p.993)

[6.3] Sartori R et al., Proc. 26th Eur. Phys. Society Conf., Maastricht, 1999

[6.4] Righi E, Nuclear Fusion, Vol. 39, No. 3, 1999 (p. 309)

[6.5] Horton L D et al., Proc. 26th Eur. Phys. Society Conf., Maastricht, 1999

[6.6] Saibene G, Horton L D, Sartori R et al., Nuclear Fusion, Vol. 39, No. 9, 1999 (p.1133)

[6.7] Pogutze, O, Igitkhanov,Y et al., Proc. 26th Eur. Phys. Society Conf., Maastricht, 1999

[6.8] Chankin, A, Saibene,G, Plasma Phys. And Control Fusion 41, (1999) 913

7. PROFILE RESILIENCE AT HIGH DENSITY

J.G. Cordey[1], R. Budny[2], L. Horton[3], G. Maddison, A. Meigs[1]

JET Joint Undertaking, Abingdon, Oxfordshire, OX14 3EA, UK.

[1] EURATOM/UKAEA Fusion Association, Culham Science Centre, Abingdon, Oxfordshire, OX14 3DB, UK.

[2] Princeton Plasma Physics Laboratory, Princeton University, Princeton, NJ., USA.

[3] Max-Planck-Institut fŸr Plasmaphysik, IPP-EURATOM Association, Boltzmannstrasse 2, D-85748 Garching, Germany.

7.1 Overview

Towards the end of the last experimental campaign of the JET Joint Undertaking a further short series of profile stiffness experiments was completed. The objective of these experiments was to see if profile stiffness was density dependent. It has been suggested by G.Janeschitz [7.1] that the reason why there appeared to be no profile stiffness in JET [7.2] whilst other smaller machines such as ASDEX Upgrade [7.3] appeared to have fairly strong profile stiffness was due to the fact that JET was working at a lower density where the ions and electrons were only weakly coupled. To test whether this hypothesis is correct the intention was to repeat the original JET profile stiffness experiments at a higher density. Unfortunately it was only possible to complete part of the high density programme due to time constraints, this was the ELMy H-mode bit.

We were however able to show that in the absence of sawteeth, that both the electron and ion temperature profiles respond to the change in the heating profiles, in the same manner as at the lower densities of the previous experiments. Thus it would appear that at densities up to 60% of the Greenwald limit the temperature profiles are still not particularly stiff.

7.2 Results

The basic experiment was to add 7.8MW of NBI heating to a 2.8 MA/2.8T discharge to form an ELMy H-mode. Then 7MW of on axis (42.5 MHz) and off axis (37.2MHz) ICRH heating was added in turn to the ELMy H-mode. The experiments were performed in the current evolution phase prior to the onset of sawteeth. This is to avoid the flattening of the temperature profiles and the heating profile by the sawteeth. To keep the density high strong gas puffing was employed.

The time traces of the on and off-axis ICR heating pulses are shown in Fig.7.1. Although the ELM behaviour in the two pulses is not identical throughout, one can choose periods when the ELM behaviour is very similar for example the period $6 \rightarrow 6.5$. In fact we complete the analysis of the pulses around t= 6.2 where the density profiles of the two pulses are very similar (see Fig.7.2). The temperature profiles during this period are very different as can be seen from Fig.7.3. Both the ion and electron temperatures being more peaked with the on-axis heating than the off-axis heating, showing that the temperature profiles respond to the changing heating profiles.

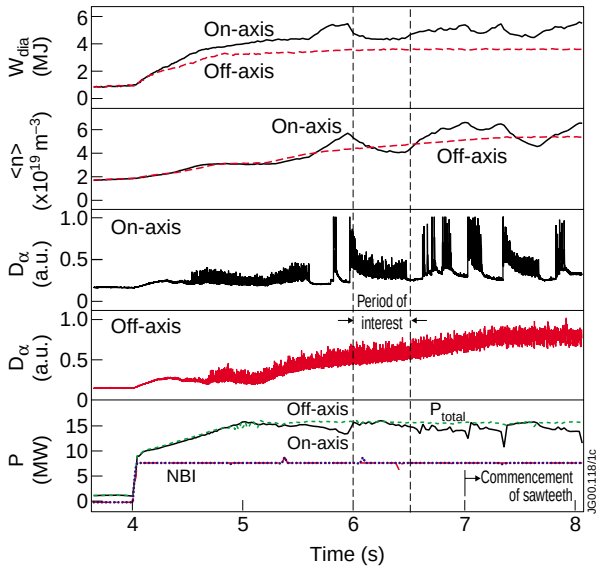

Fig.7.1: Diamagnetic Stored Energy, line average density, D^{α} emission for On-axis pulse, D^{α} for Off-axis pulse, input power versus time.

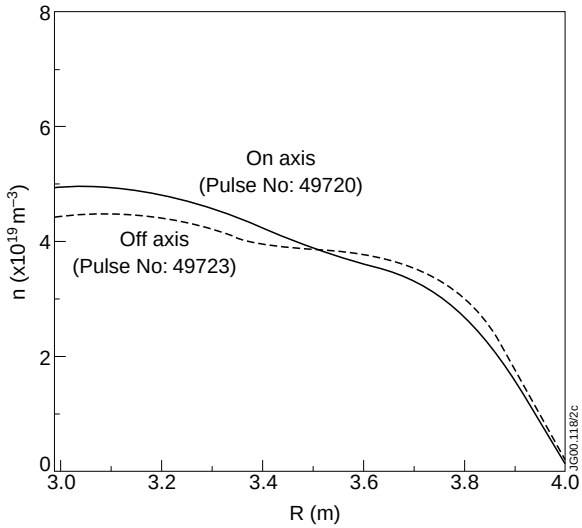

Fig.7.2: Electron density versus major radius at t = 6.2 for the on and off axis heating pulses.

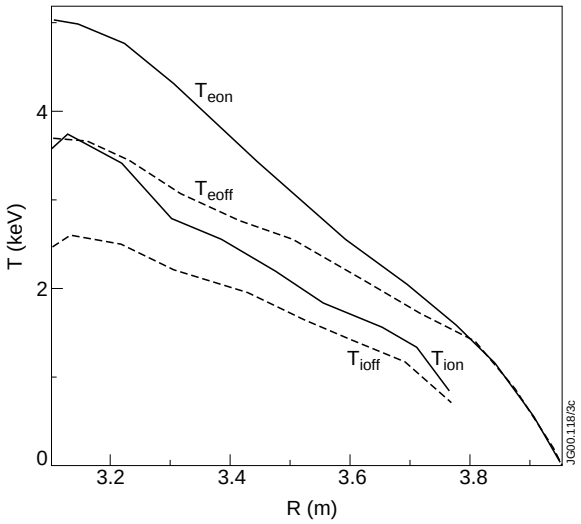

Fig.7.3: Electron and Ion temperature versus radius at τ = 6.2(s) for the on and off axis pulses.

The data from the two pulses was processed by the JET Chain II transport analysis code. This code contains the PION ICRH module and the PENCIL Fokker Planck package for the neutral beam heating. The heat flux profiles for the two cases of on/off axis heating are quite different as can be seen from Fig.7.4. In the region 0.4< r/a < 0.6 the heat flux in the off-axis heating case being approximately half that of the on-axis case, which corresponds approximately to the difference in the temperature gradients in this region as can be seen from Fig.7.3. In fact the effective thermal diffusivities are very similar indeed in this region as can be seen from Fig.7.5.

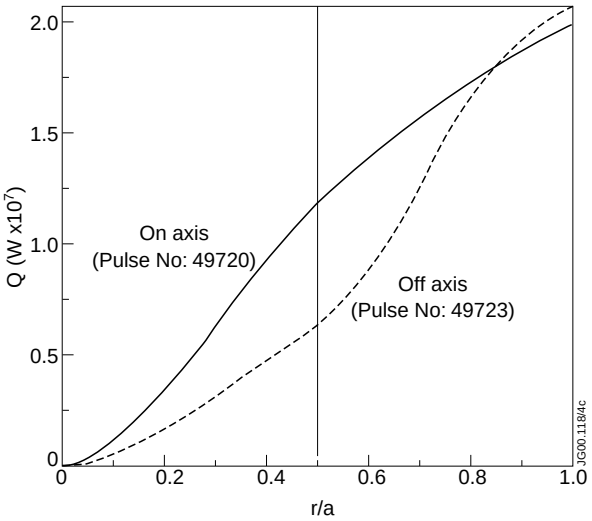

Fig.7.4: Heat flux versus the normalised radius 'r/a' for the on and off axis heating pulses.

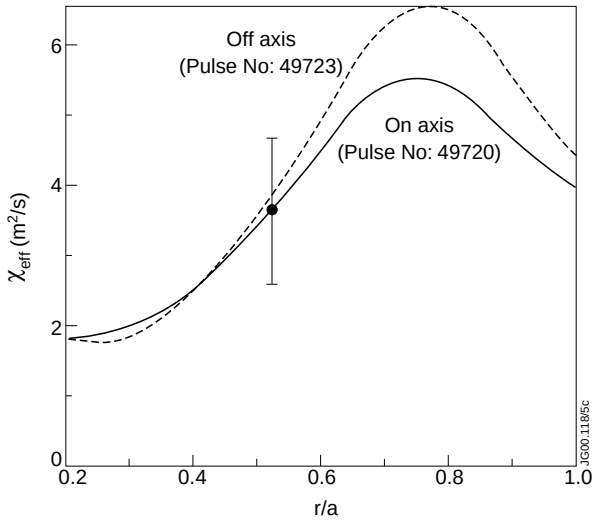

Fig.7.5: The effective thermal diffusivity by χ_{eff} versus normalised radius 'r/a'.

References:

[7.1] G. Janeschitz, et al., 26th EPS Conf. on Contr. Fusion and Plasma Physics, Maastricht, 14-18 June 1999. ECA Vol. 23 J(1999) 1445-1448.

[7.2] J.P. Christiansen, J.G. Cordey, et al., 26th EPS Conf. on Contr. Fusion and Plasma Physics, Maastricht, 14-18 June 1999. ECA Vol. 23 J(1999) 209-212.

[7.3] A. StŠbler, J. Stober, et al., 26th EPS Conf. on Contr. Fusion and Plasma Physics, Maastrict, 14-18 June 1999. ECA Vol. 23 J(1999) 1437-1440.

8. EFFECT OF q_{95} ON NTM THRESHOLDS, AND UNDERLYING PHYSICS

R. J. Buttery[1], T. C. Hender[1], D. Howell[1].
JET Joint Undertaking, Abingdon, Oxfordshire, OX14 3EA, UK.
[1] EURATOM/UKAEA Fusion Association, Culham Science Centre, Abingdon, Oxfordshire, OX14 3DB, UK.

8.1 Overview

An important issue for ITER operation, and tokamaks generally, is whether improved performance can be obtained by raising plasma current (for given shape and field), thus reducing safety factor, q_{95}. Data reported in Ref [8.1] pointed to improved confinement with higher current, without degradation at low q_{95}, but it remained to be tested whether this could be achieved at high β_N. Experiments investigating this on JET in Autumn 1999 found a strong dependence with q_{95} of the threshold in β_N for neoclassical tearing mode (NTM) onset, with thresholds falling markedly for $q_{95}<3$. In terms of likely operational limits to machine performance (for JET or ITER), this translates to a sharp fall-off in accessible β_N as the plasma current is increased at constant toroidal field.

This effect has been examined in terms of the underlying physics of the NTM. It is found that the dominant ingredient in the lower threshold at low q_{95} is the variation in poloidal Larmor radius (dependent on local temperature and B_θ values) at the resonant surface, which governs the size of stabilising ion polarisation effects, and is further out, and therefore colder at low q_{95}. To investigate the role of other terms, thresholds are corrected for variation in Larmor radius (and collisionality), using fits to other data - this isolates geometry and q dependence of the various effects (ion polarisation, seeding mechanism, Δ', etc.). Corrected thresholds are then found to be *higher* in the low q_{95} pulses. This can be understood in terms of additional explicit dependence on resonant surface minor radius (which varies systematically with q_{95}) in the ion polarisation term. This provides stronger stabilising contributions at larger resonant surface minor radii (and so at lower q_{95}), thus requiring larger seeds or higher pressure gradients to trigger the mode. Measurements of sawteeth and other effects indicate that seed size does not change substantially with q_{95}, so corrected thresholds in local β are expected to be higher at low q_{95}. This match between predicted and observed effects confirms our understanding of the NTM behaviour and the role of various effects involved. Comparison of local 'physics parameter' fits with earlier high plasma current, low q_{95}, pulses from 1998-9 plasmas show threshold scalings are in accordance with the local parameter fits used.

The basic conclusion remains **that operational limits in q_{95} will be set by NTMs, limiting benefit from better confinement at low q_{95}**.

8.2 Results

Experimental results and implications for operational limits:

A thorough scan of NTM thresholds with q_{95} was obtained in Autumn 1999, which showed thresholds falling markedly for $q_{95}<3$ (see Fig.8.1). This was performed at a constant plasma

current (1.3MA), to maximise the parameter range while obtaining NTMs. For ITER, the scenario considered is to raise the current at fixed toroidal field (to improve confinement), while the density is most likely to be governed by achievable Greenwald fraction. Therefore the data has been corrected to constant toroidal field and Greenwald fraction (using a previously obtained fit to ρ_i* [normalised toroidal Larmor radius] dependence for standard q_{95} data to map changes in temperatures to β_N). We then see that the predicted fall in thresholds is even more pronounced. This indicates that if we seek to optimise performance by raising plasma current at a given toroidal field, and allowing the benefit of higher density access (available at higher plasma current), then confinement improvements cannot be significantly exploited. For q_{95}<3, the NTM (which is m=3, n=2) slows the plasma rotation, eventually (or rapidly at lower q_{95}) stopping it, at which point an n=1 locked mode rapidly grows and causes a disruption. This will be partially error field driven (as well as by the hole in the bootstrap current - a combined locked NTM error field mode). This makes the nature of the performance limit below q_{95}=3 much harder (disruptive rather than confinement degradation).

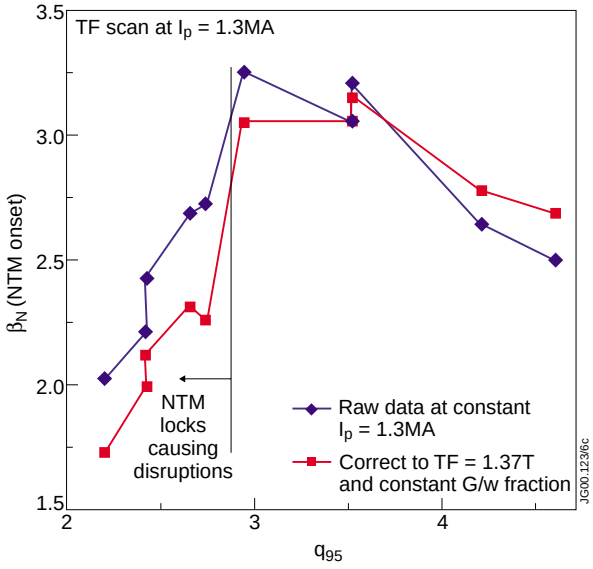

Fig.8.1: Change in β_N required for NTM onset with q_{95}: raw data and corrected for TF and Greenwald density fraction variation.

Onset criteria for NTM and separating out parameter dependence:

In order to understand this effect in terms of the underlying physics governing the onset of NTMs, it is necessary to recouch results in terms of local parameters, which are related more directly to the physics that governs NTM growth. The threshold for NTM growth is governed by the modified Rutherford equation [8.2] for the growth rate of an island of size, w:

$$\frac{\tau_r}{r^2}\frac{dw}{dt} = \Delta' + a_{bs}\varepsilon^{1/2}\left(L_q/L_p\right)\frac{\beta_P}{w}\left(\frac{1}{1+w_d^2/w^2} - \frac{w_{pol}^2}{w^2}\right) \qquad (8.1)$$

This is expressed in terms of the tearing stability parameter (Δ'), bootstrap current (β_p/w term which represent the effect of flattening of bootstrap within the island region, where a_{bs} is a constant of proportionality), ion polarisation effect (w_{pol} term) [8.3] and additional transport effects in the island (w_d term, which is small for present devices) [8.4]. L_q and L_p are the scale lengths for safety factor and pressure gradients, ε measures the minor radius of the resonant surface normalised to major radius and τ_r is the resistive time scale. The ion polarisation and transport effects act to oppose the drive for the mode (from the bootstrap effect) at small island

sizes, leading to the requirement of a seed perturbation. The seed must be generated by other forms of MHD (sawteeth in this case), and so will depend on the size of that MHD, toroidal coupling to the NTM surface, and dynamic shielding effects, which oppose seeding.

We neglect transport effects, which are thought to be small for present devices [8.5], setting w_d=0. w_{pol} is given by [8.5],

$$w_{pol} \approx [g(\nu,\varepsilon)\,(L_q/L_p)\,\varepsilon]^{0.5}\, r.\rho_{i\theta}^{*} \qquad (8.2)$$

where g is a function dependent on collisionality, ν.

In work reported under the TF C data validation report [8.6], we have already seen how fits to collisionality and ρ^* dependence can be improved using local versions of these parameters based on Eq.s 8.1 and 8.2, rather than global β_N and toroidal Larmor radius. These reduce scatter, improve correlation, and remove profile dependent systematic offsets between different divertor configurations. The key issue for understanding q_{95} dependence is separating collisionality and $\rho_{i\theta}^{*}$ dependence, from variations due to change in geometry and sawtooth size.

At NTM onset we assume a seed is generated of size, $w=w_{seed}=Aw_{pol}$ where A acts as a measure of the 'relative seed island size'. (From Eq 8.1, A must be >1 for positive growth rates). We can then write the onset criteria (obtained from dw/dt=0) as:

$$\sqrt{\varepsilon}\,(L_q/L_p)\,\beta_p \propto r_s\Delta'.\frac{A}{(1-1/A^2)}.w_{pol}/r \qquad (8.3)$$

$$\propto f_1(\rho_{i\theta}^{*},\nu)\times f_2(q_{95})$$

where the LHS is the bootstrap term from equation (8.1). The values of this term for the q scan are plotted in Fig.8.2 as 'raw data'. On the second line we have schematically separated out dependencies into two functions, f_1 and f_2. f_1 is already known from fits to other data at q_{95}~3.4 [8.6]. We can then use the local collisionality and $\rho_{i\theta}^{*}$ values in the q scan pulses, applying the previously obtained fits for f_1 to correct out collisionality and $\rho_{i\theta}^{*}$ variation. The data corrected in this way, is shown in Fig.8.2. where the remaining variation must come from either q_{95} dependence of Δ', geometry effects on w_{pol}, or changes in seed size with q_{95}.

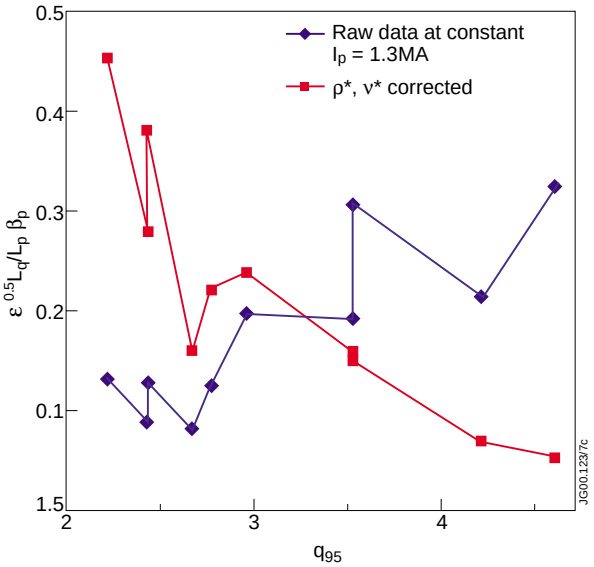

Fig.8.2: threshold for NTMs in local parameters plotted vs q_{95}. Shown are raw data, and data corrected for variation in local collisionality and ρ_θ^{*} values.

Role of the ion polarisation term:

Figure 8.2 reveals a very interesting effect - thresholds now rise as q_{95} falls. This change is a result of the very strong dependence of local $\rho_{i\theta}^*$ value on q_{95} (through variation in radius of the resonant surface, q=3/2), leading to a correction that varies systematically over the q scan. We therefore see that the dominant dependence in the raw data comes from this $\rho_{i\theta}^*$ scaling: at low q_{95} values the resonant surface is further out, and colder, leading to lower $\rho_{i\theta}^*$ values and less stabilisation from ion polarisation effects.

When the $\rho_{i\theta}^*$ and collisionality dependence is corrected out, an additional dependence on q_{95} is revealed. This indicates that as q_{95} falls, either tearing stability is improving (which seems unlikely, but will be checked), w_{pol}/r is rising, or the ratio $A=w_{seed}/w_{pol}$ is falling. If we examine the functional dependence of Eq.8.3 on A, we see this latter effect can be very strong, as shown in Fig.8.3 where small falls in A lead to a rapid rise in the function of A that appears in Eq.8.3.

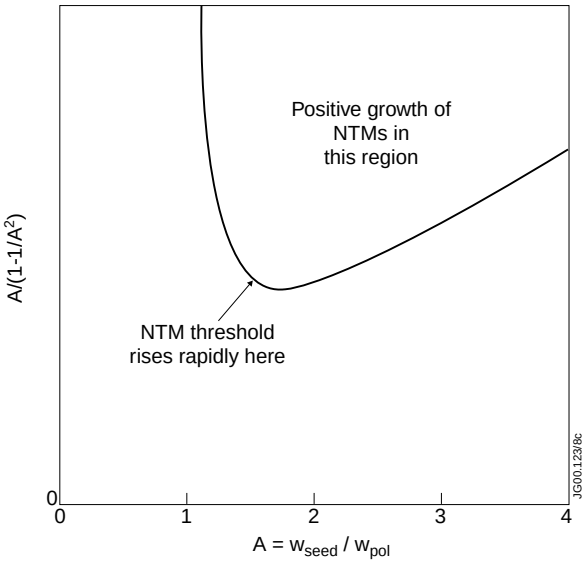

Fig.8.3: Sensitivity of NTM threshold to 'A', the ratio of seed size to w_{pol}.

Looking at the equation for w_{pol} (Eq.8.2), we see a very strong dependence on the minor radius of the resonant surface (at fixed major radius):

$$w_{pol} \propto \varepsilon^{0.5}\, r \propto r^{1.5}.$$

Thus, as q_{95} falls, the minor radius of the q=3/2 surface increases (as observed via EFIT reconstructions), leading to a rapid increase in w_{pol}. If this is not matched by w_{seed} increases, then A falls and the NTM threshold in local β_p will rise rapidly. For example, if w_{seed} and other terms remained constant, we would expect the LHS of Eq.8.3 to scale as $\varepsilon^{1.5}$. Plotting the experimental data against ε (as shown in Fig.8.4) appears to indicate exactly this type of effect, where a fit to the ε dependence of thresholds yields a scaling as $y \propto \varepsilon^{1.7}$, much steeper than the $\varepsilon^{0.5}$ expected if 'A' were constant. The behaviour of the seed is examined in the next section.

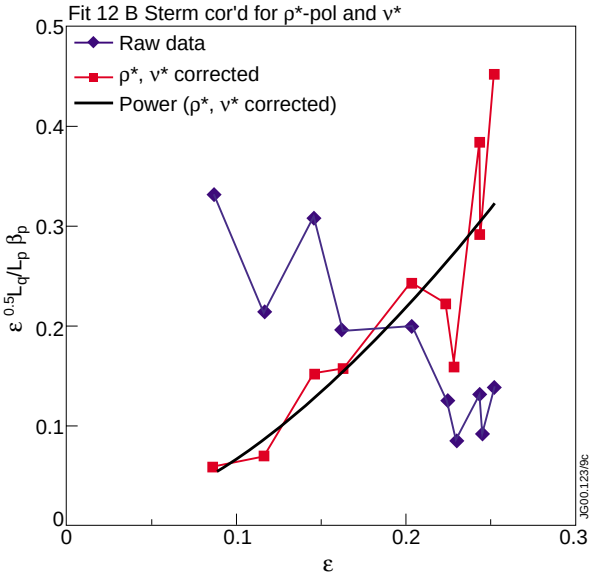

Fig.8.4: Plot of data from Fig.8.3 vs ε instead of q_{95}.

Thus we see that the ion polarisation term plays a highly significant role. It controls the size of seed and β_p required to trigger an NTM, which accounts for the principal parameter scaling for NTM onset with $\rho_{i\theta}^*$. Through its dependence on $\rho_{i\theta}^*$, it leads to very strong variation of NTM thresholds with q_{95}, as the q=3/2 surface moves out to colder regions where ion polarisation effects are less stabilising - this dominates all other effects, leading to the observed lower thresholds. When the effect of $\rho_{i\theta}^*$ variation is corrected out, there remains an explicit resonant surface radius dependence in the ion polarisation, which can lead to an opposite q dependence, that seems to match that observed in the data.

Variation of sawteeth and role in q scaling of NTM threshold:

A critical issue for understanding NTM q scaling behaviour, is examining how the seed resulting from sawtooth MHD changes with q_{95}. In addition to data from the NTM q scan, it is useful to examine behaviour in ITER shaping scans (which also scanned q_{95}), where pulses were held in steady state for long periods with many sawteeth (allowing clearer measurements of quantities such as inversion radius or SXR fall).

Turning first to the sawtooth itself: if we examine the magnetic amplitude (Fig.8.5), we see that peak n=1 amplitude associated with the sawtooth is larger at low q_{95}. However, this scaling might be expected as q=1 radius will be larger for low q_{95} values, so the activity is closer to magnetic pick up coils and will therefore generate larger signals. This is confirmed by measurements of inversion radii from the shape scans (Fig.8.6), where for a given shape, lower q values have systematically higher inversion radii.

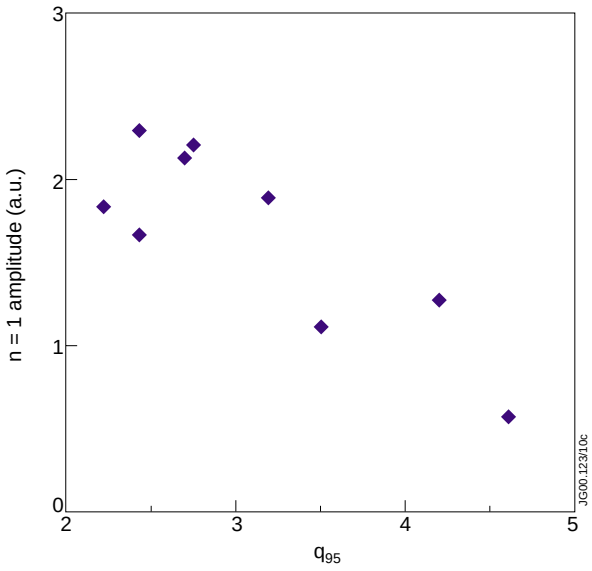

Fig.8.5: Scaling of peak n=1 amplitude (dB/dt) associated with sawtooth triggering NTM in q scan

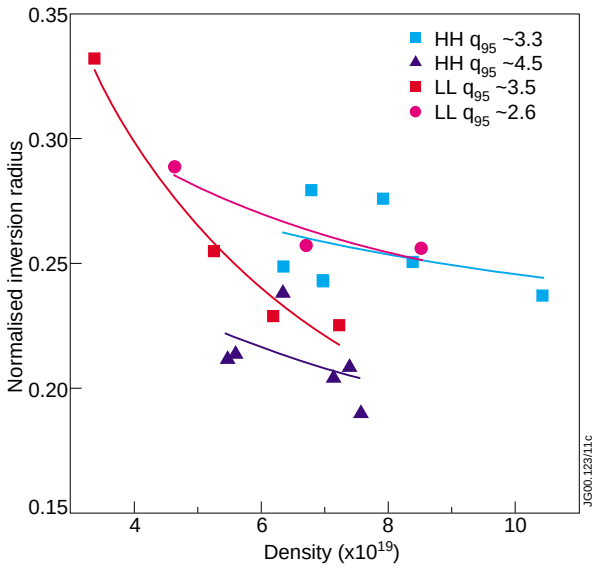

Fig.8.6: Variation of inversion radius (normalised to minor radius) versus density for different q_{95} values in ITER shaping scans for HH and LL configurations.

To gain a true measure of the sawtooth size variation, we examine fractional SXR fall with each sawtooth (Fig.8.7). We see that this quantity is not strongly dependent on q_{95} value. As

these discharges all had similar stored energies, we infer that the size of the sawtooth event does not change amplitude substantially with q_{95}, and so sawtooth variation will not cause w_{seed} to scale rapidly with ε, as w_{pol} does. This therefore means that 'A' (in Eq.8.3) is likely to fall as q_{95} falls, leading to the rapid increase in **corrected** thresholds predicted from Fig.8.3, and observed in Fig.8.2.

Another possible factor in seed size is coupling between the sawtooth and NTM resonant surfaces. However variation in this with q_{95} is not expected to be dramatic, as variations of inversion radius with q_{95} are not large (Fig.8.6), and will match to some degree motion of q=3/2 surface. Overall this is expected to be a weakly destabilising as we go to lower q_{95}, and the ratio of q=1 to q=1.5 radii rises slightly.

Finally, we take account of differential rotation between the central sawtoothing activity and the q=3/2 surface. As shown in Fig.8.8 this is higher at low q_{95}. Thus it might be expected that the seeding mechanism is more difficult (increased dynamic shielding) at low q_{95}, which may partially account for some of the observed scaling in corrected thresholds.

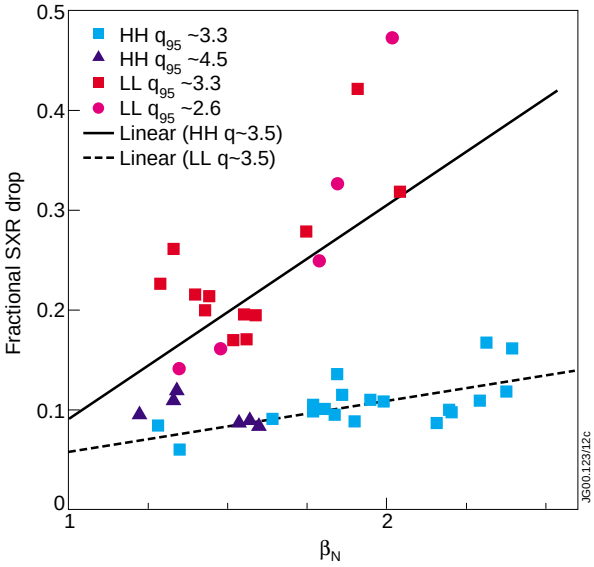

Fig.8.7: SXR fall at sawtooth for different q_{95} and shape pulses on JET, from ITER shaping scan.

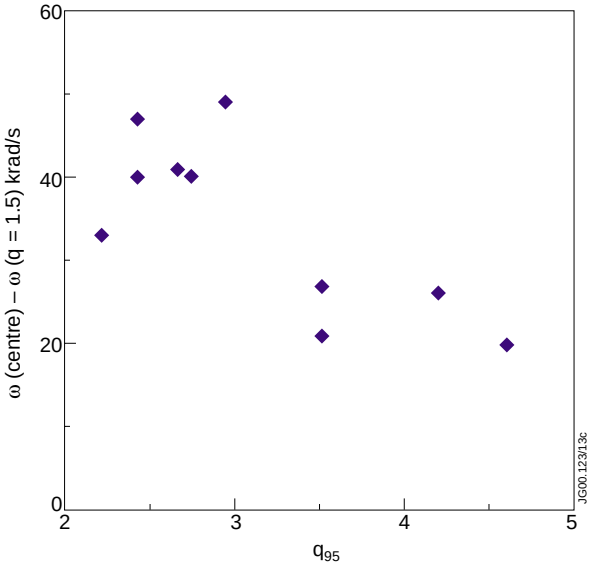

Fig.8.8: Variation in differential rotation between plasma core and q=3/2 surface with q_{95} in NTM q scan.

Summary of surface geometry and q effects

A summary of the various effects going into NTM onset, and their role in the q scaling, is given in Table 9.1. A key point to remember is that in terms of operational limits, thresholds *fall* with q_{95}, limiting β access at low q. This is because of variation in poloidal Larmor radius (dependent on local temperature and B_θ values) at the resonant surface, which governs the size of stabilising ion polarisation effects. However, correcting for variation in $\rho_{i\theta}^*$ and collisionality at the local NTM surface, to isolate dependence on surface geometry and q, leads to β_p thresholds that are *higher* at low q. This matches additional resonant surface geometry dependence of ion polarisation effects, which will require larger seeds or higher pressure gradients at lower q_{95} to trigger a mode. Measurements indicate that sawtooth size and seeding effects will undergo little variation, so corrected β_p thresholds are expected to be higher. Other effects, such Δ' and field

curvature (Glasser) terms may also play a role. However, if anything, Δ' would be expected to get more destabilising at lower q_{95}. Glasser terms are expected to be weak.

Thus we conclude that, while further studies are desired (and underway) to investigate Δ' variation, it is likely that the observed scaling, after stripping out collisionality and $\rho_{i\theta}^{*}$ effects, is due to the increase in stabilising ion polarisation current contributions as the minor radius for the NTM surface gets bigger. This is interesting, because it is precisely this mechanism (w_{seed}/ w_{pol} falling) which is predicted to raise β_N thresholds for ITER.

Table 8.1: Effect of scaling of various NTM drives on NTM threshold scaling arising through q_{95} and resonant surface shape variation (i.e. after correcting for ρ^{*} and collisionality dependence - the last line summarises effect of this correction).

Mechanism	Effect as q95 falls
Sawtooth size	None/weakly destabilising?
Geometric coupling	Weakly destabilising
Dynamic shielding	Stabilising
Overall effect on seed: w_{seed}	**little variation**
w_{pol}	Strongly stabilising
rΔ'	not known
Bootstrap current	weakly destabilising
Glasser	not known
Overall effect on corrected threshold:	**' physics' drives strongly stabilised**
Allowing for variation in ρ* and collisionality on resonant surface	strongly destabilised - operational limit

Issues of data validation - q profile:

The above analysis relies on use of EFIT to identify q=3/2 location. For the types of pulses used here, we find this gives good agreement with ECE estimates of island location, as illustrated in Table 8.2:

Table 8.2: Comparison of EFIT q=3/2 radius with ECE measurements

Pulse, time	R(ECE) (m)	R(EFIT)
43932 63.1	3.51	3.43
43938 60.0	3.52	3.47
43948 61.1	3.48	3.33
47276 59.3	3.55	3.57
49579 62.6	3.48/cor to Zmag	3.45
49586 65.1	3.57/cor to Zmag	3.56
49596 60.1	3.57	3.57

} Comparison long time into NBI phase, when EFIT erroneously and systematically raises central q values.

However, for pulses where mode onset is later in the NBI heating phase, EFIT q profiles are clearly inaccurate with central q>>1 (while 1,1 sawtoothing behaviour is still present). It is possible that this is related to the build up of bootstrap currents at the edge of the plasma, and TRANSP runs are in progress to investigate this effect. The ECE data indicates that this is not a problem for measuring q=1.5 location for NTM onset, but does make measurements of L_q (the safety factor scale length at q=1.5) rather more uncertain. Therefore, L_q values are taken as the average between q=1.5 and q=q_{95}, thus removing the uncertainty in local gradient, while retaining appropriate scaling.

Comparison of standard q fits with previous high plasma current-low q_{95} NTM thresholds:

In the past, high current low q_{95} (~2.4-2.5) discharges have often been observed on JET to be terminated by 3,2 NTMs. When comparing standard q_{95} (=3.4) NTM data with that from the low q_{95} higher plasma current pulses, we see that thresholds for the low q data lie ~30% above the fit (see Fig.8.9). This is very similar to pulses from the latest q scan (note q_{95} dependence of corrected threshold in Fig.8.2) which was performed at much lower toroidal field (and higher $\rho_{i\theta}^*$). So the local parameter fits, combined with the q scan, explain the low threshold observed for NTMs in previous higher performance ELMy H-modes on JET.

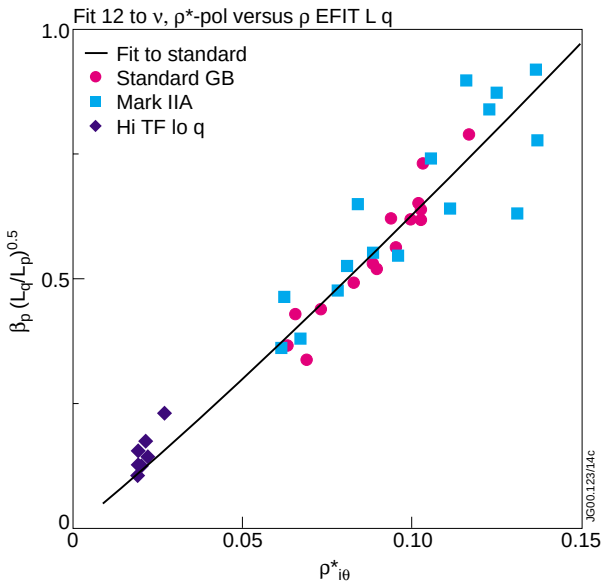

Fig.8.9: Comparison of q_{95}=3.4 threshold scaling with pulses at much higher toroidal fields, where 3,2 NTMs have been identified at q_{95}~2.5.

8.3 Summary and future direction

A strong dependence of the threshold in β_N for NTM onset with q_{95} was observed in recent experiments on JET, with thresholds falling dramatically for q_{95}<3. In terms of likely operational limit to machine performance (for JET or ITER), this translates to a sharp fall off in accessible β_N as plasma current is increased at constant toroidal field.

This effect has been examined in terms of the underlying physics of the NTM. It is found that the dominant ingredient in the lower threshold at low q_{95} is the variation in poloidal Larmor radius (dependent on local temperature and B_θ values) at the resonant surface, which governs the size of stabilising ion polarisation effects, and is further out, and therefore colder at low q_{95}. To investigate the role of other terms, thresholds are corrected for variation in Larmor radius (and collisionality), using fits to other data - this isolates geometry and q dependence of the various effects (ion polarisation, seeding mechanism, Δ', etc.). Corrected thresholds are then found to be *higher* in the low q_{95} pulses. This can be understood in terms of additional explicit dependence on resonant surface minor radius (which varies systematically with q_{95}) in the ion

polarisation term. This provides stronger stabilising contributions at larger resonant surface minor radii (and so at lower q_{95}), thus requiring larger seeds or higher pressure gradients to trigger the mode. Measurements of sawteeth and other effects indicate that seed size does not change substantially with q_{95}, so corrected thresholds in local β are expected to be higher at low q_{95}.

This match between predicted and observed effects confirms our understanding of the NTM behaviour and the role of various effects involved. Comparison of local 'physics parameter' fits with earlier high plasma current, low q_{95}, pulses from 1998-9 plasmas show threshold scalings are in accordance with the local parameter fits used.

In order to test for variation of other effects in the NTM evolution equation, and their possible role in the q_{95} scaling, further analyses are needed (and planned, in collaboration with CRPP and CEA). In particular, fitting the island evolution equation to the mode evolution, will allow estimates of Δ' variation, and test w_{pol} variation. The variation of bootstrap effects, and additional field curvature ('Glasser') terms can be calculated from first principals (given equilibrium details).

In future experiments, the lower threshold at lower q_{95} may allow wider range parametric studies, accessing lower ρ^* values, particularly for the (2,1) NTM. For the (3,2) NTM this may allow exploration of the part of (or closer to) the parameter space in which seed sizes are predicted to fall, raising thresholds. This is the mechanism predicted to lead to avoidance of NTMs for ITER.

8.4 Shot List

Standard q data and global parameter fits from 1998 and 1999 campaigns were reported in Ref [8.7].

Pulses in main q scan

Pulse	Bt	Ip	P_{NBI} MW	q95	Bet_n	Pre & Post Pulse Comments
49557	1.37	1.31	14.0	3.5	3.2	32 NTM formed
49556	1.15	1.3	8.8	2.8	2.7	32 NTM locks, 21 grows to disruption
49555	1.56	1.31	12.1	4.0	2.8	32 NTM formed
49554	1.77	1.31	15.6	4.5	2.5	32 NTM formed
49553	0.92	1.29	5.4	2.2	2.0	Mode, rapid progression to disruption
49551	1.00	1.29	6.2	2.4	2.2	32 NTM locks, 21 grows to disruption
49550	1.00	1.31	6.4	2.4	2.4	32 NTM forms then dies as rotating 21 grows, locks and disruption
49549	1.09	1.27	9.7	2.6	2.65	32 NTM locks, 21 grows to disruption
49548	1.18	1.32	15.9	2.95	3.2	32 NTM locks, 21 grows to disruption
49547	1.37	1.30	15.8	3.4	3.1	32 NTM formed

References

[8.1] HORTON, L.D. et al., Nucl Fus **39** (1999) 993.

[8.2] GATES, D. A., et al., Nucl. Fus. **37** (1997) 1593.

[8.3] WILSON, H. R., et al., Phys. Plasmas **3** (1996) 248.

[8.4] FITZPATRICK, R. et al., Phys. Plasmas **2** (1995) 825.

[8.5] LAHAYE, R. J., et al., "Dimensionless scaling of the critical beta for onset on a neoclassical tearing mode", Phys. Plas. (2000) – accepted by Phys. Plasmas.

[8.6] BUTTERY, R. J., et al., section 2 of "NTMs and sawteeth in ITER shaping studies", (see Fig.8.3 and accompanying text in particular), TF C data validation report, JET report (2000).

[8.7] BUTTERY, R. J., et al., Contr. Fus. and Plas. Phys. (Proc 26th EPS, Maastricht, 1999) , European Physical Society, Geneva (1999), Vol **23J,** 121.

9. NEOCLASSICAL TEARING MODE STABILISATION WITH ICRH

R. J. Buttery[1], N. Hawkes[1], T. C. Hender[1], M. Mantsinen[2], P. Lamalle[3].

JET Joint Undertaking, Abingdon, Oxfordshire, OX14 3EA, UK.

[1] EURATOM/UKAEA Fusion Association, Culham Science Centre, Abingdon, Oxfordshire, OX14 3DB, UK.

[2] Helsinki University of Technology, Association EURATOM-TEKES, Finland.

[3] JET-EFDA, Abingdon, Oxfordshire, OX14 3EA, UK.

9.1 Overview

In the latest attempts to stabilise the neoclassical tearing modes (NTMs) using ion cyclotron current drive on JET, there was no evidence either for a current drive effect in the plasma, or the resulting stabilisation of the NTM intended. Following previous experiments using 52MHz 2nd harmonic Hydrogen [9.1], which yielded little effect on the NTM, new experiments were attempted using 32MHz fundamental harmonic Hydrogen ICRF, which has a more localised deposition. Numerical codes predicted levels of current drive deposition comparable with other modelling [9.2] predicting a strong effect on NTM amplitude (through the modification of Δ'). Also, experimentally coupled powers were in the right range to achieve the predicted current drive in some cases (but not enough to allow an extensive campaign). However, difficulties with reproducing good coupled powers at the anticipated optimum Hydrogen fractions (~8%) may have hampered current drive efficiencies. It is possible that deposition was too broad for the unoptimised Hydrogen fractions used. The current drive effects were too small to be clearly identified by MSE measurements, with expected signal levels (and any slight trends observed) much smaller than scatter in measurements. We conclude that in these experiments, deposited current drive effects were too weak (and too irreproducible) to produce a clear effect either on the NTM, or in the MSE data.

9.2 Results

Theoretical basis, modelling and experiments

Continuous application of localised current drive is expected to have a stabilising effect on NTMs, when applied close to the resonant surface. This acts by modifying the tearing stability index, Δ', reducing free energy available in the current profile to drive the mode. Recent modelling [9.2] shows that stabilisation is best achieved with more localised peaks in driven current close to, or just outside, the island. Promising results have been achieved using lower hybrid current drive on COMPASS-D [9.3] and electron cyclotron current drive on ASDEX-Upgrade [9.4].

Recent modelling shows that ion cyclotron current drive (ICCD) can introduce similar perturbations on JET, using 32MHz fundamental harmonic Hydrogen. Predictions from the FIDO code [9.5], shown in Fig.9.1, indicate driven currents (neglecting electron back current) of ~50–100kA/m^2 were expected with 3MW coupled power to Hydrogen and 5% Hydrogen. Taking

into account the electron back current, the total driven current density is estimated to be 25–50kA/m^2, giving a total driven current of ~1–1.5% of the plasma current (1.7MA). Deposition is expected to be reasonably localised (half-height width ~10% of minor radius) with different ($\pm 90^o$) phasings giving rise to a predominantly co- or counter- current drive effect, as shown in Fig.9.1. This compares well with modelling in Ref [9.2] where slightly higher levels of current drive with similar deposition width (σ=0.06 ≡ 10% of minor radius) are predicted to lead to large reductions (~60%) in island size.

In the initial Autumn 1999 experiments, scans were performed using ramps in toroidal field, with plasma current kept in proportion. This had the effect of scanning deposition from the inboard side, towards the centre of the plasma. The ramp rate of toroidal field and plasma current were chosen such that the predicted width of the current drive peak took significantly longer to pass through the anticipated island width than the typical time scale for growth or decay of the island. However it is possible that with these large sweeps, not enough time was given for the current drive effect to develop fully, but due to problems with reproducibility of ICRF heating, not enough experiment time was available to do more detailed scans.

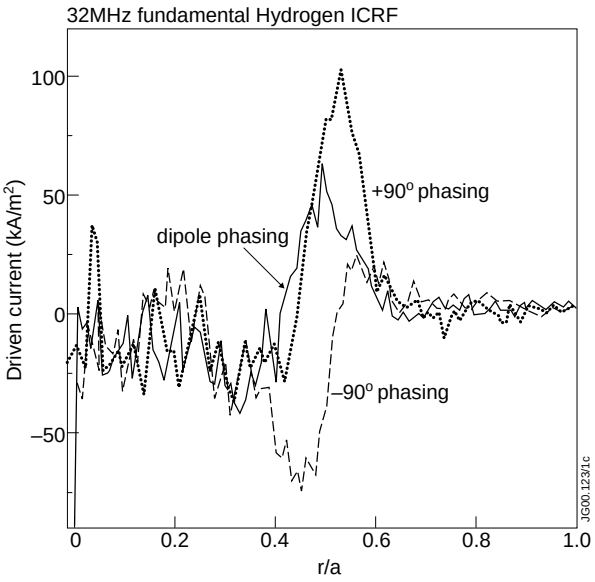

Fig.9.1: Modelling of minority current drive deposition (using the 'FIDO' code) at intermediate point in toroidal field scan (1.74T), assuming 3MW coupled power and 5% Hydrogen fraction.

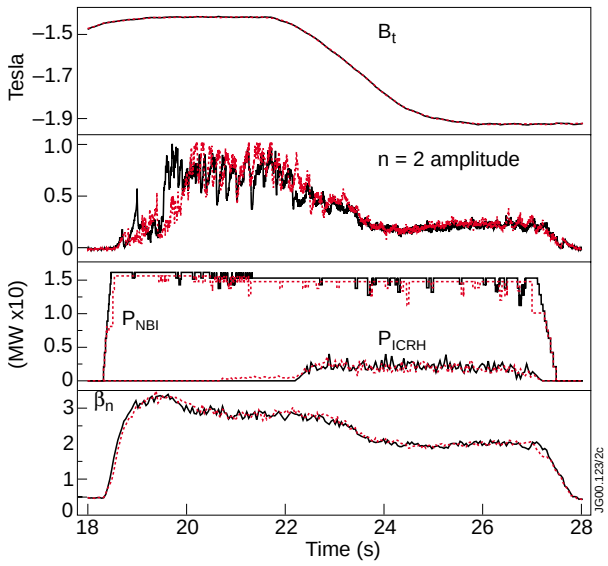

Fig.9.2: Comparison of effects of opposite phasings of ICCD on NTM amplitude for two otherwise identical pulses (49291 and 49292). Toroidal field and plasma current are ramped in order to scan deposition through the island.

Pairs of pulses were compared with opposite phasings of the ICRF antennae. A typical comparison is shown in Fig.9.2 (pulses 49291 and 49292) for edge Hydrogen fractions of 2.5% (measured by spectroscopy). After the initial phase, in which high NBI power is applied in order to make a mode, toroidal field and plasma current are ramped up (leading to a fall in β_N), while 2.5MW of ICRF is applied. The mode amplitude, measured by the rms of an n=2 combination of Mirnov coils (dB/dt), is identical for both phasings. (There is a fall in amplitude associated with slowing of the mode during the field scan).

Additional checks on this have been made using CATS fast magnetics data, by directly tracking the amplitude of the Fourier harmonic specifically identified as originating from the 3,2 NTM. The data is filtered to remove points where tracking of the mode is imperfect, and smoothed to reduce scatter. The results of this, with amplitude in Tesla $\times 10^{-4}$, are shown in Fig.9.3 for both pairs of pulses (49291 and 49292 at 2.5% Hydrogen, and 49293 and 49294 at 18% Hydrogen). Although there are some early discrepancies in mode amplitude, these are associated with bursting behaviour, most likely originating from the effects of strong sawtooth activity at the high β_N used (this occurs early in the pulse, when current drive deposition will be at the edge of the plasma, where its efficiency will be low). As deposition is swept through the q=3/2 surface (R=2.5m at ~23.8s), there is no clear effect on mode amplitude (certainly not the ~60% reduction predicted) - mode amplitude simply tracks the fall in β as field and current is ramped up.

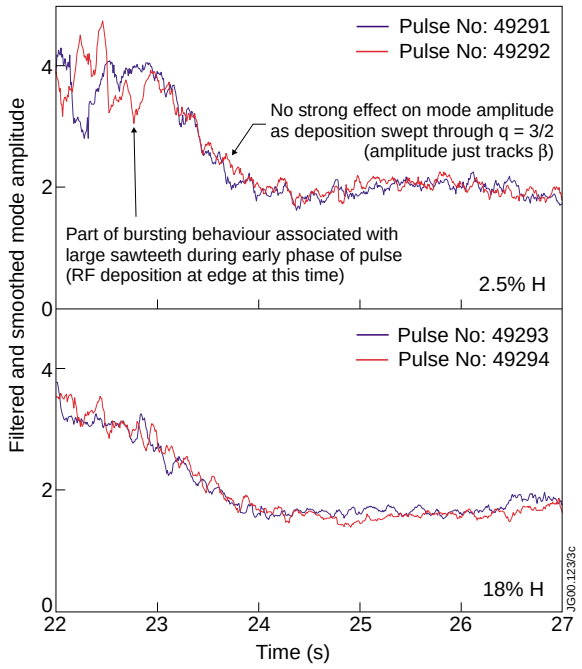

Fig.9.3: Comparison of mode amplitudes ($\times 10^{-4}$ Tesla) for opposite ICRF phasing pairs of pulses during ICCD deposition scan.

Thus we conclude that there is no current drive effect stabilising the NTM. Either coupling did not generate the desired current drive, or the current drive obtained was not enough to stabilise the mode. Similar results were obtained with edge Hydrogen fraction of 18% (pulses 49293 and 49294). At anticipated optimum Hydrogen fractions (~8%), ICRF couped powers were lower, despite many attempts in additional parasitic experiments. This is attributed to the larger ELM amplitude observed in these discharges.

Previous experiments [9.1] using 52MHz second harmonic also showed little benefit. In these, deposition widths were broader, and there was evidence of the ICRH coupling to a higher harmonic Deuterium resonance (which is why 32MHz fundamental was tried here).

MSE EFIT measurements of current drive

In order to examine whether a current drive effect was obtained, MSE measurements were taken during the pairs of pulses and used to constrain EFIT reconstruction of the current profile. Profiles are compared at various time points. In Table 9.1 toroidal field values and anticipated deposition radii are listed at some of the time-points used to illustrate time history.

Current profiles for 49291 are given in Fig.9.4, plotted versus major radius at the times listed in Table 9.1. The differences between these for 49291 and 49292 are plotted in Fig.9.5 versus major radius for all time points (to give an idea of scatter) where reconstructions were

Table 9.1: List of times and deposition radii for MSE EFIT profile comparison

Time (s)	B_T (T)	R (m)
23.3	1.63	2.34
23.7	1.71	2.46
24.6	1.85	2.66
25.4	1.90	2.73

possible for both pulses (earliest 23.3s, latest 25.4s). The region of interest is where the ICCD deposition is expected (~2.4-2.9m), with any co-current drive effect expected as a negative peak (as total current profile is negative). The MSE measurements were made somewhat more difficult by unanticipated interference from PINIs 6 and 7 (although they were operating with lower energies to avoid this problem), and problems of dirty windows in the Autumn campaign.

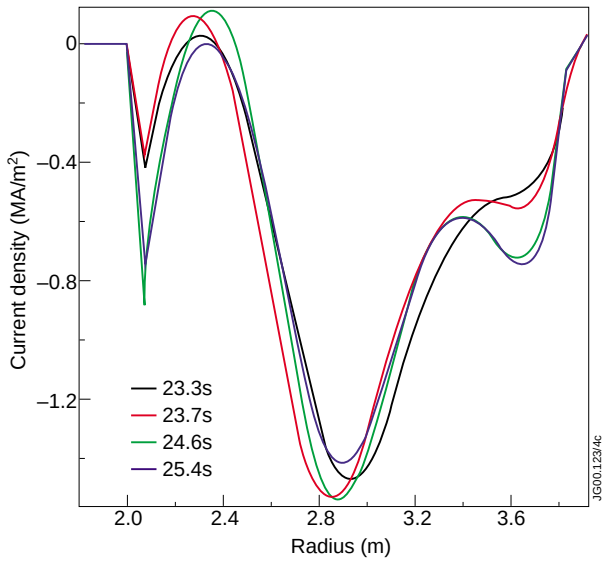

Fig.9.4: MSE constrained EFIT profiles for pulse 49291 during the ICCD deposition scan.

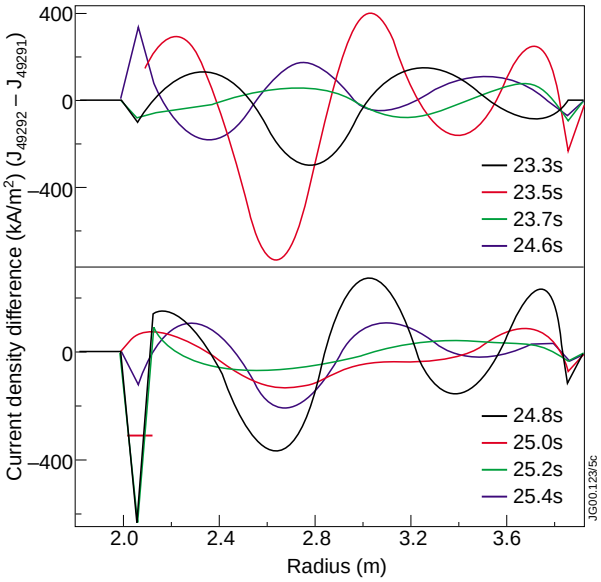

Fig.9.5: Difference between current profiles at various times: pulse 49292 minus pulse 49291, in two plots (first four time points then next four) for clarity.

Examining Fig.9.5, clearly the variation between consecutive time points is much larger than any systematic variation over the scan. There is large scatter between the first 3 time points, indicating the error bars of the technique. Certainly scatter in the data is large compared to the predicted differences between ±90 phasings (~75kA/m^2, including electron back currents, see Fig.9.1). Similar scatter and lack of clear effect is also observed for the other pair of pulses, 49293 and 49294.

Thus we conclude that there is little clear evidence of any trend developing indicating a current drive effect in the MSE constrained EFITs. Given the lack of effect on the NTM, the main conclusion must be that higher levels of current drive are needed in order to be measurable with MSE, and in order to have an effect on the NTM.

9.3 Summary and future direction

In the latest attempts to stabilise the neoclassical tearing modes (NTMs) using ion cyclotron current drive on JET, there was no evidence either for a current drive effect in the plasma, or the resulting stabilisation of the NTM intended. Following previous experiments using 52MHz 2^{nd} harmonic Hydrogen [9.1], which yielded little effect on the NTM, new experiments were attempted using 32MHz fundamental harmonic Hydrogen ICRF, which has a more localised deposition. Numerical codes predicted levels of current drive deposition comparable with other modelling [9.2] predicting a strong effect on NTM amplitude (through the modification of Δ'). Also, experimentally coupled powers were in the right range to achieve the predicted current drive in some cases (but not enough to allow an extensive campaign). However, difficulties with reproducing good coupled powers at the anticipated optimum Hydrogen fractions (~8%) may have hampered current drive efficiencies. It is possible that deposition was too broad for the unoptimised Hydrogen fractions used. The current drive effects were too small to be clearly identified by MSE measurements, with expected signal levels (and any slight trends observed) much smaller than scatter in measurements. We conclude that in these experiments, deposited current drive effects were too weak (and too unreproducible) to produce a clear effect either on the NTM, or in the MSE data.

The difficulties with ICRH coupling are not especially surprising given the short time to optimise the scenario, and the requirements on the system: high coupled power and current drive, well off-axis, at fields low enough to trigger NTMs, in high β plasmas with significant ELM activity. More recently lower NTM thresholds have been observed at lower q95 (reported in section9), and (seperately) with the use of ICRH to assist initial triggering of the NTM. Therefore, it is possible that options exist for NTM generation at higher toroidal fields, where ICRH coupling is better. However, workable scenarios, with efficient ICCD coupling should be investigated and demonstrated first (for example through observation of effects on sawteeth, with MSE current profile measurements).

9.4 Shot List

Pulses providing good data for analysis are listed. Other pulses done as part of the campaign, such as scenario development or those with technical problems, are not included, but details can be found in the PIC logs.

Main ICCD experiments, 4^{th} November 1999:

All pulses had an NTM form during max NBI phase at 1.4T 1.4MA, before a ramp up in field and current was applied, while ICCD applied (to obtain deposition scan).

Pulse	Bt	Ip	P_{NBI}	P_{RF}	RF phase	β_N	H:D %	Comments
49282	1.4	1.4	15	2	-90	3.22	2.2	Good ref pulse for ICRF - no NTM
49283	1.4	1.4	17	2.6	-90	3.31	2.5	NTM produced, but NB step down too large after this
49291	1.4	1.4	15.3	2.2	-90	3.35	2.0	Good pulse
49292	1.4	1.4	14.8	2.1	+90	3.3	2.6	Good pulse
49293	1.4	1.4	15.6	2.5	+90	3.0	18	Good pulse
49294	1.4	1.4	15.5	1.8	-90	3.1	17	Good pulse
49295	1.4	1.4	15.5	1.3	-90	3.3	10.5	Poor ICRF coupling
49297	1.4	1.4	14.8	1.0	-90	3.0	5.8	Different NB waveform. Poor ICRF coupling.

Additional parasitic experiments with ICCD attempted in the tail, 19th November 1999:

These pulses were performed as part of the q scan experiments, but had a second phase after the NTM was formed, where toroidal field values were varied to achieve the same ramps as those in the previous campaign, above (with Ip maintaining proportion). Pulses where disruptions occurred before RF phase are excluded.

Pulse	Bt	Ip	P_{NBI} MW	q_{95}	P_{RF} MW	Bet_n	H:D %	Pre & Post Pulse Comments
49557	1.37	1.31	14.0	3.5	0.6	3.2	5.0	Poor ICRF coupling
49555	1.56	1.31	12.1	4.0	1.0	2.8	5.1	Poor ICRF coupling
49554	1.77	1.31	15.6	4.5	1.0	2.5	4.0	Poor ICRF coupling
49547	1.37	1.30	15.8	3.4	1.0	3.1	4.1	Poor ICRF coupling

Acknowledgement

Many thanks to Dr. D. Borba, for his considerable assistance with fast data and mode tracking software.

References

[9.1] BUTTERY, R. J., et al., Proceedings 26th Fusion EPS Conf., Maastricht (1999).

[9.2] PLETZER, A. and PERKINS, F. W., Phys. Plas. **6** (1999) 1589.

[9.3] WARRICK, C. D. et al., (Proc. 26th EPS, Maastricht) Contr. Fus and Plas. Phys **23J** (1999) 153.

[9.4] ZOHM, H. et al., (Proc. 26th EPS, Maastricht) Contr. Fus. and Plas. Phys **23J** (1999) 1373.

[9.5] CARLSSON, J., HELLSTEN, T., and ERIKSSON, Proc. Joint Varenna Lausanne Workshop on 'Theory of Fusion Plasmas' 1994 (Editrice Compositori, Bologna, 1994), p.351.

10. RI-MODE EXPERIMENTS

G P Maddison[1], G L Jackson[2], B Unterberg[3], M Tokar[3], J D Strachan[4], L C Ingesson[5], M von Hellermann[5], J Ongena[6], G F Matthews[1].

on behalf of the International RI Group (see Appendix A10.1)

JET Joint Undertaking, Abingdon, Oxfordshire, OX14 3EA, UK.

[1] EURATOM/UKAEA Fusion Association, Culham Science Centre, Abingdon, Oxfordshire, OX14 3DB, UK.

[2] DIII-D National Fusion Facility, San Diego, CA 92186-5698, USA.

[3] IPP, Forschungszentrum Jülich GmbH, EURATOM Association, D-52425 Jülich, Germany*.

[4] Princeton Plasma Physics Laboratory, Princeton University, NJ 08543, USA. (assigned to JET)

[5] FOM-IVP, EURATOM Association, Postbus 1207, NL-3430 BE Nieuwegein, Netherlands*.

[6] LPP, Association EURATOM-Belgian State, ERM-KMS, B-1000 Brussels, Belgium*.

* Partners in the Trilateral Euregio Cluster (TEC).

10.1 Overview

Initial JET experiments on impurity puffing into ELMy H-modes in January 1999 have been extended during Autumn 1999 by seeding of: (a) divertor L-modes at lower Greenwald fraction before the onset of sawteeth; (b) higher density L-modes limited on the outboard discrete limiters; and (c) septum H-modes, then with more protracted phases after all puffing ends. While pronounced gains in confinement such as obtained in DIII-D and TEXTOR-94 have not yet been seen, radiated power fractions have been increased up to ≈ 60% for a rather broad range of Z_{eff} values ($\approx 2 \rightarrow 6$), and definite indications of improvements have been found. Local transport analyses of diverted cases reveal a decrease in ion thermal diffusivity across the whole plasma, while gyro-kinetic calculations show reduction of ion temperature gradient (ITG) fluctuations tends to be mitigated by emergence of trapped electron modes (TEM). A key difference of JET limiter cases from radiative improved (RI) states in TEXTOR-94 is an inability yet significantly to peak the density profile, even when inboard pellet fuelling was incorporated. A recent theory of ITG and TEM transport discloses a bifurcation to greater peaking and improved confinement when the former is sufficiently moderated by added impurities, and accounts for the TEXTOR-94 RI transition. When applied to JET conditions, though, the bifurcation is seen to remain inaccessible, consistent with experimental results. More concentrated central particle sources, possibly in combination with heavier impurity species, could help to reach the transition state. In septum cases, adding argon enabled high confinement in their “afterglow” stages exceptionally to be combined with high normalized density, leading to one of the largest products of confinement and Greenwald factors ever achieved in JET. These findings therefore clearly point to the potential benefits of impurity seeding for integrated plasma performance. The present report is chiefly a summary of authoritative accounts to be presented by G Jackson et al [10.1] and B Unterberg et al [10.2] at the 27$^{\text{th}}$ EPS Conference on Controlled Fusion and Plasma Physics, Budapest, 2000. Unpublished material has also kindly been provided by J Strachan.

10.2 Results

Background

The reference plasma regime for the ITER-FEAT next-step tokamak, namely ELMy H-mode, presently is limited by two features: (i) confinement tends to degrade as the Greenwald density is approached, impeding attainment of best conditions for nuclear burning; and (ii) higher confinement tends to be accompanied by large, low frequency Type I ELMs which would seriously impair divertor performance. Approaches mitigating both these difficulties are actively being sought. One scheme which has been investigated over the last several years for example on the TEXTOR-94 device is based upon deliberate introduction of impurities into the plasma periphery, in order to facilitate power exhaust by dispersing a larger fraction as radiation. Simultaneously, though, it was found that this intervention could elicit a spontaneous transition to a steady, higher confinement and density regime, the so-called radiative improved (RI) mode, in which all the requirements for a next-step state could therefore potentially be realized together. This advance into higher regions of fusion parameter space is illustrated in Fig.10.1 (reproduced from [10.3]), and discloses immediately the possible importance of RI-modes. A vital next task is to study their scalability by demonstrating such states also on larger machines. Consequently efforts are being pursued on JET by a large international group of collaborators (see Appendix A10.1), in addition rehearsing new arrangements for its operation under EFDA.

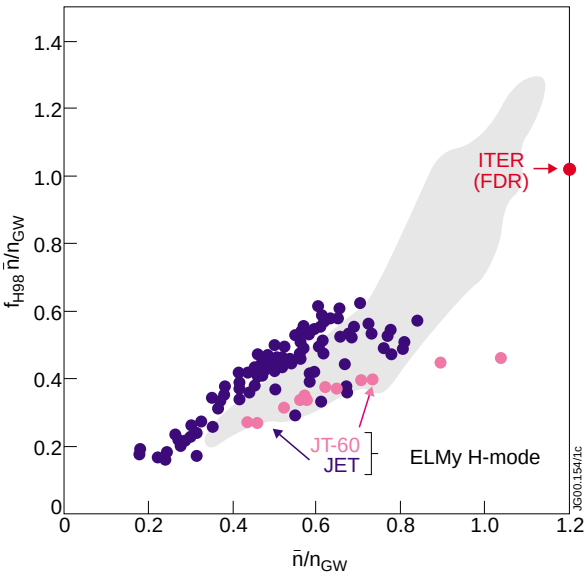

Fig.10.1: Product of normalized density with confinement normalized to the ITER-H93 scaling law, against normalized density, for: (points) samples of ELMy H-mode data from JET and JT-60 - saturation owing to the H-mode density limit is apparent; (shaded) region populated by RI-modes on TEXTOR-94 (from [10.3]).

First trials conducted in January 1999 had concentrated upon impurity seeding actually of ELMy H-modes, to try to combine their good confinement characteristics with exhaust- modifying effects of augmented radiation. Results have already been reported separately [10.4]. Subsequent experiments in November 1999 then focused on seeding of L-modes, both more directly following the TEXTOR-94 limiter experience, and before this addressing enhancements recently observed in diverted plasmas on DIII-D. Shortly afterwards, novel impurity benefits were seen too in the later “afterglow” stages of plasmas resting on the MkIIGB septum. A résumé is presented of findings across all of these cases together, before highlighting some aspects of each one in more detail.

Configurations examined

Three distinct arrangements were adopted :-

(i) "DIII-D like"

In DIII-D single-null diverted plasmas with NBH, neon had been injected prior to any transition into H-mode and before the onset of sawteeth, deferred by using early beam injection and higher $q_{95} \approx 5$. Improvements in confinement up to H-mode level had been seen, while retaining the advantageous L-mode edge. In contrast to TEXTOR RI-modes, furthermore, **low** normalized densities were involved $f_{\mathrm{Gwd}} \equiv \bar{n}_e / n_{\mathrm{Gwd}} \approx 0.2$, together with moderate radiated power fractions $f_{\mathrm{rad}} \equiv P_{\mathrm{rad}} / P_{\mathrm{in}}^{\mathrm{total}} \approx 0.6$. Similar conditions were sought in JET with the conventional vertical target equilibrium in MkIIGB (see Fig.10.2), at $B_{\mathrm{t}} \approx 3$ T to raise the H-mode threshold and help sustain an L-mode phase, plus $I_{\mathrm{p}} \approx 2.5$ MA, giving $q_{95} \approx 4$. Some comparisons of argon with neon seeding were attempted.

(ii) limiter

RI-modes were discovered and have been most extensively studied in circular, (pumped-) limiter plasmas in TEXTOR-94, beginning from L-modes involving at least ≈ 20% heating by NBI, then reaching or exceeding f_{Gwd}, $f_{\mathrm{rad}} \approx 0.8$ [10.3]. These conditions have been most closely replicated in JET by forming moderately elongated (κ = 1.4) discharges against its 12 discrete outboard carbon limiters (see Fig.10.2). To assist power-handling on these elements, $B_{\mathrm{t}} \approx 2.9$ T, $I_{\mathrm{p}} = 1.8$ MA yielding $q_a \approx 5$ were chosen. Two purely Ohmic pulses were also included to test for saturated (SOC) to improved (IOC) confinement transitions, since properties for these have been associated with those for access to RI-modes when adding NBH. As discussed later, an especially important factor is believed to be peaking of the density profile. A specific attempt to increase this was therefore made by introducing inboard pellet fuelling in some cases.

(iii) septum "afterglow"

The power threshold for entry into H-mode is known to be considerably lower for plasmas in which the X-point is lowered onto or just inside the septum cap of the MkIIGB divertor (see Fig.10.2). In a separate series of experiments scanning the density whilst staying well above the threshold in such "septum" pulses, addition of argon was noticed to have a beneficial effect on performance in the later stages **after** its injection had ceased, the so-called "afterglow" phase. Two of these

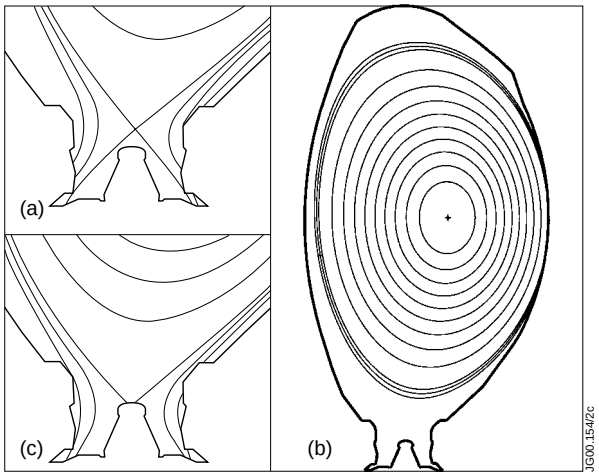

Fig.10.2: Equilibria used in each trial: (a) "DIII-D like" (X-point); (b) limiter; (c) septum.

discharges, together with a number of their unseeded counterparts as references, are thus also discussed.

Résumé of behaviour

Typical discharge waveforms for each situation are illustrated in Fig.10.3, comparing respective shots without and with impurity seeding. In each case, introduction of a noble gas can be seen to lead **after a short delay** to a marked increase in radiated power, and almost simultaneous rises in central line-average Z_{eff} and soft X-ray (SXR) emission, suggesting rapid permeation of the impurities across the entire plasma. **After a further short delay**, small increases also in stored energy and density occur. In the septum tests these were not significant with the small

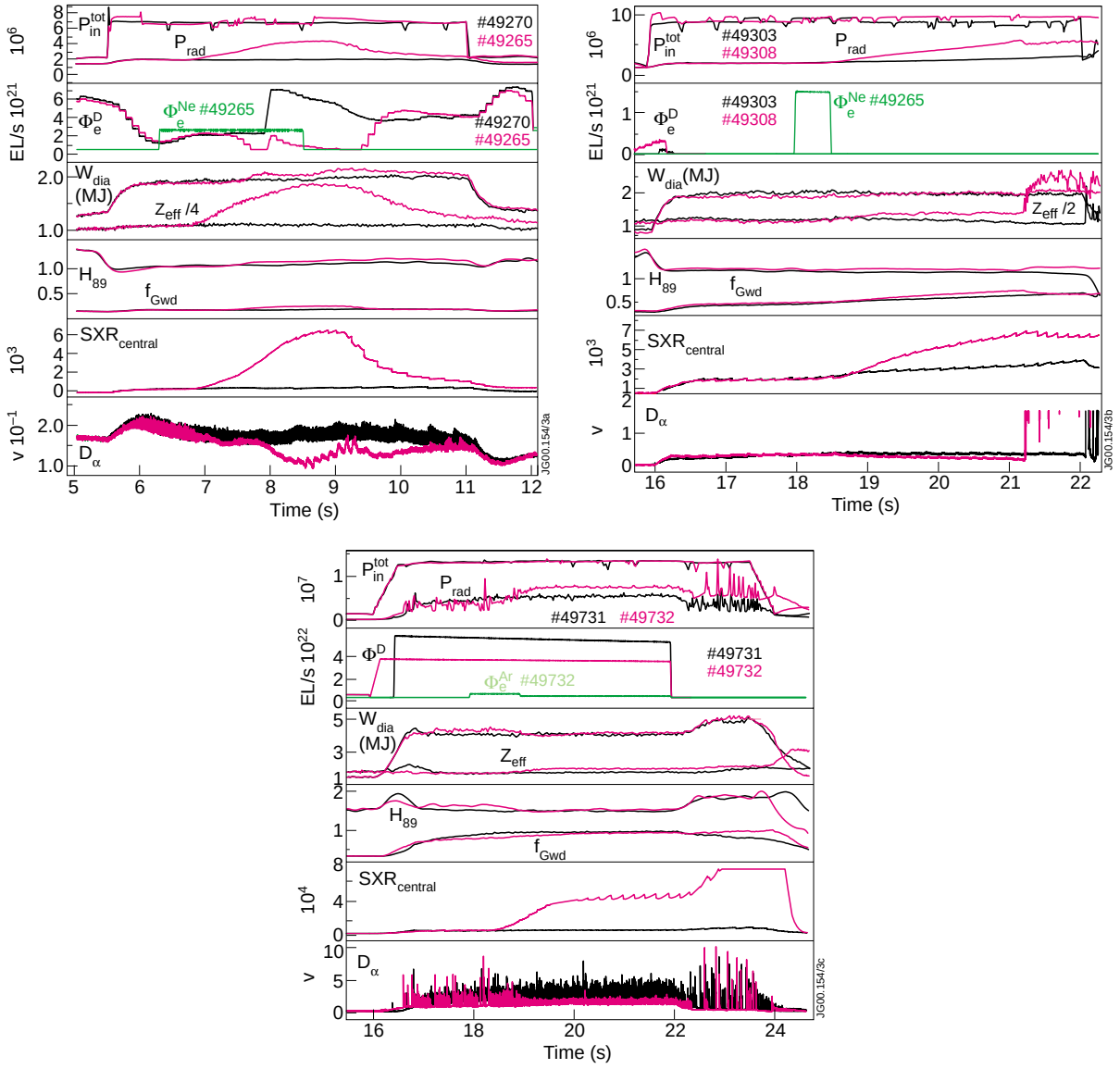

Fig.10.3: Time traces of typical pulses without and with impurity seeding in each set of experiments, showing: total input power (mainly NBH) and radiated power; gas puffing rates; diamagnetic stored energy and central Z_{eff}; confinement normalized to the ITERH89P L-mode scaling and density to the Greenwald level; central SXR emission; vertical {a,c} or horizontal {b} LoS Dα emission. (a) "DIII-D like" (X-point); (b) limiter; (c) septum "afterglow".

amount of argon added, but more prominent increments do emerge instead after all gas puffing ceases. Note also that the limiter experiments had no direct fuelling other than from the NBI itself. In the DIII-D like seeded instances, deuterium puffing is greatly reduced relative to the unseeded counterparts, suggesting that the impurities were contributing significantly to their fuelling. A corresponding decline in radiation and Z_{eff} after seeding ends in the X-point plasmas points to effective divertor cryopumping of the neon in this configuration. In contrast, MARFEs were often observed to develop at the inboard side in the seeded limiter pulses (eg. note the strong rise in horizontal D_α signal at 21.2s in Fig.10.3(b)). Spectroscopic analyses nevertheless indicate that carbon still remains the dominant impurity, possibly due to interactions with the discrete limiters.

As clearly seen in Fig.10.3, substantial gains in confinement like those in TEXTOR-94 and DIII-D upon injecting impurities have not yet been observed in JET. Results over all appropriate shots are summarized in terms of confinement normalized to the ITERH89P L-mode scaling in Fig.10.4(a), which also identifies the range in heating power they spanned. Note that throughout Figs 10.4 & 10.5 a single point is plotted for each DIII-D like and limiter pulse, at a time following seeding, when applied, chosen for greatest steadiness, primarily of the stored energy. In the former plasmas, the time is always taken before sawteeth begin, even though this may not coincide with the maximum properties achieved. For the latter cases, the points are sometimes during a MARFE, when one arises. In each of the septum shots, two points are plotted, one during and one after the puffing phase.

Confinement in the X-point and limiter series is modestly above the L-mode scaling, and is only slightly increased by impurity seeding. The latter appear to be marginally higher than the former at similar power, although a decline even of **normalized** confinement with greater heating is suggested for the limiter points. On the other hand, seeded X-point performance seems to be

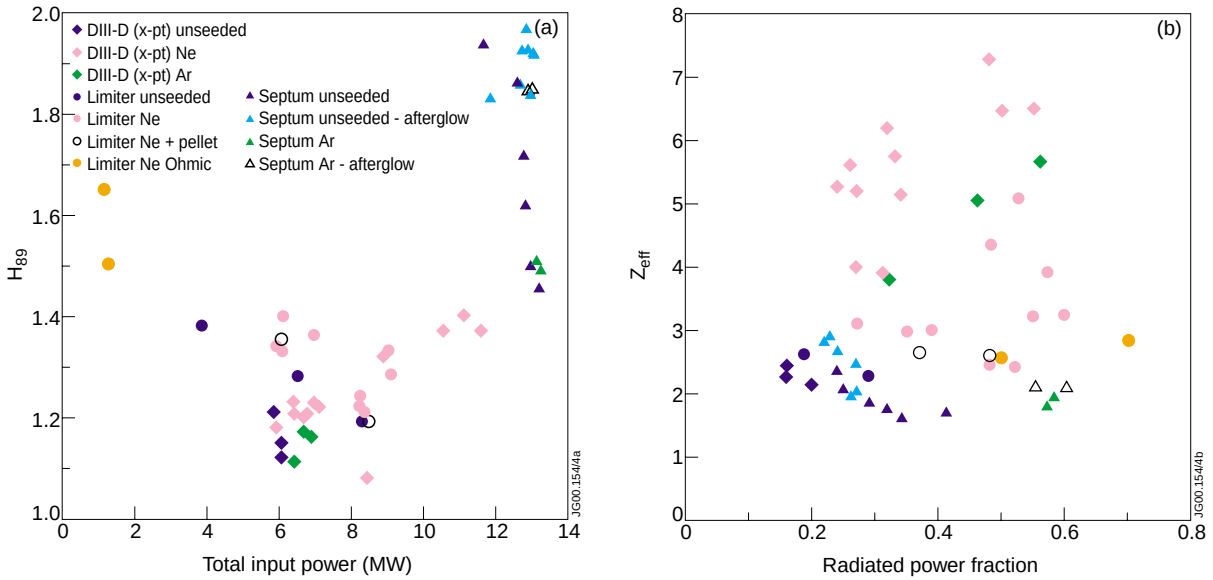

Fig.10.4: Summary of all cases: (a) normalized confinement against total input power; (b) central line-average Z_{eff} against radiated power fraction (bolometer estimates, limiter points not yet corrected).

better at higher power. The septum data, which were collected at the highest input powers, display the higher confinement typical of H-mode operation. Note that their spread actually represents the density scan involved, and correlates with the recognized Saibene degradation for rising Greenwald fraction. Best performance of all occurs when there is no fuelling into these plasmas, in their “afterglow” phases.

There is a hint in Fig.10.4(a) that X-point confinement might be just better with neon than with argon seeding, at similar powers. On the other hand, Fig.10.4(b) reveals that neon leads to higher Z_{eff}, ie more contamination, for a given radiated power fraction. The limiter values of f_{rad} here may in fact systematically under-estimate their emission, owing to a bolometer discrepancy discussed below. However, a maximum value of roughly $f_{\text{rad}} \approx 0.6$ was reached over all cases, and up to this level it is evident that whereas Z_{eff} has no clear trend in the limiter plasmas, it is both generally higher and tending to increase in the X-point ones. In these terms, there thus appears to be no effective divertor control of added impurities. Core purity is actually better in the septum plasmas, and importantly is not worsened by argon sufficient to reach even ≈ 60% radiation.

A defining feature of RI-modes in TEXTOR-94, although more weakly in DIII-D cases, is a strong correlation of their improved confinement with accentuated central peaking of the density profile; an illustration for similar $q_a \approx 5$ is inset in Fig.10.5(a) . One key difference in these JET experiments is that conversely the density remains quite **flat**. Confinement now normalized to ITERH97 scaling is shown against a profile-fitting measure of density peaking (NEX/GAM) in Fig.10.5(a), the exponent γ is the best fit $(n_e(0) - n_e(1))(1-x^2)^{\gamma} + n_e(1)$, where $0 \le 1x \le 1$ is a normalised flux-surface co-ordinate. While this may not be precise, owing to its derivation from a small number of interferometer chords, neverthless it is hinted that performance could be improving

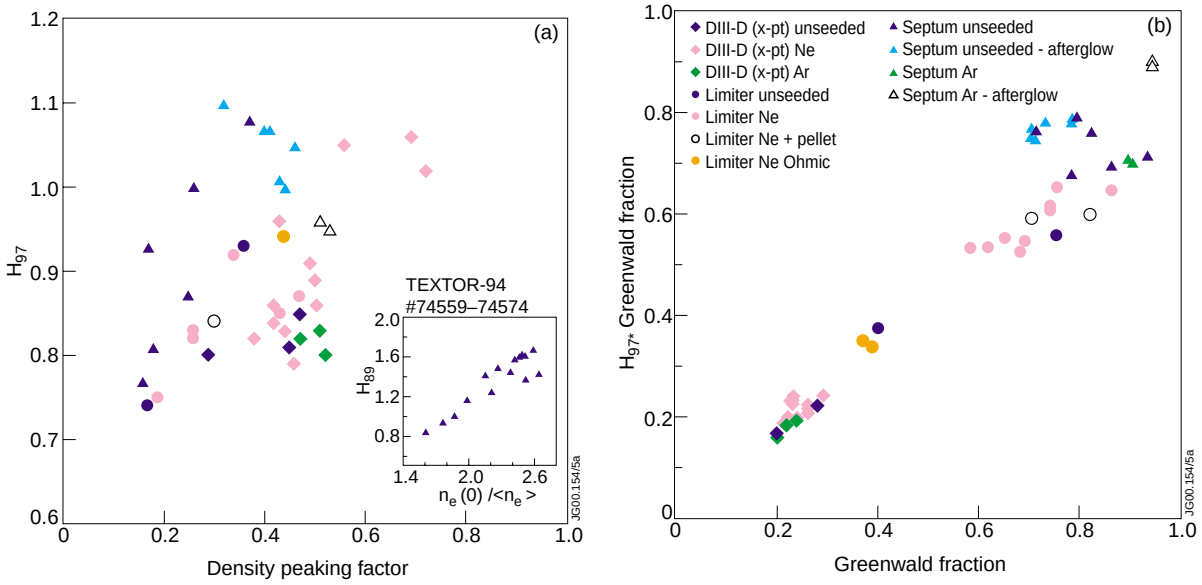

Fig.10.5: Summary of all cases: (a) confinement normalized to the ITERH97 scaling against density peaking factor; (b) product of normalized confinement and density against normalized density.

with peaking, but far too small a range has yet been achieved. Even high-field-side pellet fuellingdid not alter the ituation[‡]. Moreover the Ohmic plasmas also do not access greater density peaking,which ssimilarly may underlie their lack of SOC to IOC enhancement, as typical of JET (though they are below the Greenwald fraction generally required for IOC; see the next figure.) This profile issue is a crucial part of present understanding of RI transitions, and is consequently explored in more detail for the limiter cases below.

While actual RI-modes may not have appeared in JET, these seeded plasmas have nevertheless maintained or even extended good confinement, most significantly at line-average densities **in excess of the conventional H-mode density limit**. This achievement is disclosed in Fig.10.5(b), where the product of normalized confinement and density is plotted against Greenwald fraction. Recall that ordinarily, ELMy H-modes would tend to saturate around ≈ 0.7 in such a plot, as confinement degradation at the H-mode density limit emerges. Conversely, the seeded data tend to sustain confinement almost up to the Greenwald density, and in the argon "afterglow" of the already superior septum discharges, one of the highest $H_{97}\cdot f_{\mathrm{Gwd}}$ numbers ever achieved in JET is produced. This emphasizes that adding impurities can have benefits for integrated plasma conditions, warranting its further investigation in JET.

DIII-D like effects

Analyses of local transport with the TRANSP code are shown in Fig.10.6 for a representative neon-seeded plus an unseeded pair of X-point pulses. A clear decrease of ion thermal diffusivity in the outer region of the plasma is seen almost to coincide with the start of neon puffing, while a similar relative decline farther inwards follows after some delay.

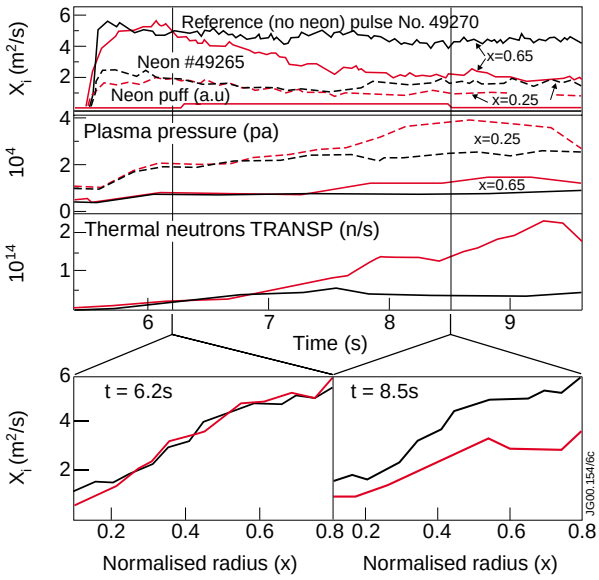

Fig.10.6: Local analyses with TRANSP of ion thermal diffusivity and plasma pressure at two normalized radii in two X-point plasmas without and with neon seeding. Total thermal neutron emission is also traced.

Increases in the energy stored within each radius are closely correlated with the respective falls. At the end of neon injection, χ_i is considerably reduced over the whole cross-section. Inspection of the accompanying LIDAR temperature profiles for electrons at least in Fig.10.7 indicates their greater central peaking with than without neon, presumably owing to radiative cooling of the edge, but otherwise reveals no systematic perturbation of T_e as neon radiation builds up (cf Fig.10.3(a)). Hence there is no evidence of a merely gyro-Bohm like reduction of χ_i due to lower temperatures, and a clear improvement at least in ion transport does seem to ensue from the impurity seeding.

[‡] Note that NEX signals are unreliable for one pellet shot, #49312.

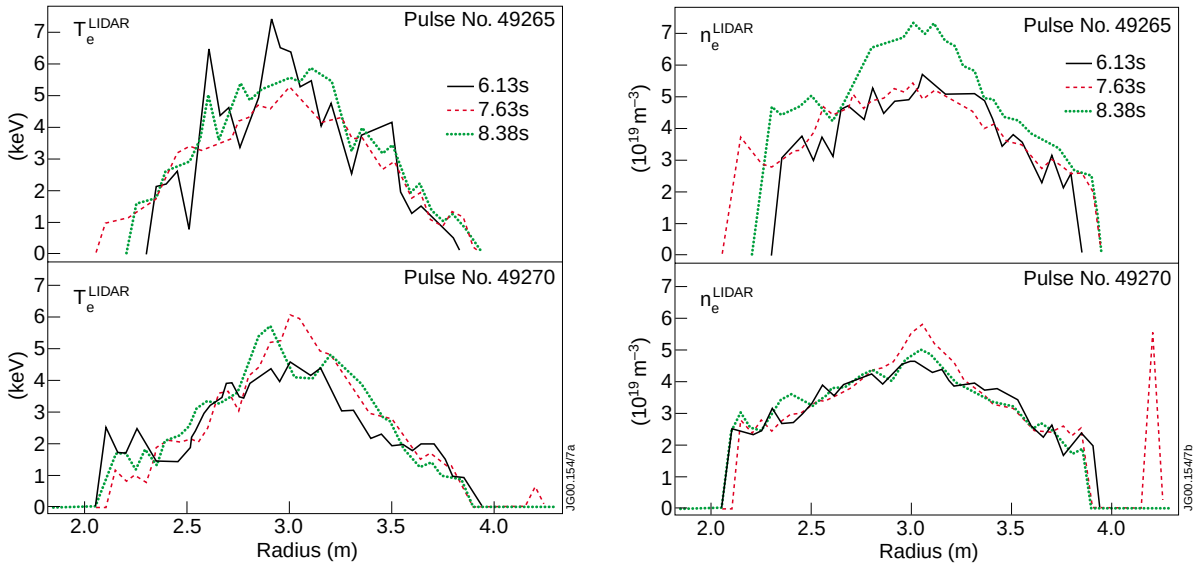

Fig.10.7: LIDAR electron temperature and density profiles in the preceding X-point pulse pair.

Electron density profiles in Fig.10.7 suggest an incipient central peaking towards the end of the neon puff, even though this is just after the onset of sawteeth (at 8.25 s in shot #49265). In fact the role of sawteeth is still under discussion for these cases, but it is noticeable that here they begin at almost the same time as in the unseeded counterpart (8.35 s in shot #49270), while being much more frequent and larger in magnitude on the SXR signal in the presence of neon. All major effects also seem to occur before a delayed start of sawteeth at all in the higher power plasmas. Further examination is therefore required to determine whether $q(0) > 1$ is indeed influential in these DIII-D like states, as initially expected. An incidental point regarding current density distributions is that although internal inductance l_i rises with impurity radiation in JET, it is not instrumental in improved confinement conditions in DIII-D.

Gyro-kinetic simulations with the GKS code imply the important properties outlined in Fig.10.8 . Although ion temperature gradient (ITG) instabilities do seem to be reduced following neon injection, trapped electron modes (TEM) on the other hand then exhibit the highest normalized growth rates in the outer part of the plasma, and dominate until gradually declining away as the neon is pumped out. Hence any benefits of stabilizing ITG turbulence are partially offset by persisting TEM transport, which interestingly is also not

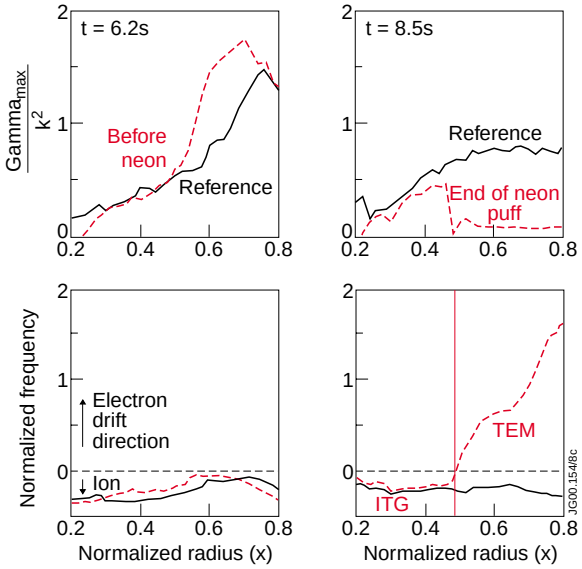

Fig.10.8: Gyro-kinetic calculations of turbulent transport, indicated by instability growth rate over wavenumber squared, and normalized mode frequencies. Trapped electron modes (TEM) dominate in the outer part of the plasma following neon injection. They are not observed in the unseeded reference state, for which ion temperature gradient (ITG) instabilities remain influential.

found in the unseeded counterpart pulse. This aspect of JET plasmas may help explain the absence of appreciable confinement gains so far from its impurity seeding trials. Additional support seems to be lent by a preliminary finding that in the best argon "afterglow" conditions, both ITG and TEM effects appear to be small together.

Even despite an inclination exemplified in Fig.10.6 for added impurities to affect the plasma across its entire cross-section, a further detrimental adjunct in JET is that, as already mentioned above, they tend not to be adequately retained within its boundary. An illustration is given in Fig.10.9, where rapid penetration of neon into the core is manifest, as well as its persistence after puffing ends (at 8 s). This strong intrusion, correlated with the large Z_{eff} values previously described, is again in contrast to RI-modes in TEXTOR-94, where minor disturbance of central dilution and peripheral concentration of intensified radiation are usually obtained. It remains a key issue for JET studies, potentially relating to the particle transport features contrasted for limiter pulses below.

The departure of JET behaviour here in X-point configuration from improved DIII-D states may be clarified by the non-dimensionalized comparisons made in Fig.10.10 . Tracing quantities as functions of time normalized by the ITERH89P L-mode energy confinement time, it can be seen that whereas the neon input per unit volume is larger in JET, auxiliary NBH per unit volume, f_{rad} , f_{Gwd} , the fall in χ_i at a mid-radius, and so $H89$ factor, are all lower than for an equivalent DIII-D shot. Their lack of correspondence may therefore be understandable. It is also evident that responses tend to occur more promptly upon seeding in DIII-D, but are somewhat delayed in JET, as remarked before.

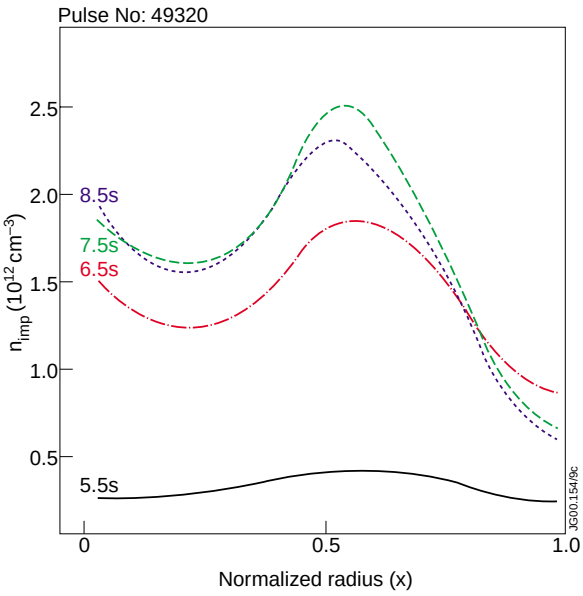

Fig.10.9 Inferred impurity density profiles throughout and just after neon puffing (from 5.3 s to 8 s).

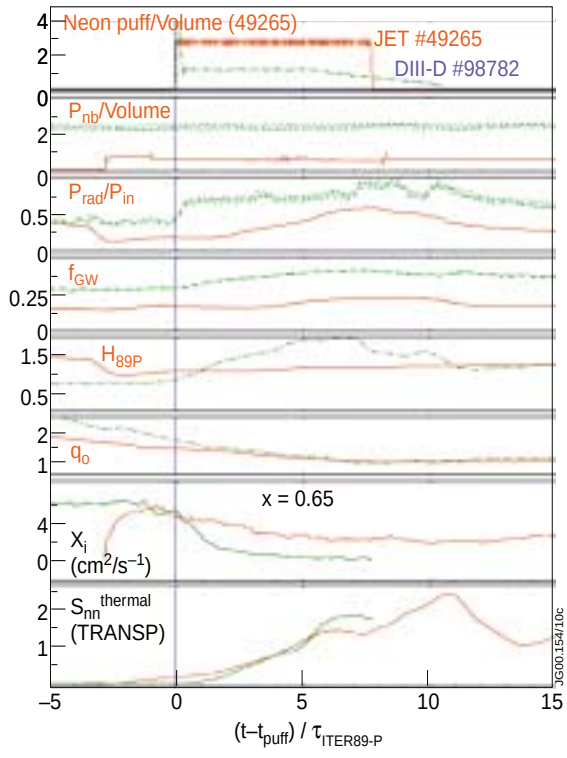

Fig.10.10: Comparison of normalized properties in JET and DIII-D discharges against multiples of the ITERH89P L-mode energy confinement time, beginning from the start of neon injection: neon input per unit volume; NBH per unit volume; f_{rad} ; f_{Gwd} ; normalized confinement; central safety factor; χ_i at a mid-radius; and thermal neutron emission.

Furthermore, the decline of neon effects after stopping its input occurs gradually, with the stored energy in particular decaying more slowly even than the density (cf Fig.10.3(a)). Attempts could therefore be made more closely to match such DIII-D parameters (neon input, volumetric heating, Greenwald fraction) in continuing tests.

Limiter effects

The top inboard space inside JET is not presently well viewed by its vertical bolometers, and emission from this position can be missed by global estimates of radiation, eg as used in Fig.10.4(b) (BOLO/TOPO). A careful reconstruction of 2-D radiation distributions for limiter configuration, represented in Fig.10.11, has found that a lobe of significant emission does indeed tend to arise at this position, presumably due to local surface interactions. Corrected values of total radiated power have been deduced accordingly. Interestingly, these data then correspond very closely with the Matthews radiative plasma scaling, as established in Fig.10.12 by comparing measured $Z_{\rm eff}$ with scaling predictions incorporating the revised emission. Hence impurity behaviour still seems to conform to the general principle prevailing in other experiments, as embodied in the Matthews scaling.

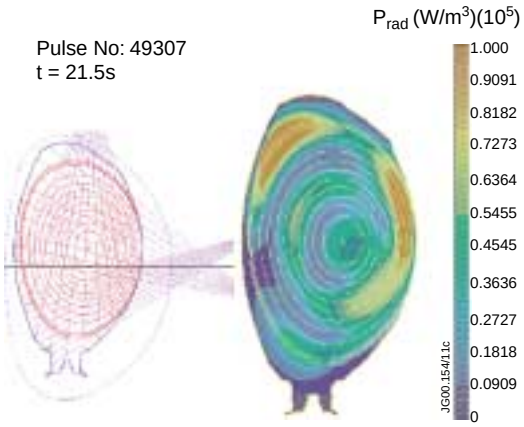

Fig.10.11: Bolometer lines-of-sight and amended 2-D reconstruction of radiated power density in a limiter pulse, showing poloidally asymmetric shape with bright emission from the top inboard region. Note no MARFE is present.

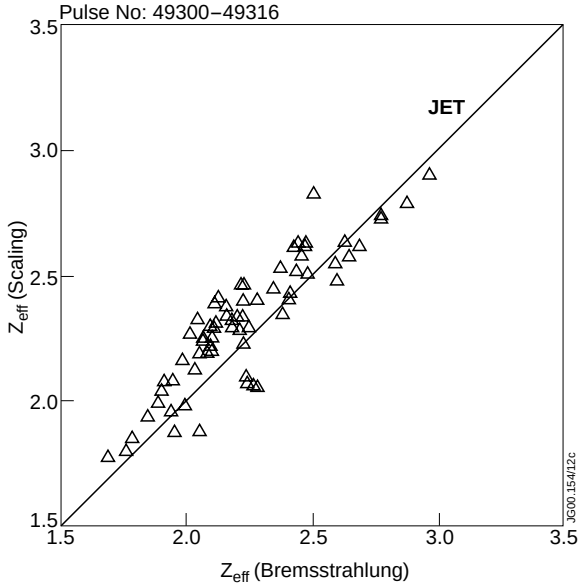

Fig.10.12: Comparison for sample limiter shots of measured Z_{eff} with predictions from the Matthews scaling using corrected estimates of total radiated power.

The relative weakness of density peaking in JET, however, does seem to point to an important departure from TEXTOR-94 properties. Using the RITM self-consistent particle and heat transport code, shaping factor $s \equiv (v^{\rm pinch} / D_\perp) (a^2 / r) q$, where $D_\perp$ and $v^{\rm pinch}$ are the particle diffusivity and inward pinch velocity, has been adjusted so as to match the JET profiles in a typical neon-seeded limiter case with $f_{\rm rad} \approx 0.7$ (yielding $s \approx 0.5$). Keeping this **identical** s

but taking full account of the different source distribution due to fuelling and added impurities, profiles have then been computed for an RI shot in TEXTOR-94 at similar $f_{\rm rad}$ and q_a. In contrast to its actual experimental peaking of $n_e(\,0\,) / \langle n_e \rangle \approx 2.5$, it is apparent in Fig.10.13 that this procedure implies a rather flat density profile also for TEXTOR-94, similar to the JET shape, notwithstanding its quite different sources. In other words, the sources alone cannot account for their difference in density peaking, and distinct underlying transport ($v^{\rm pinch} / D_\perp$) seems to be involved.

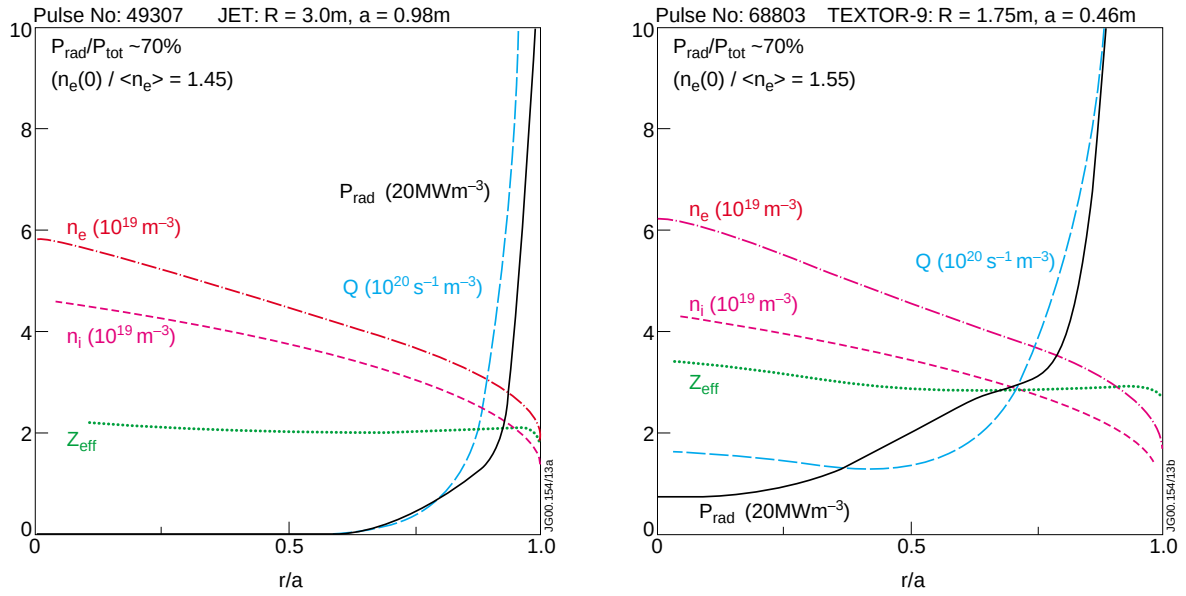

Fig.10.13: Calculations with the RITM transport code for JET and TEXTOR-94 limiter cases at $f_{rad} \approx 70\%$. Particle transport is adjusted to match the JET profiles, then using exactly the same function but accounting for its different sources, predictions are computed for TEXTOR-94. Derivation of a similar flat density, in contrast to the actually more peaked experimental data, suggests respective sources alone cannot explain their different peaking responses.

A quantitative theory of the fluxes due to ITG and dissipative TEM instabilities in (moderately collisional) L and RI regimes has been elaborated by Tokar et al [10.5]. The former are predicted to dominate in L-modes, resulting in a rather flat density profile, but when they are quenched, the latter can produce a relatively strong inward pinch and consequently increased central peaking; this modification is associated with the transition to RI-mode. The interplay may be expressed in terms of an integral steady-state continuity equation $\Gamma_r - (1 / r) \int_0^r S_e \, r \, {\rm d}r \equiv G(p) = 0$, where G is a governing function of the ratio of scale-lengths $p \equiv L_T / L_n = 1 / \eta_i$. Determination of peaking p from the balance of sources and transport is illustrated for TEXTOR-94 conditions in Fig.10.14(a), at an intermediate radius where the change in density gradients is largest. During L-mode, large ITG contributions produce a folded form for G with two stable points, but only the lower, flatter one with higher turbulence is accessible. However, as impurities are added, the impact of rising $Z_{\rm eff}$ on ITG growth rates lowers the intervening maximum value of G, until beyond a certain critical position it falls below zero, making a bifurcation to the now accessible upper stable point feasible. The resulting transition to a more

peaked density state with reduced ITG components is quantitatively well correlated with the entry to RI-mode in TEXTOR-94 [10.5], increasing confidence in this proposed mechanism.

An equivalent calculation of $G(p)$ at a similar normalized radius is shown during neon seeding of a JET limiter plasma in Fig.10.14(b). It is exposed at once that it remains above the critical form of G, with persisting ITG transport, and thus denoting a flat, low p density distribution just as detected in the experiment. The failure so far to induce RI like improvements may therefore be understandable. The theory may also be exploited to infer adjustments which should help JET to attain transitions into RI regime. Superimposed in Fig.10.14(b) are calculated effects of higher Z_{eff}, eg produced by choosing other seed species , and a stronger interior particle source, each of which separately would require roughly a threefold increase to reach the critical G. In fact the former recourse may be less attractive, since Z_{eff} is already reasonably high in the tests to date, while the latter action ought best to avoid higher central temperatures at the same time, eg accompanying strengthened central NBH, since these would tend to exacerbate ITG growth. A possible scheme which might be tried in next experiments hence could be to optimize deep pellet fuelling by inboard launch, in combination with incremental nitrogen or argon puffing.

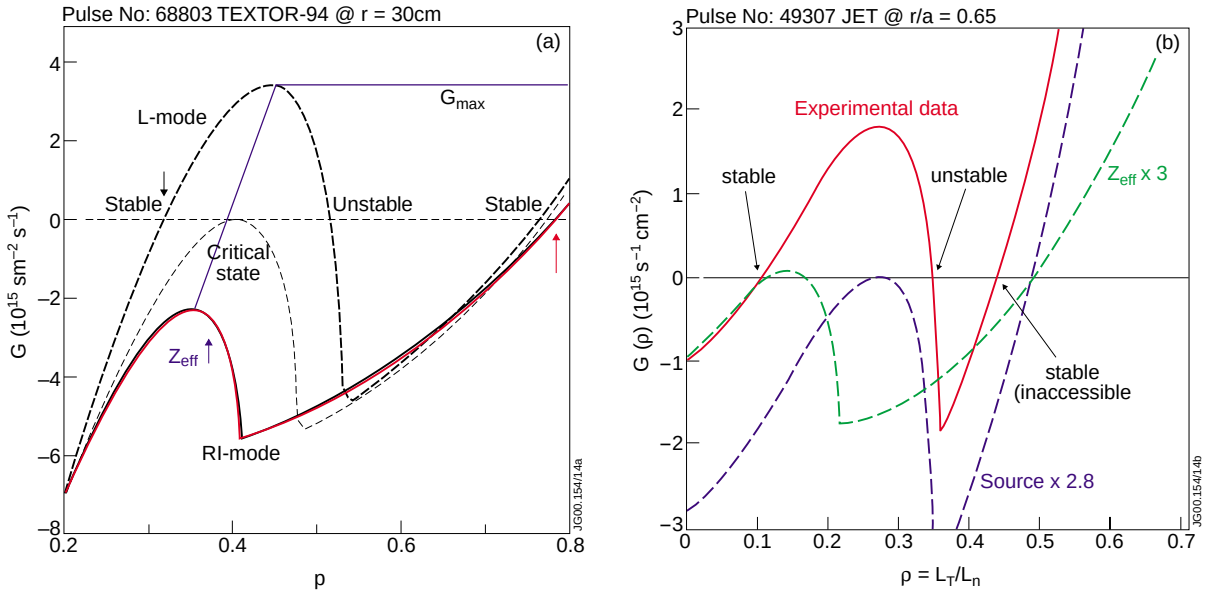

Fig.10.14: Tokar profile peaking function due to ITG plus DTEM turbulence [10.5]. (a) TEXTOR-94 conditions, showing two stable points for L-mode properties. Only the lower solution is accessible, leading to a flat density profile with predominantly ITG transport. Impurity seeding raises Z_{eff} and inhibits ITG growth, eventually making bifurcation to the upper stable point feasible, so leading to the more peaked, improved-confinement RI-mode. (b) Calculated peaking function during neon seeding into a JET limiter plasma. Access to more peaked states is denied, as found in the experiments. Higher Z_{eff} or stronger interior particle sources could promote entry into RI states.

Septum "afterglow" effects

It emerges in Fig.10.3(c) that a pronounced recovery of confinement occurs in the septum pulses after gas puffing ends, whether or not argon is added. The crucial supplement in the "afterglow" just with argon, though, is that **the density also does not decline**. This enables exceptionally

high values of normalized confinement and density to be realized together, as seen in Fig.10.5(b). Furthermore, Fig.10.5(a) suggests that some slight increase in peaking of the density profile is developing as well. A major qualification attaching to these cases, on the other hand, is that good confinement is retrieved by **a reversion to large Type I ELMs**, as evident in Fig.10.3(c). The pedestal expected for heating well above H-mode threshold is presumably being re-established as edge sources and sinks diminish without continuing gas input. These conditions therefore seem less compatible so far with the complementary aim of moderating large ELMs, although the key effect which allows good confinement and high Greenwald fractions to be maintained together clearly calls for further study.

10.3 Summary and future directions

Although substantial increases in confinement such as observed with impurity seeding in divertor cases on DIII-D and particularly in limiter RI-modes on TEXTOR-94 have not yet been seen in JET, considerable information on effects in L-modes and after puffing into septum H-modes has been added to earlier results. Radiation fractions up to ≈ 60% have been achieved, for a range of Z_{eff} values, and with definite signs of improving properties. Ion thermal diffusivity is reduced across the whole plasma by neon or argon seeding into diverted pulses, though competing turbulence mechanisms may contribute to a more modest impact on confinement. Further analysis of the electron response and especially whether intervention of sawteeth actually does influence behaviour is still needed. Seeded limiter L-modes clearly demonstrate different particle transport to that in TEXTOR-94, so that the absence of strong density peaking so far in JET cases cannot be attributed just to different source distributions. This distinction from RI-modes seems to be crucial, as suggested by a theory of ITG and TEM instability driven fluxes, which reveals the transition in TEXTOR-94 to arise from a bifurcation to more peaked density profiles as impurities restrain growth rates. The same analysis of JET conditions suggests greater central particle sources, eg by optimized inboard pellet fuelling and/or heavier impurity species, would help it to realize such transitions too. Additional examination of radiation distributions is required to ascertain whether plasmas with larger gaps from the inboard wall can reduce interactions there which appear to cause carbon impurities still to dominate discharges undertaken. The most remarkable result with impurity injection was perhaps that seen in the later stages of septum ELMy H-modes at high density, after all puffing had stopped. When argon had been added, these cases recovered good confinement whilst simultaneously maintaining a high Greenwald fraction, thereby reaching a product well above the conventional H-mode density limit. Continuing investigation is needed to understand the different processes underlying this advance, as well as to determine the extent to which accompanying Type I ELMs are abated by heightened radiation.

10.4 Shot List

"DIII-D like" early seeding into single X-point L-modes

shot #	B_0 (T)	I_p (MA)	P_{in}^{total} (MW)	$t(q_0=1)$ (s)	seed	Comments
49255	2.58	2.5	5.85		-	reference cases (L-mode)
49263	2.99	2.5	6.09	48.23	-	
49270	2.99	2.4	6.1	48.35	-	
49256	2.58	2.5	7.11	47.5	Ne	short (beam trip, disruption)
49260	2.99	2.5	6.46	48.3	Ne	disruptive end
49262	3	2.5	6.42	48.3	Ne	gas puff throughout
49264	2.99	2.5	6.65	48.06	Ne	*W* & *H* rises during Ne?
49265	2.99	2.5	5.94	48.25	Ne	more Ne
49266	2.99	2.4	6.8	47.85	Ne	earlier Ne
49272	2.99	2.4	6.99	47.59	Ne	good pulse
49273	2.99	2.4	8.44	47.95	Ne	disruptive end
49275	2.99	2.4	8.86	48.4	Ne	good pulse
49320	2.99	2.5	11.61	48.95	Ne	(interesting differences)
49321	2.99	2.5	11.15	49.4	Ne	higher power cases
49323	2.99	2.5	10.56	49.44	Ne	
49267	2.99	2.4	6.69	48.23	Ar	argon comparisons (reduced sawteeth?)
49268	2.99	2.4	6.94	47.9	Ar	
49269	2.99	2.4	6.46	47.44	Ar	

Limiter L-modes

shot #	B_0 (T)	I_p (MA)	P_{in}^{total} (MW)	seed	Comments
49303	2.94	2.0	8.34	-	reference cases
49304	2.94	2.0	6.54	-	
49309	2.93	1.8	3.88	-	
49299	2.94	2.0	3.47	Ne	low power (NIB4 only)
49300	2.94	2.0	8.26	Ne	longer Ne puff (disruptive end)
49301	2.94	2.0	8.25	Ne	earlier Ne, MARFE & disruptive end
49306	2.94	1.8	6.16	Ne	disruptive end
49307	2.93	1.8	6.98	Ne	more Ne, I_p ramp down, MARFE
49308	2.94	1.8	9.02	Ne	RIG control, n_e rise, MARFE
49310	2.94	1.8	9.12	Ne	increased RIG, good pulse
49315	2.94	1.8	6.08	Ne	disruptive end
49316	2.94	1.8	8.4	Ne	higher NBI
49317	2.94	1.8	5.97	Ne	reduced RIG again
49312	2.93	1.8	8.46	Ne	(one pellet during Ne, NEX unreliable)
49313	2.94	1.8	8.52	Ne	HFS pellet injection
49314	2.94	1.8	6.06	Ne	(later pellet, disruptive end)
49318	2.94	1.8	1.2	Ne	Ohmic cases
49319	2.94	1.8	1.31	Ne	(SOC)

Septum ELMy H-modes (“afterglow”)

shot #	B_0 (T)	I_p (MA)	P_{in}^{total} (MW)	seed	Comments
49726	2.5	2.5	12.86	-	density (gas puffing) scan cases
49727	2.4	2.4	12.92	-	
49728	2.5	2.5	13.03	-	
49729	2.4	2.4	12.72	-	
49730	2.5	2.5	12.7	-	
49731	2.5	2.5	12.95	-	
49732	2.5	2.5	13.02	Ar	high n_e with argon, "afterglow" rise
49739	2.5	2.5	12.91	Ar	earlier end of gas puffing + seeding

Acknowledgements

Participation of GPM is supported jointly by the UK Department of Trade & Industry and by Euratom.

References

[10.1] G L Jackson et al "Impurity seeding of JET L-mode diverted plasmas" to be presented to the 27th EPS Conference on Controlled Fusion & Plasma Physics, Budapest, June 2000

[10.2] B Unterberg et al "Radiative mantle experiments in JET limiter plasmas and comparison to the Radiative Improved mode in TEXTOR-94" to be presented to the 27th EPS Conference on Controlled Fusion & Plasma Physics, Budapest, June 2000

[10.3] R R Weynants et al Nuclear Fusion 39,11Y (1999) 1637

[10.4] J D Strachan et al Plasma Physics & Controlled Fusion 42 (2000) A81

[10.5] M Z Tokar et al Physical Review Letters 84 (2000) 895

Appendix A10.1 International RI group collaborators

M Brix[2], R Budny[3], I Coffey[1], P Dumortier[4], S K Erents[1], N C Hawkes[1], M von Hellerman[5], L D Horton[6], L C Ingesson[5], G L Jackson[7], A Kallenbach[6], K D Lawson[1], A Loarte[8], G P Maddison[1], G F Matthews[1], G R McKee[7,9], A Meigs[1], A M Messiaen[4], F Milani[1], P Monier-Garbet[10], M Murakami[7,11], M F F Nave[12], J Ongena[4], M E Puiatti[13], J Rapp[2], G M Staebler[7], J D Strachan[3], M Tokar',[2], B Unterberg[2], M Valisa[13], M Wade[7,11], K-D Zastrow[1].

[1] EURATOM/UKAEA Fusion Association, Culham, UK.

[2] IPP, Forschungszentrum Jülich GmbH, EURATOM Association, D-52425 Jülich, Germany†.

[3] Princeton Plasma Physics Laboratory, Princeton University, NJ 08543, USA.

[4] LPP, Association EURATOM-Belgian State, ERM-KMS, B-1000 Brussels, Belgium†.

[5] FOM-IVP, EURATOM Association, Postbus 1207, NL-3430 BE Nieuwegein, Netherlands†.

[6] Max-Planck IPP, EURATOM Association, D-85748 Garching, Germany.

[7] DIII-D National Fusion Facility, San Diego, CA 92186-5698, USA.

[8] EFDA-CSU, D-85748 Garching, Germany.

[9] University of Wisconsin-Madison, Madison, Wisconsin, USA.

[10] CEA Cadarache, F-13108 St Paul lez Durance, France.

[11] ORNL, Oak Ridge, Tennessee , USA.

[12] CFN, EURATOM-IST Associação,1096 Lisbon, Portugal.

[13] Consorzio RFX, Corso Stati Uniti 4, 35127 Padova, Italy.

† Partners in the Trilateral Euregio Cluster (TEC)

11. HYDROCARBON YIELDS

M F Stamp[1], S K Erents[1], W Fundamenski[1], G F Matthews[1], R D Monk[2].

JET Joint Undertaking, Abingdon, Oxfordshire, OX14 3EA, UK.

[1] EURATOM/UKAEA Fusion Association, Culham Science Centre, Abingdon, Oxfordshire, OX14 3DB, UK.

[2] Present address: Max Planck Institut für Plasmaphysik, Boltzmannstrasse 2, 85748 Garching, Germany.

11.1 Overview

The low Z and good thermal and mechanical properties of graphite make it a candidate material for the walls and divertor of a fusion reactor. Its major drawbacks are the high erosion rate from chemical sputtering and the tritium codeposition in redeposited carbon films. Recent in-situ erosion measurements [11.1-11.3] have indicated a promising trend of reduced erosion yields at high incident particle fluxes, though these studies assumed a constant photon efficiency (D/XB) for their determination of the methane flux from spectroscopic observation of the CD molecular band intensity at 431nm.

To investigate the behaviour of the hydrocarbon erosion yield in the JET divertor a series of dedicated experiments were carried out in which methane (CD_4 and CH_4) and ethane/ethene (C_2H_4, C_2H_6) hydrocarbons were puffed from the divertor gas introduction modules (GIMs) into either deuterium or hydrogen plasmas. Ohmic and L-mode (2MW NBI) 2.4MA, 2.5T vertical target X-point plasmas were mainly used for this study. The typical magnetic configuration is shown in fig.11.1, which also shows the locations of the divertor Langmuir probes and some spectroscopic lines-of-sight. Light collected from the inner and outer divertor views was routinely monitored by the KS3 survey spectrometer, and clearly showed molecular band features, figs 11.2a,b (CD from CD_4 break-up, and C_2 from C_2H_4 and C_2H_6 break-up).

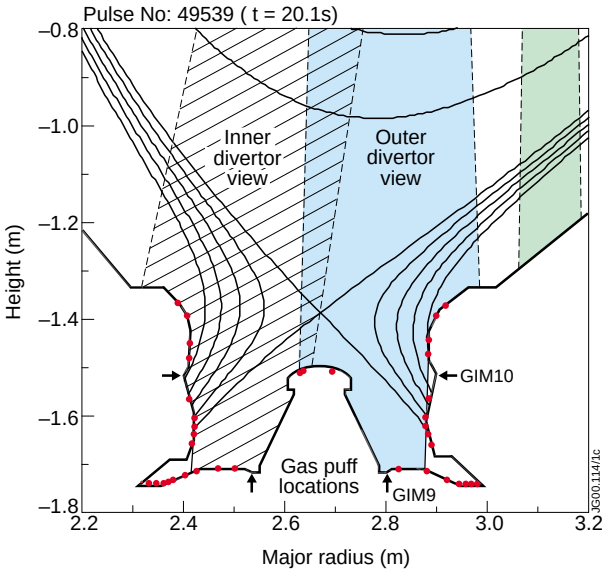

Fig.11.1 The magnetic configuration of the discharges used, showing the fixed Langmuir probe positions and the lines-of-sight of the visible spectroscopy.

The hydrocarbon gases were mostly injected through GIM 9 (slots in a toroidal ring in the floor of the outer divertor) rather than GIM 10 (in the sidewall of the outer divertor) because the spectroscopy has an un-vignetted view of GIM 9. The observed increases in molecular band intensities, compared with deuterium/hydrogen puffed reference pulses, were used to deduce the intrinsic hydrocarbon fluxes and erosion yields, as well as the D/XB. The assumption has to

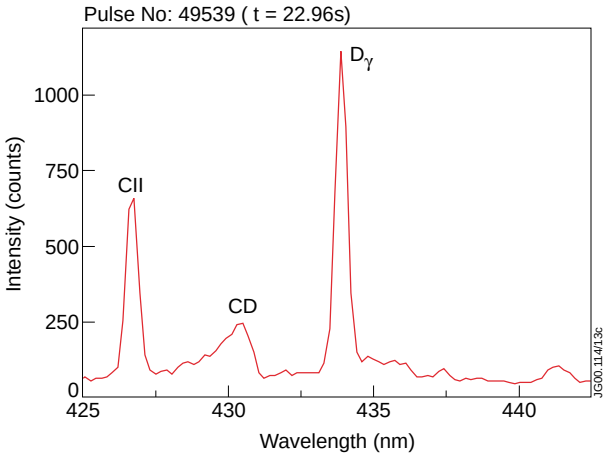

Fig.11.2a A portion of the outer divertor emission spectrum recorded by the KS3 survey spectrometer. The CD ($A\,^2\Delta - X\,^2\Pi$) molecular band is clearly observed.

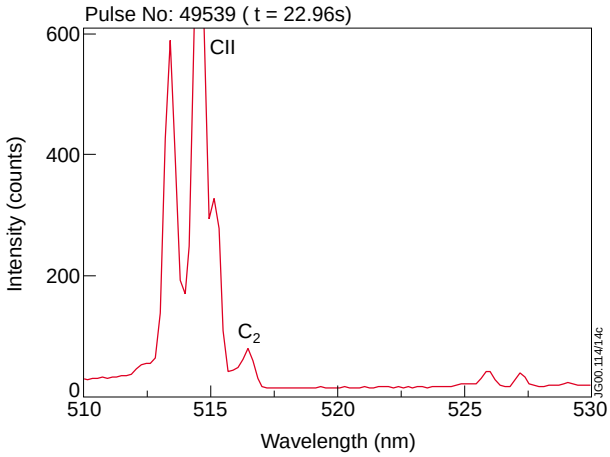

Fig.11.2b A portion of the outer divertor emission spectrum recorded by the KS3 survey spectrometer. The Swan C_2 ($A\,^3\Pi_g - X\,^3\Pi_u$) molecular band head is clearly observed.

be made that the different source distributions (intrinsic vs. puffed) does not have a significant effect on the measurements. This assumption is supported by earlier measurements of D/XB in Elmy H-mode plasmas that found the same value whether the methane was injected into the private flux region (as here), or into the scrape-off-layer [11.4].

11.2 Results

Typical outer divertor edge plasma parameters in the 2.4MA 2.5T L-mode plasmas are shown in fig.11.3. The profiles are reconstructed from small sweeps of the outer strike point at times corresponding to the low and high density phases of the discharge. The peak divertor electron

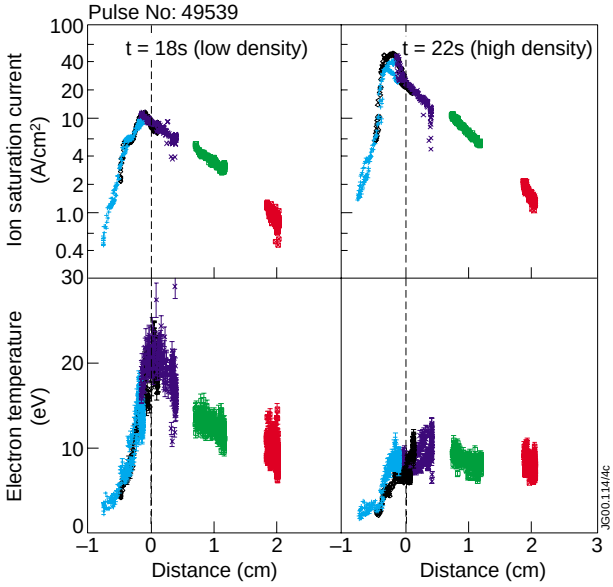

Fig.11.3 Ion saturation current and electron temperature profiles at the outer divertor target during the low and high density phases of these discharges. The distance scale is midplane centimetres relative to the separatrix, as determined by EFIT.

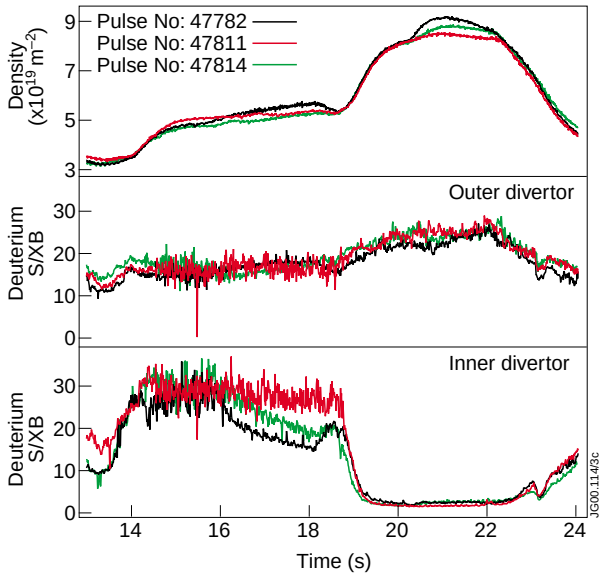

Fig.11.4 Typical time evolution of the central line integral density. Also shown is the D-alpha S/XB at the inner and outer divertor, calculated from the calibrated D-alpha signal and the integrated ion flux from the fixed Langmuir probes.

temperature is typically 20eV at low density, and 8eV at high density. The peak divertor density is more variable, but typically varies from $2x10^{19}$ m^{-3} to $1x10^{20}$ m^{-3}. The plasma in the outer divertor is attached in all these plasmas, as is illustrated in fig.11.4, where the D-alpha photon efficiency is calculated from the observed photon intensity and the ion flux measured by the probes. Values of about 20, that increase slowly with density are characteristic of an attached plasma. Values that drop as the plasma density is increased are indicative of an increasing level of plasma detachment. Hence fig.11.4 also shows that the inner divertor is only completely attached at the lowest plasma densities.

The hydrocarbon puffs in these discharges leads to increases in molecular signals (figs 11.5a and 11.5b), and some increase in the low charges states of carbon. However, the line-averaged Z_{eff} shows almost no change (ΔZ_{eff} <0.1). Figure 11.5a shows data for CD_4 puffs into a deuterium plasma, whereas fig.11.5b shows data for CH_4 puffs into a hydrogen plasma. The CD (CH) signals can be seen to increase when CD_4 (CH_4) is puffed into the line-of-sight, though at high density twice as much methane is needed to achieve the same increase in CD (CH) signal as at low density. This implies that the photon efficiency is higher at higher edge densities (lower edge temperatures). Figures 11.5a, b also illustrate that the intrinsic outer divertor CD intensity in deuterium discharges is about twice as large as the intrinsic outer divertor CH intensity in hydrogen discharges. This suggests that the intrinsic erosion yield of CD_4 is twice that of CH_4 (assuming that D/XB is isotope independent).

Figure 11.6a shows the effect of ethane and ethene puffs in similar hydrogen discharges. Again it can be seen that twice as much gas needs to be puffed at high density in order to achieve the same increase in molecular C_2 intensity as at low density. It is also striking that the C_2

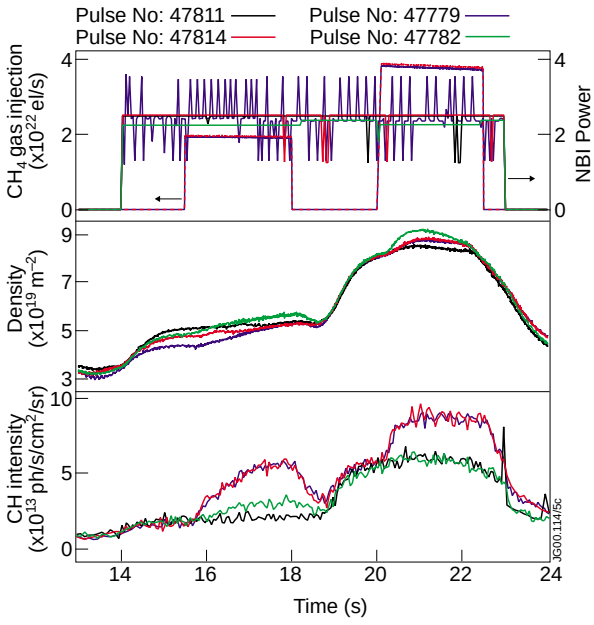

Fig.11.5a The time evolution of the NB power, the central line integral density, the hydrocarbon puff rates and the outer divertor CD intensity for deuterium plasmas.

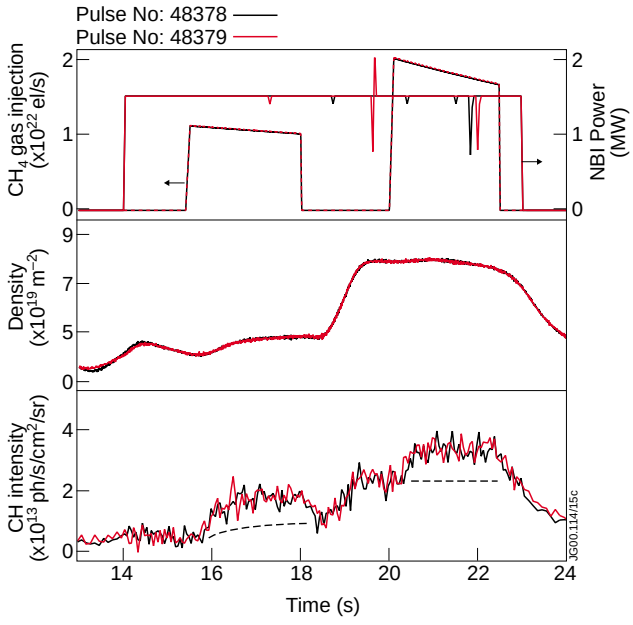

Fig.11.5b The time evolution of the NB power, the central line integral density, the hydrocarbon puff rates and the outer divertor CH intensity for hydrogen plasmas.

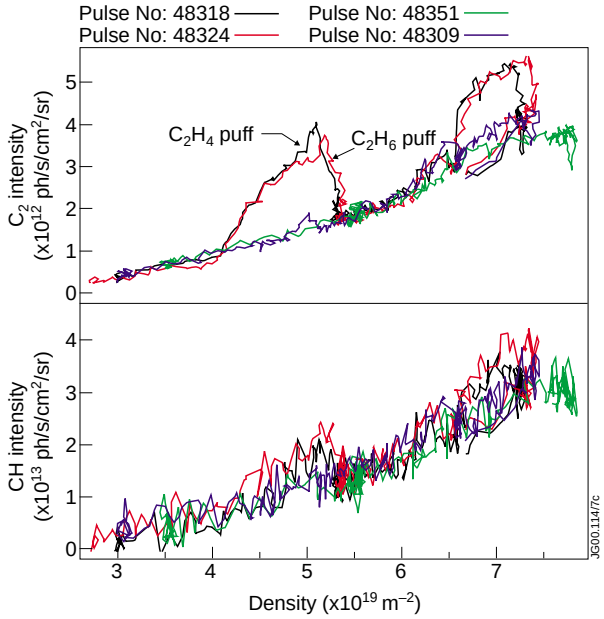

Fig.11.6a The evolution of the outer divertor C_2 and CH intensities as a function of density for C_2H_4 and C_2H_6 outer divertor gas puffing into similar deuterium target plasmas.

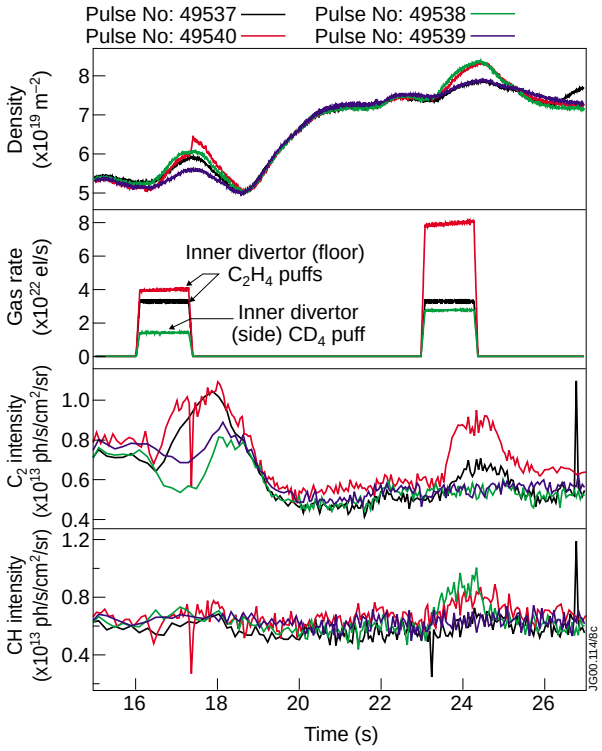

Fig.11.6b Time evolution of signals for deuterium discharges with C_2H_4 gas puffing from the inner divertor.

intensity is identical in the C_2H_4 and C_2H_6 puffed discharges, implying identical D/XB. Figure 11.6a also illustrates that the CH intensity is possibly showing a small increase when C_2H_4 and C_2H_6 are puffed, although no increase in CH is seen for a strong inner divertor C_2H_4 puff, fig.11.6b. Thus we conclude that the break-up of C_2H_y molecules produces few CH molecules, though this is an area worth further study.

The isotopic dependence of the methane D/XB was also explicitly investigated (fig.11.7). CD_4 was puffed from GIM 9 into a 2.4MA 2.5T ohmic deuterium plasma (#48864) with a density ramp. The filling gas to GIM 9 was then changed to CH_4, and the discharge repeated (#48866). Figure 11.7 indicates that the increases in CD and CH intensities, as a result of the methane puffs, are the same (within approximately 30% error bars), and hence the methane photon efficiency (D/XB) is isotope independent.

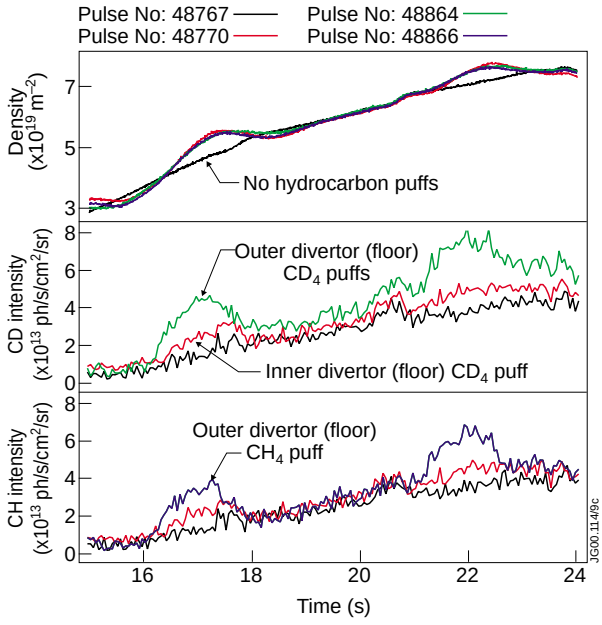

Fig.11.7 The time evolution of central line integral density, and outer divertor CD and CH intensities for CD_4 and CH_4 gas puffing into similar deuterium target plasmas.

Figures 11.8a and 11.8b show the full datasets for the hydrocarbon erosion yields and photon efficiencies. The erosion yields are all measurements from the outer divertor, except for a single point from the inner divertor, which will be discussed later. Each erosion yield measurement is represented by two data points; one where the yield is calculated from an incident flux derived from the D-alpha measurement and a constant S/XB=20, the other where the yield is calculated from an incident flux derived from the sum of the Langmuir probe signals. The probe measurement ought to be the more robust, but depends critically on the relative location of the strike point relative to the probe positions. If the strike point is just missing a probe, so that this nearest probe is in the private flux region, the total integrated ion flux will be significantly underestimated, as is probably the case for the high density data-point in #48318 (the C_2H_4 puff into a hydrogen plasma).

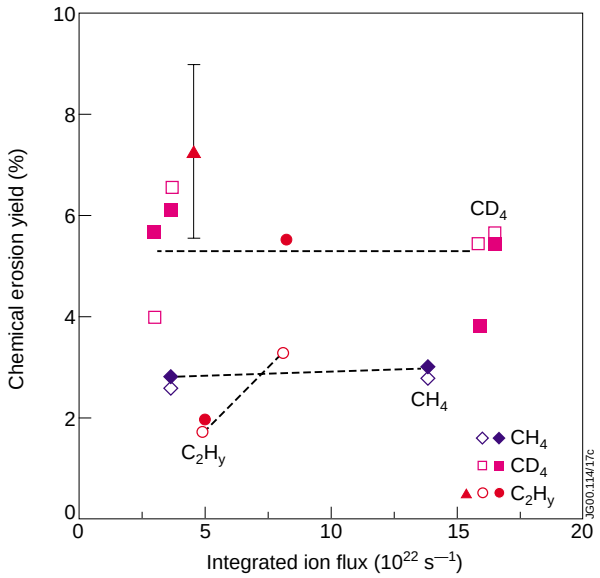

Fig.11.8a Hydrocarbon erosion yields as a function of the integrated ion flux to the outer divertor. The incident flux is calculated from Langmuir probe data for the solid data points, and from D-alpha (S/XB=20) for the open points. The ▲ is a C_2H_4 yield measurement from the inner divertor.

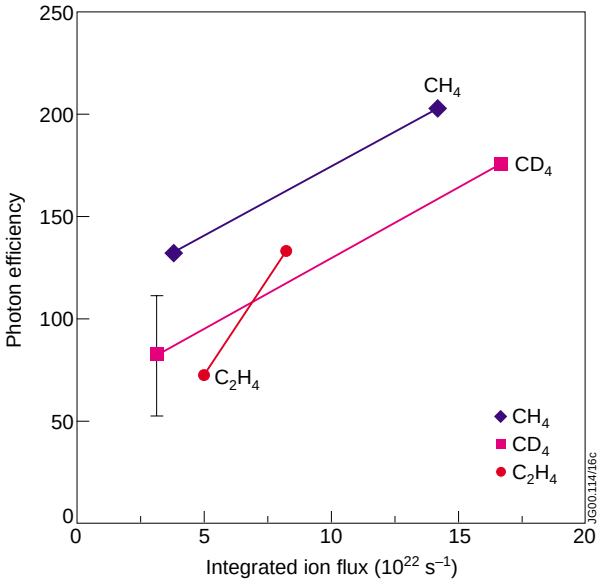

Fig.11.8b Hydrocarbon photon efficiencies as a function of the integrated ion flux to the outer divertor.

Figure 11.8a shows that the methane erosion yields are constant, about 5% for deuterium plasmas and 3% for hydrogen plasmas, and do not show any flux dependence. The erosion yield for C_2H_y (in hydrogen plasmas) actually shows an increase with the ion flux to the divertor target, rising from 1.8 to 3%. This means that at high density (i.e. high ion flux, or low electron temperature) in hydrogen plasmas the total chemical carbon erosion yield is three times the methane erosion yield! If the C_2D_y hydrocarbon yield behaves the same way in deuterium plasmas, then the total chemical carbon erosion yield would be 15% in deuterium plasmas.

Figure 11.8a also includes a data point for C_2H_4 injection into the inner divertor of a deuterium plasma. Assuming that the ethene D/XB is isotope independent, as found for methane,

then the intrinsic erosion yield at the inner divertor is determined to be about 7%. Thus the total chemical carbon erosion yield at the inner divertor could be as high as 19% (assuming 5% CD_4 yield at the inner divertor: When CD_4 was puffed into the inner divertor, no change in CD signal was observed, #49539 in fig.11.6b).

The photon efficiencies plotted in fig.11.8b show a strong increase with increasing ion flux (i.e. increasing density, decreasing electron temperature). This is not consistent with the modelling of Naujoks [11.5], which showed that the D/XB for methane was not very density dependent, and increased with increasing electron temperature.

Earlier JET hydrocarbon yield data [11.3] was analysed with the assumption of constant photon efficiency, and showed a decrease of the hydrocarbon yield with increasing flux density. If this earlier JET data is re-analysed using the measured photon efficiency, then the hydrocarbon yield becomes constant with increasing flux density, fig.11.9. Other measurements that assumed a constant D/XB [11.1, 11.2] and which showed a decreasing erosion yield with increasing ion flux for would show a similar effect. Their results need to be reassessed.

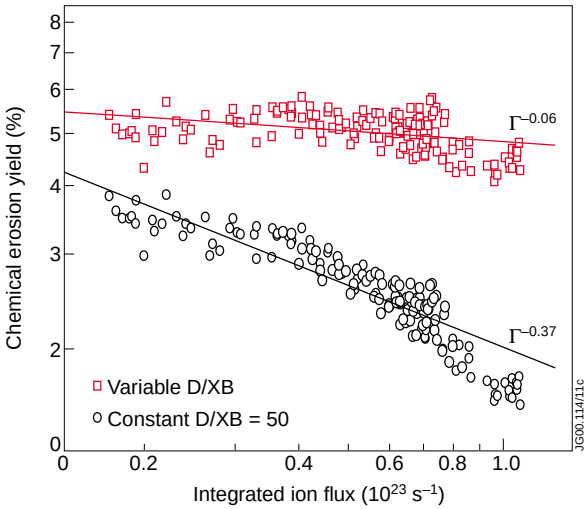

Fig.11.9 Revised plot of the chemical erosion yield from [11.3] as a function of the integrated ion flux to the outer divertor, both for a constant D/XB (=50), and the measured variable D/XB. (JG00.114/11c)

11.3 Summary and future directions

In deuterium plasmas, the outer divertor CD_4 erosion yield was determined to be 5% at both low and high plasma density. In hydrogen plasmas, the CH_4 yield was determined to be 3% at both low and high plasma density, whilst the C_2H_4 and C_2H_6 yields were 1.8% at low density, rising to 3% at high density. Thus in hydrogen plasmas at high density, the total chemical carbon erosion yield is three times as large as the methane yield.

If we assume that deuterium plasmas show the same behaviour, then the total chemical carbon erosion yield would be as high as 15%. Such a high level of erosion would be unacceptable for ITER. A measurement of the inner divertor ethene yield was made by injecting C_2H_4 into a deuterium plasma. Assuming that the photon efficiency is isotope independent (as indicated by methane), then the ethane erosion yield at the inner divertor was about 7% (i.e. 14% carbon erosion yield). This is higher than the yield in the outer divertor, and supports the hypothesis of readily eroded soft films that has been invoked to explain the thick carbon layers found on the inner louvers at JET [11.6].

Further measurements of the erosion yield at the outer and inner divertors are obviously required to confirm and extend the above important results. It would also be wise to repeat the experiments with C_2D_4 (or C_2D_6) injection into deuterium plasmas to check the assumptions made about the isotopic independence of the D/XB.

The photon efficiency derived from these experiments increases with decreasing plasma edge electron temperature. This is the opposite behaviour predicted by the theoretical calculations of Naujoks [11.5]. Photon efficiencies for other species like C II, C III, O II, etc., all increase with electron temperature, so these results are puzzling. It must be pointed out that it is not clear from this study whether the changes in photon efficiency are due to the changing plasma electron density, or the changing edge electron temperature. Attempts to address this question by variable amounts of ICRF heating were unsuccessful because of different monster sawteeth at different heating powers, and poor density control. This is clearly another area to be addressed in future experiments.

11.4 Shot List

2.4MA, 2.5T, V/SFE/LT, 2.0MW NBI ($D^o \rightarrow D$), L-mode

Pulse number	Gas Puff Details	Gas Rate ($x10^{22}$ el/s)	Comment
47779	CD4 from GIM 9 (Base, outer-X)	1.90, 3.75	Divertor CD4 source
47782	D2 from GIM 10 (Side, outer-X)	0.67, 1.30	Reference – match Γ_D
47810	CD4 from GIM 4 (Oct.1 midplane)	0.67, 1.30	Wall CD4 source
47811	D2 from GIM 10 (Side, outer-X)	0.25, 0.50	Reference– match $\int$ nedl
47814	CD4 from GIM 9 (Base, outer-X)	1.95, 3.80	Repeat 47779

2.4MA, 2.5T, V/SFE/LT, hydrogen plasmas , OHMIC density ramp 55-63s.

Pulse number	Gas Puff Details	Gas Rate ($x10^{22}$ el/s)	Comment
48309	No puff		Reference
48311	C2H4 from GIM 9 (Base, outer-X)	2.60 2.40	Ethene puffs
48318	C2H4 from GIM 9 (Base, outer-X)	1.37, 2.60	Smaller first puff
48324	C2H6 from GIM 9 (Base, outer-X)	1.55, 2.90	Ethane puff
48351	H2 from GIM 9 (Base, outer-X)	0.47, 0.80	Reference (ne high)

2.4MA, 2.5T, V/SFE/LT, 1.5MW NBI ($H^o \rightarrow H$), L-mode

Pulse number	Gas Puff Details	Gas Rate ($x10^{22}$ el/s)	Comment
48352	C2H4 from GIM 5 (Top, octant 2)	1.85	NBI trip at 54.6s, H/(H+D) about 90%
48365	CH4 from GIM 7 (Top, octant 6)	1.7, 3.3	2.2MW of NBI, H/(H+D) about 40%
48378	CH4 from GIM 9 (Base, outer-X)	1.05, 1.8	H/(H+D) over 80%
48379	CH4 from GIM 9 (Base, outer-X)	1.05, 1.8	Accidental repeat
48380	C2H6 from GIM 8 (Top, octant 8)	1.8, 3.1	
48381	CH4 from GIM 7 (Top, octant 6)	1.5, 2.5	

2.4MA, 2.5T, V/SFE/LT, Deuterium plasmas , OHMIC density ramp 55-63s.

Pulse number	Gas Puff Details	Gas Rate ($x10^{22}$ el/s)	Comment
48767	No puff		No puff reference
48769	CD4 from GIM 11 (Base, inner-X)	0.6	Density ref. for ‘ 64/66
48770	CD4 from GIM 11 (Base, inner-X)	1.0, 1.9	Density ref. for ‘ 64/66
48864	CD4 from GIM 9 (Base, outer-X)	1.4, 2.6	
48866	CH4 from GIM 9 (Base, outer-X)	1.5, 2.7	

2.4MA, 2.5T, V/SFE/LT, 2.0MW NBI ($D^o \rightarrow D$), L-mode

Pulse number	Gas Puff Details	Gas Rate ($x10^{22}$ el/s)	Comments
49537	C2H4 from GIM 11 (Base, inner-X)	3.3, 3.3	Inner divertor ethene
49538	CD4 from GIM 12 (Side, inner-X)	1.4, 2.8	Inner divertor methane
49539	CD4 from GIM 9 (Base, outer-X)	1.5, 2.9	Outer divertor methan.
49540	C2H4 from GIM 11 (Base, inner-X)	4.0, 8.0	Larger ethene puff

2.5MA, 3.2T, V/SFE/LT, 1.0MW NBI ($D^o \rightarrow D$) + ICRH, L-mode

Pulse number	Gas Puff Details	Gas Rate ($x10^{22}$ el/s)	Comments
49541	CD4 from GIM 9 (Base, outer-X)	1.4, 2.8	1.0MW RF
49542	CD4 from GIM 9 (Base, outer-X)	1.4, 2.8	3.0MW RF
49543	CD4 from GIM 9 (Base, outer-X)	1.5, 2.9	1.0MW RF
49544	CD4 from GIM 9 (Base, outer-X)	2.5, 5.0	2.0MW RF
49545	CD4 from GIM 9 (Base, outer-X)	2.5, 5.0	4.2MW RF

11.5 References

[11.1] A. Pospiezczyk et al., J. Nucl. Mater. **241-243** (1997) 833.

[11.2] A. Kallenbach et al., Nucl. Fusion **38** (1998) 1097.

[11.3] R. D. Monk et al., Physica Scripta **T81** (1999) 54.

[11.4] M F Stamp et al., J Nucl. Phys. **266-269** (1999) 685.

[11.5] D Naujoks, D Coster, H Kastelewicz, and R Schneider, J Nucl. Phys. **266-269** (1999) 360.

[11.6] P Coad et al., Proceedings of the 26th European Physical Society Conference on Controlled Fusion and Plasma Physics (Maastricht, Netherlands, 14th - 18th June 1999), and JET-CP(99)07.

12. JET METHANE SCREENING EXPERIMENTS

J.D.Strachan[2], S.K.Erents[1], W.Fundamenski[1], M.G.vonHellermann[3], L.D.Horton[4], K.D.Lawson[1], G.M.McCracken[1], J.Spence[1], M.F.Stamp[1], K-D.Zastrow[1].

JET Joint Undertaking, Abingdon, Oxfordshire, OX14 3EA, UK.

[1] EURATOM/UKAEA Fusion Association, Culham Science Centre, Abingdon, Oxfordshire, OX14 3DB, UK.

[2] Princeton Plasma Physics Laboratory, Princeton University, Princeton, NJ, USA.

[3] now at FOM Instituut voor Plasmafysica Rijnhuizen, EURATOM Association, Postbus 1207, NL-3430 BE Nieuwegein, The Netherlands

[4] now at Max-Planck-Institut für Plasmaphysik, IPP-EURATOM Association, Boltzmannstrasse 2, D-85748 Garching, Germany.

12.1 Overview

Methane screening experiments were performed in JET L-Mode plasmas. Potentially, methane puffing quantifies the SOL processes governing the intrinsic carbon, its penetration to the plasma core, and its removal to the divertor. We measured the perturbations to the core and the SOL plasmas as a function of CD_4 and D_2 injection rates. The deduced screening, i.e. probability of an injected carbon atom crossing the LCFS, was independent of the methane injection rate indicating that the methane itself did not significantly perturb the screening measurement. Identification of appropriate reference plasmas is important. For JET L-Modes, the reference plasma should have enough deuterium puffing to achieve the same density as occurred with the methane. The screening results are susceptible to systematic errors in the visible and charge exchange determination of the core carbon density. For JET, these two measurements yield screening values that differ by a factor-of-three.

12.2 Results

The ultimate goal of this research is to understand the magnitude of tokamak impurities. Impurities deplete the fuel ion species in relation to the plasma electron species. The depletion can reduce the fusion power if the electron density is limited (e.g. by the Greenwald limit), or when the total plasma pressure is limited (e.g. by the Troyon β limit), or when radiation losses (e.g. bremsstrahlung) are important in the energy balance. If impurity generation and contamination mechanisms are understood, then impurity control techniques can be envisioned, evaluated, and projected to future experiments. Methane screening experiments relate to these goals since they evaluate the ability of the SOL to ionise carbon and transport it to the divertor, preventing it from contaminating the plasma. This benchmarking is especially relevant for JET since chemical sputtering from the main chamber walls is thought to be a significant source of the dominant (carbon) impurity [12.1].

The purpose of the present paper is to evaluate the methodology and accuracy of the JET methane screening experiments. Methane screening experiments have been performed on several

tokamaks [12.2-12.9] however, little systematic evaluation of the methodology has been reported in the literature. Usually, the screening has been reported as a single number or upper limit. The work reported here is being used as a basis for the connection to the intrinsic JET impurities using DIVIMP [12.10] and those results will be reported elsewhere.

Methane was injected into JET L-Mode plasmas with 2.5T toroidal magnetic field, 2.5MA plasma current, and neutral beam heating of 2.5 MW. The power was low enough to ensure L-Mode operation thus avoiding the analysis complications of ELMs. The plasma was attached to the JET Gas Box divertor with the strike points hitting the vertical targets.

The data was collected from a series of 12 plasmas comprising a shot-to-shot scan in the methane puffing rate (seen in Fig.12.1 from 16 to 19 sec), and a scan in the deuterium puffing rate (seen in Fig.12.1 from 20 to 23 sec). The time evolution of three plasmas is overlaid in fig.12.1. Although the density rise was about equal from the methane and the deuterium (in Fig.12.1), the main purpose was to accomplish both scans and determine the best reference plasma for the methane injection. The methane fuelling was toroidally localised (an extended port of about 0.8 m linear dimensions, 0.5 m away from the plasma edge), at the horizontal, outer mid-plane. The deuterium fuelling was toroidally distributed from the divertor.

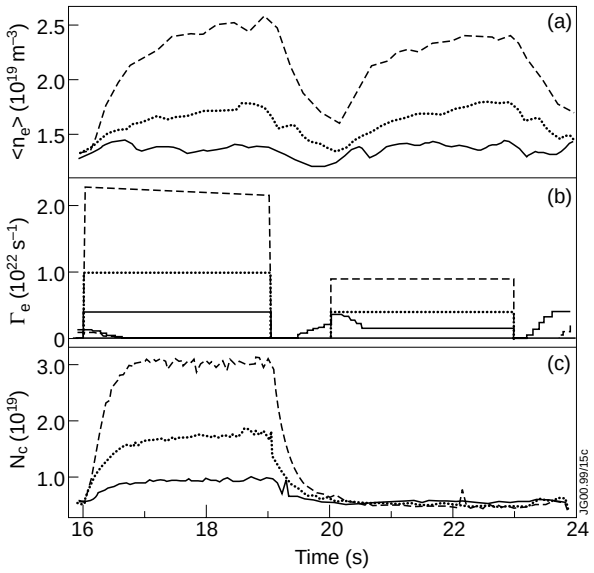

Fig.12.1. The time evolution of the density, (a), gas injection rate of electrons, (b), and the total carbon particle number measured by charge exchange recombination spectroscopy (c), for three discharges each with a different gas injection rate. Methane (CD_4) was injected from 16 to 19 sec, and deuterium was injected from 20 to 23 sec.

Key diagnostics included:

1. Carbon density measurements from charge exchange recombination spectroscopy (CX) [12.11] (Fig.12.1),
2. Z_{eff} measurements from visible bremsstrahlung (VB) [12.12].
3. SOL density and temperature measurements by the reciprocating Langmuir probe (RCP) [12.13].
4. The inferred SOL properties from the divertor Langmuir probes using an Onion Skin Model (OSM) [12.14, 12.15]. The strike points were swept about 2 cm from 18.5 to 19 sec and from 22.5 to 23 sec in order to improve the target density and temperature profiles, as input to the OSM.
5. The Mach probe was not used on these experiments, but results from similar L-Mode plasmas [12.16] indicated maximum Mach numbers of about 0.5 at the RCP location, with about 50% accuracy.

The RCP is located in the same toroidal location as the methane puffing, but displaced about 80 degrees poloidally above the horizontal mid-plane. The OSM temperature and density profiles (predicted for the RCP location) were in good agreement with the direct RCP measurements.

While the SOL measurements agree reasonably well, the CX and VB core Carbon measurements are discrepant. Commonly, JET H-Mode plasmas have CX Z_{eff} values about 0.75 of the VB values. However, for these L-Mode plasmas the differences are somewhat larger. Since the core carbon content is proportional to Z_{eff} -1, and since the actual Z_{eff} values were small, the differences are magnified resulting in "factor-of-three" differences in the inferred core carbon content. Each diagnostic has several sources of error, which could cause the discrepancy. Of particular note is that the methane puff itself, seemingly caused a contaminating continuum radiation for VB chords located near the puff (or in its plume). The origin of the discrepancy is beyond the scope of the present paper and instead we quote each potentially valid measurement.

12.2.1 Discussion

The magnitude of the methane injection rate (up to a carbon injection rate of 2.2 10^{21} sec^{-1}) did not influence the magnitude of the screening inferred for JET L-Mode plasmas. The methane injection did cause some perturbations to the SOL and core plasmas. The methane modified the plasma's radiation pattern, the core carbon content, the electron density in the SOL, and increased the core electron density (Fig.12.1). However, these perturbations did not influence the deduced screening so long as the methane-puffed plasma was compared to a discharge with the same core electron density.

The scan in the injection rates indicates (Fig.12.2) that the core density is uniquely related to the deuterium injection rate, whether the deuterons were injected as D_2 or as CD_4. At the same core density, the remaining core and edge parameters are similar for D_2 and CD_4 injection (Fig.12.2). Thus we conclude that the carbon content due to the methane puff should be compared to deuterium-fuelled plasmas at the same core density. Since the fuelling locations are different (D_2 from the divertor vs. CD_4 from the main chamber), and consequently the fuelling efficiencies are different, the deuteron injection rate fortuitously provides a convenient x-axis for Fig.12.2. In other words, if different fuelling rates were needed to obtain the same core density, then undoubtedly, the plasma parameters would be related to the core density and not the fuelling rate.

After normalising to the density, the core radiation, carbon content, and Z_{eff} were the only core parameters that changed due to the methane injection. The core radiation was about twice as high when methane was injected (Fig.12.2(a)) as when deuterium was injected. Apparently, the extra carbon in the core caused higher core radiation. However, the core radiation was <25% of the total radiation and was <10% of the power input. From the energy balance perspective,

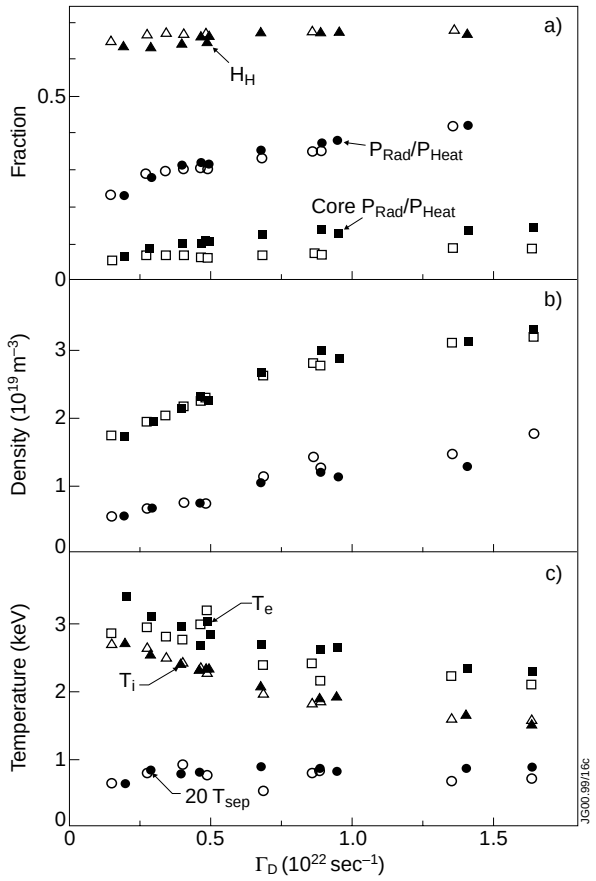

Fig.12.2: Variation of the plasma parameters as a function of the deuteron injection rate. The open symbols represent D_2 gas injection, and the closed symbols represent CD_4 gas injection. In (a) are plotted fractions: $H89_H$ (triangles), total radiated fraction (circles), and radiated fraction from the plasma core (squares). In (b) are plotted densities: the central density (squares), and the separatrix density (reciprocating probe measurement extrapolated to the Last Closed Flux Surface). In (c) are plotted temperatures: the central electron temperature (squares), the central ion temperature (triangles), and 20 times the separatrix temperature (circles) (RCP measurements extrapolated to the LCFS).

the radiation is insignificant. Moreover, the X-point radiation decreased, making the total radiated power about constant.

In the SOL, the temperature profile was unchanged by the methane puffing (Fig.12.3). Also, the electron density < 1 cm from to the LCFS (mid-plane projected distance), was unchanged (Fig.12.3), but outside this distance (about 2-5 cm from the LCFS) the density was higher by as much as a factor 3 for the highest methane injection rates. The density perturbation was proportional to the magnitude of the methane injection, and was clearly related to it. However, the geometry is complicated and we do not yet quantitatively understand the density increase. Wall temperature carbon atoms (0.05 eV) incident normally to the SOL, would be ionised in that region of the SOL (2-5 cm from the LCFS). Alternatively, higher energy carbon might arrive at the RCP location tangentially and cause the density increase through ionisation at that location. Interpretation of the density increase requires three dimensional modelling, and accurate knowledge of the flows between the injection region and the RCP.

The carbon (Fig.12.1(c)) approached its new steady-state value exponentially after the methane injection begins (16-17 sec), and falls exponentially at the end of the injection (19-20 sec). The rate of increase of the carbon in the plasma core, the total carbon content as measured by the charge exchange spectroscopy (CX), and the Z_{eff} as measured by visible bremsstrahlung (VB) all rise in proportion to the methane injection rate (Fig.12.4). The methane injection rate is expressed in fig.12.4 as the associated deuterium injection rate. This allows us to plot the deuterium injection plasmas on the same graph, and to relate to deuterium plasmas at the same density as for Fig.12.2. The carbon content due to the methane puffing is the difference between the solid and open symbols. At a high methane injection rate, we also performed a scan in deuterium injection rate (the X symbols). For that scan the carbon rate of rise was unchanged, the CX total carbon content fell about 10%, and VB Z_{eff} dropped from 2.2 to 1.8.

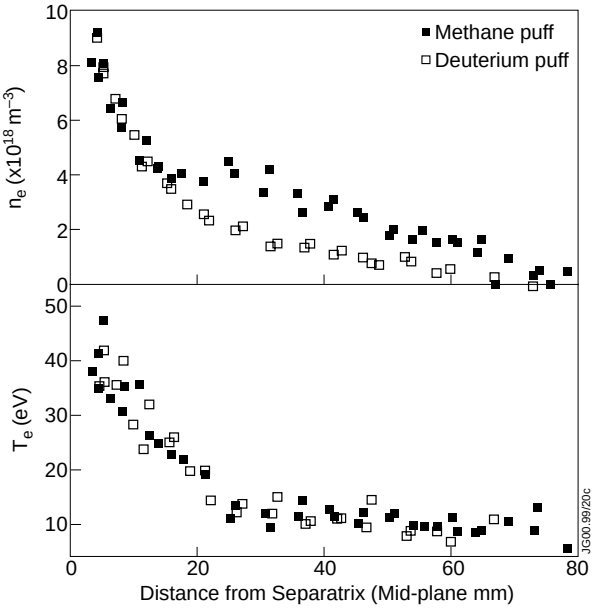

Fig.12.3: The temperature and density measured in the SOL by the RCP with the distance being projected back to the horizontal mid-plane. The solid points are with the methane puff, and the open points are at the same core density but with deuterium puff.

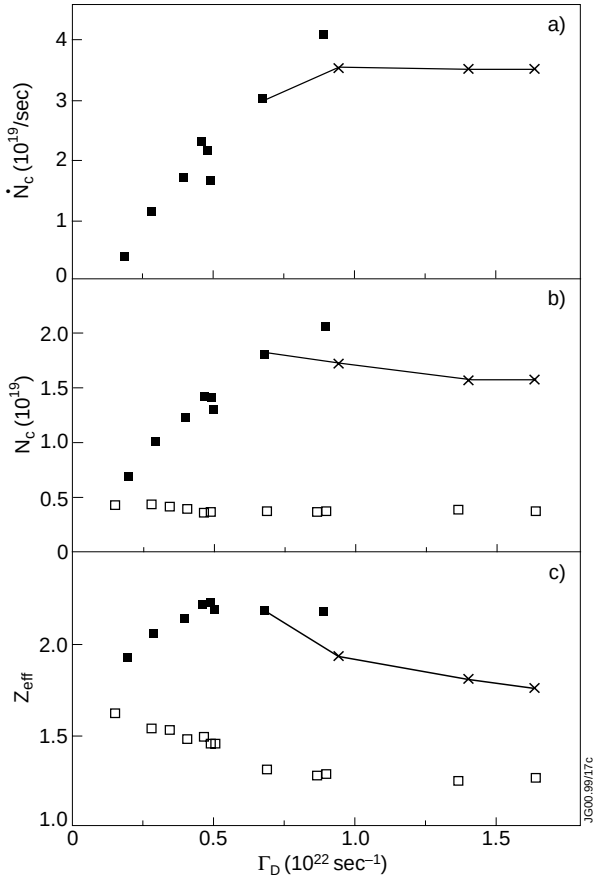

Fig.12.4: The change of the signals indicating the core carbon content as a function of the injection rate of deuterium. The solid points had only methane injection, the open points had only deuterium injection, and the X symbols had combined methane and deuterium injection. The line connects those combined injection data having the same methane injection rate. In (a) are plotted the initial rate of rise of the total number of carbon particles (CX) in the core. In (b) are plotted the total number of carbon particles (CX) after steady state was reached. In (c) are plotted the VB Z_{eff} values after steady-state was reached.

The fraction, η, of carbon that reaches the LCFS, provides a boundary condition for the subsequent evolution of the core carbon density:

$$\eta = \Delta N_C/(\Gamma_C \tau_p^*) \quad (1).$$

where: ΔN_C is the increase of total core carbon content (associated with the methane puff), Γ_C is the carbon influx rate, and τ_p^* is the effective carbon particle confinement time. τ_p^* was measured for these plasmas from the core carbon content time evolution. For these L-Mode JET plasmas, τ_p^* was within 20% of the gross energy replacement time, τ_E.

The random errors on the CX measurements are sufficiently small that the initial rate of rise of N_C can be determined. For times short compared to τ_p^*, η is described by equation (2), [12.2]. This presumes that the methane flows quickly out of the valve to the SOL:

$$\eta = dN_C/dt \,/\, \Gamma_C \qquad (2).$$

The carbon screening values from equation (2) were the same as those from equation (1) so long as the CX was used to measure N_C (Fig.12.5). Apart from the differences due to the CX and VB discrepant values of the carbon content of the core, both methods of determining the screening yield were independent of the methane injection rate, although the VB deduced screening decreased with density (Fig.12.5).

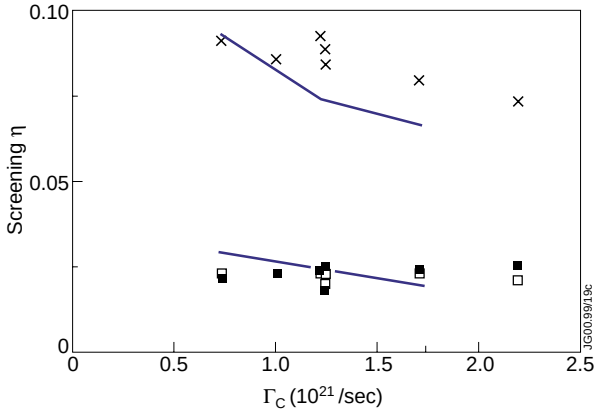

Fig.12.5: The carbon screening (probability of an injected carbon atom crossing the LCFS) as a function of the carbon injection rate from the methane puffing. The X symbols used the VB to measure the core carbon content, the solid points used the CX to measure the core carbon content, and the open points deduced the screening from the initial rate of rise of the CX carbon content. The lines indicate DIVIMP modelling of the screening.

12.3 Summary

Our ultimate goal is to understand the magnitude and the source of the intrinsic impurities. Methane puffing experiments contribute to that understanding by benchmarking the effects of the SOL on the carbon transport in to the LCFS and along the field lines to the divertor. DIVIMP [12.9] modelling of the SOL was able to reproduce the experimental screening results as deduced by either the VB or CX measurements. A reasonable fit to the CX measurements was obtained with incident carbon energies of 0.05 eV, carbon SOL diffusion coefficient of 0.15 m^2/sec (about equal to the SOL χ_i), and an imposed SOL Mach number of 0.5 (velocity of 20 km/sec). The VB screening results were well fitted by SOL properties with higher carbon energies (0.1 - 0.5 eV), higher carbon diffusion coefficient (1 - 2 χ_i), and lower Mach numbers (M = 0 - 0.3).

12.4 Shot List

The shot list for shots used in this Report, and other useful ones for Methane Screening investigations, is shown in Table 1.

Methane Screening Studies

Useful shot list **Showing Puff time, gas and location**

shot	time	location	regime	config	gas
38748	61.5	divertor	H	Mark I	CD4
38757	62		H	Mark I	D2
38758	62	vessel	H	Mark I	CD4
39994	62	divertor	H	Mark II	CD4
39995	61	divertor	H	Mark II	CD4
40000	62		H	Mark II	D2
40001	60		H	Mark II	D2
43731	62	divertor	H	Mark II	CD4
43732	61.5	divertor	L	Mark II	CD4
43733	61.4	divertor	III Elms	Mark II	CD4
43734	61.4	divertor	Elm free	Mark II	CD4
43751	61.6	divertor	III Elms	Mark II	CD4
43754	61.4	divertor	L	Mark II	CD4
43755	61.4	divertor	H	Mark II	CD4
43756	61	divertor	H	Mark II	CD4
43758	61.3	divertor	L	Mark II	CD4
46593	57		dithering	GB	D2
46593	60.8		L	GB	D2
46600	57		dithering	GB	D2
46600	61		L	GB	D2
47516	58.8		H	GB	D2
47517	58	vessel	compound	GB	CD4
47519	58.5	divertor	H	GB	CD4
47520	58.5	divertor	H	GB	CD4
47521	58.6	divertor	H	GB	CD4
47522	58	vessel	III Elms	GB	CD4
47523	58	divertor	H	GB	CD4
47524	58.6	divertor	compound	GB	CD4
47527	57	vessel	L	GB	CD4

shot	time	location	regime	config	gas
47527	61.5	vessel	L	GB	CD4
47528	57.5	divertor	L	GB	CD4
47528	61	divertor	L	GB	CD4
47529	57		L	GB	D2
47529	61.5		L	GB	D2
47530	58.3		H	GB	D2
47531	57.5		L	GB	D2
47531	63	vessel	H	GB	CD4
47779	57.5	divertor	L	GB	CD4
47779	61.5	divertor	L	GB	CD4
47782	48		L	limiter	D2
47782	57.5		L	GB	D2
47782	61.5		L	GB	D2
47810	48	vessel	L	limiter	CD4
47810	57.5	vessel	L	GB	CD4
47810	61.5	vessel	L	GB	CD4
47811	48		L	limiter	D2
47811	57.5		dithering	GB	D2
47811	61		L	GB	D2
47812	59.5	vessel	L	GB	CD4
47812	62.5	vessel	dithering	Septum	CD4
47813	59		L	GB	D2
47813	63		dithering	Septum	D2
47814	48		L	limiter	D2
47814	57.5	divertor	L	GB	CD4
47814	61.5	divertor	L	GB	CD4
47828	59		L	GB	D2
47828	63		dithering	Septum	D2
48330	61		L	GB	H2

Methane Screening Studies

Useful shot list **Showing Puff time, gas and location**

shot	time	location	regime	config	gas
48330	63		L	GB	H2
48331	61		L	GB	H2
48352	49	vessel	L	limiter	C2H6
48365	49	vessel	L	limiter	CH4
48365	57	vessel	L	GB	CH4
48365	62	vessel	L	GB	CH4
48376	49	divertor	L	limiter	CH4
48377	49	divertor	L	limiter	CH4
48378	49	divertor	L	limiter	CH4
48378	57.5	divertor	L	GB	CH4
48378	62	divertor	L	GB	CH4
48379	49	divertor	L	limiter	CH4
48379	57.5	divertor	L	GB	CH4
48379	62	divertor	L	GB	CH4
48380	49	vessel	L	limiter	C2H8
48380	57.5	vessel	L	limiter	C2H8
48380	62	vessel	L	GB	C2H8
48381	49	vessel	L	limiter	CH4
48381	57.5	vessel	L	GB	CH4
48381	62	vessel	L	GB	CH4
49697	57.8	vessel	L	GB	CD4
49697	62		L	GB	D2
49698	58	vessel	L	GB	CD4
49698	62		L	GB	D2
49699	58	vessel	L	GB	CD4
49699	62		L	GB	D2
49700	58		L	GB	D2
49700	62		L	GB	D2
49701	58	vessel	L	GB	CD4

shot	time	location	regime	config	gas
49701	62		L	GB	D2
49702	58	vessel	L	GB	CD4
49702	62		L	GB	D2
49703	58	vessel	L	GB	CD4
49703	62		L	GB	D2
49704	58.2	vessel	L	GB	CD4
49704	62		L	GB	D2
49705	58	vessel	L	GB	CD4
49705	62		L	GB	D2
49706	58	vessel	L	GB	CD4
49706	61.8		L	GB	D2
49707	58	vessel	L	GB	CD4
49707	62		L	GB	D2
49708	57.7	vessel	L	GB	CD4
49708	62.1		L	GB	D2
49709	58.2	vessel	L	GB	CD4
49709	62		L	GB	D2
49733	58.5	vessel	dithering	Septum	CD4
49733	62		III Elms	Septum	D2
49734	58.5	vessel	dithering	Septum	CD4
49734	62		III Elms	Septum	D2
49735	58.5	vessel	L	Septum	CD4
49735	62		III Elms	Septum	D2
49736	58.5	vessel	L	Septum	CD4
49736	62		III Elms	Septum	D2
49737	58.2	vessel	L	Septum	CD4

References:

[12.1] G.F. Matthews, P.C. Stangeby, J.D. Elder, *et al*, J. Nucl. Mat. **196-198**, 374 (1992)

[12.2] G.M.McCracken,U. Samm, P.C. Stangeby, *et al*, Nucl. Fus. **33**, 1409 (1993)

[12.3] S.Sergoku and H.Ohtsuka, J.Nucl.Mater. **93-94**, 75 (1980)

[12.4] R.S.Granetz, G.M. McCracken, F. Bombarda, *et al*, J. Nucl. Mat. **241-243**, 788 (1997)

[12.5] C.S.Pitcher, G.M. McCracken, P.C. Stangeby, *et al*, J. Nucl. Mat. **145-147**, 539 (1987)

[12.6] A. Kallenbach, R. Neu, W. Poschenrieder, *et al*, Nucl. Fus. **34**, 1557 (1994)

[12.7] G.M.McCracken, U. Samm, B. Bertschinger, *et al*, J.Nucl.Mat. **196-198**, 199 (1992)

[12.8] M.Stamp, D. Elder, H.Y. Guo, *et al*, J.Nucl.Mat. **266-269**, 685 (1999)

[12.9] G.M.McCracken, B. Lipschultz, B. LaBombard, *et al*, Phys. Pl. **4**, 1681 (1997)

[12.10] P.C.Stangeby and J.D.Elder, J.Nucl.Mat. **196-198**, 258 (1992)

[12.11] MG von Hellermann, *et al*, in Diagnostics for Experimental Thermonuclear Fusion Reactors (PE Stott, G Gorini, E Sindoni, Eds) Plenum Press, New York and London (1996) p.321

[12.12] P.D.Morgan, *et al*, (REF).

[12.13] S.K.Erents, J.A. Tagle, G.M. McCracken, *et al*, J. Nucl. Mater. **162-164**, 22 (1989)

[12.14] P.C.Stangeby, J.D.Elder, W. Fundamenski, *et al*, J. Nucl. Mater. **241-243**, 358 (1997)

[12.15] W.Fundamenski, P.C. Stangeby, J.D.Elder, *et al*, J. Nucl. Mater. **266-269**, (1999)

[12.16] K. Erents, *et al*, Controlled Fusion and Plasma Physics, To be published

13. SURFACE ANALYSIS OF JET DIVERTOR TILES

J P Coad[1], N Bekris[2], R-D Penzhorn[2], D E Hole[3].

JET Joint Undertaking, Abingdon, Oxfordshire, OX14 3EA, UK.

[1] EURATOM/UKAEA Fusion Association, Culham Science Centre, Abingdon, Oxfordshire, OX14 3DB, UK.

[2] Forschungszentrum Karlsruhe, D-76021 Karlsruhe, Germany.

[3] School of Engineering, University of Sussex, Brighton, East Sussex, BN1 9QH, UK.

13.1 Overview

Deposition in JET when operating in a divertor configuration has always been asymmetric, in that heavy deposition is found in the SOL at the inner divertor, but very little deposition at the outer divertor. The phenomenon was first reported for the 1990-1991 campaign when JET was operated with an X-point formed within the vessel and the wall protection tiles at the top of the vessel were used as targets [13.1]. Since the construction of a divertor within the vessel in 1992-1994, the asymmetry has been reported for both the Mk I (using both carbon and beryllium target tiles) [13.2,13.3] and the Mk IIA divertor campaigns [13.4,13.5].

The principal result of divertor modelling is that most eroded material is re-deposited locally, so that there is net erosion close to the strike-point, and net deposition deeper into the scrape-off layer (SOL) [13.6]. Since the greater power flux (and hence the greater erosion) occurs at the outer divertor target, the observed deposition is not easily reconciled with predictions. Furthermore, heavy deposition of carbon leading to flaking was observed on the water-cooled louvres, and the majority of the tritium retained in JET following DTE1 is believed to be in such flakes that have spalled from these louvres and fallen beneath the divertor structure.

Attempts to correctly model the deposition in JET require additional physical processes such as drifts in the SOL, and different parameters to cover interaction at the inner divertor. Some new ideas on processes taking place at the inner divertor are necessary to explain the deposition, and this paper presents some fresh experimental evidence for the processes involved. It is imperative that the mechanisms resulting in this very large deposition rate is understood before one may rely on predictions of deposition in future tokamak devices.

13.2 Results

Tritium retention following DTE1

In 1997 JET operated for several months with deuterium/tritium fuelling, the percentage of tritium entering the vessel varying from 1 to 100%; the campaign was called the first Deuterium Tritium Experiment (“DTE1”). Over the campaign a total of 35g tritium entered the vessel. Despite a thorough clean-up campaign lasting three months, at the start of the subsequent shutdown 6g tritium still remained in the vessel [13.7]. For the shutdown the vessel was vented to, and continuously purged with, air. During the shutdown all the divertor tiles were removed and stored in ventilated containers, to make way for the installation of the new Mk II Gas Box (GB)

divertor. All flakes and loosely adherent material that remained in the vicinity of the inner louvres was collected with a brush and vacuum cleaner, however it is known that a large number of flakes have fallen beneath the divertor structure and could not be retrieved. A selection of tiles was also removed from around the vessel walls. All the air passing through the vessel, and the air ventilating the tile storage containers, was passed through the Exhaust De-tritiation System (EDS) [13.8]. The amount of tritium recovered from this airflow was 2g [13.7]. It is important for planning and assessing the radiological implications of future work in JET to know the amount and whereabouts of the tritium remaining in the machine. To this end, a detailed T analysis programme has been carried out on the material removed from the vessel.

The total T content of the flakes removed from JET following DTE1 was determined by calorimetry to be 520 mg, and the weight of the flakes was ~154g [13.9]. The total T content of the divertor tiles was estimated by sampling from a poloidal set of divertor tiles. Ten tiles form the set, and were numbered 1 to10 as shown in Fig.13.1(a).

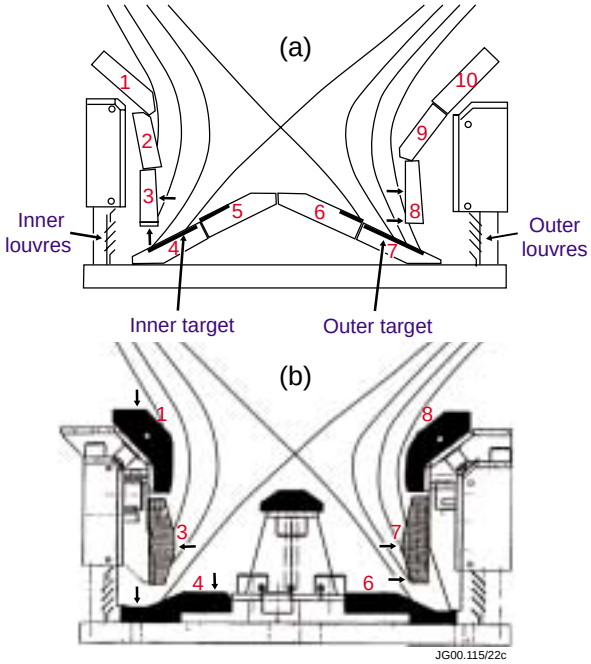

Fig.13.1: Cross-sections of (a) the Mk IIA and (b) the Mk IIGB divertors. The positions of analysis points referred to in the text are indicated by arrows

The T content of the wall tiles was estimated from the analysis of six inner wall limiter tiles and three outer bumper limiters. In each case for each tile a number of cylindrical samples were cut using a hollow drill, and the T contents of the outer 1 mm thickness of the samples was determined by total combustion. The samples were cut from previously agreed locations, to provide an average overall estimate for the T content of the tile. Additional samples were cut from the edge of tile 3 adjacent to the pumping duct between tiles 3 and 4, since a 40 μm thick film with high hydrogen isotope concentration was found here on samples removed prior to DTE1. Two samples could be cut from the width of the tile, one from the half nearer the front of the tile, and one from the rear half. A T content of 3.3 GBqcm^{-2} was found over the rear half of this edge (10 to 100 times the usual T level from plasma-facing surfaces), but this would be equivalent to only ~ 12 μm of flake-like material; the T level from the front half was similar to levels at the front surface. In total well over 100 T determinations have been made.

From the average T content and the number of tiles in the torus at that poloidal position, the total amount of T in the torus can be plotted, as shown in Fig.13.2.

The 520 mg T at the louvres represents the T contained in the collected flakes. The total T near the surface of the divertor tiles (which have been removed from the vessel) is only 78 mg

(29.4 TBq), and the T content of the various wall tiles (which, apart from the sample tiles, remain in the vessel) is 71 mg (27.3 TBq). Profiles for T through the bulk of a number of tiles have also been made and are reported elsewhere [13.10], but show that there is not a large additional contribution to the inventory.

A further 1.25g T has been recovered from the torus by the AGHS since the post-DTE1 shutdown from venting/purging during a subsequent shutdown, and outgassing while baking the machine [13.9]. This, combined with the removal of 0.52g of T with the flakes and the (estimated) removal of 0.1g tritium with the divertor tiles, has reduced the quantity of T assumed to remain in the torus to 2.1g. The analyses of wall tiles suggest that they do not contribute more than about 0.1g to this figure. The remaining 2g is assumed to be retained in the flakes that have spalled from the louvres and fallen beneath the divertor structure. Since 154g of flakes removed after DTE1 contained 0.52g tritium, it implies 2g of T requires ~600g of flakes. However, the reduction by 1.25g of the in-vessel inventory since the analysed flakes were removed from the torus must also have come predominantly from flakes remaining in the machine, so their current T content must be proportionately reduced, and a total of almost 1kg is required. It is planned to attempt to recover as many flakes as possible from underneath one section of the divertor during the next shutdown, so that the total quantity remaining in the torus may be estimated, and the present activity measured.

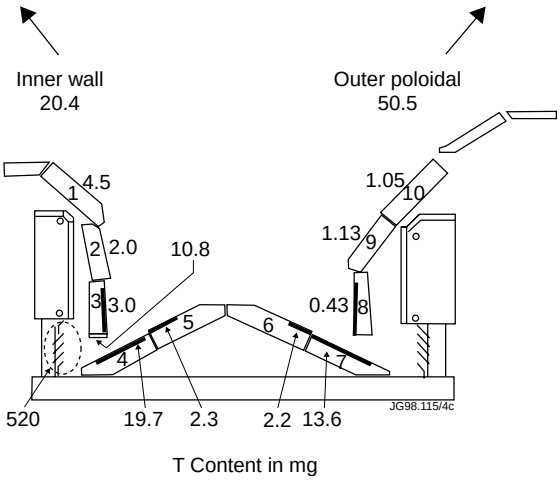

Fig.13.2: The amounts of tritium found at each tile location, integrated toroidally around the vessel (expressed in mg). The amount of tritium in the flakes collected from the region of the louvres is also included.

Analysis of Mk IIGB tiles and comparison with Mk IIA

A cross-section of the Mk IIGB divertor was included in Fig.13.1, together with a set of field lines for a typical plasma. A poloidal set of six divertor tiles, together with a septum tile, were removed in June 1999 after an eight-month campaign of approximately 2500 plasma discharges. The tiles have been analysed using the two Ion Beam Analysis (IBA) techniques, Nuclear Reaction Analysis (NRA) and Rutherford Backscattering (RBS). The overall appearance of the tiles indicated heavy deposition on the inner divertor wall tiles 1 and 3 and negligible deposition on the outer divertor wall tiles 7 and 8, as for Mk IIA. There was evidence of strong plasma interaction with the section of tile 4 exposed to the plasma, with deposited films evident in the sections of this tile shadowed by both by tile 3 and by the septum. Tile 6 showed a similar strong plasma interaction zone, but no evidence of films in the shadowed areas. No sampling from the louvres was possible at this time. The strike points for operation with Mk IIGB are normally close to the

corners of the divertor. The campaign was dominated by experiments aimed at developing optimised shear discharges, for which the strike points were normally on the horizontal tiles 4 and 6. For the (smaller) divertor physics programme, the (vertical) tiles 3 and 7 acted as targets.

A selection of results of IBA analyses from the Mk IIGB divertor tiles is given in Table 13.1. For comparison, IBA data from similar points on tiles from the Mk IIA divertor are included. The sensitivity of NRA depends on the depth distribution of each element, so the quantification may be in error by up to a factor of two. The Mk IIA tiles were removed prior to the DTE1 campaign after 2000 discharges, and have been analysed previously [13.5]. A feature of the IBA results is that the films deposited on the surface of the divertor wall tiles 1 and 3 have a very high beryllium/carbon ratio. The NRA data indicates the presence of a film over tile 3 up to 7 μm in thickness, with the greatest D concentration at the surface. Analysis of the top (horizontal) surface of tile1 from Mk IIGB reveals a slightly lower Be/C ratio than on tile 3, and the D feature suggests a film of about 5 μm with a more uniform D concentration. It is significant that heavy deposition occurs over all the inner divertor wall, to points deep into the SOL, and including the region explored by laser ablation [13.11]. It can be seen from Table 13.1 that similar films existed at the inner divertor wall in the MkIIA configuration.

Table 13.1: Surface analyses (of outermost ~1 μm) at selected points on JET divertor tiles by Nuclear Reaction Analysis (NRA) and Rutherford Backscattering (RBS)

Divertor	Tile/Position	Be/C (NRA)	Be/C (RBS)	D/C+Be (NRA)	D/C+Be (RBS)	Ni/C (RBS)
Mk IIA	3 front face	1.5		~0.15*		
Mk IIA	3 bottom edge	<0.003		0.77	0.81	
Mk IIA	8 centre front	<0.003		0.017		
Mk IIA	8 lower front	~0.01		0.02		
Mk IIGB	1 top edge	0.31	0.34	0.1	0.13	0.027
Mk IIGB	3 front face	1.0	1.03	~0.2*	0.07	0.06
Mk IIGB	4 private region	<0.007		0.31	0.25	
Mk IIGB	4 end under tile 3	<0.003		0.8	0.65	
Mk IIGB	7 centre front	~0.02	~0.027	0.05	~0.056	~0.0056
Mk IIGB	7 lower front	~0.04		~0.2*		

* approximate value for outermost micron, when D concentration varies through surface region

Data from the Mk IIGB tile 4 is also given in Table 13.1, from the regions shadowed by tile 3 and by the septum. In contrast to analyses of tiles 1 and 3, there is negligible Be on these areas of tile 4. There is also a much greater ratio of D to C. The film composition from the region shadowed by tile 3 is similar to that from the end of tile 3 in the Mk IIA divertor (which was indistinguishable from the composition of flakes from the inner louvres). The D concentration in the shadow of the septum is somewhat lower.

The difference in analyses is shown graphically by the RBS spectra in Fig.13.3.

In the RBS reported here a 2.5 MeV ion beam was incident on the surface, and incident particles were elastically scattered by atoms in the surface region. The energy of the particles reaching the detector is determined by conservation of energy and momentum, so depends on the atomic weight of the scattering atom. Particles scattered within the surface lose energy by inelastic processes as they travel from and back to the surface. Thus the quantity of each mass number and its depth distribution in the outermost ~10 μm can be determined; for greatest sensitivity to light elements an incident proton beam has been used in this work. For uniform concentrations through the analysed depth, each element gives rise to a step in the spectrum, for example Fig.13.3(a) shows the RBS spectrum from the region of tile 4 shadowed by tile 3. Steps due to C, D and a small amount of O are seen, but no Be can be resolved. A D/C ratio of 0.65 gives the best-fit simulation. In contrast Fig.13.3(b) is a spectra from the front face of tile 3, and in this case the C edge is largely replaced by a Be peak. To obtain the best fit a Be peak concentration of 35% in the outermost few microns is required, with C, O, D and Ni at 34, 24, 5 and 2%, respectively. A small peak appears in this and other spectra from the inconel constituents Ni, Cr and Fe (referred to here as "Ni"), and it is noticeable that the peak always has the same spatial distribution as the Be.

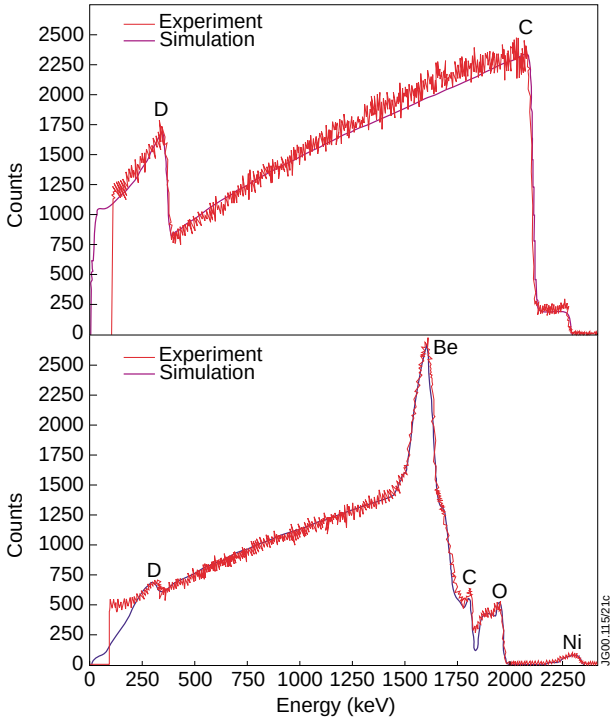

Fig.13.3: RBS spectra from (a) tile 4 in the region shadowed by tile 3 and (b) from the front face of tile 3 (both Mk IIGB divertor).

Analyses of the outer divertor tiles confirm that the surfaces are much cleaner than those from the inner tiles. In Table 13.1 are values for the Mk IIGB tile 7, and for comparison for the Mk IIA tile 8 (which was in the equivalent position on the outer divertor wall, as shown in Fig.13.1). Just trace amounts of Be are present, and much lower D concentrations than elsewhere, except for the lower front of Mk IIGB tile 7.

Discussion

If drift in the SOL is included in the DIVIMP modelling, the asymmetry in the JET deposition pattern can be reproduced. To get sufficient deposition in the inner divertor channel it is necessary to increase plasma interaction in the main chamber, but this is in accord with erosion/deposition measurements on wall components, and the observation that the first wall (rather than the divertor) is the major source of plasma impurities. However, to convert the impurity flux to the inner

strike zone into the massive deposition at the JET louvres requires very different processes at the target to that normally assumed in divertor modelling. Recent laboratory experiments [13.12], and spectroscopic data [13.13] suggest that the recycling parameters used previously are inappropriate.

The results above provide a number of new pointers to the processes involved. Firstly, the T analyses for Mk IIA confirm that the vast majority of the T retention is, indeed, in flakes that form on the water-cooled louvres, and that all the plasma-facing surfaces contain much lower T concentrations (in line with the previous D retention data [13.5]). The films formed on the edge of the Mk IIA tile 3 (adjacent to the divertor corner) prior to DTE1 were identical to those on the louvres. Following DTE1 even thicker films would be expected to have accumulated, but the T retention data do not agree. The T present on the half of the edge farthest from the front face of the tile would correspond to a relatively thin (~12 μm) film. The half of the edge nearer the front face was blueish in colour, which may indicate a thin (sub-micron) film. A number of explanations are possible. It may be that during DTE1 tile 3 reached higher temperatures than previously, which greatly reduced the probability of incident particles sticking at the surface. The experiments of von Keudell et al [13.12] suggest that sticking coefficient is a critical function of temperature, and this would fit in with the gradation from front to back across the edge. Alternatively, although the 40 μm films formed prior to DTE1 were still adherent to the tile whereas they had started to spall from the louvres, it may be that as the film thickness increased sufficient internal stresses built up so that it spalled off the tile. Analyses are to be carried out on more of these Mk IIA tiles.

It was estimated above that nearly 1 kg of flakes might remain in the JET vessel. Figures 13.1 and 13.2 show, correctly, that the louvres are angled such that loose material on the surface would under gravity fall **away** from the divertor centre. However, the figures also include the (occasional) louvre support pillars: around most of the torus flakes spalling off the louvres would be able to fall directly down through the divertor support structure towards the bottom of the vessel. It is therefore possible that the material collected in the shutdown following DTE1 (from between the inner louvres and tile 4, plus material still loosely adhering to the louvre surfaces) amounted to only about 10% of the total material condensed at the louvres.

There is a build-up of Be on the inner side-wall of both divertors, and the formation of thick carbonaceous films with no Be content elsewhere (on tile 4 in Mk IIGB, and mostly on the louvres in Mk IIA). Impurities are transported to the inner divertor wall tiles along the inner SOL, having been eroded from the walls of the main chamber. No measurements are made in JET of the impurity composition in the SOL. Likely sources of impurities in the inner SOL are the surfaces of the inner wall limiter tiles closest to the plasma, which from the visible “footprint” are erosion zones. The Be/C ratio in these areas of the tiles sampled is typically close to 10%. Furthermore, the relative amounts of C, Be and Ni in the plasma are (relative to the average electron density) typically 1-10%, 0.2-0.3% and 0.001-0.008%, respectively. (Be levels may be higher immediately following a Be evaporation, but decrease within a few pulses. There are

often short bursts of much greater Ni influx during a pulse.) Although there may be no direct correlation between the concentrations of impurities transported along the SOL and those entering the plasma, let us assume that the relative values are similar. On that basis there should be at least ten times more C than Be deposition at the divertor wall. It is possible for the C to be re-eroded chemically as C_xD_y by the D ion flux, whereas the Be and Ni will remain on the surface, since ion energies are insufficient for physical sputtering. The amount of carbon required to form the deposits at the louvres is ~4 % of the ion flux [13.3], so this is consistent with both the above approximation and with recently observed yields [13.13]. These hydrocarbon species then have a probability of travelling to the shadowed regions at the inner divertor, where their probability of sticking may be temperature dependent (as suggested in [13.12]), and the resultant deposits will be based purely on carbon (as described above). The amount of the carbon re-deposition would thus, on the basis of the above approximation, be ten times that remaining on the wall, i.e. if the deposits at the inner divertor wall average 5 μm in thickness, then about 50 μm may be re-deposited over a similar area. This is certainly of the correct order of magnitude to explain the deposition found in Mk IIA. The total deposition in Mk IIGB cannot yet be quantified, but gas balance measurements show average D retention over many months as about 9% [13.14], which is comparable to (or a little less than) retention of D+T in the Mk IIA divertor (~15% [13.7]).

Tiles in the outer Mk IIGB divertor channel appeared much cleaner than in the inner channel, as has always been the case in JET. However, there was an extra D surface peak on the lower part of tile 7, and there was some discoloration of surfaces around the outer louvres, which was not visible in the Mk IIA campaigns. The D may be the result of operation towards the end of the campaign with the strike-point on the end of tile 7. Alternatively, for a week just before the end of the MkIIGB campaign prior to the shutdown in which the tiles were removed, JET operated with reverse ∇B. Measurements with the RCP showed that at this time the SOL flow was also reversed (though its magnitude was much less), and the power was more equally balanced on the divertor legs. For the ~100 pulses in this period the deposition in the two divertor legs may also be more equitable.

13.3 Summary and future directions

Analyses of JET Mk IIA tiles following DTE1 show that only ~0.1 g tritium is contained in the divertor tiles that have been removed from the machine. This implies that about 1 kg of flakes are still in the vessel and have fallen below the divertor structure, containing about 2 g tritium.

There are deposits on the tiles of the JET inner divertor wall that are several microns thick, and rich in Be and other metallic impurities. This implies that the great majority of the C incident at these areas has been chemically sputtered, and transported with high efficiency to shadowed areas.

Similar results (presented in Table 13.1) were obtained from MkIIA tiles removed before the start of the DTE1 campaign, and from MkIIGB tiles. Recently over 100 cylindrical samples

have been analysed from divertor and wall tiles that were present during DTE1 (including a poloidal set of MkIIA divertor tiles). The samples were cut from adjacent sites to the samples analysed for tritium and used to compile the data in fig.13.2. The analyses are still being evaluated, but it is clear that samples from the inner wall of the divertor continue to show films with high Be:C ratio. There is also evidence that these films are now thicker than on the tiles removed prior to DTE1, as might be expected from the longer campaign period to which the tiles were exposed.

It is clear that one effect of the different Mk IIGB divertor geometry is to produce deposition in the shadow of the septum. There is also deposition in the inner corner in the channel to the louvres. However, the amount of deposition at the louvres, and the overall amount of deposition in the divertor region has not been established. Gas balance measurements suggest there may be less overall retention (implying less deposition) in Mk IIGB than in Mk IIA. It is important to establish whether the geometry is affecting the overall deposition, by procuring further tiles, parts of the septum support, and deposit from the louvres, for analysis. Reversing the ∇B drift is expected to have a dramatic effect on the pattern of deposition in JET, and it is planned to make an experiment at the end of 2000, which would provide further samples to remove for analysis in the following shutdown.

References

[13.1] J P Coad and B Farmery, *Vacuum*, **45** 435 (1994)

[13.2] J P Coad, M Rubel and C H Wu, *J Nucl Mater*, **241-243** 408 (1997)

[13.3] M Mayer et al, *Physica Scripta*, **T81** (1999) 13

[13.4] A T Peacock et al, *J Nucl Mater*, **266-269** 423 (1999)

[13.5] J P Coad et al, *Physica Scripta*, **T81** (1999) 7

[13.6] J Brooks, *J Nucl Mater*, **170** 164 (1990)

[13.7] P L Andrew et al, *Fus. Eng. Design*, **47** (1999) 233

[13.8] R Lasser et al, ibid, p173

[13.9] P D Brennan et al, 18th Symposium on Fusion Engineering (SOFE), Albuquerque, USA, October 1999

[13.10] R-D Penzhorn et al, to be presented at PSI-14, Rosenheim, May 2000

[13.11] D D R Summers et al, to be presented at PSI-14, Rosenheim, May 2000

[13.12] A von Keudell et al, *Nuclear Fusion*, **39** (1999) 1451

[13.13] M F Stamp et al, to be presented at PSI-14, Rosenheim, May 2000

[13.14] M Mayer et al, to be presented at PSI-14, Rosenheim, May 2000

14. IN-SITU MEASUREMENT OF HYDROGEN RETENTION IN JET CARBON TILES

D.D.R.Summers[1], M.N.A.Beurskens[1], J.P.Coad[1], G.Counsell[1], W.Fundamenski[1], G.F.Matthews[1], M.F.Stamp[1].

JET Joint Undertaking, Abingdon, Oxfordshire, OX14 3EA, UK.

[1] EURATOM/UKAEA Fusion Association, Culham Science Centre, Abingdon, Oxfordshire, OX14 3DB, UK.

14.1 Overview

A limitation in large fusion devices is the amount of hydrogen isotopes, particularly tritium, retained in the plasma-facing walls of the vessel. Present methods for assessing this hydrogen inventory require the detailed analysis of components after removal from the device. Such methods are rather inconvenient and because of the need to vent the device to atmosphere in order to remove samples, investigation of techniques to reduce this inventory is severely hampered. Such investigations would require a more prompt method of measuring the hydrogen content of plasma facing components, ideally on a shot-by-shot basis.

This work demonstrates a means to measure the hydrogen content of a Jet carbon tile during plasma discharges. A more complete description was presented as poster P2.27 at 14th PSI conference Rosenheim, 21-26 May 2000.

A brief laser pulse is used to ablate a small quantity of material from a carbon-faced section of the vessel wall. This material enters the plasma edge region where it is excited and ionised. Fig.14.1. Spectral emission from this cloud of excited material is collected at 250kHz and compared with the particle flux incident onto the same area of wall, as measured by a Langmuir probe. Fig.14.2. For this study, a train of 4 laser pulses (~300psec, ~2J) was used at 1 second intervals.

Fig.14.1: Camera view of ablation.

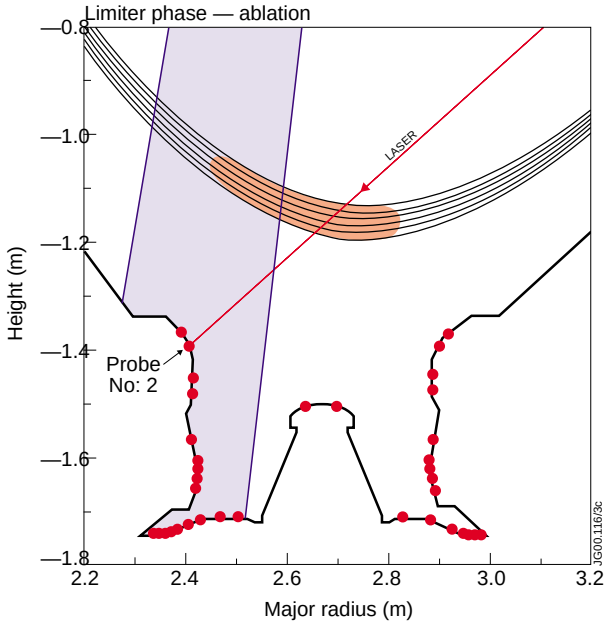

Fig.14.2: Experimental arrangement

A sequence of JET discharges was studied in which a divertor phase was followed by a limiter phase. The vertical position of the strike points during the divertor phase was altered for successive discharges so as to vary the flux at the point of measurement. Data were collected during each limiter phase, allowing the effects of the preceding divertor phase to be examined.

14.2 Results

Both the spectral data shown in Fig.14.3 and the probe data were integrated in order to make the comparison shown in Fig.14.4. In this latter figure, the spectral intensities have been converted to number of hydrogen atoms using values of electron temperature and density data in the boundary region obtained from a reciprocating probe. Although only 10 discharges were examined, it is clear that offset linear relations exist between the observed CIII and the Dalpha signals and the incident flux.

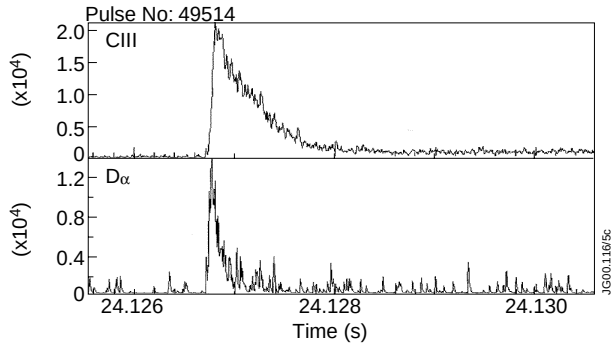

Fig.14.3: Observed CIII and Dalpha signals.

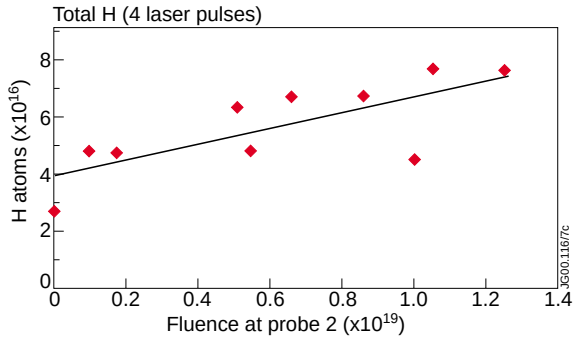

Fig.14.4: Plot of hydrogen influx against particle fluence.

By connecting a spectrometer to the optical system, it was found that the carbon signal included a significant contribution from diatomic lines. This indicates that the laser ablates some carbon in the form of clusters of atoms.

The measured hydrogen/carbon ratio is clearly unreasonable and indicates that mostâV the carbon emission occurs outside the field of view of the optical system. Comparing the raw CIII data with output from the DIVIMP code shows a good reproduction of the signal rise time but the model suggests a decay time 3x longer than the observations in Fig.14.5. This may be another indication of cluster ablation since DIVIMP does not include molecular effects.

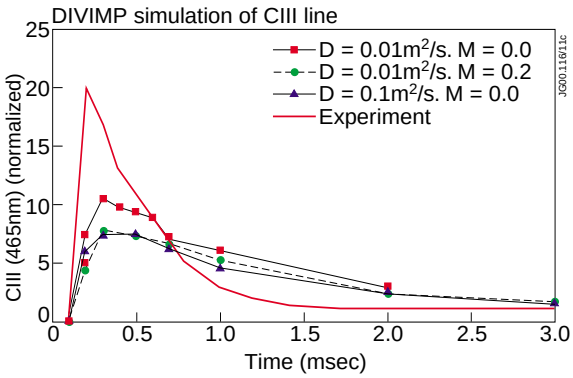

Fig.14.5: Comparison of raw CIII data with DIVIMP calculations.

14.3 Summary and future directions

The results show a linear relation between the observed Dalpha signals and the incident flux, although the database is small. This result is encouraging and it is intended to pursue the investigation in the forthcoming experimental campaign.

14.4. Shot List

The data shown were from JET pulses 49514-49524

15. DIVERTOR ENERGY DISTRIBUTION

G.F.Matthews[1], W.Fundamenski[1], C.Ingesson[2], V.Riccardo[1].

JET Joint Undertaking, Abingdon, Oxfordshire, OX14 3EA, UK.

[1] EURATOM/UKAEA Fusion Association, Culham Science Centre, Abingdon, Oxfordshire, OX14 3DB, UK.

[2] FOM Instituut voor Plasmafysica Rijnhuizen, EURATOM Association, Postbus 1207, NL-3430 BE Nieuwegein, The Netherlands.

15.1 Overview

Despite extensive studies of the power deposition profiles in JET using fast IR cameras and target Langmuir probes, significant uncertainties have remained about the power deposition profiles in ELMy H-modes. Fast IR data appear to be confused by the presence of thermally detached surface layers [15.1]. The ELM power flow determined by fast diamagnetic measurements corresponds to up to 20% of input power and 30% of the power flow to the divertor. Target Langmuir probe analysis can only give reliable profiles in the inter-ELM periods and then only the power flow in the electron channel can be determined.

The tiles in the JET MkIIa and MkIIGB divertors are thermally isolated from the support structure and cool radiatively after a pulse with a time constant of order 1000s. Thermocouples monitor this cooling process and by back extrapolation to the time of the pulse an accurate estimate for the energy deposited on each divertor tile can be obtained. When the total energy input to the plasma minus the radiated energy determined by the bolometers is compared with the energy deduced from the divertor thermocouples, the discrepancy is <20% for the whole of the steady state database and significantly less than this for systematic scans of similar configuration. Comparisons of L and H-mode imply that a majority of the ELM energy goes to the divertor rather than to the main chamber even though strong interactions are often seen on the wide-angle cameras. Examination of the energy distribution between tiles shows that in a wide range of L and H-mode discharges 2-3 times as much total energy goes to the outer strike target than to the inner. This asymmetry is too large to be due simply to toroidal geometry and this is supported by a significant reduction in energy asymmetry in pulses with reversed toroidal field ($\mathbf{B}\times\nabla\mathbf{B}$ away from the divertor). These results imply that neo-classical drifts [15.2] and/or ion orbit losses [15.3] play an important role.

The spatial resolution of the energy measurements is limited by the flux expansion of the divertor configuration and the number of tiles, and there is zero time resolution. However, by shifting the plasma strike points on a pulse to pulse basis, we have mapped out the energy profile for a typical ELMy H-mode. This provides a very accurate determination of the average power profile which cannot, at present, be obtained in any other way. The most striking feature of the power profile is a narrow peak carrying 50% of the total divertor power which is 2-3mm (mid-plane) in width. Consistency of these profiles with Langmuir probe data has been checked using the OSM2/NIMBUS interpretative code which suggests the presence of hot collisionless ions in this layer.

15.2 Results

Energy determination using the thermocouple data

Figure 15.1 shows the location of the tile thermocouples in the MkIIa and MkIIGB divertors. In MkIIa the thermocouples were pressed on the backs of each tile whilst in MkIIGB the thermocouples were inserted to within 1cm of the tile surface and there were more than one thermocouple per tile. It will be shown later that in MkIIGB information can be gained from the temperature evolution within a pulse whilst in the case of MkIIa the thermal time constant is too long to do this.

Despite these differences, the integrated energy arriving at each tile in MkIIa and MkIIGB is calculated in exactly the same way. After each pulse the thermocouple data is typically collected for a period of around 1200s. Figure 15.2 shows typical data from the inner and outer vertical tiles of MkIIGB for an ELMy H-mode pulse heated with 12MW of neutral beams.

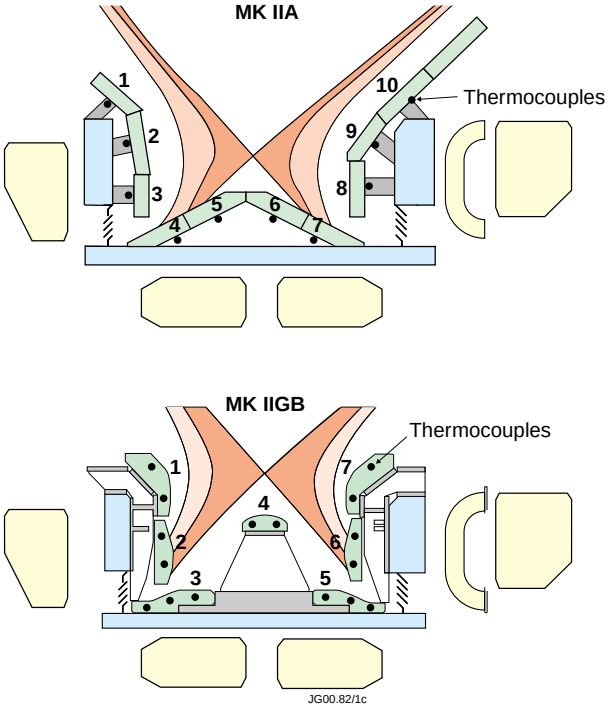

Fig.15.1: Location of the thermocouples in MkIIa and MkIIGB

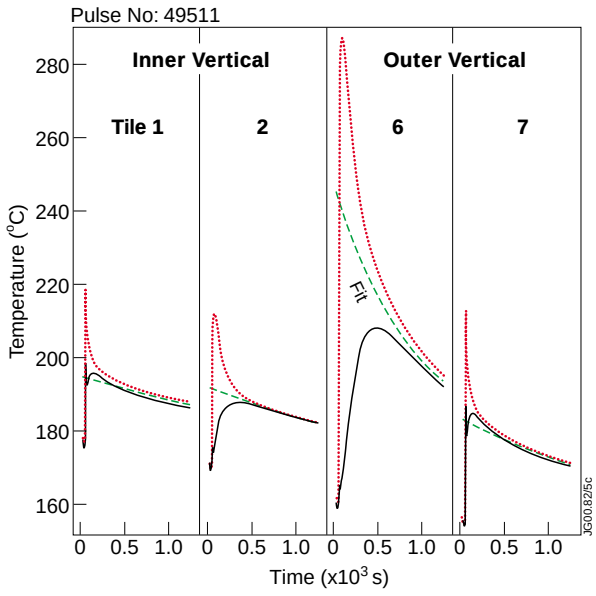

Fig.15.2: Long term thermal response of inner and outer vertical MkIIGB tiles following a typical 12MW ELMy H-mode pulse. A radiation cooling curve is fitted after 500s and extrapolated back to the end of the pulse.

There are two thermocouples in each tile and during the pulse the thermocouple nearest to the strike point shows the greatest temperature rise while that further away rises more slowly as the heat is redistributed within the tile. After 500s the tiles have more or less reached internal thermal equilibrium. The procedure adopted here is to average together the two tile thermocouples after 500s and fit a radiation cooling curve from numerical integration of:

$$\frac{dT_{TC}}{dt} = a(T_0^4 - T_{TC}^4)$$

where T_{TC} is the thermocouple temperature in °K, T_0 is the temperature of the radiation sink and a is a constant. Both a and T_0 are determined from the non-linear least squares fitting procedure. Having determined these constants the cooling curve for the tile at a single uniform temperature is back extrapolated to the end of the heating pulse. This gives us a bulk tile temperature rise for the whole pulse which combined with the temperature dependent specific heat data and tile mass is used to calculate the tile energy. Clearly this procedure is not exact for a whole variety of reasons perhaps the greatest of which is that the surface temperature distribution is not known. However, since the bulk cooling rate is rather slow, typically on the timescale of 1000s, the details of the model are not so important. This conclusion is justified by the quality of the energy balance which has been obtained for a wide variety of pulses.

Global energy balance

The analysis described in the last section has been applied to all pulses in the JET steady state database for both MkIIa and MkIIGB. The results are presented in fig.15.3 which shows the total divertor energy determined from tile thermocouples E_{TC} plotted against that which would be expected from the difference between the energy input, E_{in}, minus the radiated energy, E_{rad}, calculated for the X-point phase of each discharge. The database covers a wide range of equilibria and plasma conditions including low and high triangularity discharges, impurity seeded H-modes and pulses with RF heating. Despite this range almost all the data falls within ±20% of the expected value. This is a good result since the uncertainties in the total input power and radiated power are on the order of 10%.

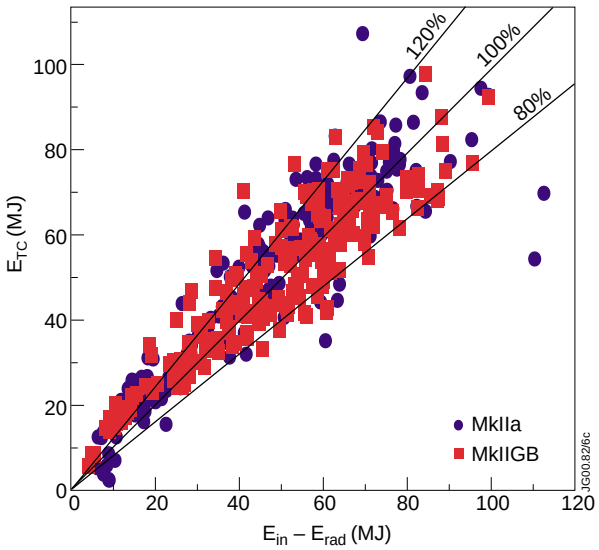

Fig.15.3: Measured, E_{TC}, and expected E_{in}-E_{rad} energies for all pulses in the JET steady state database for MkIIa and MkIIGB.

The radiated energy comes from integration of the PPF BOLO/TOPO and no account is taken of the radiation falling on the divertor, amounting to ~10% of the total. It turns out however, that this omission is just sufficient to offset an underestimate (~10%) in the total radiated power deduced from comparing BOLO/TOPO with full tomographic reconstructions of the data [15.4].

The pulse to pulse reproducibility of the energy balance is much higher than for the database as a whole, a few percent error is typical. Figure 15.4 shows a plot of the global energy balance for a more restricted set of L and H-mode data. The purpose is to see whether there is a systematic

difference in the energy balance between L and H-mode which might be expected if a significant fraction of the ELM energy went to the walls rather than the divertor. The ELM energy is defined by:

$$E_{ELM} = \Delta W_{dia}\, f_{ELM}\, t_{heat}$$

where ΔW_{dia} is the average energy drop per ELM as determined by the fast diamagnetic loop, f_{ELM} is the average ELM frequency and t_{heat} is the duration of heating pulse for which ELMs are present. If all the ELM energy went to walls then we would expect that $E_{TC} = E_{in} - E_{rad} - E_{ELM}$. In fig.15.4 one can see that the absolute values are more consistent with all the ELM energy going to the divertor, i.e. $E_{TC} = E_{in} - E_{rad}$. Given the possible absolute errors however the more significant result is that there is no apparent jump in energy accounting between L and H-mode. From 15 to 30% of the energy flow to the divertor is expected to be due to ELMs and the results suggest that the majority of this is deposited in the divertor.

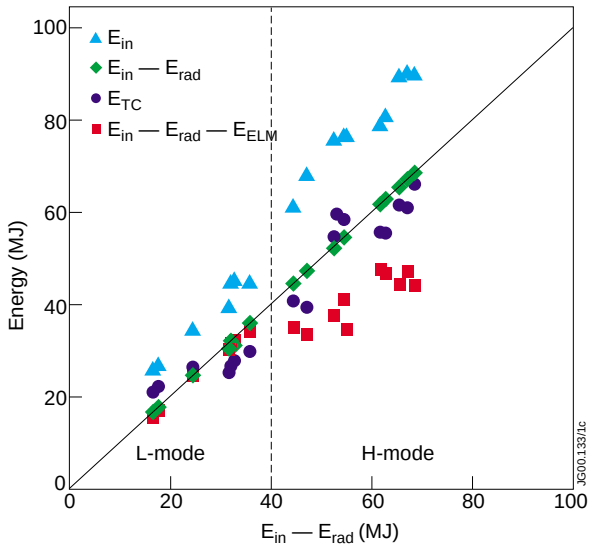

Fig.15.4: Measured, E_{TC}, and expected E_{in}-E_{rad} energies for selected L and H-mode pulses. Also shown is the predicted energy balance if all the ELM energy were deposited outside of the divertor.

Energy distribution

In the last section the total divertor energy was discussed. However, in all pulses there is some spatial resolution due to the fact that the energy deposited on each tile is calculated independently. Figure 15.5 shows an example of the individual tile energies from a typical ELMy H-mode in MkIIGB. In addition to the individual tile energies, this figure also shows the E_{in} and E_{in}-E_{rad} which is in good agreement with E_{TC}.

Two features of fig.15.5 are worthy of note: The first is the large asymmetry between the inner and outer divertor. The second is the small but real amount of energy recorded by tiles 3, 4 (septum) and 5 which is due to electromagnetic plasma radiation and

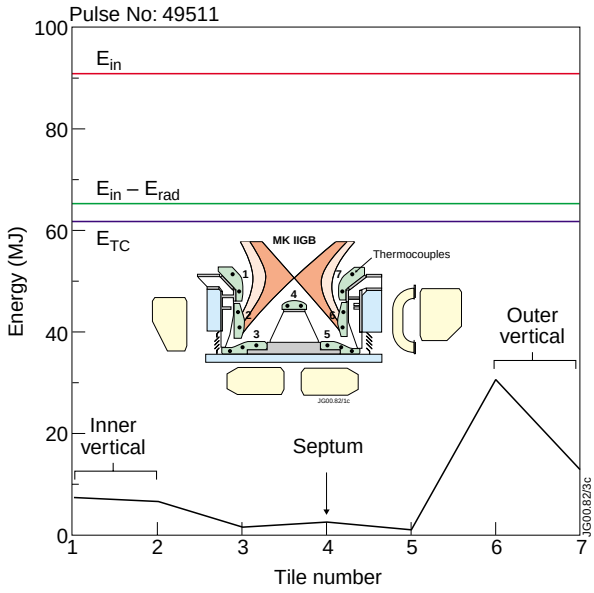

Fig.15.5: Distribution of energy between tiles in MkIIGB for a typically ELMy H-mode

bombardment by neutral particles. Averaged over the surface area of each tile, in the case of pulse 49511 the surface power density due to these sources is: 0.12MWm^{-2} on inner horizontal tile 3, 0.16MWm^{-2} on the septum and 0.07MWm^{-2} on outer horizontal tile 5.

Although the precise distribution of energy between tiles depends on the time history of the plasma equilibrium, the in/out energy asymmetry does not. Figure 15.6 shows a plot of the ratio of outer to inner divertor energy, E_{outer}/E_{inner}, versus radiated energy fraction, E_{rad}/E_{in}, for the whole of steady state database (excluding septum equilibria). It was decided to plot the data as a function of E_{rad}/E_{in} since one might expect that as this parameter increases there would be a tendency for the inner divertor to detach and hence become more asymmetric. This plot only includes pulses with **B**×∇**B** towards the target and the bulk of data has an energy asymmetry in the range 2-4. There is some evidence in Fig.15.6 that the divertor gets more asymmetric as the radiated energy fraction rises but at a certain point it rolls over perhaps corresponding to more symmetrical detachment. It is interesting also to note that in the more closed MkIIGB divertor we were never able to achieve as high a radiated power fraction as in MkIIa. Figure 15.6 suggests that this may be due to the earlier onset of detachment at the inner divertor since the divertor becomes in/out asymmetric more rapidly as the radiated energy fraction is raised.

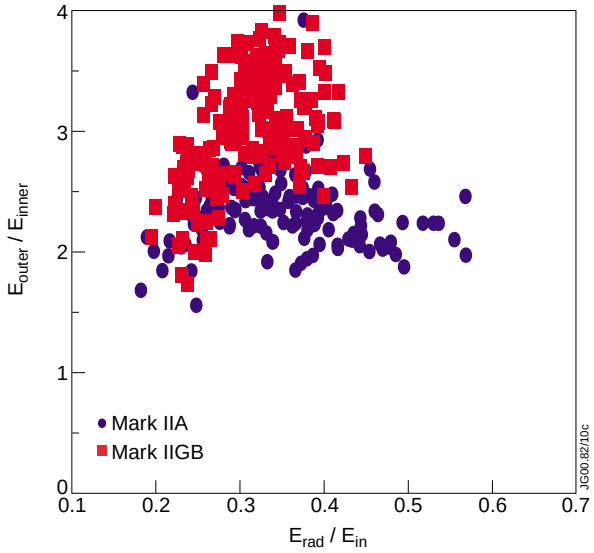

Fig.15.6: Variation of outer to inner divertor energy ratio with the fractional energy radiated for the steady state database (excluding septum equilibria).

In fig.15.7 the outer to inner energy ratio is plotted for a narrower more similar set of discharges at 2.5MA/2.5T with vertical low triangularity configurations. Pulses are categorised according to ELM frequency and confinement mode. Also compared are pulses with the **B**×∇**B** drift towards ↓ and away ↑ from the X-point.

The results of fig.15.7 show that the in/out asymmetry does not change significantly with ELM frequency from zero (L-mode) to 12Hz (type I ELMs) to 250KHz (type III

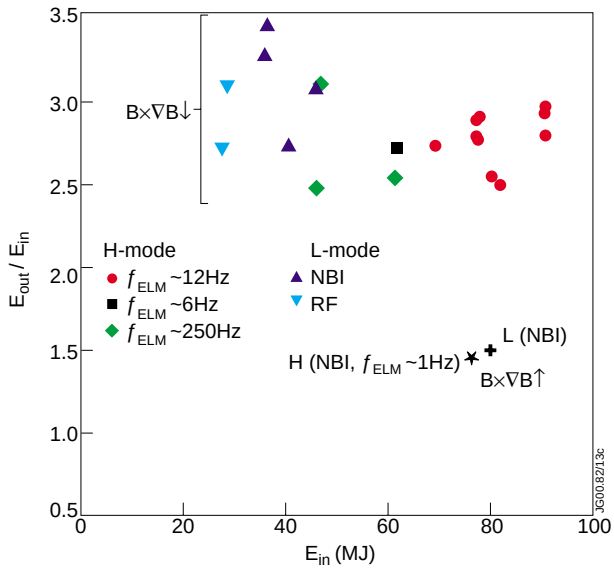

*Fig.15.7: Ratio of outer to inner divertor energy for a range of conditions. The most significant change is observed when the direction of the **B**×∇**B** drift is reversed.*

ELMs). Since ELMs carry up to 30% of the energy to the divertor, this implies that the ELM energy must be split between outer and inner divertors in a similar ratio i.e. 3:1. This ratio is quite sensitive to the in/out distribution of the ELM energy because the total energy arriving at the inner target is comparable to the ELM energy. If we assume that the E_{outer}/E_{inner} ratio is reduced by 0.5 in H-mode compared to L-mode due to the way the ELM energy is shared between the two targets (i.e. from 3.2 to 2.7) then this implies a split in ELM energy of at least 2:1 in favour of the outer divertor. This calculation does however assume that E_{outer}/E_{inner} for the inter-ELM periods is not larger than it is in L-mode.

Power profile determination

A dedicated series of pulses was carried out in which a high clearance plasma configuration was shifted vertically up the divertor target on a pulse to pulse basis. An example of this equilibrium is shown in fig.15.8 (a). The pulses were all standard ELMy H-modes with 12-14MW of neutral beam injection or L-modes with 3.5-5MW of NBI. The pulse list is given in section 15.4. The H-modes were unaffected by the change in vertical position and an example of the basic parameters is shown in fig.15.8 (b).

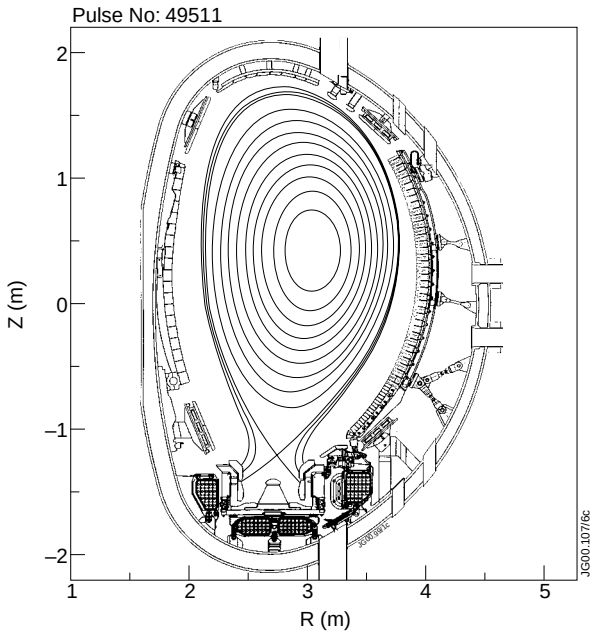

Fig.15.8: (a) High clearance equilibrium used in the X-point height scan.

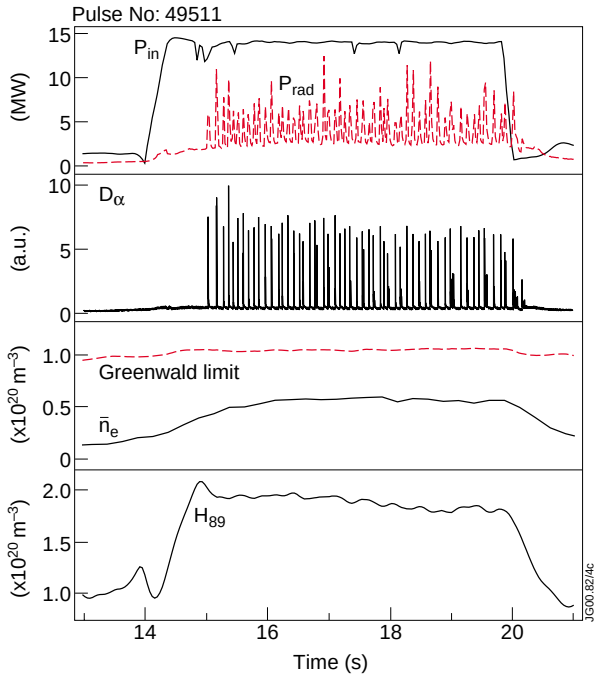

Fig.15.8: Typical main plasma parameters for the X-point heights scan in H-mode.

Since the energy input is not exactly the same in all pulses the fraction of the energy going to each lower vertical tile is normalised to the total energy measured on both inner and outer vertical tiles. Hence the fractional energy deposited on tile 2 is F2 /(E1+E2) while that on tile 6 is F6 = E6/(E6+E7). These fractions are plotted in fig.15.9 (a) and 15.9 (b) as functions of the vertical displacement with respect to the gap between the two vertical tiles.

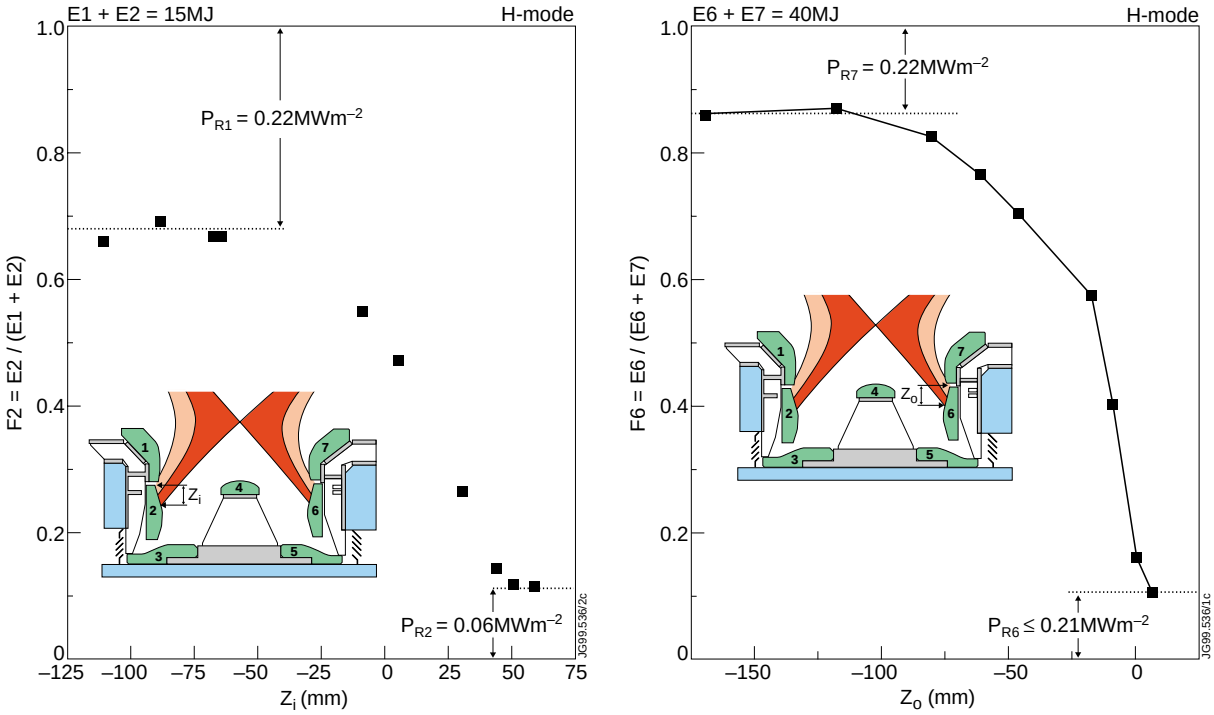

Fig.15.9: (a) Normalised energy to inner tile 2 and (b) outer tile 6 vs. vertical displacement of the strike point.

Shifting the plasma vertically does not result in a 100% transfer of energy from one tile to the next. The main reason for this is the volumetric power losses from electromagnetic and energetic neutrals which are deposited on the divertor surfaces. Estimates for the average surface power loads on the vertical tiles due to those sources are given in fig.15.9. Similar estimates can also be made for the horizontal tiles and septum tiles. Thermocouple results are to be compared with the surface power load due to electromagnetic radiation derived from tomographic inversion of main chamber bolometer data, as shown in table 15.1 below. The bolometer data underestimates the power in all cases and it is possible that the difference may be accounted for by the contribution due to neutrals.

Table 15.1 Average surface power density estimated from thermocouple data, $P_{R,TC}$ and from tomographic inversion of main chamber bolometer data $P_{R,Bolometer}$

Pulse 49511	**$P_{R,TC}$ (MWm^{-2})**	**$P_{R,Bolometer}$ (MWm^{-2})**
Tile 1 – upper inner vertical	0.21	0.10
Tile 2 – lower inner vertical	0.06	0.05
Tile 3 – inner horizontal	0.12	0.07
Septum cap	0.16	0.09
Tile 5 – outer horizontal	0.07	0.048
Tile 6 – lower outer vertical	<0.21 (upper limit)	0.046
Tile 7 – upper outer vertical	0.23	0.12

In the case of steady state discharges the average power density to a vertical surface can be calculated from the derivative of the energy with respect to the strike point displacement:

$$P_{Surface} = \frac{\Delta E}{2\pi R t \Delta Z}$$

Where ΔE is the change in tile energy when the strike point is shifted vertically a distance ΔZ, R is the major radius of the strike point and *t* the duration of the heating pulse. The results of this procedure are plotted in fig.15.10.

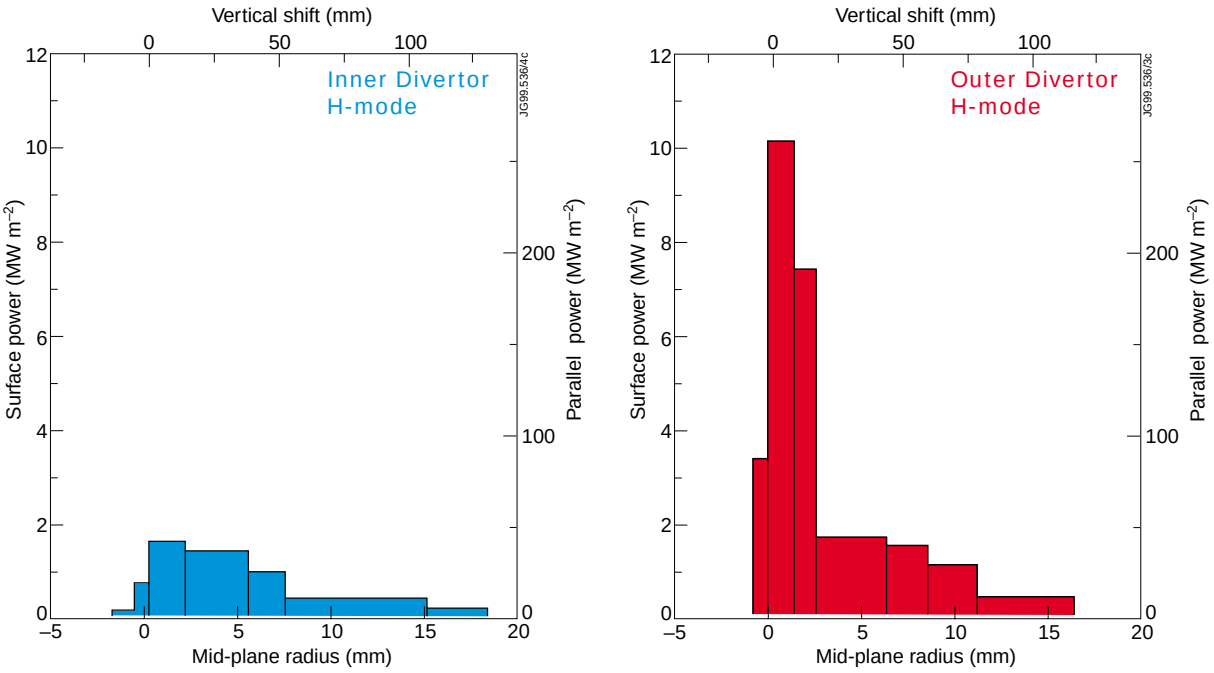

Fig.15.10: Power profiles for 12MW unfuelled H-modes for (a) the inner divertor and (b) the outer divertor.

The most striking feature of the power profiles of fig.15.10 is the narrow peak at the outer strike point. Apart from this feature the underlying profile is only slightly asymmetric in favour of the outer outside as one might expect simply from geometric considerations.

Confirmation of the existence of this narrow power profile is also given by H-mode discharges with the X-point resting on septum (i.e. 49049 and 49050). The high flux expansion associated with these equilibria means that the septum only intercepts flux surfaces out to 2mm (mid-plane). Despite this small effective cross-section ~50% of the energy is deposited there.

Thermal analysis using the ABAQUS finite element code

The ABAQUS finite element thermal model was run to test the interpretation of the time dependence of the thermocouple temperatures. The extracted power profiles of fig.15.10 were used as input and this deposition pattern was shifted up the tiles on a shot by shot basis. The mesh geometry and assumption that went into the model are shown in fig.15.11. This also shows an example of the predicted and measured thermocouple response.

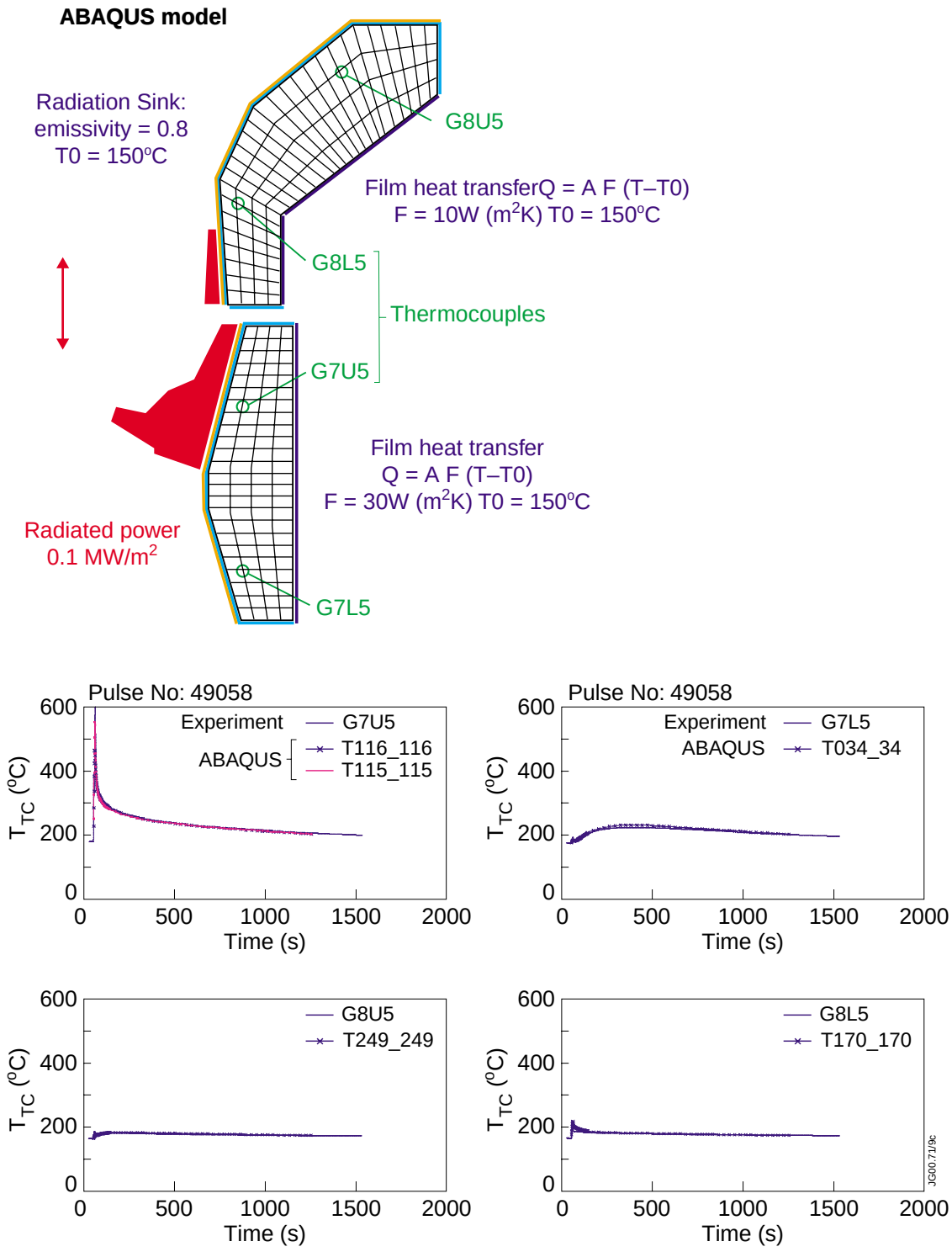

Fig.15.11: Geometry and assumptions used in the ABAQUS simulations of the outer vertical divertor target and an example of the match to the experimental thermocouple data.

To some extent the fit to the long term cooling of the tile illustrated by fig.15.11 is the result of selecting appropriate values for the radiation sink and heat transfer to the tile carrier. However, during the plasma pulse these factors are not important and fig.15.12 shows that there is a good fit to the time development of the thermocouple temperature in the pulse where the

strike point was sat almost on top of the thermocouple. This provides additional evidence that the peak surface power density is correctly determined.

The quality of this fit led to the idea that it might be possible to extract the surface power density from the time derivative of the thermocouple temperature. To this end ABAQUS simulations have been carried out in which the thermocouple response to a uniform power distribution was simulated. The results are shown in fig.15.13 and show that a few seconds after the start of the heating pulse the surface power density is well approximated by $P_{surface}=0.1dT_{TC}/dt$.

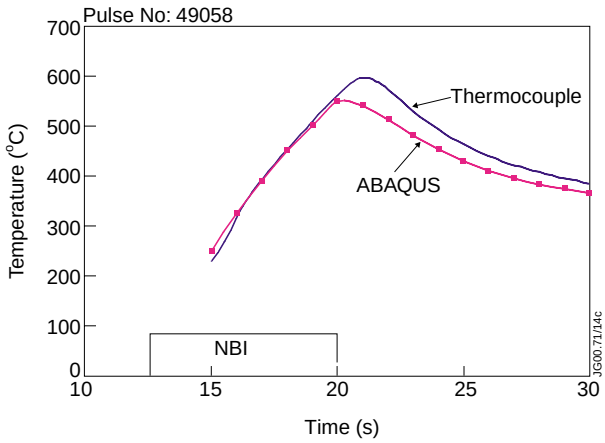

Fig.15.12: Time evolution of the tile thermocouple temperature during a plasma pulse compared with an ABAQUS simulation.

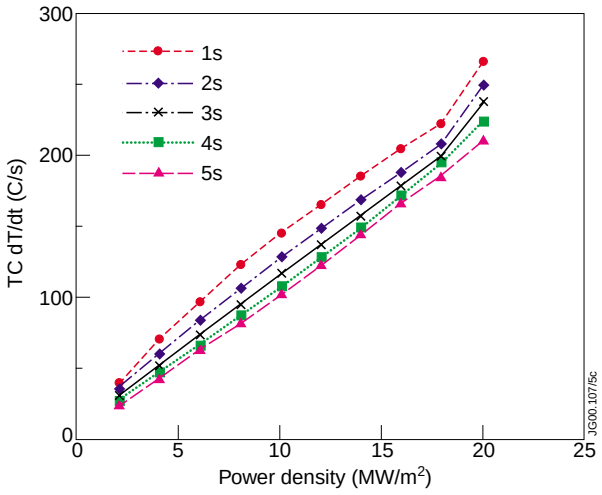

Fig.15.13: Relationship between surface power density and first derivative of the thermocouple temperature as predicted by the ABAQUS code.

The outer target thermocouple data has proven of sufficient quality that the time derivative of the thermocouple temperatures could be calculated for the X-point height scan experiment. The surface power density derived in this way is plotted on top of that derived from the tile energy in fig.15.14. The agreement between thermocouples in the upper and lower tiles and between octants is excellent. Consistency between the power profile determined by the energy shifts and the time derivative of the temperature is also very good although it is unfortunate that the narrow power peak was never placed directly on top of any of the thermocouples. A similar evaluation was attempted for the inner target but the data proved too noisy perhaps due to differences in the in-vessel wiring.

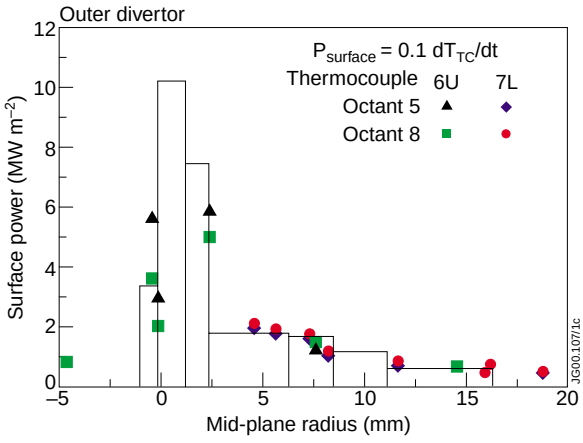

Fig.15.14: Comparison of outer power profile determined from the time derivative of thermocouple temperature with that derived from the change in tile energy with vertical position.

Target probe data and comparison with OSM2/NIMBUS

During the X-point, height measurements were also made using the target Langmuir probes. Figure 15.15 shows that outer target data averaged over several seconds in each pulse. The scatter is associated with ELMs and the outlying points should be regarded as unreliable. The probes show the same narrow feature at the outer strike point as is observed in the thermocouple data although the parallel power density calculated assuming that $T_i=T_e$ is only one quarter of the value derived from the thermocouples. The main cause of the peak in power seen by the probes is the peak in the ion flux which is ten times higher than the base value. There is some peaking of the electron temperature but nothing dramatic.

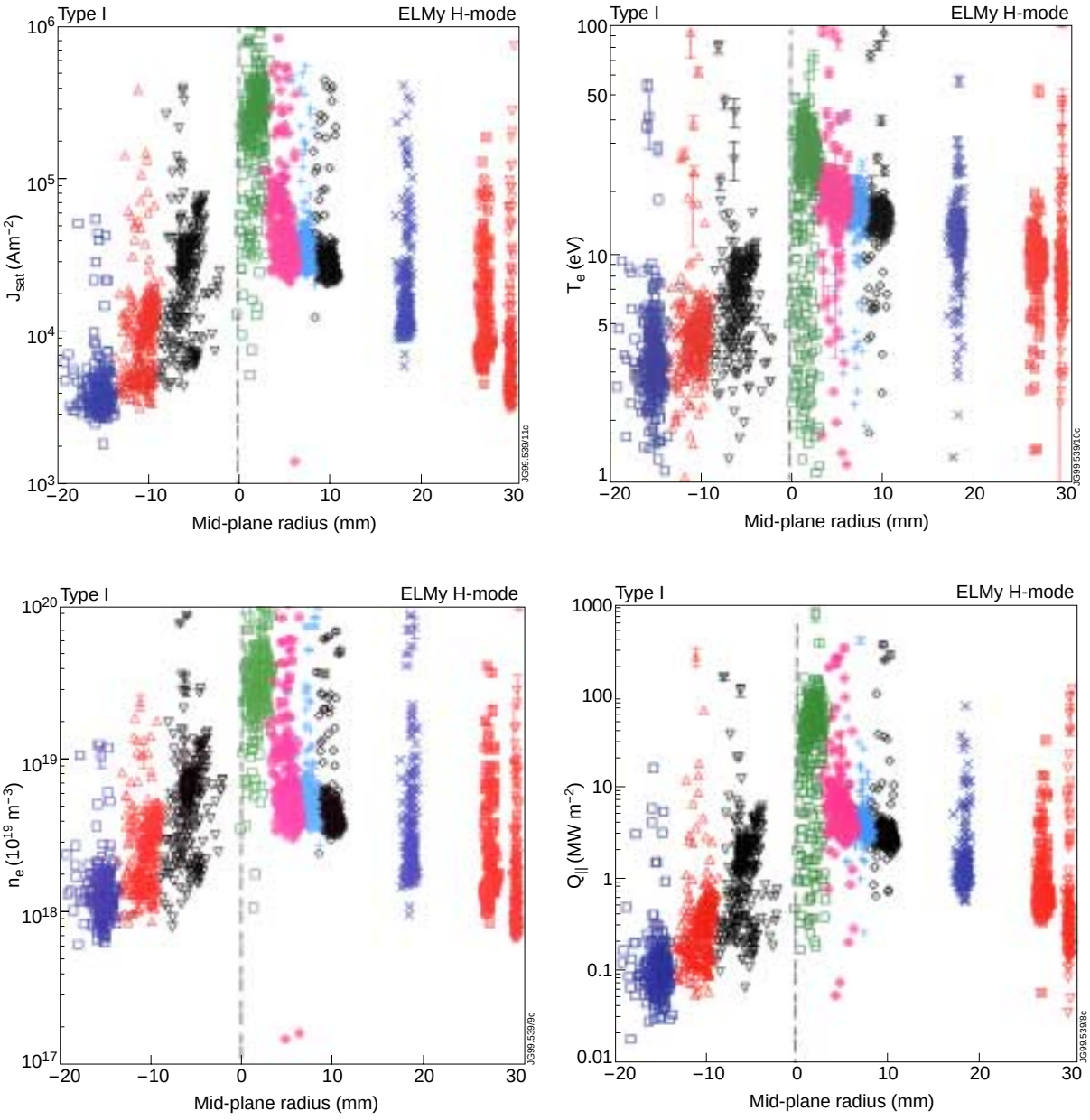

Fig.15.15: Outer target probe profiles taken from several seconds of ELMy H-mode during the X-point height scan (a) ion saturation current density $J_{sat,}$ *(b) electron temperature* $T_{e,}$ *(c) electron density* n_e *and (d) parallel power density Q// (assuming that* $T_i=T_e$*).*

The interpretative “onion-skin” plasma model OSM2/NIMBUS [15.5] has been applied to the probe data. It uses the outer target probe data as a constraint and tries to get the best fit to the inner target data by adjusting the momentum sources (equivalent to allowing arbitrary drifts). Figure 15.16 shows the inner and outer parallel power profiles from OSM2 as compared with the thermocouple derived parallel power. Although the probe power profiles are a similar shape to those from the thermocouple we have to assume that the ion power entering the SOL, P_i, is ten times the electron power P_e, for the absolute values to match reasonably well. However, because the power density is very high near the separatrix this has the inevitable consequence that a similar peak in the power is also observed at the inner divertor. There is also a poor match to the measured profiles of density and temperature at the inner divertor in this case. This strongly suggests that the observed asymmetry can never be reproduced by conventional fluid models,

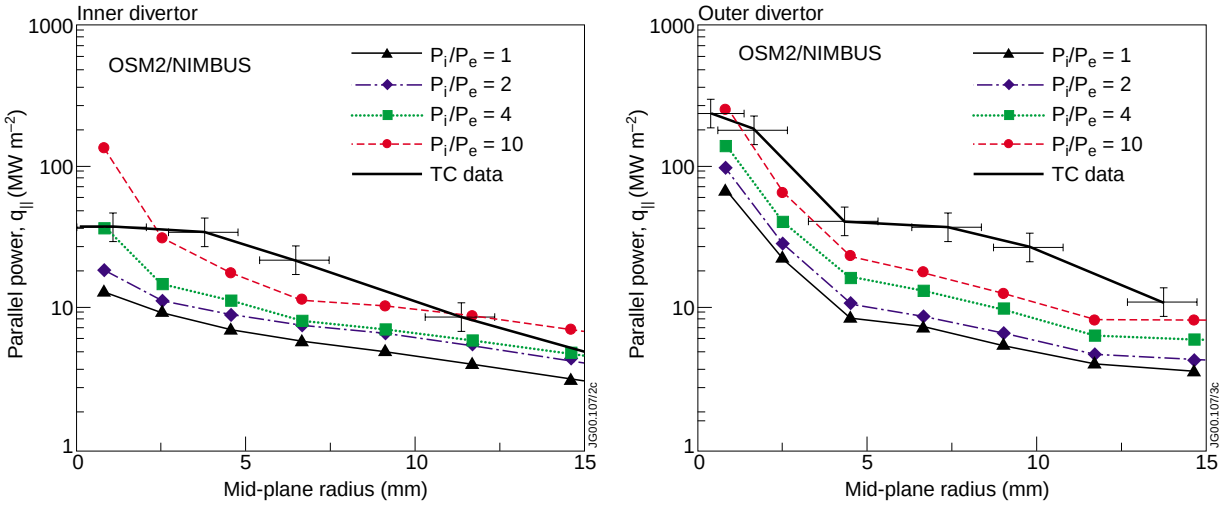

Fig.15.16: Power profile at (a) the inner target and (b) the outer target as predicted by OSM2/NIMBUS for various electron to ion power ratios. The case where P_I/P_e=1 can be regarded as the power profile as determined by standard probe analysis.

even if they include the effect of neo-classical drifts. The explanation of this feature is now thought to be kinetic in origin – namely, the loss of ions from inside the pedestal which are deposited primarily at the outer target when the **B**×∇**B** drift is towards the divertor [15.5].

The OSM2/NIMBUS analysis can also be used to extract the perpendicular transport coefficients in much the same way as the TRANSP code. The results are plotted in fig.15.17. This shows that the cross-field transport is very low and of the order of the neo-classical (plateau regime) value near the

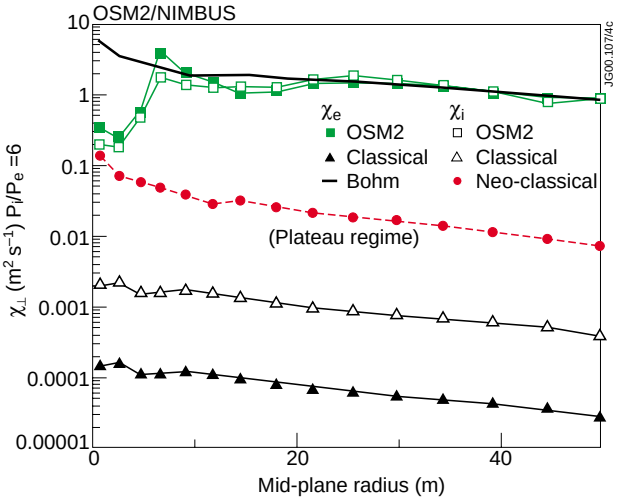

Fig.15.17 Radial variation of cross-field thermal conductivity as determined by OSM2/NIMBUS. Comparison is made with classical, neo-classical and turbulent (Bohm) predictions for χ_e and χ_I

separatrix and rises to a level consistent with Bohm further out. One can speculate that the narrow region near the separatrix is the foot of the H-mode pedestal whilst further out turbulence re-establishes itself.

15.3 Summary and future directions

Experiments carried out in MkIIGB have shown the value of divertor thermocouple analysis in diagnosing the energy and power distribution in the divertor. The results show that there is good energy balance in most discharges and that a substantial part of the ELM energy must be deposited on the divertor target. Power profiles deduced from pulse by pulse shifting of the plasma show a narrow high power feature at the outer target which cannot be explained by conventional models. Further work on the contribution due to ion orbit losses is recommended.

ABAQUS simulations have shown that it should be possible to map out power profiles in a single pulse using a slow sweep of the plasma over a thermocouple and using the time derivative of the temperature to determine the power. This would allow a faster exploration of the scaling of the divertor power profiles. Of particular interest is higher density discharges where one might expect the higher collisionality to suppress the peaking of the outer power profile.

15.4 Shot List

The detailed analysis described in this section was based on a series of experiments carried out in a single session and the pulse list is given below. Additional pulses of special interest are also listed. Some overview plots have been presented for which the pulse list corresponds to the whole of the steady state H-mode database.

Week 46 X-point height scan

Session Leader:

G.F.Matthews

Physicists in Charge:

J.Lingertat/G.P.Maddison

Aims:

Determine energy profile in the divertor using divertor tile calorimetry plasma shift technique. In parallel use limiter phases for hydrogen desorption study using the KE9D laser. Specific swept discharge to measure target profiles during ELM free phase.

Machine Configuration:

D1 and D4 were positive with 4KA of current to increase flux expansion in the divertor. However, EFIT showed negligible increase in flux expansion contrary to PROTEUS predictions. Divertor cryo-pump was on.

Pulse No.	P_{NBI}	DW_{ELM} (MJ)	f_{ELM}(Hz)	XLOC/ZSOL	XLOC/ZSIL	Comment V/HFE/LT **2.5MA/2.5T**
49510	13.7	0.25	12	-1.498	-1.465	H-mode disrupts at 58.6s
49511	13.7	0.32	11	-1.467	-1.444	H-mode
49512	13.7	0.34	10	-1.448	-1.422	H-mode
49515	11.8	0.20	14	-1.447	-1.412	H-mode
49516	13.7	0.24	17	-1.431	-1.394	H-mode
49514	12.2	0.24	11	-1.437	-1.403	H-mode
49520	8.6	0.22	6.7	-1.456	-1.430	H-mode reduced power
49509	4.2			-1.490	-1.464	Not quite L-mode
49522	3.5			-1.475	-1.441	L-mode
49518	5.0			-1.448	-1.420	L-Mode
49517	3.55			-1.433	-1.401	L-mode
49523	5.3			-1.477	-1.449	Type III or L-mode?
49621	5.6	?	250	-1.456	-1.430	Type III ELMy H-mode

Other similar pulses from a previous session which provide additional outlying points for the height scan are: 49056, 49058, 49059 (similar but not identical high clearance equilibrium with D1 and D4 forward).

Pulses with reversed grad B

Pulse No.	Ip (MA)	B_T (T)	P_{NBI} (MW)	Comment V/SFE/LT
48148	2.5	2.5	11	L-mode
49511	2	2	11	H-mode

Acknowledgements

The work presented here was made possible by the target thermocouple system which was originally developed under the guidance of L.D. Horton and P. Andrew. The work on automated analysis of the thermocouple data was initiated by R.D. Monk with the help of H.Bötger.

References

[15.1] S.Clement, J. Nucl. Mater. **266-269** (1999) 285

[15.2] A.Chankin, invited paper 14th PSI Conference, Rosenheim 2000

[15.3] A.V.Chankin, G.M.McCracken, Nuclear Fusion, Vol. 33, No.10 (1993) 1459

[15.4] L.C.Ingesson, JET-R(99)06

[15.5] W.Fundamenski, P.C.Stangeby, J.D.Elder, J. Nucl. Mater, **266-269** (1999) 1045-1050

16. SOL PROFILES AND PERPENDICULAR TRANSPORT

S. K. Erents[1], W. Fundamenski[1].

JET Joint Undertaking, Abingdon, Oxfordshire, OX13 3EA, UK.

[1] EURATOM/UKAEA Fusion Association, Culham Science Centre, Abingdon, Oxfordshire, OX14 3DB, UK.

16.1 Overview

'Onion Skin' modelling, associated with the DIVIMP/NIMBUS [16.1] code, has been validated in the recent JET Mk-IIGB divertor configuration by comparing upstream profiles of density, $n_{eu}(r)$, and temperature, $T_{eu}(r)$, measured by the Reciprocating probe with those predicted by a new code OSM2 using target probe data. This validation has been completed for 18 Ohmic, L-mode and H-mode discharges in JET Mk-IIGB, and compared with earlier OS-modelling, OSM1, of 61 MkII discharges.

OS-modelling in JET Mk-IIGB has been extended further into the SOL than that in MkII, and radial profiles of SOL widths for density and electron temperature, λ_T, λ_n and cross-field heat transport coefficient, $\chi_\perp$, extending to 30 mid-plane mm into the SOL have been obtained. This new and exciting data shows that both λ and $\chi_\perp$ show a minimum at r ~ 20 mid-plane mm, at just the radial position of maximum parallel flow in the SOL, [16.2], suggesting that parallel flow is associated with a reduction in cross-field transport.

It is demonstrated that there is little difference in scaling of upstream parameters near to the separatrix, n_{e0}, T_{e0}, heat transport coefficient, $\chi_{\perp 0}$ and scrape-off lengths λ_{T0} and λ_{n0} between JET Mk-IIGB (OSM1 or OSM2) vertical target configuration and MkII horizontal target configuration. $\chi_{\perp 0}$ is found to decrease with increasing density and power to the SOL, and a similar scaling is reflected in measured radial profiles of SOL width, λ_{T0}, and λ_{n0}.

16.2 Results

16.2.1 Validation of the Onion-Skin Model OSM2

The DIVIMP/NIMBUS Onion-Skin Model (OSM) relies on solving the four 1-D plasma transport equations, for particles, momentum, electron energy and ion energy, along individual flux surfaces, and adjusts the cross-field source terms to best match the measured target probe density and temperature profiles. The solutions obtained are therefore two dimensional. The plasma solutions are iterated several times with the NIMBUS neutral hydrogen Monte-Carlo code. For the data presented here recombination is included, together with parallel heat convection in the power balance equations, in addition to standard parallel heat conduction. Volumetric power loss due to deuterium recycling was also included. It is assumed that at the targets ion temperatures $T_{it} = T_{et}$. A global power balance suggests that this assumption is reasonable, at least for ohmic and L-mode plasmas, however in JET MkII H-mode plasmas it was found that $T_{it} >> T_{et}$ was required to achieve power balance. A more complete description of the model is described in [16.3].

As an interpretative tool, the OSM has two clear advantages over the standard 2-D approach: i) speed (by circumventing the need for lengthy parameter searches to match the diagnostic data, convergence times are reduced by two to three orders of magnitude, with the potential for inter-shot analysis), ii) no assumptions about the magnitude of anomalous transport coefficients. The previous OSM solver (OSM1) was unfortunately limited to treating "attached" plasmas. Given that JET Mk-II GB plasmas are often partially detached in the inner divertor, this limitation was particularly serious for analysing high density JET data. The newly developed, improved solver [OSM2] overcomes this shortcoming and has been shown to capture detached solutions well into the recombination regime, although all discharges reported here were attached, at least at the outer target. In addition it includes new physics such as ion viscosity effects, ion-electron collisional energy exchange, smooth supersonic transition, and more accurate treatment of plasma-neutral interactions. OSM2 also treats the flux-tube as a whole (continuous target-to-target solutions) rather than breaking it up into two discontinuous parts (target-upstream) as was done by the previous solver. This latter development, especially, should improve the accuracy of the extracted cross-field coefficients. Finally, unlike traditional onion-skin approaches (based exclusively on target probes) OSM2 includes a formalism (termed Diagnostic Variance Minimisation or DVM) which allows one to constrain the plasma solution by additional, upstream diagnostic data (eg. Thomson scattering, Li-beam or hydrogen spectroscopy). In DVM the statistical variance of the error between the solution and the diagnostic data would be minimised by adjusting the cross-field sources. Aside from increasing the fit to experiment and the accuracy of extracted cross-field energy transport coefficients, DVM would permit the modelling of strongly detached discharges.

A common criticism of O-S solvers in general is that they do not contain meaningful 2-D information. This question was addressed [16.4] in terms of theoretical considerations (a variational analysis of the modelling equations, and a study of the sensitivity of the OSM2 solutions on the functional form of the cross-field sources), as well as code-code and code-experiment comparisons for specific JET Mk-IIGB discharges. Fully 2-D plasma solutions obtained with the EDGE2D-U/NIMBUS coupled fluid and Monte-Carlo neutral codes were compared with OSM2/NIMBUS solutions for a range of attached and partially detached conditions, demonstrating a high level of agreement.

Only relatively few discharges are analysed using the reciprocating probe (FRP) systems, compared with those having target probe data. It is therefore important to validate the O-S model using FRP measurements. This is of greater importance for MkII OSM since very few of the upstream data were validated with the FRP. In recent JET Mk-IIGB measurements, all of the discharges reported here were validated with FRP measurements, and some examples of the match between FRP and OSM upstream $n_{eu}(r)$ and $T_{eu}(r)$ profiles are shown in figs 16.1.a. to 16.1.f. for ohmic, L-mode and H-mode discharges.

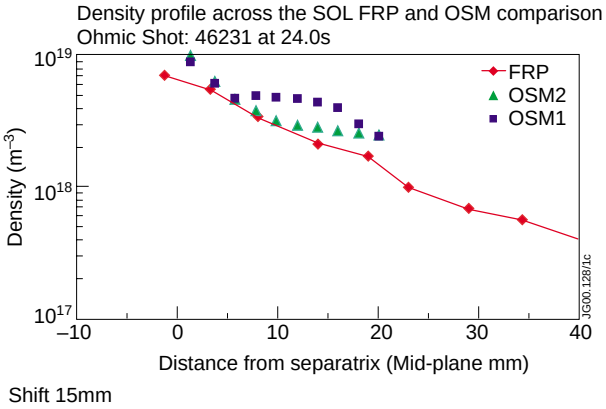

Fig.16.1:(a) Comparison of Density profiles measured with FRP and calculated using OSM2 for a typical ohmic discharge in Gas Box divertor configuration.

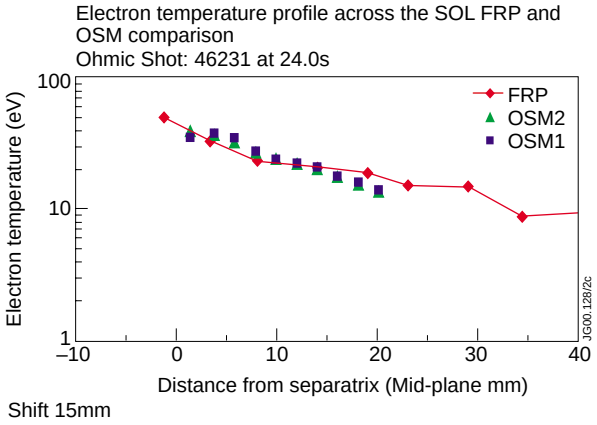

Fig.16.1:(b) Comparison of Electron Temperature profiles measured with FRP and calculated using OSM2 for a typical ohmic discharge in Gas Box divertor configuration.

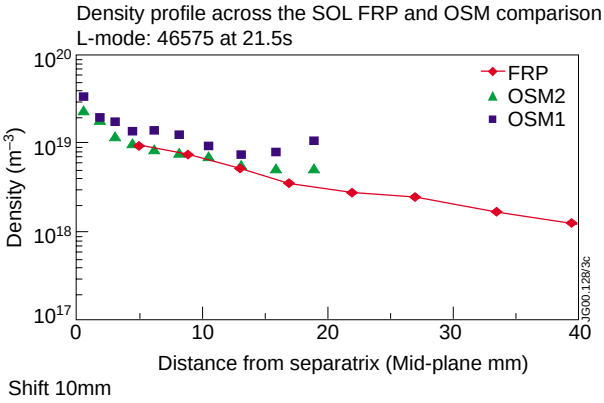

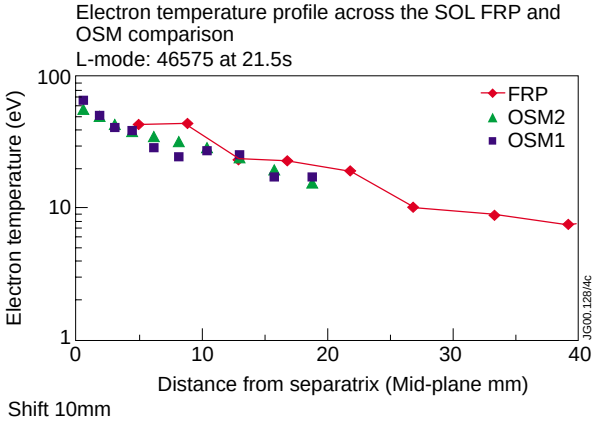

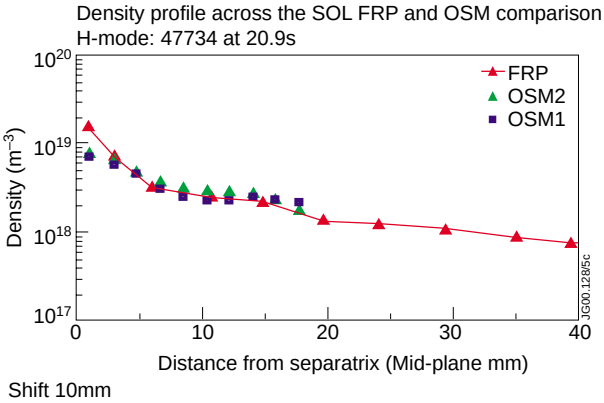

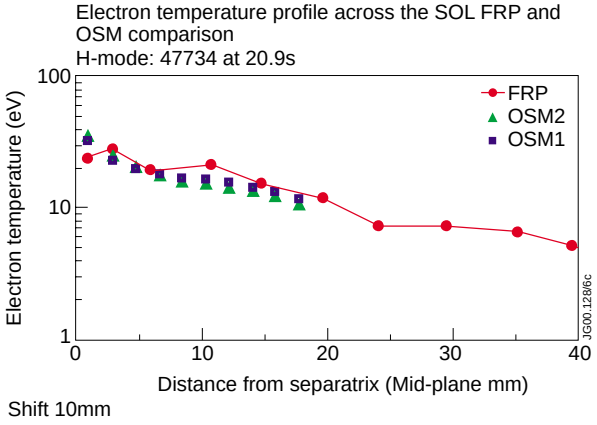

Figs 16.1:(c to f) Similar FRP / model comparisons for L-mode and H-mode discharges.

Because of an uncertainty in the magnetic configuration (EFIT) at the FRP position at the top of the torus (R=3.25 m) of about 50 mm (which corresponds to ~ 20 mid-plane mm because of field line compression) the FRP profiles have to be shifted to match the OSM profiles. All profiles are usually mapped to the mid-plane to facilitate comparison with other machines. In order to make a better estimate of the separatrix position we apply the momentum conservation

equation between the fixed probes in the target tiles and the reciprocating probe. It is believed that the position of the separatrix at the target tiles is known to within a few mm. These calculations were done within OSM2. The OSM calculates the total (static plus dynamic, electron plus ion) pressure at the location of the reciprocating probe from the pressure measured at the target and allowing for any neutral friction between the two locations. The radial shift required for pressure balance is usually between +10 and +20 mid-plane mm.

The agreement between FRP measured profiles and those calculated from target data using OSM2 is generally good, with both upstream densities and temperatures in agreement to better than a factor 2.

16.2.2 Radial Profiles of Heat Transport Coefficients and Scrape-off Lengths in the SOL.

Transport coefficients $\chi_{\perp e}$ (r) and $\chi_{\perp i}$ (r), for electrons and ions, are summed and averaged round the flux tube having radius r outside the separatrix. The details of the method of extracting $\chi_{\perp}$ from the OSM are given in [16.5]. Generally, for each grid location k:

$$\chi_{\perp ik} \propto \frac{\nabla_{\perp} T_{ik}}{Q_{\perp k}} \qquad (1)$$

Where $Q_{\perp k}$ is the heat flowing across the grid location k.

Calculation of the cross-field particle transport coefficient, $D_{\perp}$, is difficult using OSM because of large ionisation source terms in the SOL. Scaling of $\chi_{\perp}$ close to the separatrix with upstream density and main plasma parameters, central volume average density $\langle n_e \rangle$ and power to the SOL, P_{sol}, are given in [16.6] for OSM1 analysis. However, no radial profiles of $\chi_{\perp}$(r) across the SOL, or scrape-off layer width, λ_{Te}(r) or λ_{ne}(r) were analysed for JET Mk-IIGB. These profiles are presented here, and using the more sophisticated OSM2 analysis. Profiles using OSM2 analysis, fig.16.2.1.a, are compared with OSM1 analysis (again not previously presented) for ohmic discharges in fig.16.2.1.b. For these attached plasma cases, there is little difference in the results between the original (OSM1) and the more sophisticated (OSM2)

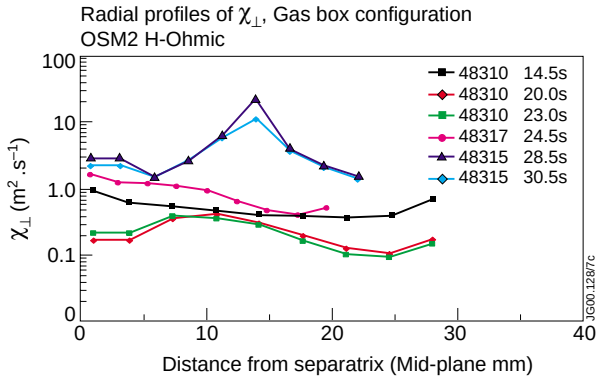

Fig.16.2.1: (a) Radial Profiles of $\chi_{\perp}$ across the SOL for JET MkIIGB Ohmic discharges, using OSM2. (just $\chi_{\perp i}$ is used for discharge 48315 because of some $\chi_{\perp e}$ instability).

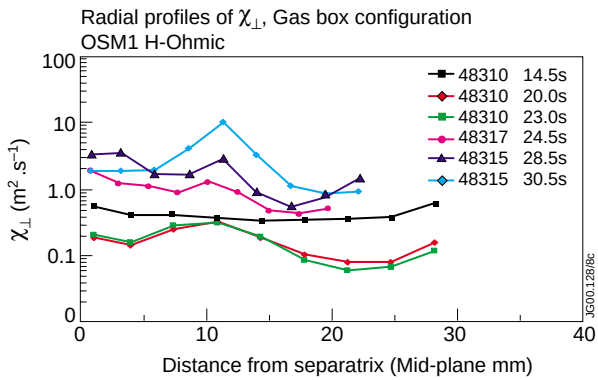

Fig.16.2.1: (b) Radial Profiles of $\chi_{\perp}$ across the SOL for JET MkIIGB Ohmic discharges using OSM1.

models. In fig.16.2.2 all data from OSM2 fully converged runs for ohmic, L-mode and H-mode discharges are shown. For further comparison with JET Mk-II, some $\chi_\perp(r)$ profiles for this older divertor configuration are shown in fig.16.2.3 for ohmic, L-mode and H-mode discharges, (presented previously in [16.5]). Note that in this earlier data, modelling was only made to r = 15 – 20 mid-plane mm into the SOL, and the subsequent fall following a maximum in $\chi_\perp(r)$ was thought to be possibly erroneous – this is clearly not the case!

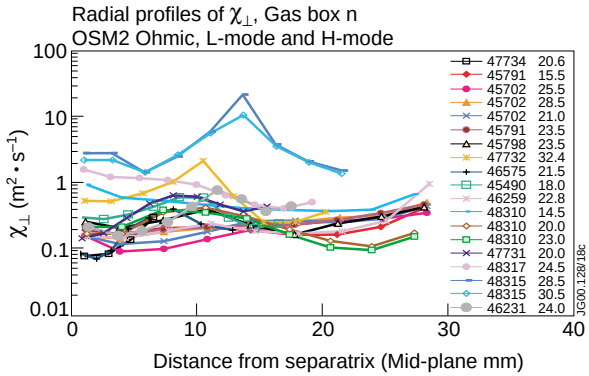

Fig.16.2.2: Radial Profiles of $\chi_\perp$ across the SOL for JET MkIIGB, all discharges in the database, Ohmic, L-mode and H-mode.

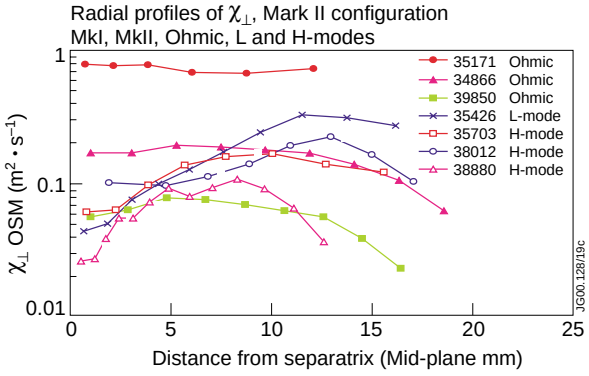

Fig.16.2.3: Earlier JET MkII $\chi_\perp$ profiles, for comparison with figure 16.2.2.

A note about possible errors in $\chi_\perp(r)$ profiles at this point is in order. It is difficult to quantify such errors in a sophisticated code, however it is clear that discharges with higher values of $\chi_\perp$ will be subject to much larger errors than those with lower values. This is because one parameter in determining $\chi_\perp$ is $\nabla_\perp T\,(r)$, equation 1, and clearly when gradients are small, i.e. profiles are almost flat, errors can be large. Another possible error could arise from the assumption that $T_{it} = T_{et}$ at the divertor targets. This cannot be confirmed experimentally in the absence of ion temperature measurements at the targets. Global power balance suggests that this is true for many ohmic and L-mode dischrges, but there is a considerable shortfall in power to the targets in MkII H-mode analysis.

Profiles of $\chi_\perp(r)$ tend to be highest for low power, ohmic discharges, and decrease as the density (and heating power) increase. Minimum $\chi_\perp$ values are found in high power H-mode discharges, for example, see fig.16.2.3 for MkII and 47734 for MkIIGB in fig.16.2.2, although this discharge is just above the L – H-mode threshold. Scaling of $\chi_\perp(0)$, i.e. near to the separatrix, with other plasma parameters is shown in a later paragraph.

A feature of most $\chi_\perp(r)$ profiles not observed before is a rise to a maximum $\chi_\perp$ at ~ 10 mid-plane mm, followed by a minimum at r = 20 – 25 mm, and a subsequent rise again far into the SOL. The exact positions of these maxima and minima could be in error by ~ 5 mm, and depend on a target to upstream pressure balance assumption in the OSM analysis.

This minimum in $\chi_\perp$ at 20 – 25 mid-plane mm corresponds closely to the position of maximum parallel flow measured using a Mach reciprocating probe in the JET SOL, [16.2]. An example of this behaviour is shown in fig.16.2.4.

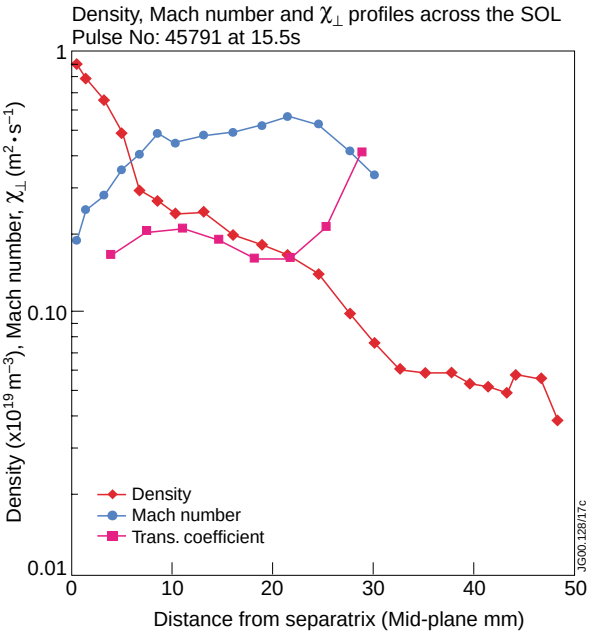

Fig.16.2.4: Radial profile of density in an L-mode discharge, showing measured Mach number and $\chi_\perp$(r) profiles.

This minimum in $\chi_\perp$(r) also corresponds closely to the position of a peak in the density profile which is seen during methane puffing experiments, [16.7], and which is believed to be due to carbon ionisation (C^{++}) at this radius. Discharges with no methane puffing, as presented here, could have an intrinsic carbon impurity which may influence $\chi_\perp$(r). The question thus arises: Are all these effects connected?

Historically, in limiter plasmas, density and electron temperature were found to decay exponentially across the SOL. This is not the case in most diverted plasmas, so an overall 'scale-length' cannot be defined. Instead, SOL widths for small regions of SOL, typically Δr=2mm, are calculated here. 'Separatrix' values of SOL width are calculated between 2 and 5mm from the separatrix; this avoids high fluctuations often found at the separatrix. Radial profiles of SOL width, λ_{Te}(r) for density and λ_{ne}(r) for electron temperature at the outer mid-plane are shown in figs 16.2.5 and 16.2.6 respectively.

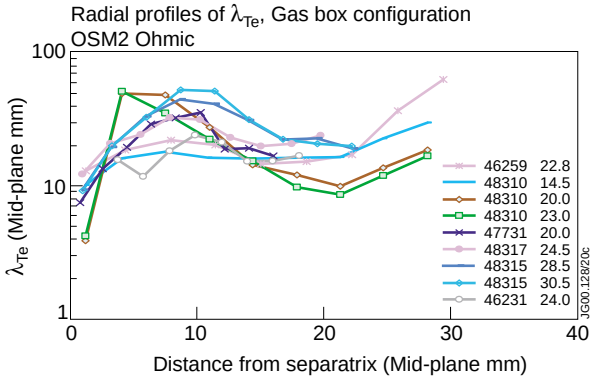

Fig.16.2.5: (a) Radial profiles of electron temperature SOL width from OSM2 analysis at the outside mid-plane – Ohmic plasmas.

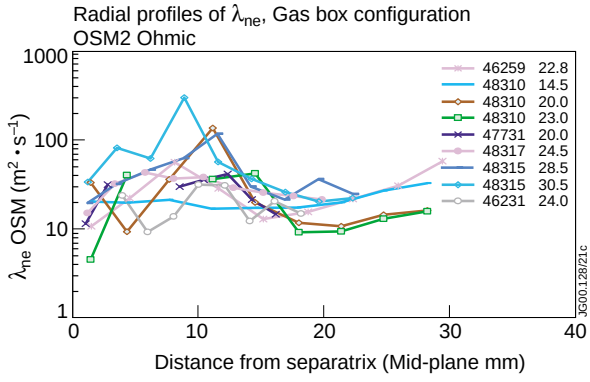

Fig.16.2.5: (b) Radial profiles of density SOL width from OSM2 analysis at the outside mid-plane – Ohmic plasmas.

The SOL width profiles show a similar behaviour with radius to the $\chi_\perp$(r) profiles, this being particularly noticeable for λ_{Te}(r). This is not surprising, since the fundamental parameter, $\chi_\perp$controls the gradient of the T_e(r) profile, and, to a lesser extent, the n_e(r) profile. It is most important to note that the SOL width is not constant across the SOL. So general e-folding lengths cannot be quoted. In the case of λ_{Te}(r), the SOL width increases by up to an order of magnitude in the first ~ 10 mid-plane mm, then falls again to a minimum value at ~ 20 mid-plane mm. The variation in the density SOL width with radius is somewhat less, in general.

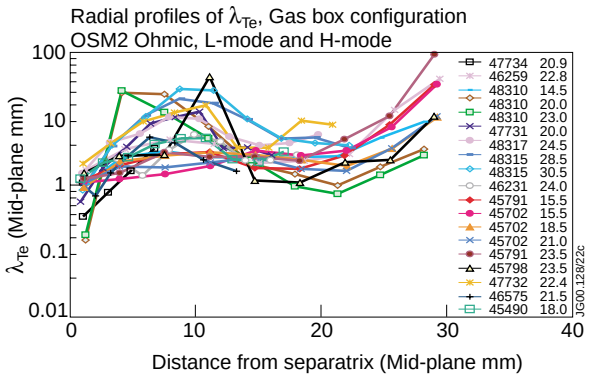

Fig.16.2.6 (a) Radial profiles of electron temperature SOL width from OSM2 analysis at the outside mid-plane – all discharges, Ohmic, L-mode and H-mode.

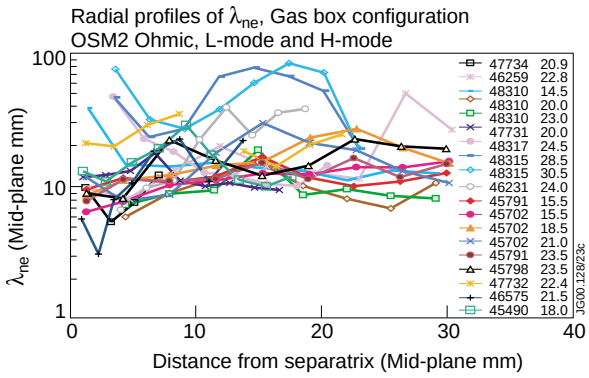

Fig.16.2.6: (b) Radial profiles of density SOL width from OSM2 analysis at the outside mid-plane – all discharges, Ohmic, L-mode and H-mode.

16.2.3 Scaling of Heat Transport and SOL Widths with other Plasma Parameters.

Because of the variation in $\chi_\perp$ and SOL widths with radius, it is difficult to define a radius at which scaling of these parameters with other plasma parameters can be made. Certainly the OSM derivation of $\chi_\perp$ can be in error in the first cell of the discretised grid used for the OSM (at ~ r = 1 mm), because of mesh boundary assumptions. In earlier work, [16.5], average results from cells 2 and 3 (~ 3 to 5 mm from the separatrix) were used, and this average is used here for scaling studies. The choice is somewhat arbitrary, but it is consistent for all discharges, and it allows direct comparison with earlier JET MkII results.

The scaling of $\chi_{\perp 0}$ with upstream (separatrix) density, n_{eu}, is shown in fig.16.2.7. for JET MkIIGB. Here the data is separated into ohmic hydrogen plasmas, ohmic and L-mode deuterium plasmas and one H-mode near-threshold plasma. In fig.16.2.8 are previous data for JET MkII included for comparison. Although there is considerable scatter, the MkII data, which is from discharges with the separatrix on the horizontal target plates in the divertor, shows the same trend and magnitude as that from MkIIGB discharges using vertical targets.

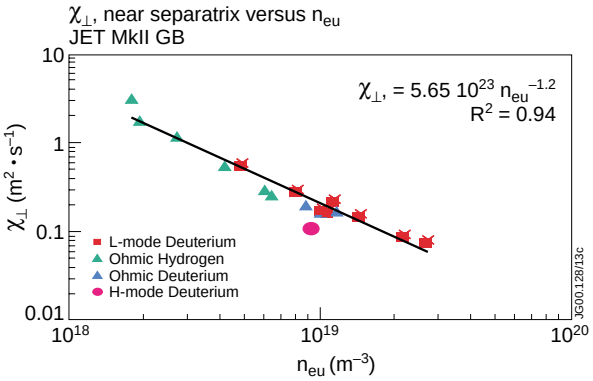

Fig.16.2.7: $\chi_{\perp 0}$ near to the separatrix versus upstream separatrix density, from OSM, for JET MkIIGB.

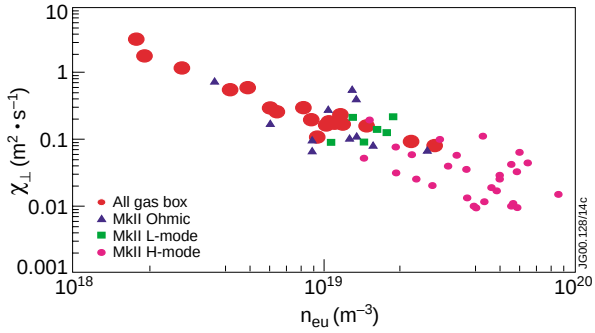

Fig.16.2.8: Comparison of $\chi_{\perp 0}$ near to the separatrix versus upstream separatrix density, JET MkIIGB and JET MkII.

The result is only slightly different to that found in [16.6] for JET MkIIGB deuterium plasmas, using OSM1, namely $\chi_{\perp 0} \propto n_{eu}^{-1}$. The OSM2 analysis suggests $\chi_{\perp 0} \propto n_{eu}^{-1.2}$ for the JET MkIIGB dataset, and also for the complete dataset including JET MkII. For just the JET MkII dataset in [16.5] the best correlation was with upstream temperature, suggesting $\chi_{\perp 0} \propto T_{eu}^{-2}$. These results are practically consistent with the upstream electron temperature / density relationship found in [16.3], namely: $T_{eu} \propto n_{eu}^{0.5}$.

The density scrape-off width for JET MKIIGB close to the separatrix (r ~ 3 – 5 mm) also falls with increasing density as shown in fig.16.2.9(a). In fig.16.2.9(b). JET MkII SOL width data is also plotted for comparison.

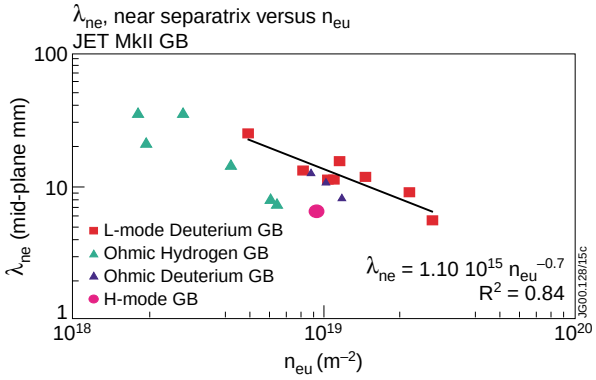

Fig.16.2.9: (a) λ_{ne0} near to the separatrix versus upstream separatrix density, from OSM, for JET MkIIGB.

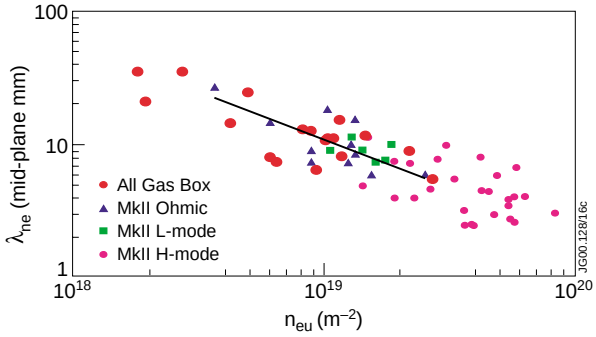

Fig.16.2.9: (b) Comparison of λ_{ne0} near to the separatrix versus upstream separatrix density, JET MkIIGB and JET MkII.

Here, $\lambda_{ne0} \propto n_{eu}^{-0.7}$ for the L-mode deuterium dataset, and $\lambda_{ne0} \propto n_{eu}^{-1.1}$,for the ohmic hydrogen dataset, although fitting errors could mean $\lambda_{ne0} \propto n_{eu}^{-1}$ approximately. For both JET MkIIGB and JET MkII datasets, figure 2.2.9.b, $\lambda_{ne0} \propto n_{eu}^{-0.75}$. The variation in SOL width is quite large, from ~ 30 mid-plane mm at $n_{eu} = 2\ 10^{18}$ m^{-3}, down to ~ 2 mm for high power (12 MW) H-modes in MkII at ~ $5\ 10^{19}$ m^{-3} separatrix density. In JET, there is a strong co-linearity between upstream density and power to the SOL, so it is difficult to say if increasing density, or increasing power results in a fall in SOL width. However, in fig.16.2.10 λ_{ne0} is shown as a function of power to the SOL, and the fitting is clearly not as good with power as it is with upstream density; the trend is approximately $\lambda_{ne0} \propto P_{sol}^{-0.5}$

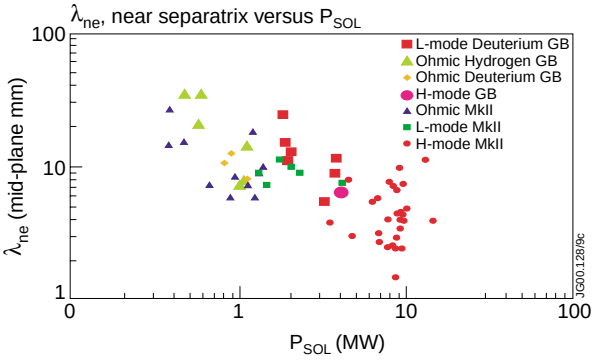

Fig.16.2.10: λ_{ne0} near to the separatrix versus power to the SOL, from OSM, for JET MkIIGB and JET MkII.

In fig.16.2.11 the trend in λ_{ne0} with central line average density is shown. The trend is very similar to that for power to the SOL, (fig.16.2.10), but with somewhat more scatter. Unfortunately, there is a strong co-linearity between P_{sol} and $\bar{n}_e$ in this database.

The upstream density profiles are useful for the modelling of the RF power which can be coupled from the RF antennas, for example, but power SOL widths at the divertor targets are important for calculation of power densities to divertor tiles. So for this dataset, although not a result of O-S modelling (it is a direct measurement from the target probe data) the power SOL width λ_{qt} is plotted as a function of upstream density in fig.16.2.12 and power to the SOL in fig.16.2.13.

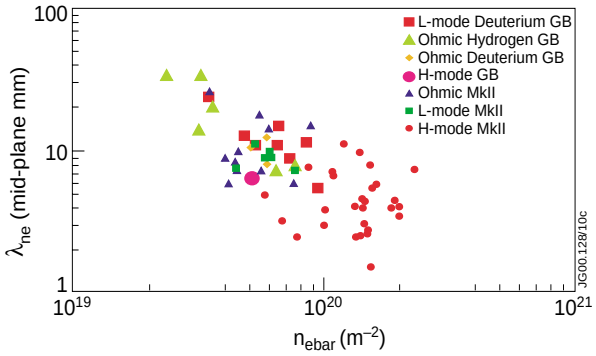

Fig.16.2.11: Comparison of λ_{ne0} near to the separatrix versus upstream line averaged density, JET MkIIGB and JET MkII.

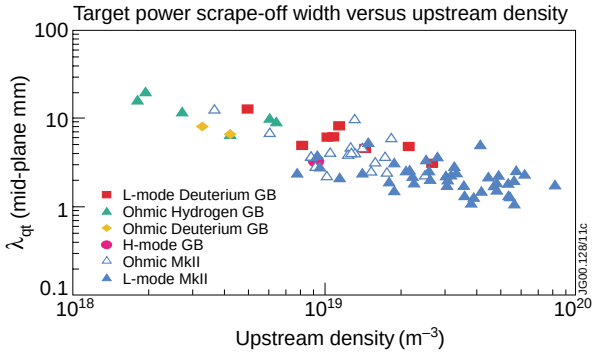

Fig.16.2.12: λ_{qt} near to the separatrix versus upstream density, JET MkIIGB and JET MkII.

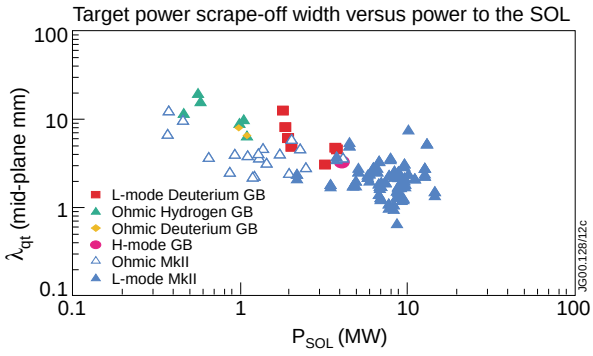

Fig.16.2.13: λ_{qt} near to the separatrix versus power to the SOL, JET MkIIGB and JET MkII.

For upstream density and power to the SOL, $\lambda_{qt} \propto n_{eu}^{-0.6}$ and $\lambda_{qt} \propto P_{sol}^{-0.6}$ for the overall JET MKIIGB dataset. The scaling is similar for the JET MkII dataset.

16.3 Summary and future directions

A new Onion-Skin model, which includes more physics and solves the transport equations from target to target along flux tubes, rather than from each target to a point upstream, has been validated by comparing with reciprocating probe radial profile measurements of density and electron temperature in the SOL.

Poloidally averaged radial profiles of cross-field heat transport coefficients using the model have been extracted for JET MkII Gas Box discharges.

Radial profiles of scrape-off layer widths at the torus mid-plane have been calculated from upstream parameters of electron temperature and density deduced from the model, and verified with reciprocating probe data.

The radial profiles of both $\chi_{\perp}(r)$ and $\lambda_T(r)$ show distinct maxima, and minima which correlate radially with maximum parallel flow observed using a Mach probe, and also maximum carbon ionisation rate during methane puffing experiments.

The suggestion is that, even in deuterium fuelled plasmas, carbon impurity ionisation strongly influences density profiles, which causes a parallel pressure gradient, which drives a parallel flow, which in turn suppresses turbulent fluctuations and therefore the perpendicular diffusion. This drive would not be expected to change sign with a change in field direction, but could explain the strong asymmetry observed in flow magnitude between two different field directions, [16.2].

Further experiments, including O-S modelling and $\chi_\perp(r)$ and $\lambda_T(r)$ extraction of discharges in which methane is puffed, is required. In addition, if cross-field transport is being suppressed by parallel flow in the SOL, then Mach number and fluctuation measurements in plasmas with varying Mach number (by increasing densities up to detachment, for example) may throw light on the mechanisms involved.

16.4 Shot List

A description of the discharges which make up the figures shown in this report is given in Table 1. In addition to the main plasma parameters, the SOL densities and electron temperatures at the separatrix derived from OSM2, and verified with the FRP, are given, together with values of $\chi_\perp(0)$, $\lambda_n(0)$ and $\lambda_T(0)$ close to the separatrix.

Acknowledgements

This work is funded by the UK Department of Trade and Industry and EURATOM.

References

[16.1] Stangeby, P.C., *et al*, J. Nucl. Mater. **241-243** (1997) 358.

[16.2] S K Erents, A V Chankin *et al*, Proc. 26th. EPS Conf. On Controlled Fusion and Plasma Phys., (Maastricht, 1999) P-1.040, Internet: http://epsppd.epfl.ch/

[16.3] S K Erents, P C Stangeby *et al*, 'Simple relations between Scrape-Off Layer Parameters of High Recycling Divertors. Part I: The Relation between Upstream Density and Temperature. Nucl.Fusion, **40**, 3 (2000) 295.

[16.4] Wojciech Fundamenski, Ph.D Thesis 'Tokamak Edge Plasma Modeling using an Improved Onion-skin Method' University of Toronto, (1999).

[16.5] S K Erents and P C Stangeby, Nucl. Fusion **38**, 11 (1998) 1637.

[16.6] S K Erents, P C Stangeby *et al*, 'Simple relations between Scrape-Off Layer Parameters of High Recycling Divertors. Part II: Further Relations. Nucl.Fusion, **40**, 3 (2000) 309.

[16.7] J Strachan *et al*, 'JET methane screening experiments', this Report, and to be presented to 14th. PSI conf, Rosenheim, Germany, May 22 – 26, (2000).

Table 1: Shot list used for the figures shown in this report.

Gas Box Ohmic, L-mode and H-mode OSM2 Modelled Shots.

Shot	Type	Time (s)	Gas	Ip (MA)	BT (T)	$<n_e>$ (m^{-3})	P_{sol} (MW)	T_{et0} (eV)	n_{et0} (m^{-3})	$T_{e(0)}$ (eV)	$T_{i(0)}$ (eV)	$n_{e(0)}$ (eV)	$\chi_\perp$ ($m^2.s^{-1}$)	λ_{Teu} (mm)	λ_{neu} (mm)	λ_{qt} (mm)
46231	Ohmic	64.0	Deuterium	2.45	2.43	2.30E+19	1.10	11.5	2.25E+19	42.2	73.5	1.17E+19	0.17	13.7	8.1	5.0
46259	Ohmic	62.8	Deuterium	2.45	2.90	2.17E+19	0.80	11.7	2.18E+19	40.8	68.0	1.01E+19	0.17	20.3	10.6	8.6
47731	Ohmic	60.0	Deuterium	1.69	1.80	2.05E+19	0.88	9.4	2.81E+19	43.1	80.9	8.79E+18	0.20	16.4	12.5	6.0
48310	Ohmic	54.5	Hydrogen	2.35	2.50	1.20E+19	1.10	33.7	6.28E+18	62.3	127.7	4.20E+18	0.56	17.0	14.3	6.6
48310	Ohmic	60.0	Hydrogen	2.35	2.50	2.54E+19	0.99	18.3	2.71E+19	72.9	162.3	6.43E+18	0.26	48.9	7.3	9.2
48310	Ohmic	63.0	Hydrogen	2.35	2.50	3.03E+19	1.05	14.0	3.19E+19	76.7	168.9	6.05E+18	0.30	22.6	7.9	10.1
48315	Ohmic	68.5	Hydrogen	0.87	0.99	1.28E+19	0.58	10.8	5.71E+18	42.1	89.2	1.80E+18	3.19	26.5	35.1	16.2
48315	Ohmic	70.5	Hydrogen	0.87	0.99	1.35E+19	0.56	8.5	8.32E+18	40.2	84.7	1.94E+18	1.80	33.7	20.9	20.0
48317	Ohmic	64.5	Hydrogen	0.88	0.98	9.70E+18	0.46	21.1	2.85E+18	37.9	72.1	2.71E+18	1.19	22.6	35.0	11.9
45490	L-mode	58.0	Deuterium	1.85	1.95	1.86E+19	2.03	19.1	1.55E+19	48.8	100.8	8.16E+18	0.30	15.5	12.9	4.9
45702	L-mode	55.5	Deuterium	2.80	2.90	2.77E+19	3.72	24.4	2.81E+19	78.6	170.9	2.17E+19	0.09	11.6	8.9	4.8
45702	L-mode	58.5	Deuterium	2.80	3.00	3.29E+19	3.80	18.1	4.84E+19	63.1	134.2	1.45E+19	0.16	15.8	11.6	4.6
45791	L-mode	55.5	Deuterium	2.37	2.50	2.09E+19	1.93	20.3	1.73E+19	55.6	118.2	1.03E+19	0.18	15.5	11.1	6.1
45791	L-mode	63.0	Deuterium	2.36	2.50	2.31E+19	1.94	18.3	2.33E+19	56.7	118.4	1.08E+19	0.18	15.0	11.1	6.2
45798	L-mode	63.5	Deuterium	2.36	2.50	2.71E+19	1.87	14.1	3.00E+19	43.6	74.9	1.14E+19	0.23	16.8	15.2	8.1
46575	L-mode	61.5	Deuterium	2.78	2.92	3.45E+19	3.22	16.1	1.10E+20	72.0	128.3	2.68E+19	0.08	10.3	5.5	3.1
47732	L-mode	72.4	Deuterium	0.89	0.97	1.52E+19	1.81	11.0	9.10E+18	30.2	54.5	4.93E+18	0.60	25.3	24.4	12.6
47734	H-mode	60.9	Deuterium	1.86	1.96	4.00E+19	4.07	15.3	1.45E+19	44.7	84.0	9.25E+18	0.11	10.8	6.4	3.3

Index:

I_p	Plasma Current
B_T	Toroidal Field
$<n_e>$	Central volume average density.
P_{sol}	Power to the SOL.
T_{et0}	Target electron temperature at separatrix.
n_{et0}	Target density at separatrix.
$T_{e(0)}$	Upstream electron temperature at separatrix, from OSM.
$T_{i(0)}$	Upstream ion temperature at separatrix, from OSM.
$n_{e(0)}$	Upstream density at separatrix, from OSM.
$\chi_\perp$	Average heat transport coefficient near separatrix.
λ_{Teu}	Electron temperature SOL width near separatrix.
λ_{neu}	Density SOL width near separatrix.
λ_{qt}	Target power SOL width referred to mid-plane.

17. PARALLEL CORRELATION STUDIES

H. Thomsen[1], A. Chankin[2].

JET Joint Undertaking, Abingdon, Oxfordshire, OX14 3EA, UK

[1] Max-Planck-Institut für Plasmaphysik, EURATOM Association, Wendelsteinstr. 1, D-17491 Greifswald, Germany

[2] EURATOM/UKAEA Fusion Association, Culham Science Centre, Abingdon, Oxfordshire, OX14 3DB, UK.

17.1 Overview

The correlation of the ion saturation current fluctuations beween Langmuir probes located in the inner and outer divertor plates (KY4) and on the KY3B reciprocating probe drive was investigated. The safety factor of the discharges was chosen in such a way that two probes were located on the same magnetic field line in the JET scrape-off layer (SOL). For connection lengths of 23 m and 66 m, maximal correlations below 50 % were found [17.1].

Similar experiments on the Wendelstein 7-AS stellarator had shown qualitatively the same results [17.2], and numerical dift-wave simulation in a sheared geometry agree with the experimental findings [17.3, 17.4].

On JET, however, a different amount of correlation was found for seemingly identical discharge conditions in different pulses. Therefore, it was not clear, whether a maximal correlation below 50 % is a genuine physical property of SOL turbulence, or whether fluctuations in the magnetic configuration had caused an additional decorrelation by a time-dependent misalignment of the two probe tips along the connecting field line. (See Fig.17.1).

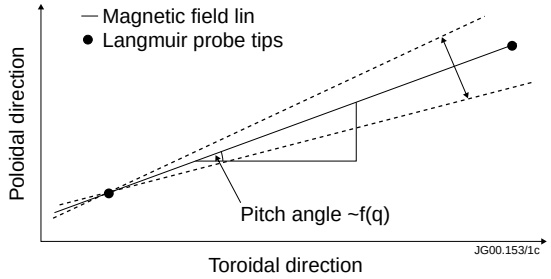

Fig.17.1: A reduction in the correlations could as well be caused by misalignment of the two probe tips. The arrow shows the poloidal displacement due to fluctuations in the magnetic configuration. The pitch angle is a function of the safety factor.

To clarify this issue, eperiments were performed recently, in which the changes in the magnetic plasma equilibrium were sampled on a fast time scale (5 kHz).

17.2 Results

17.2.1 Importance of fluctuations in the magnetic configuration.

The changes in the magnetic configuration can only have an impact on the previously obtained results, if the fieldline displacement is in the order of the typical poloidal scale of the turbulence in the SOL (few cm) or larger. The poloidal displacement of the fieldline is related to the safety factor q_{95}, as shown in fig.17.2. A change in q_{95} of 0.01 leads to a poloidal misalignment of a field line connecting a outer divertor probe and the KY3B reciprocating probe of roughly $^1/_2$ cm.

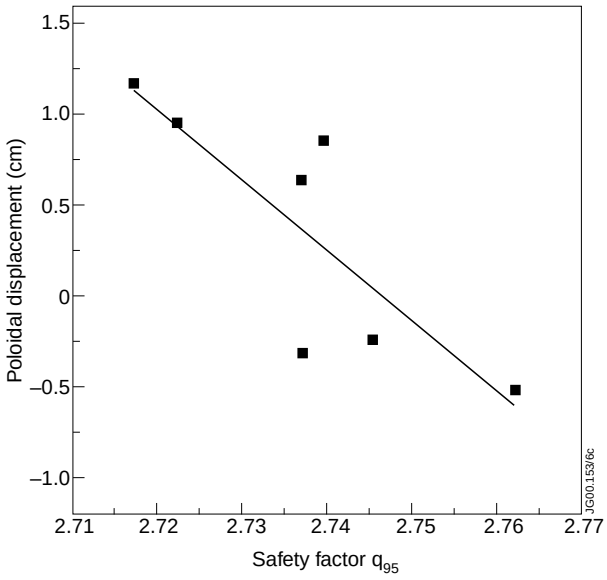

Fig.17.2: The poloidal shift at the KY3B reciprocating probe system of a magnetic field line starting from one outer divertor probe (connection length 23 m) versus the safety factor q_{95}. The results are obtained with the fieldline tracing code ORBITB using the magnetic configuration from several discharges with different safety factors (squares). The red line is the linear fit.

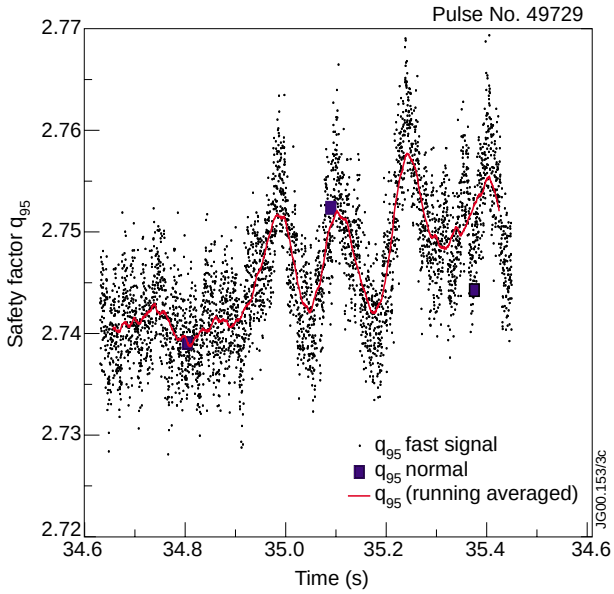

Fig.17.3: Time series of the safety factor. Black dots: the fast q_{95}, red curve: q_{95} averaged over 20 ms, blue squares: q_{95} with normal sample rate.

The rather large scatter in the results is explained by the uncertainty in the field line tracing, due to the perturbation of the magnetic configuration (see below).

During the latest parallel correlation experiments, the magnetic data was sampled with 5 kHz within a fast window (the normal sample rate for magnetic data is below 10 Hz). By using the EFIT code, it is possible to calculate the important quantities (i.e. the *safety factor q* and the magnetic flux surfaces) on the same time basis. In fig.17.3 a time series of the safety factor q_{95} is shown. The amplitude of the fluctuations is about 0.02. This is related to a poloidal shift of the connecting fieldline of 2 cm. If the magnetic signals were correct, the influence on the previousely obtained results would be critical.

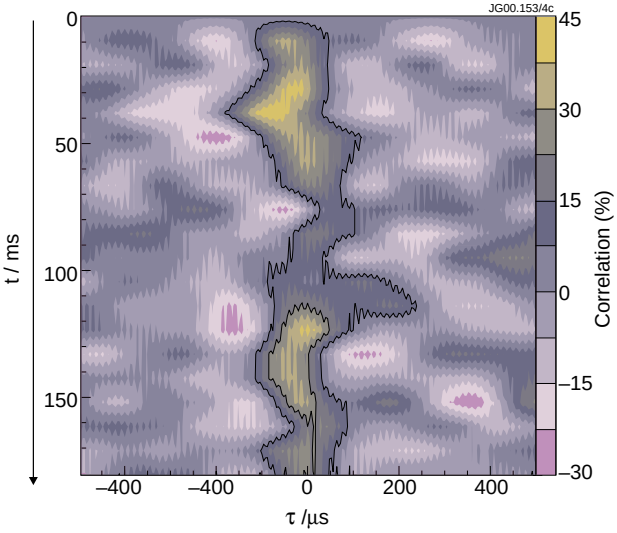

Fig.17.4: Time evolution of the cross correlation of the established connection beween one inner and one outer divertor probe (connection length: 66 m). A fluctuation in the magnetic configuration on a 20 ms time scale could provide an explanation for the change in correlation.

17.2.2 Fluctuations in magnetic signals

During the parallel correlation studies the ion saturation current was collected during a 100 ms time window. Therefore, dynamics on a slower time scale than 100 ms are not important for this analysis.

Magnetic fluctuations on a time scale from 10-100 ms can explain some not yet understood findings of the previous campaign. One example for this can be seen in fig.17.4 showing the correlation for the connection between the inner and ouer divertor probes. The decrease in correlation around t = 100 ms is due to the intersection of the reciprocating probe with the connecting field line. However, the changes in the time lag (30-40ms) could be explainable by a misalignment of the probes due to a drift of the magnetic configuration on that timescale. Unfortunately, a direct comparison is not possible, because there was no fast magnetic data collected during that discharge (#46806).

17.2.3 The origin of the fluctuations in the magnetic signals

The vertical instability due to the toroidal plasma current is the most likely reason for the fluctuations in the magnetic configuration. There is a high correlation between the vertical plasma movement and the fluctuations of the safety factor. However it seems, that this correlation is dependent on the time scale as well: the two signals show virtually no correlations on time scales shorter than 1 ms, see fig.17.5, whereas the correlation is almost 80 % on slower time scales. A few ms is the expected timescale for vertical instabilities in JET ohmically heated pulses [17.5]

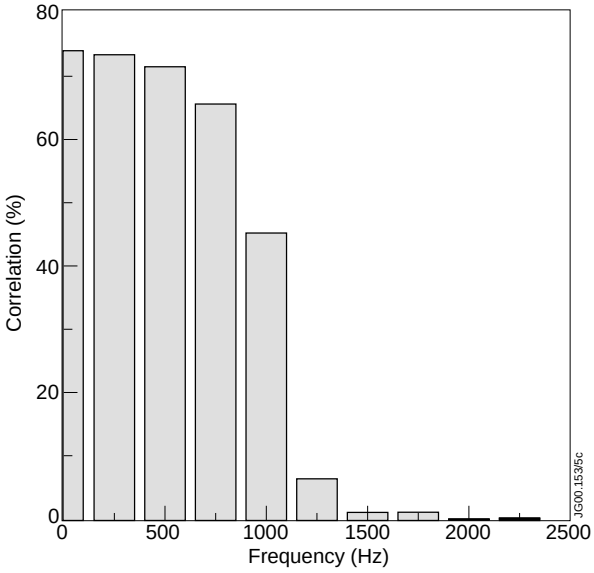

Fig.17.5: Correlation of the vertical plama movement with the safety factor q_{95} in different frequency bands.

In the higher frequency range the flutter in the magnetic signals might originate from noise pick-up from the magnetic probes used for the measurement. This would mean that there is no actual fluctuation of the magnetic configuration with frequencies > 1 kHz. However, this can not be proven from the data.

17.2.4 Discussion of the effects of the flutter in the magnetic configuration

It is useful to divide the fluctuations in the magnetic configuration into two components on a slower and a faster timescale.

1. The slower component (10-100 ms):
   As discussed above, the slower component explains well the changes found in an experiment in the earlier campaign of 1999, where two fixed probes were aligned along one magnetic field line and the correlations showed unexpected changes on a rather slow time scale of (10-50 ms).
2. The faster component (< 10 ms)
   The fast component could at least in part be resposible for decorrelation of the probes as well as broadening of the correlation function.

17.3. Summary

The fluctuations in the magnetic configuration of the plasma equilibrium can explain the difficulties of the parallel correlation studies and uncertainties of the results presented in [17.1]. It could be shown, that the origin of these fluctuations is almost certainly caused by the vertical instability, at least the fluctuations on time scales slower than 2 ms.

As there is no correlation with the vertical instability on the faster time scale, one might suspect that the apparent fast magnetic flutter is just noise pick-up by the magnetic probes.

Yet, it can not totally be ruled out, that at least a part of the reduction in correlation of the electrostatic fluctuations may be caused by the magnetic flutter. On the other hand, similar experiments on the Wendelstein 7-AS reveal a reduction of the correlation of the electrostatic fluctuations as well - and there exists no vertical instability in a stellarator (no current drive).

Further analysis is planned to address this problem by the use of a simple decorrelation model and preliminary results of this modelling indeed show changes in time lag and amplitude of the correlation on the experimentally observed timescales.

17.4 Shot List

Shot	Type	Time [s]	Line averaged density (net/av) [10^{19} m^{-3}]	Plasma current (magn/ipla) [MA]	Toridal field (magn/bvac) [T]
49538	Ohmic	71.5	2.17	-2.4	-1.929
49539	Ohmic	71.5	2.18	-2.4	-1.931
49540	Ohmic	71.5	2.18	-1.14	-1.935
49699	Ohmic	71	1.99	-2.38	-1.940
49705	Ohmic	75	1.04	-1.25	-1.068
49706	Ohmic	75	2.02	-1.26	-1.068
49708	Ohmic	75	2.26	-1.33	-1.068
49709	Ohmic	75		-1.33	-1.078
49729	Ohmic	75	1.93	-1.33	-1.073
49730	Ohmic	74	1.9	-1.33	-1.067
49731	Ohmic	74	1.92	-1.33	-1.067

17.5 Acknowledgements

S. Gerasimov, V. Drozdov and G. Lloyd for helping to get familiar with the EFIT Code and useful discussions. F. Sartori for discussions about the vertical instability feedback and M. Endler for many fruitful discussions.

17.6 References

[17.1] H. Thomsen, M. Endler et. al., EPS-Paper 1999

[17.2] M. Endler, J. Nucl. Mat. 1999, vol. 266-269 and references therein

[17.3] Zeiler et. al., Phys. Plas. 1996, p. 2951 and p. 3947

[17.4] S Scott, Plas. Phys. Nucl. Fus. 1997, p. 1635

[17.5] E Perrone and J A Wesson, Nucl. Fus. 1981, p.871

18. TURBULENT TRANSPORT STUDIES IN JET EDGE PLASMAS IN X-POINT CONFIGURATIONS

I. García-Cortés[1], A. Loarte[2], R. Balbín[1], J. Bleuel[3], A. Chankin[4], S.J. Davies[4], M. Endler[3], S.K. Erents[4], C. Hidalgo[1], G.F. Matthews[4], H. Thomsen[5].

JET Joint Undertaking, Abingdon, Oxfordshire, OX14 3EA, UK.

1 Asociacion EURATOM-CIEMAT, 28040 Madrid, Spain.

2 EFDA Close Support Unit Garching, Max-Planck-Institut für Plasmaphysik, Boltzmannstrasse 2, D-85748 Garching, Germany.

3 Max-Planck-Institut für Plasmaphysik, IPP-EURATOM Association, Boltzmannstrasse 2, D-85748 Garching, Germany.

4 EURATOM/UKAEA Fusion Association, Culham Science Centre, Abingdon, Oxfordshire, OX14 3DB, UK.

5 Max-Planck-Institut für Plasmaphysik, EURATOM Association, Greifswald, Germany

18.1. Overview

Turbulent transport is normally regarded as the mechanism responsible for the anomalous edge transport in tokamaks. Most of the experimental observations that form the basis for such hypothesis come from experiments in which the plasma is limited by a material element (limiter configuration). For divertor discharges it is assumed as well that turbulent transport is the driving mechanism of anomalous edge transport. However, the experimental basis for such assumption is more sparse. In principle, there are characteristics of divertor discharges that could lead to significatively different transport mechanisms, such as the large magnetic shear at the edge and drifts associated with the gradients of plasma edge parameters.

Reciprocating Langmuir probe measurements have been obtained in dedicated JET divertor experiments to investigate turbulent transport at the edge and SOL plasmas. The plasmas for which measurements exist include Ohmic, L-mode and H-mode regimes. Comparable measurements have been carried out in limiter discharges, which allow the direct experimental comparison of the different observations in limiter and divertor discharges.

From the measurements obtained the turbulent radial particle flux, radial velocity and diffusion coefficient have been calculated. These values have been compared with results for similar plasma conditions from 2-D plasma edge code B2-EIRENE. Qualitatively, the experimental results and the modelling calculations show a similar behaviour with the radial particle flux increasing from inside the separatrix to some point in the SOL (close to the separatrix) and then decreasing again. However, there is a large quantitative disagreement between code calculations and measurements. In particular, the turbulent particle flux measured in JET (at the top of the plasma), if it were poloidally uniform would lead to energy convective losses incompatible with global power balance. At present two explanations have been put forward to explain these observations. First, temperature fluctuations (not measured in JET) with the appropriate phase could substantially modify the derived particle turbulent flux, although no

evidence for that exists from other machines. Second, code simulations that include the effect of drifts at the plasma edge show that large convective cells can appear in this region leading to large parallel flows in the SOL, which have been measured. Such drifts could lead to a net inwards particle pinch which could compensate for the measured large turbulent out flux.

18.2. Results

18.2.1 Experimental Results

The experiments reported in this paper were carried out in the Joint European Torus (JET Gas-box Pumped Divertor) [18.1] boundary plasmas. The plasmas were produced in limiter and X-point magnetic configurations.

The turbulent particle transport has been studied in the JET plasma boundary with a Langmuir probe array, the details of the probe design is in ref [18.2]. The system is installed at a major radius of R=3.253 m, on the top of the machine. The plasmas for which measurements exist include Ohmic, L-mode and H-mode regimes. Comparable measurements have been analysed in limiter discharges [18.2], which allows the direct experimental comparison of the different observations in limiter and divertor discharges.

To determine if the edge particle transport is dominated by anomalous turbulent diffusion, we compare $\Gamma_r = \left\langle \tilde{n}\tilde{E}_\theta \right\rangle / B_T$ across changes in confinement regimes. We normalize Γ_{turb} to the local electron density, n_e, measured by the Langmuir probe. This normalization creates a quantity which mimics a real radial velocity coefficient and which is equivalent to an effective radial velocity, v_{reff}, in the B2-EIRENE local transport analyses. Moreover, this coefficient is not affected by the uncertainties in the probe area, it only depends on the correlation of ion saturation current and poloidal electric field fluctuations, as the relation: $v_{reff} = \left\langle \tilde{I}_{sat}\tilde{E}_\theta \right\rangle / I_{sat} B_T$.

The profiles shown in fig.18.1 have been measured in the ohmic phase of the shot 46571 (B_T = 1.4 T, I_P = 1.8 MA and $\langle n_e \rangle$ = 1.5 10^{19} m^{-3}). The position of the Last Closed Flux Surface (LCFS) is determined by magnetic equilibrium codes. The accuracy of the magnetic code calculations is about ±10 mm, at the outer mid-plane of JET. Different

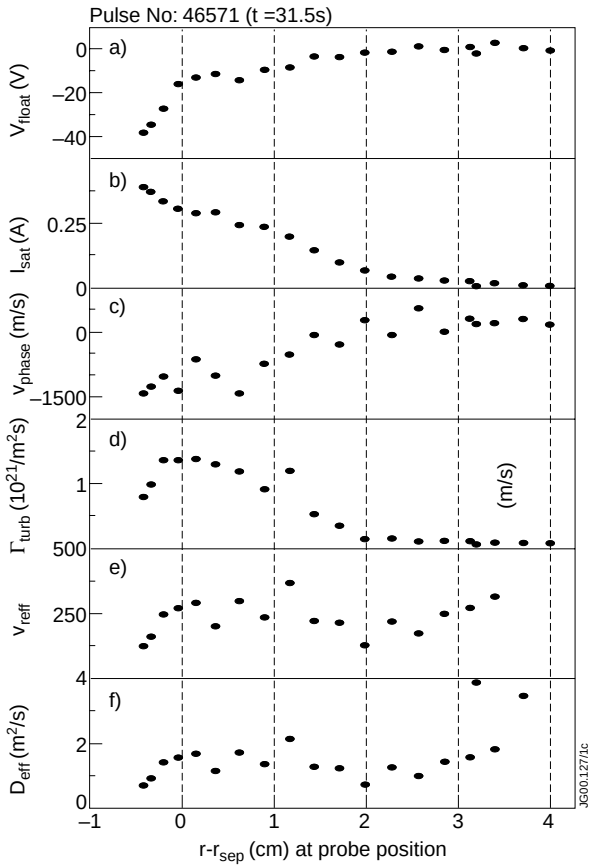

Fig.18.1: Radial profile of floating voltage (a), ion saturation current (b), poloidal phase velocity of the fluctuations (c), E×B turbulent particle flux (d), radial effective velocity (e) and diffusion coefficient from turbulent measurements (f).

fluctuating quantities are plotted in fig.18.1 versus the distance from the LCFS mapped at the probe position.

The ion saturation current increases and the floating voltage goes to more negative values as the probe moves into the plasma edge (figs 18.1b and 18.1a, respectively). The normalized ion saturation current density fluctuation levels approaches 60 % near the wall and decreases across the SOL as the probe moves towards the edge of the main plasma, reaching values about 20 % at the separatrix and 10 % at the innermost probe position. Similar results have been obtained in other devices [18.3, 18.4] and in JET limiter configuration [18.2]. The poloidal phase velocity of fluctuations (fig.18.1c) is not well defined far in the SOL and becomes negative (in the electron drift direction) close to the LCFS and into the edge of the main plasma. The radial position where this change occurs is called the velocity shear layer (VSL) [18.5]. In all the analyzed cases in X-point configuration and in this particular shot (see fig.18.1c) *the velocity shear location seems to be at least (1-2) cm outside the LCFS, in the SOL region*. On the other hand the VSL in limiter plasmas has been localized to be around the limiter radial location or into the edge of the main plasma [18.2]. That can be an indication of the different origin of the radial electric field between SOL plasmas created by limiter and X-point configuration. The poloidal wave number is in the range of k_θ = (1-1.5) cm^{-1} and changes sign at the velocity shear layer radial position as is observed in limiter magnetic configuration.

The radial profile of the time averaged turbulent flux is shown in fig.18.1d. The maximum of the flux is localized about the LCFS calculated by the magnetic codes. *The maximum of the turbulent particle flux is about a factor (3-5) larger than in limiter magnetic configurations [18.2], which seems to be in contradiction with the plasma global particle and energy confinement time*s. Figure 18.1e shows the radial profile of the effective radial velocity calculated from fluctuating parameters. This velocity shows a maximum about the separatrix position, which is probably induced by the maximum in the turbulent particle flux. The comparison between these experimental values with code predictions will be carried out in next section.

Figure 18.2 shows the turbulent particle flux in a frequency resolved plot (in a frequency band of 2 < f < 250 kHz). These values are plotted for three different radial positions, in the SOL region (r-r_{sep} = 2 cm) (fig. 2.2a) at the LCFS (r-r_{sep} = 0 cm) (fig.18.2b) and in the edge

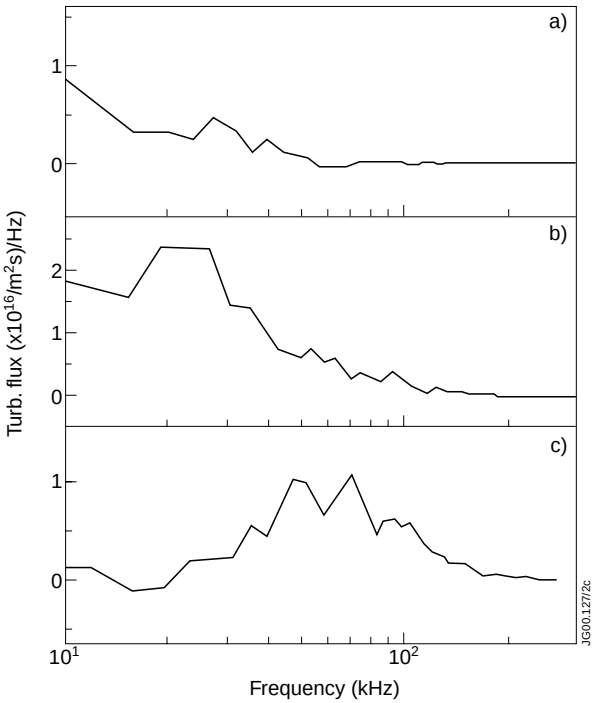

Fig.18.2:. Turbulent flux resolved in frequencies, for three radial positions: SOL (a), at the LCFS (b) and into the edge of the main plasma (c).

of the main plasma (r-r_{sep} = -1 cm) (fig.18.2c), being calculated the LCFS position by magnetic codes. The coherency and the phase between poloidal electric field and ion saturation current are critical for the estimation of the radial turbulent particle flux. With the data shown in fig.18.2 it has been found that the contribution of the low frequency range dominates the turbulent flux in the SOL region. In contrast, the contributions from high frequencies become significant as the probe goes towards the edge of the main plasma while turbulent transport at low frequency in this region is almost negligible.

Turbulent particle flux measurements have been also carried out in plasmas with different NBI power heating in order to determine whether or not there are any trend with heating power in the characteristics of the turbulence. The shot analysed was produced with a power scan and the global plasma parameters are kept constant: 46576 (I_P = 2.8 MA, B_T = 3 T and n_e = 3.5 10^{19} m^{-3}). Figure 18.3 shows the radial profile of the turbulent flux (fig.18.3a), the density normalized fluctuation levels (fig.18.3b) and the effective radial velocity calculated from the turbulent fluxes (fig.18.3c) for three different NBI heating: 1, 2 and 5 MW. The density decay length is about 0.7 cm at the outer mid-plane, in the three cases. The D_{perp} calculated from this measurements does not show any trend with power, and its value is about 1 m^2/s at the LCFS position, which is approximately one order of magnitude larger than the D_{perp} expected from the power balance and the code analyses. The conclusion extracted from this preliminary analysis is that no *significant differences in the turbulent transport in L-mode with different NBI heating, have been observed*.

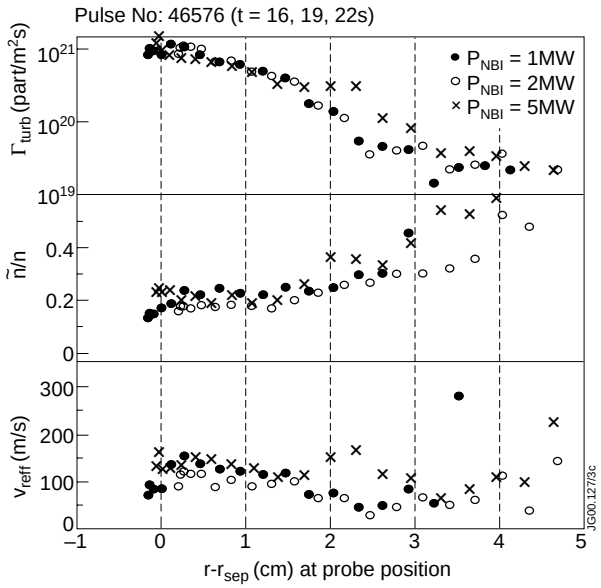

Fig.18.3: Radial profile of turbulent flux (a), normalized density fluctuations (b) and radial effective velocity (c) for three power heating: 1, 2 and 5 MW.

The comparison of the turbulence behaviour between ohmic plasma, #46580 (I_P= 1.3 MA, B_T= 1 T and n_e = 1.5 10^{19} m^{-3}) and H-mode plasma, #46584 (I_P= 0.9 MA, B_T= 1 T and n_e = 3.5 10^{19} m^{-3}) is shown in fig.18.4. The data in H-mode were taken between ELMs, with ELMs more than 50 ms apart from the time of the measurements. Strong changes in the edge profile and turbulent transport parameters have been found between these two plasma regimes. The Isat profile (fig.18.4) steepens and the poloidal phase velocity of the fluctuations (fig.18.4b) seems to show stronger radial electric field in H-mode. *The turbulent fluxes are reduced on the top of the plasma by at least one order of magnitude in H-mode relative to the ohmic plasmas* (fig.18.4d) and a dramatic reduction of the effective diffusion coefficient have been found in part of the SOL (fig.18.4e).

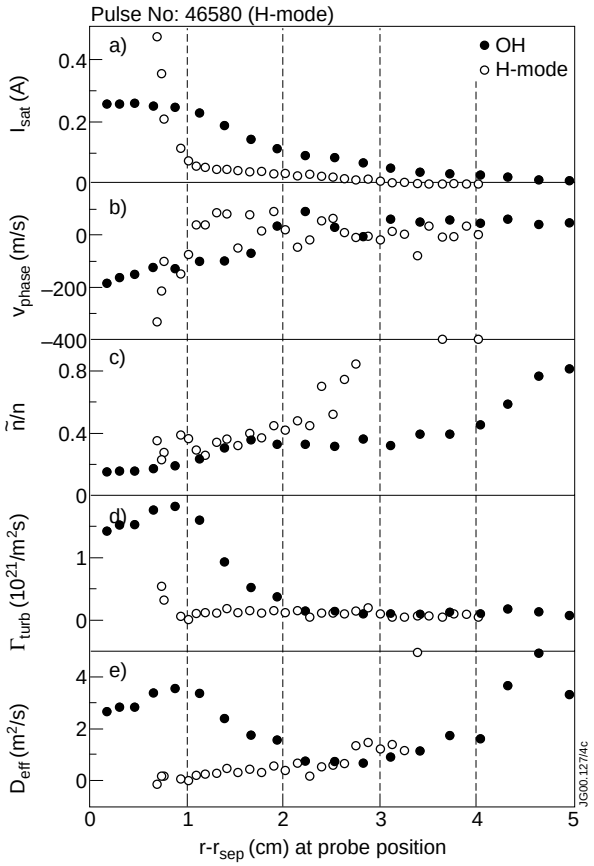

Fig.18.4: Radial profile of ion saturation current (a), poloidal phase velocity (b), normalized fluctuation levels of density (c), turbulent particle flux (d) and effective diffusion coefficient (e), for ohmic and H-mode plasmas. The H-mode data stop 1cm outside the separatrix because of arcing in the probe.

As is observed in the limiter phase [18.2] and in other machines [18.6], the analysis of the floating potential fluctuation spectra shows the existence of three distinct fluctuation ranges. In each of these ranges, and in the absence of MHD activity, the spectrum is well described by an algebraic function. In the lowest frequency range, the spectral decay index seems to be independent of the frequency and the spectrum is basically flat. In the highest frequency range, the spectral decay index is of the order of –2 or even higher. The most interesting region is the intermediate frequency range. In this range, the spectral decay index is around –1 when the Doppler shift effects induced by the plasma velocity has been taken into account. *It is interesting to note that the frequency region where the spectrum shows a decay index close to -1 corresponds to the frequency range where the turbulent particle flux spectral function is maximum*. That is found both in the SOL and in the edge of the main plasma. On the other hand, in the framework of SOC models, this 1/f behaviour arises from the existence and ramdon superposition of avalanches [18.6].

18.2.2 B2-Eirene Modelling

B2-EIRENE modelling for typical JET-Gas Box Plasma conditions has been carried out in order to compare the modelled anomalous fluxes with the measurements. In the absence of turbulence measurements, the transport coefficients used in the modelling are determined by the decay length of the temperature and density profiles at the reciprocating probe position in JET. In the simulations presented here four models that produce a density profile with typical decay length of ~ 1 cm have been tested. Model 1 assumes that particle transport at the plasma edge is characterised by a constant diffusion coefficient of 0.1 m^2/s. Model 2 assumes that transport at the edge is characterised by a constant diffusion coefficient of 0.3 m^2/s and an inwards pinch velocity of 5 m/s. Model 5 assumes an Alcator-like scaling of the diffusion coefficient at the plasma edge with density. Model 6 assumes a Bohm-like dependence of the diffusion coefficient at the plasma edge and Model 1B is similar to Model 1 but assumes a radial increase of the

transport coefficient in the SOL with distance to the separatrix. The diffusion coefficient profiles for these models are shown in fig.18.5a.

In the vicinity of the separatrix all density profiles are similar despite the different transport assumptions. This indicates that transport phenomena along the filed line have a deep influence in determining the shape of the density profiles in the SOL of JET Gas-Box discharges. The corresponding anomalous fluxes driven by the different transport mechanisms are given in fig.18.5b. All show an increase of the perpendicular flux when moving from the plasma into the SOL with maximum located at typically (5–8) mm from the separatrix at the midplane. The anomalous flux decays with distance from the separatrix in the SOL. *The shape of the modelled profile shows the same qualitative trends as the experimental measurements but the values of the anomalous flux are typically an order of magnitude lower.*

Density scans with these transport assumptions reveal some qualitative trends which can be used to determine which of these models compares best with experiment, in terms of the changes of the decay length with density and the perpendicular anomalous velocity. The e-folding length increases with density for all transport assumptions at sufficiently high densities.

Comparison of the anomalous velocity obtained with two different models for all calculated density scans is shown in Fig.18.6a (Model 1) and 18.6b (Model 6). The first obvious conclusion is that *the modelled values in the vicinity of the separatrix are typically more than an order of magnitude smaller than*

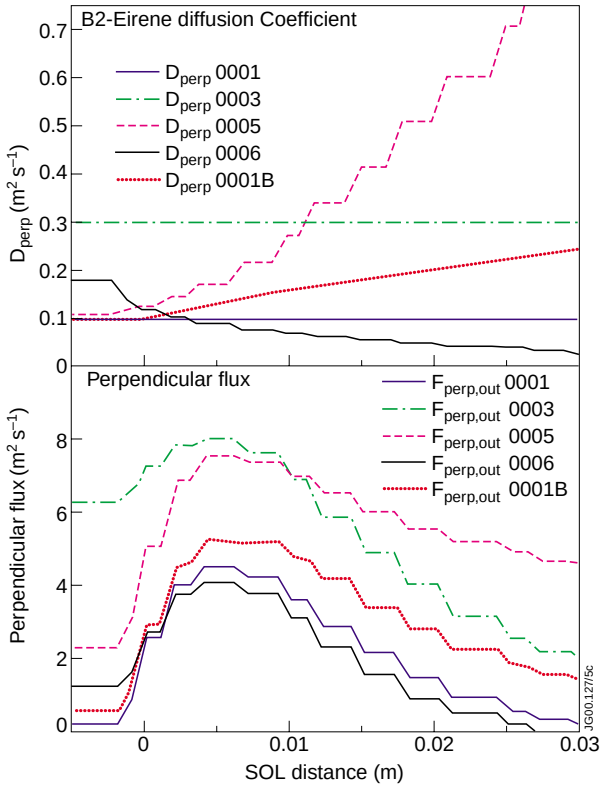

Fig.18.5: Radial profiles of the diffusion coefficient (a) and calculated anomalous fluxes (b) for the different models for pulse 46576 with 5MW of NBI.

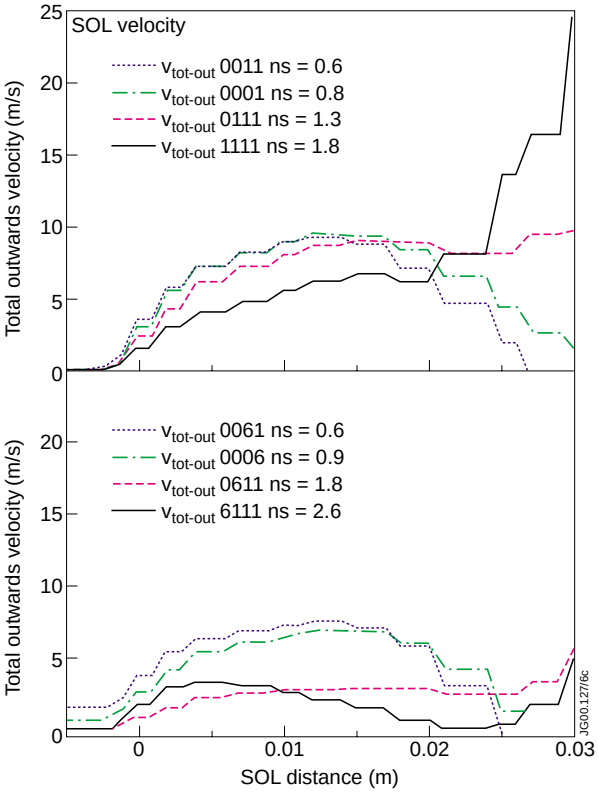

Fig.18.6:. Anomalous velocity across the SOL for the Model 1 (a) and Model 6 (b) density scan for pulse 46576 with 5MW of NBI.

the measurements, in the same way as the anomalous particle fluxes. The shape of the velocity profiles is very transport model dependent. The shapes for model anomalous velocity from Models 5 and 1B seem to be in contradiction with experimental measurements. All models show some decrease of the velocity with density but the size of the decrease is very transport model dependent.

Two conclusions can be extracted from these preliminary studies. One is that the disagreement between the measured and calculated fluxes in the SOL indicates the existence of complex particle transport phenomena in the SOL of diverted discharges and/or questions the diffusive nature of the SOL particle transport. There is evidence that large parallel flows exist in the SOL of JET-Gas Box diverted discharges. Such flows can create large convective cells in the SOL so that parallel transport along the field can be significantly different from the modelling calculations presented here (without drifts) and this can influence anomalous perpendicular transport. Comparisons of the predicted trends for the anomalous velocity and the measured one together with SOL thickness and detachment behaviour could be used to determine the transport model which describes best the JET SOL plasmas in diverted discharges following the approach presented here.

18.3. Summary and future directions

18.3.1 Summary

Reciprocating Langmuir probe measurements have been obtained in dedicated JET divertor experiments to investigate turbulent transport in the edge and SOL plasmas. The plasmas for which measurements exist include Ohmic, L-mode and H-mode regimes. Comparable measurements have been carried out in limiter discharges, which allow the direct experimental comparison of the different observations in limiter and divertor discharges.

Differences in the profile of the poloidal phase velocity between limiter and X-point configuration seems to indicate that the radial electric field has different origin for these two magnetic configurations. Furthermore, the turbulent particle flux in divertor plasmas is about one order of magnitude larger than in limiter magnetic configurations (for similar plasma conditions), in conflict with the plasma global particle and energy confinement times.

From the measurements obtained, the turbulent radial particle flux, radial velocity and diffusion coefficient has been calculated. These values have been compared with results for similar plasma conditions from calculations with the 2-D plasma edge code B2-Eirene. Qualitatively, the experimental results and the modelling calculations show a similar behaviour with the radial particle flux increasing from inside the separatrix to some point in the SOL (close to the separatrix) and then decreasing again. However, there is a large quantitative disagreement between code calculations and measurements. In particular, the turbulent particle flux measured in JET (at the reciprocating probe position), if it were poloidally uniform would lead to energy convective losses incompatible with global power balance.

At present, different explanations have been put forward to explain these observations. First, temperature fluctuations (not measured in JET) with the appropriate phase could modify substantially the derived particle turbulent flux, although no evidence for that exists from other machines. Second, a diffusive model might not be adequate to describe transport in divertor plasmas. In particular, code simulations that include the effect of drifts at the plasma edge show that large convective cells can appear in this region leading to large parallel flows in the SOL, which have been measured. Such drifts could lead to a net particle pinch, which could compensate for the measured large turbulent flux. On the other hand, the possible role of large scale transport events (i.e. self organized criticality models), as a mechanism connecting the edge and core regions, should be considered to explain the bursty behaviour of turbulent transport and the 1/f feature for a given range of frequencies in the flux spectrum. The investigation of the dynamic interplay between fluctuations in gradients and ExB turbulent fluxes might help test the importance of diffusive versus SOC transport mechanisms.

18.3.2 Future directions:

18.3.2.1. Experimental proposal (Memo A. Loarte, Sept. 1999)

Measurements of turbulent transport show very large values at the position of the RCP, particularly in divertor discharges and in various plasma regimes. The region of these large fluxes seems to coincide with the region in which a large Mach number for a global flow from the inner to the outer divertor is seen (Erents EPS 99). It is not clear if the parallel flows in any way affect the turbulence measurements, either by some kind of contamination (parallel flows interpreted as radial flows) or because they create convective cells that close through perpendicular transport. In either case, it would be worth to try and repeat some of the turbulence measurements done in the JET-GB campaign in a SOL plasma where the parallel flows are close to zero. This is the purpose of the proposed experiment.

There are two ways of obtaining a low Mach number at the RCP position in JET SOL plasmas: one by using a limiter configuration and the other with a divertor configuration. The best way to lower the Mach number at the RCP in limiter discharges is to use a limiter which is far away from the probe. This was done in JET-Mk0 by limiting the plasma on the lower belt limiter and (best) on the inner wall (Harbour and Loarte JET-P (93) 96).

In divertor discharges, it seems that the Mach number is very low when the density of the plasma is large (Matthews JET-EPW IPP 99).

The proposal, therefore, is to carry out an ohmic discharge limited first on the outer limiter then on the inner wall and followed by a divertor phase and measure parallel and anomalous fluxes with both reciprocating probe systems simultaneously. In order keep the Mach number as close to zero as possible in all phases, a density of around 2-3 10^{19} m^{-3} should be maintained in the three phases. Such a density is close to the density limit at 2MA/2.5T both for limiter discharges and Mk II-GB discharges (Loarte RI-mode Memo 99 and Monk IAEA 99), therefore; care must be taken when doing the gas puff feed forward.

In principle, a density scan and/or power scan using a reference shot: 46571, as a basis for the experiment would be very interesting. It could clarify the role of parallel and turbulent flows in limiter and divertor discharges and, in particular, their possible connection to poloidal drifts.

18.3.2.2. Multiprobe probe and turbulent transport measurements

Turbulent transport has been studied in the plasma boundary of JET tokamak. Turbulent particle transport is consistent with global particle losses in limiter plasmas but this is not the case in divertor plasmas. A more complete picture of particle and energy transport due to fluctuations requires a better knowledge of the level of electron temperature fluctuations. To address this problem, a modified triple probe technique will be developed which should reduce the phase delay errors introduced by finite tip separations in the so called standard triple probe technique. The main difficulty of this JET multiple probe development is to avoid the effects of probe shadowing while reducing the phase delay and decorrelation effects.

A new probe is currently being design. This probe upgrade will allow measurements of electron temperature fluctuations and to study the effect of perturbations due to the probe itself on the edge turbulent ExB transport. These results should be considered as an input in the modelling of the SOL and divertor with 2-D codes.

18.4 Shot List

Shot	Type	Time (s)	I_P (MA)	B_T (T)	$< n_e > (m^{-3})$	P_{NBI}(MW)
45783	Limiter	47	2.2	2.6	$2.0x10^{19}$	
45798	Limiter	47	2	2.4	$1.5x10^{19}$	
46571	(OH)	72	1.8	1.5	$1.5x10^{19}$	
46580	(OH)	73	1.3	1	$1.0x10^{19}$	
46575	L-mode	62	2.8	3	$3.5x10^{19}$	5
46576	L-mode	56, 59, 62	2.8	3	$3.5x10^{19}$	1,2,5
46584	H-mode	68.5	0.9	1	$3.0x10^{19}$	2

References

[18.1] Keilhacker M. and the JET Team Nucl. Fusion **39** (1999) 209.

[18.2] García-Cortés I *et al* 2000 *Plasma Phys. Control. Fusion* **42** 389.

[18.3] García-Cortés I *et al* 1992 *Phys. of Fuids* **B 4** 4007-4011.

[18.4] Giannone L, Balbín R, Niedermeyer H *et al* 1994 *Phys. of Plasmas* **1** 3614.

[18.5] Ritz Ch P, Rhodes T L, Lin H *et al.* 1991 *Plasma Physics and Controlled Nuclear Fusion Research (Proc. 13th Conf. Washington, DC), Vol. 2, IAEA, Vienna* 589.

[18.6] Carreras B.A., Balbín R. B. van Milligen, *et al* 1999 *Phys. of Plasmas* **6** 4615.

19. DENSITY AND TEMPERATURE MEASUREMENTS IN DETACHED RECOMBINING JET DIVERTORS

A.G. Meigs[1], W. Fundamenski[1], C. Jupen[2], A. Larsen[3], S. Loch[4], M. O'Mullane[4], H. Summers[4]

JET Joint Undertaking, Abingdon, Oxon OX14 3EA, UK

[1] EURATOM/UKAEA Fusion Association, Culham Science Centre, Abingdon, Oxfordshire, OX14 3DB, UK

[2] Lund University, Lund, Sweden.

[3] Niels Bohr Institute, University of Copenhagen, Denmark.

[4] University of Strathclyde, Glasgow, UK

(Work done partly in the framework of the JET Joint Undertaking)

19.1 Introduction

Diagnosis of detaching, high-density divertor plasmas is crucial to understanding them. Traditionally, Langmuir probes are used to measure the electron temperature and density at the target plates near the strike point, but the electron temperature (and thereby also the density) becomes unmeasureable below a few eV. An alternative diagnostic method applicable to these conditions has been applied on JET which involves measuring the high-n lines of hydrogen to determine the electron density. Simultaneously, measurements of the continuum near the series limit have been made where photo-recombination effects that are temperature and density dependent can be used to infer the temperature. Photo-recombination continuum modelling codes [19.1] have been constructed at JET using the results of Pigarov [19.2]. Measurements have been made in a variety of high density, detaching plasmas for two divertor geometries of increasing closure (Mark II **AP** and **Gasbox**). L-mode results with inner divertor fuelling will be presented. The line-averaged electron densities and temperatures in these detached Gasbox divertor plasmas are similar to those in the AP divertor at around $1\text{-}3\text{x}10^{20}$ m^{-3} and about 1 eV. However, the behaviour in the approach to detachment can be much different for the more closed Gasbox divertor. In addition, simultaneous measurements of the spectra near the Balmer and the Paschen series limits have been made. Electron densities and temperatures from observations of the spatially resolved Stark/Continuum emission are compared to the results of the Advanced Onion Skin Model[19.3].

Figure 19.1 shows a representative spectrum near the Balmer series limit prior to detachment and during detachment. Figure 19.2 shows the Paschen spectrum near the series limit for a detaching divertor plasma. The Paschen spectrum is not absolutely calibrated in the figure. The diagnostic used consists of 3 spectrometers viewing the divertor via a mirror link from above. The lines of sight are around 13 mm in radial width and 150 mm of the outer divertor (around 80% in Mark II Gasbox) can be imaged. See [19.1,19.4] for a more detailed description of the diagnostic.

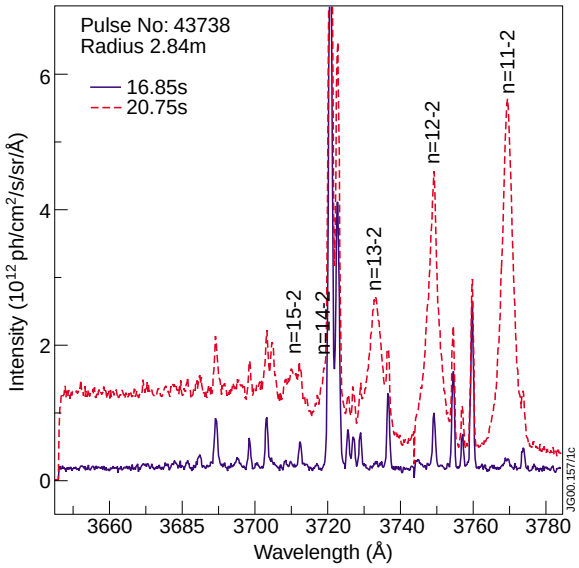

Fig.19.1: Sample Balmer spectra

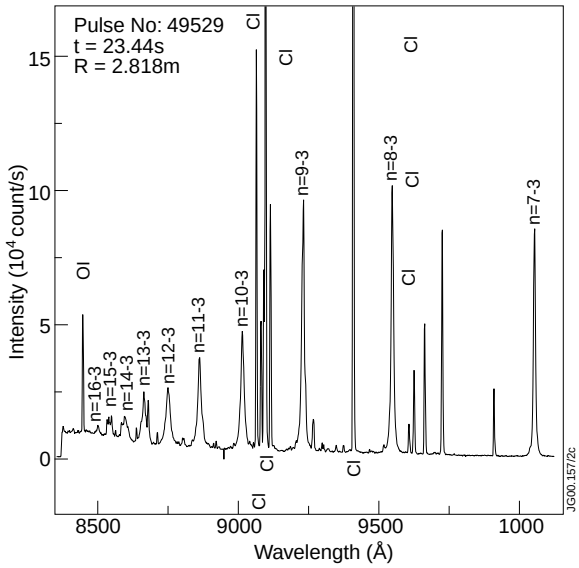

Fig.19.2: Sample Paschen spectra

19.2 Results

19.2.1 Method

Electron density and temperature can be inferred from various features of the Balmer and Paschen spectrum. Stark broadening of the high-n transition lines give the electron density weighted by the emissivity along the line of sight. The electron temperature can be inferred from one of three methods: the photo-recombination continuum, the ratio of intensities of the high-n hydrogen lines, or from the ratio of the intensity of the high-n hydrogen lines to the continuum away from the series limit. The first two methods have been used.

For the electron density profiles from the Stark broadening the spectrum is fit using Voigt profiles to the Stark broadened lines with the Gaussian component fixed to the instrumental width. It is assumed that the Lorentzian FWHM of the Voigt profile is same as the Quasi-Static Stark Effect profile width to derive n_e. Also, the fit includes only the transitions up to 13-2 and 10-3 respectively to avoid the photo-recombination baseline. Figure 19.3 shows a typical fit. Initial analysis of density profiles from the same pulse for the Balmer 11-2 line and the Paschen 8-3 and 7-3 lines shows reasonable agreement between the 8-3 and the 11-2, but the 7-3 deviates..

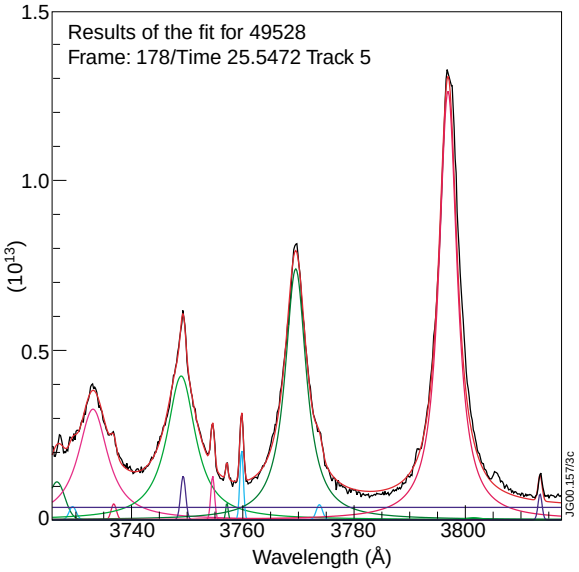

Fig.19.3: Example of a Balmer spectra fit.

For photo-recombination continuum modelling, a single shell for the emission has been assumed. Also, the model is fixed to the experimental data at the long wavelength end (to ~3815Å) 'calibrate' the model. As the model is sensitive to Z_{eff} and the neutral density both of these values are fixed to reasonable plasma values in order to get initial estimates (Z_{eff} ~2.5 and n_n/n_e ~ 0.01). Although there is not room in this paper to present the results graphically, they do yield electron temperatures in the range of 1 eV or lower during detachment.

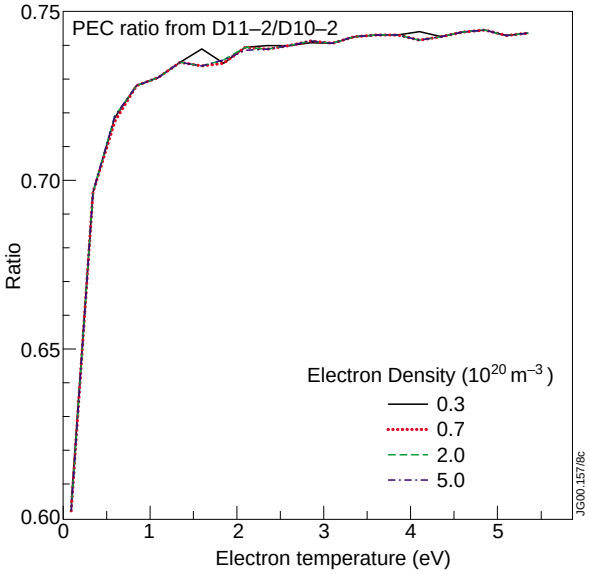

Fig.19.4: ADAS[19.4] results for the line ratio 11-2/10-2.

The other method used to estimate the electron temperature is the Balmer emissivity ratio of the 11-2 to the 10-2 transition. The emissivity as a function of n_e and T_e is taken from ADAS[5] for recombination only. The n_e dependence is negligible over the range T_e 0.2-5.0eV and n_e (0.3- 5)x10^{20} m^{-3}. As shown in fig.19.4, the ratio is insensitive outside of 0.5 to 1.5 eV, but is a clear indicator for Te going through 1eV.

19.2.2 Divertor Closure's effect on the Density Profile Behaviour (Mark II AP and Gasbox)

Four L-modes discharges are considered with nominally I_p=2MA, B_T=2.4T, P_{NBI}=1.9MW and inner divertor fuelling. Figure 19.5 shows the global behaviour of the pulses. The central line-averaged densities are nearly the same at the time of disruption. The Gasbox requires much more fuelling to detach in the outer divertor than the AP divertor. This may just a measure of how the septum separates the inboard divertor chamber from the outboard. Figure 19.6 shows the electron density (from 11-2) and temperature (ratio of 11-2/10-2) profiles for the pulses. From this figure the following observations can be made: Outer divertor electron density detachment occurs on a slower time scale in the Gasbox than the AP divertor. The Gasbox pulses show three distinct

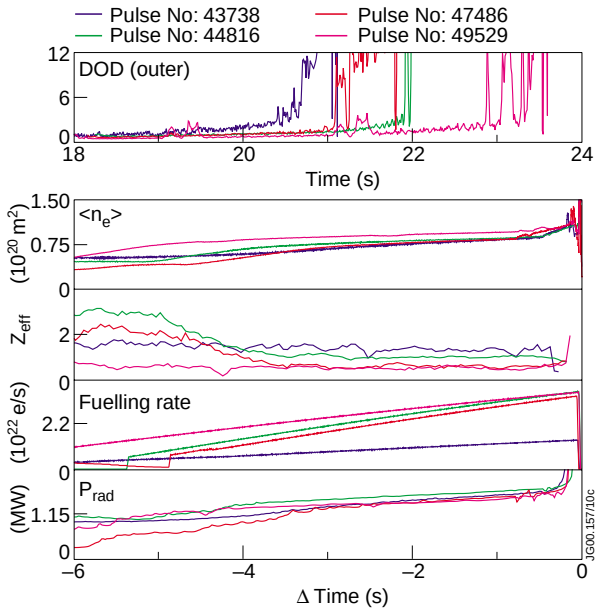

Fig.19.5: Global behaviour of the 4 pulses. 43738 is AP-geometry and the rest are Gasbox. Note absolute time shown in the top figure and the rest show time relative to disruption.

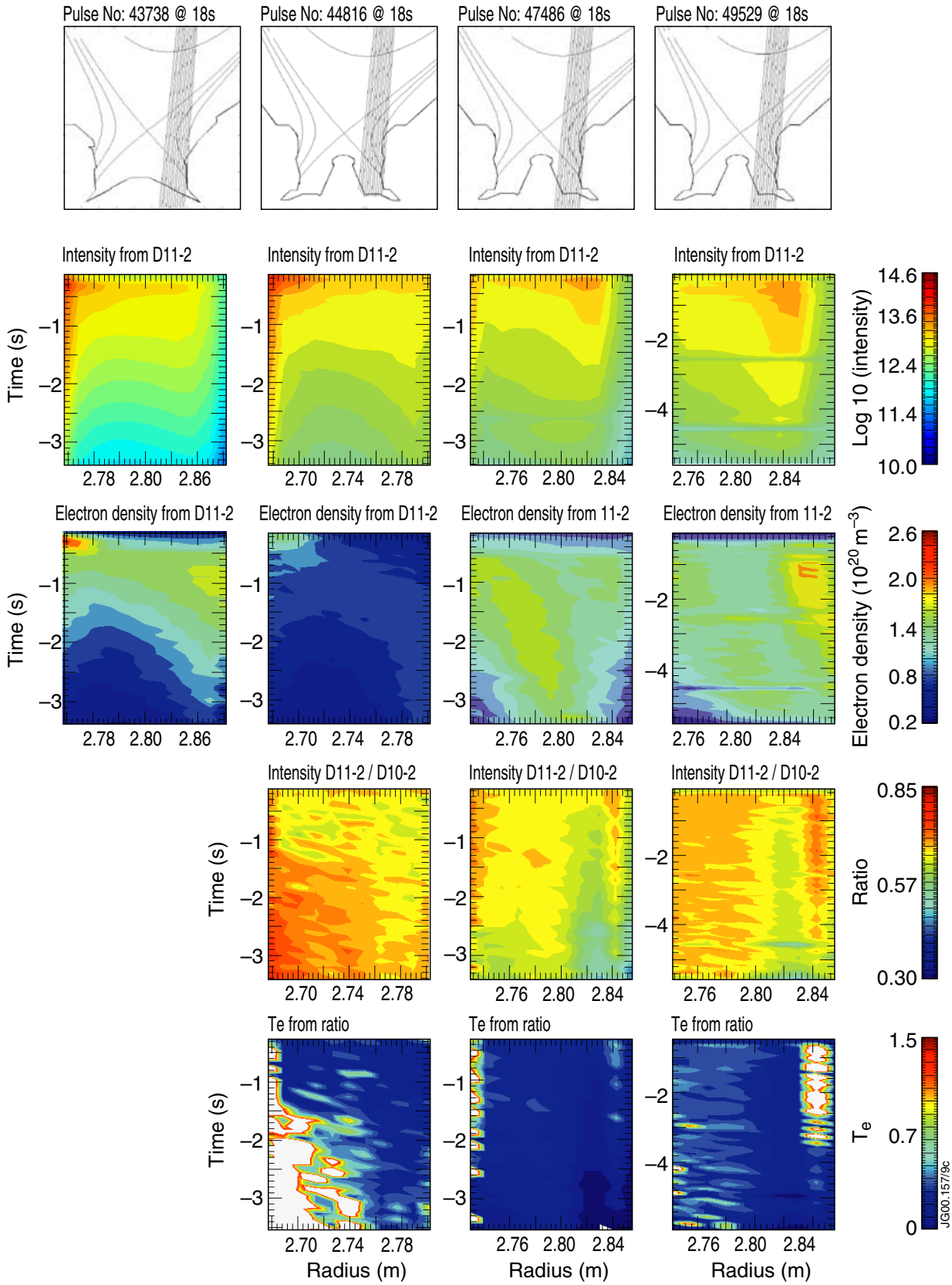

Fig.19.6: D11-2 profiles with pulse geometry shown in the first row followed by intensity of the line, electron density from Stark broadening, the intensity ratio of D11-2 to D10-2 and finally the electron temperature derived from the ratio. The AP pulse (43738) does not have T_e from the ratio as the 10-2 line was not in the spectral range.

behaviours in the electron density profile: ‘quick’ (44816), ‘slow’ (47486) and ‘reluctant’ (49529) to detach. And finally, electron temperatures from line ratios are around 1eV with the coldest spots around the vertical plate moving inwards for the ‘quick’ detachment case (44816). However, hotspots above 1.5 eV are seen which may actually indicate regions where excitation is strong (shown as white regions) or bad statistics. The low spots (< 0.5 eV) should be de-emphasized due to sensitivity

19.2.3 Divertor Onion Skin Model Results for an L-mode Density Limit (Pulse 47486) with comparison to Inferred Electron Density and Temperature

OSM2/NIMBUS reconstructs the 2-D plasma distribution based on target Langmuir probe n_e and T_e measurements, D_α, and plasma conservation equations. Three times are modelled (t=19,20,21 s) corresponding to gradual outer target detachment (DOD rises from 1 to 2). Figure 19.7 shows the global behaviour for the pulse including inner and outer divertor parameters. The input to the onion skin model are: Target Langmuir probe profiles (I_{sat}, T_e). In the absence of information on T_e or I_{sat} in the private flux region, a sharp radial decay is assumed; and D_α profile is taken from the line-of-sight view of the divertor. Probe T_e’s are not reliable below ~ 5 eV so T_e is adjusted (lowered) to match the outer peak in D_α. The output from the model is a 2-D solution of plasma (n_e, T_e, $T_{I,...}$) , neutrals, and line-emission. Figure 19.8 shows the contours shown in the vicinity of the outer strike point. The model shows some signatures of detachment: The ionization front moves away from the target (D_α peak) and the total pressure (static + kinetic) ratio upstream rises; however, a strong recombination front is seen in the simulation only when T_e(Target) < 0.3eV [19.6]. In comparing the onion skin model with the vertical line-of-sight n_e from $D_{11\text{-}2}$ (figure 19.6 third column), the following observations can be made: $n_{e,OSM}$ peak appears closer to target than $<n_{e,D11\text{-}2}>$ and the $n_{e,OSM}$ peak is stationary, although the D_α peak moves away from the target. Further work in the recombination dominated regime (lowering T_e to below 0.3 eV) is expected to better reproduce the experimentally seen behaviour; this work will be pursued in the near future. So far the following conclusions on the simulation can be made: Recombination appears to be necessary to explain the movement of the front away from the target; ‘sub-eV’ target temperatures are required for onset of recombination dominated detachment.

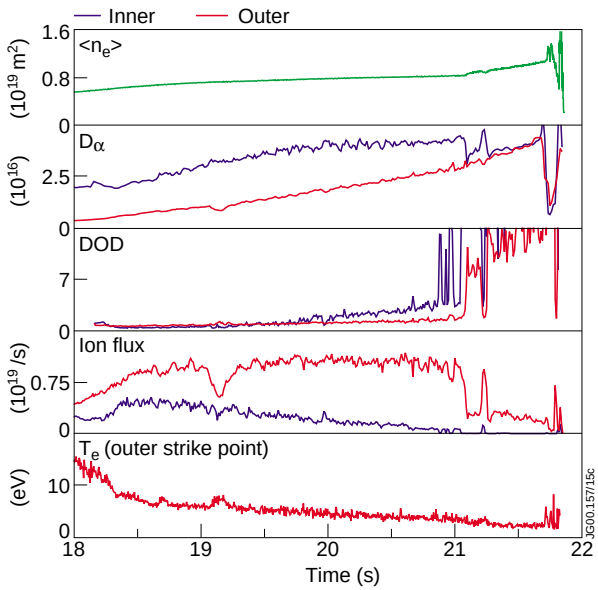

Fig.19.7: The behaviour of 47486 for both inner and outer divertor.

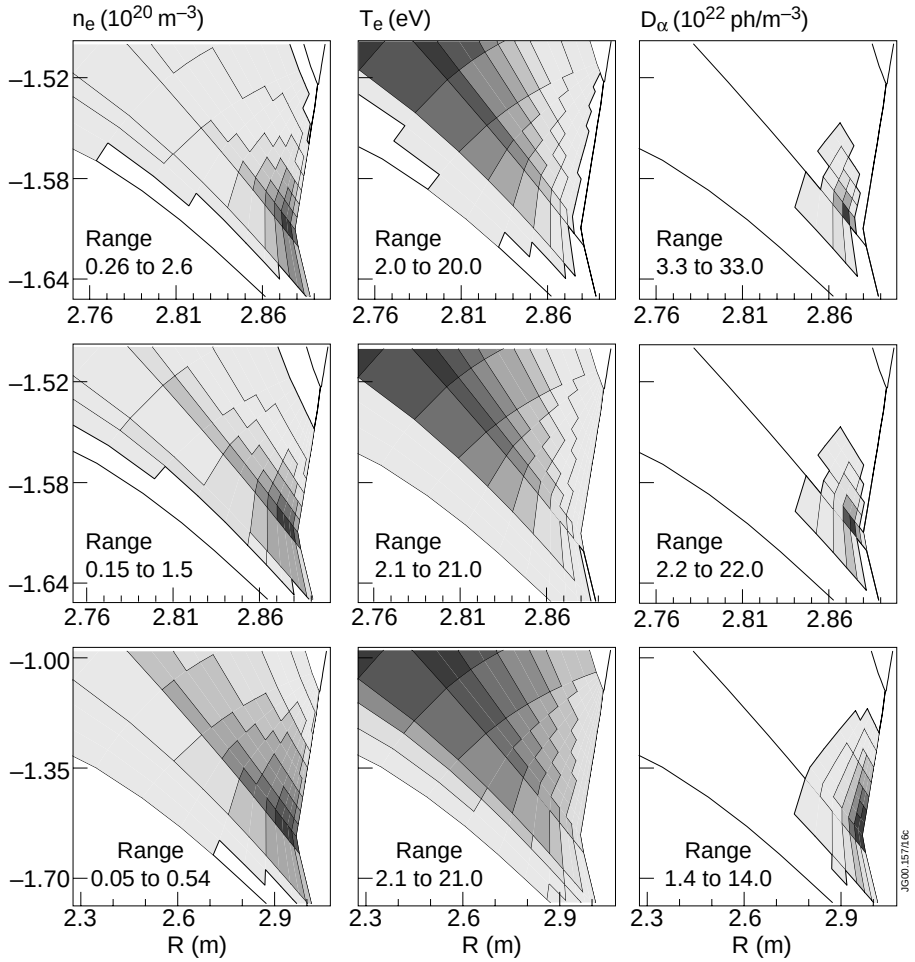

Fig.19.8: Output from the onion skin model for n_e, T_e and D_α. Time increases going upwards from 19, 20, and 21 s.

19.3 Summary and future directions

At JET many measurements of the behaviour of the Balmer and Paschen series in high density discharges have been made. Analysis codes are still in their infancy. The fitting package is progressing, but needs refinement. The continuum model(s) need to be included as part of the least squares fit, and simple model(s) for line-of-sight integrals are needed to obtain more realistic modelling of the data (the single shell model is probably not sufficient). Finally, much more is needed in comparing the experimental results to divertor plasma models.

19.4 Shot List

In the JET Mark IIAP both vertical and horizontal target plate diverted plasmas were observed in both L-mode and H-mode high density/density limit pulses. In Mark II Gasbox the discharges were predominately vertical plate strike points although there are a few corner strike point pulses. Table 1 shows a subset of the pulses observed consisting of L-mode density limits. Note that the diagnostic subsystem (KT3C) used to obtain the Paschen series data was not available until the autumn of 1999 (around pulse 49012). In the table the pulses marked in bold have been initially analysed for density profiles from the Stark broadening. 47486 is the only pulse for which initial OSM2 modelling to Balmer spectra measurements have been performed.

Table 1. Pulse list.

Description	Pulses		
AP vs GB Vertical	**AP: 43738**	**GB: 44816, 47486, 49529**	
AP Horizontal vs. Vertical	**43735**	**43738**	
AP 320 vs. AP 150 Horizontal	**43735 @ 320C**	**43759 @ 150C**	
AP 320 vs. AP 150 Vertical	**43738**	43766	
GB Hydrogen vs. Deuterium	**Hydrogen: 48348** or 48334	**Deuterium: 44816, 47486 or 49529…**	
GB Inner divertor fuelling versus outer divertor fuelling	**Inner: 49529 Outer: 49528**	Inner: 44893	Outer: 44895
GB Paschen vs. Balmer Results	**49529…**		
T_e from Pigarov/Larsen Model	47486		

Acknowledgements

This work was partly supported by EURATOM and the UK Department of Trade and Industry

References

[19.1] A. Larsen, Master's Thesis, Niels Bohr Institute, University of Copenhagen, 2000.

[19.2] A.Y Pigarov, J.L Terry, B.Lipschultz,, MIT report PFC/JA-97-26, 1999

[19.3] W. Fundamenski, U. Toronto, Ph.D. Thesis, 1999 and Plasma Surface Interactions-14, 2000

[19.4] A.G. Meigs et al, Proceedings of 1998 ICPP & 25th EPS CCFPP, Prague Czech Republic

[19.5] H. Summers et al, JET Report IR(94) 06, JET Joint Undertaking

[19.6] W. Fundamenski, Plasma Surface Interactions-13, 1998

20. TASK FORCE P ITER DATABASE ENTRIES

D. McDonald[1], L.D. Horton[2].

JET Joint Undertaking, Abingdon, Oxfordshire, OX14 3EA, UK.

[1] EURATOM/UKAEA Fusion Association, Culham Science Centre, Abingdon, Oxfordshire, OX14 3DB, UK.

[2] Max-Planck-Institut für Plasmaphysik, IPP-EURATOM Association, Boltzmannstrasse 2, D-85748 Garching, Germany.

From data acquired during Task Force A/P experiments entries have been made into two types of ITER database, the global confinement database and the edge pedestal database.

20.1 Global confinement database entries

Inclusion of pulses in the confinement database requires the selection of stable pulses showing steady confinement, typically for at least two energy confinement times. The “good” time windows are then marked by physicists and data is then read in, through an automated procedure, before being validated by the physicists.

Task force P produced 65 pulses for the global confinement database. These are principally ELMy H-mode discharges, but also include a number of L-mode discharges (46933 and 46985) from the edge impurity experiments. The data provides good ITER relevant data, especially regarding high currents and high densities (through pellet fuelling). The pulses are listed in Table 20.1.

Table 20.1 Task Force P pulses entered into the ITER Global Confinement Database

49054	49056	49065	49078	49080	49081	49082	49238
49243	49244	49246	49247	49248	49249	49250	49251
49252	49454	49456	49470	49472	49473	49474	49475
49478	49480	49481	49482	49498	49501	49502	49503
49504	49510	49511	49512	49514	49515	49516	49519
49520	49521	49547	49548	49555	49557	49687	49688
49689	49690	49691	49693	49694	49695	49722	49723
49724	49726	49727	49728	49729	49730	49731	49732
49739							

20.2 Edge Pedestal Database Entries

From data taken during the Autumn 1999 Task Force P campaign 38 entries are being made to the ITER Edge Pedestal Database. These pulses are listed in Table 20.2.

Table 20.2 Entries being made from the Autumn 1999 Campaign into the Pedestal Database

Pulse	T_{DATA}	T_1	T_2
49054	58.3618	55.5313	59.2711
49056	57.8722	56.2072	58.6853
49078	63.1354	61.9750	63.8224
49080	61.6258	60.8498	61.9637
49470	55.8730	54.3091	56.1165
49472	57.1378	55.5044	57.4819
49473	57.3826	55.8279	57.7905
49474	57.3826	56.3069	58.0475
49475	57.3826	55.8922	58.2227
49510	56.3762	55.5465	56.6746
49511	58.3618	56.4581	59.5371
49512	58.6474	55.7739	59.7206
49514	58.8922	56.4293	59.7260
49515	58.6474	57.0451	59.7561
49516	58.8922	55.7009	59.7110
49519	60.3610	59.8202	60.8148
49520	58.3618	56.1965	59.2980
49521	59.1370	58.2078	59.6831
49547	63.8698	63.2253	64.4819

Pulse	T_{DATA}	T_1	T_2
49548	61.8842	61.4925	62.2209
49555	63.1354	62.0100	63.7673
49557	63.8698	62.7635	64.1684
49687	64.4002	63.2495	64.9049
49688	66.3994	65.7277	66.8208
49689	64.4002	61.8991	65.8291
49690	62.8906	60.6688	64.0009
49690	65.1346	64.6165	65.3358
49691	65.8690	63.0317	66.8166
49693	60.6466	59.6753	61.1973
49694	62.6458	61.5558	63.6810
49694	64.8898	64.4101	65.2707
49695	65.3794	61.9829	66.7608
49724	65.1346	63.7352	66.8192
49726	61.6258	57.9981	63.2749
49727	61.1362	59.0788	61.7723
49728	60.6466	59.2599	61.7231
49729	60.8914	58.7660	61.7698
49730	60.8914	59.2666	61.7365